Unravelling the Mystery of Dark Matter with Stars & Black Holes

A Thesis

submitted to the

Tata Institute of Fundamental Research, Mumbai

for the degree of Doctor of Philosophy

in Physics

by

Anupam Ray 

Department of Theoretical Physics

Tata Institute of Fundamental Research, Mumbai

June 2022

Final version submitted in August 2022

Acknowledgements

As I conclude this remarkable journey, I feel indebted to an endless list of people who have been a constant source of encouragement and support over the last few years.

First and foremost, I would like to express my sincere gratitude and regards to my PhD advisor, Prof. Basudeb Dasgupta. No adjective can suffice to express my gratitude towards him. He is the one who encouraged me to learn and work on various different topics, which immensely helped me to broaden my research interests. I really enjoyed the long discussions that we had over the last few years, which not only helped me to think critically, but also to be independent in my research. I thank him for the continuous support and guidance through all these years.

I would also like to thank my collaborators, Prof. Ranjan Laha, Prof. Girish Kulkarni, Dr. Anirban Das, Dr. Aritra Gupta, and Shikhar Mittal for providing me a very pleasant collaborative environment. I have learned numerous things from them via some stimulating discussions. I am also grateful to Prof. Tuhin Roy, Prof. Shiraz Minwalla, Prof. Sourendu Gupta, Prof. Rishi Khatri, Prof. Amol Dighe, Prof. Rajdeep Sensarma and Prof. Kedar Damle for their courses, and for many insightful discussions. Furthermore, I must say that I have benefited a lot from our weekly journal clubs and seminars.

I also thank the DTP office staff for their prompt and efficient help over the last few years. I acknowledge the financial support received from TIFR and the Max Planck Partner Group for Astroparticle Physics.

A big 'Thank You' to all my friends in Jadavpur University and TIFR for the delightful times that we spent together and the memories that we created. Life would have been extremely boring, if you were not there. The list is pretty long, however, I would like to take this opportunity to mention a few names here − Shouvik, Soumen, Mursalin, Subhajit, Aman, Pranav, Rabisankar, Rohan, Ion, Avirup, Sudipta, Jyotirmoy, and Sourav, each of whom has contributed immensely in my life in their own unique way. I am also very grateful to some of my senior colleagues, Jaydeep, Lankeswar, Sabir, Saikat, Sounak, Subhajit, Triparno, and Uttiya for the wonderful discussions that we had over the last few years. A warm thanks to my junior colleagues, Anoma, Arghya, Aritra, Avijit, Siddhartha, Souvik, Sulagna, Unmesh, Zahid, and all the members of 'Bengal Cricket Tigers' for all the indelible moments.

I would take this opportunity to mention someone here − without her this journey is incomplete. Anumita, you have always been there, supporting me through my highs and lows, and listening to me whenever I needed.

Finally, I would like to take this opportunity to convey my heartfelt regards to my parents and grandparents for being my constant support system. I will refrain myself from expressing “thanks” to them, as no words of gratitude can ably be used for that purpose. This thesis is for you.

To my parents & grandparents

Publications included in the thesis:

1. Dark matter capture in celestial objects: improved treatment of multiple scattering and updated constraints from white dwarfs
   Basudeb Dasgupta, Aritra Gupta, **Anupam Ray**
   JCAP 08 (2019) 018, arXiv: 1906.04204

2. Neutrino and Positron Constraints on Spinning Primordial Black Hole Dark Matter
   Basudeb Dasgupta, Ranjan Laha, **Anupam Ray**
   Phys. Rev. Lett. 125, 101101 (2020), arXiv: 1912.01014

3. Dark matter capture in celestial objects: light mediators, self-interactions, and complementarity with direct detection
   Basudeb Dasgupta, Aritra Gupta, **Anupam Ray**
   JCAP 10 (2020) 023, arXiv: 2006.10773

4. Low Mass Black Holes from Dark Core Collapse
   Basudeb Dasgupta, Ranjan Laha, **Anupam Ray**
   Phys. Rev. Lett. 126, 141105 (2021), arXiv: 2009.01825

5. Near future MeV telescopes can discover asteroid-mass primordial black hole dark matter
   Anupam Ray, Ranjan Laha, Julian B. Muñoz, Regina Caputo
   Phys. Rev. D 104, 023516 (2021), arXiv: 2102.06714

6. Constraining primordial black holes as dark matter using the global 21-cm signal with X-ray heating and excess radio background*
   Shikhar Mittal, **Anupam Ray**, Girish Kulkarni, Basudeb Dasgupta
   JCAP 03 (2022) 030, arXiv: 2107.02190
   (*The paper may also be included in the thesis of Shikhar Mittal, and our individual contributions are delineated in the main text.)

Publications not included in the thesis:

1. Galactic positron excess from selectively enhanced dark matter annihilation
   Anirban Das, Basudeb Dasgupta, **Anupam Ray**
   Phys. Rev. D 101 (2020) 6, 063014, arXiv: 1911.03488

ACRONYMS

DM - Dark Matter

SM - Standard Model

BH - Black Hole

PBH - Primordial Black Hole

TBH - Transmuted Black Hole

WIMP - Weakly Interacting Massive Particle

IGM - Inter Galactic Medium

GC - Galactic Center

MW - Milky Way

NS - Neutron Star

WD - White Dwarf

GW - Gravitational Wave

CMB - Comic Microwave Background

DSNB - Diffuse Supernovae Neutrino Background

AMS - Alpha Magnetic Spectrometer

INTEGRAL - International Gamma-ray Astrophysics Laboratory

AMEGO - All-sky Medium Energy Gamma-ray Observatory

EDGES - Experiment to Detect the Global EoR Signature

Contents

1 Introduction **1**

1.1 Evidences for Dark Matter 2

1.2 Properties of Dark Matter 5

1.3 DM Candidates and Searches 6

1.4 Our Contributions & Outline of the Thesis 22

2 White Dwarfs as DM Detectors: Effect of Multiple Collisions **25**

2.1 Particle DM accretion in Stellar Objects 25

2.1.1 Motivations for Multi-scatter Stellar Capture 26

2.2 DM Capture: Effect of Multiple Collisions 28

2.2.1 Capture Probability for N^{th} Collision 29

2.2.2 Capture Rate for N^{th} Collision 30

2.2.3 Maximum Number of Scatterings 31

2.3 White Dwarfs as DM Detectors 34

2.4 Summary & Conclusions 39

3 Neutron Stars as DM Detectors: Effect of Mediator Masses **41**

3.1 DM Capture: Effect of Mediator Mass 41

3.1.1 General Form of $s(z)$ 43

3.2 DM Self-Capture: Effect of Mediator Mass 45

3.3 Neutron Stars as DM Detectors 47

3.3.1 Annihilating DM & Dark Kinetic Heating 49

3.3.2 Non-annihilating DM & Dark Core Collapse 54

3.3.3 Effect of DM Self-interactions on the DM-nucleon Interactions . . 58

3.3.4 Constraining DM Self-interactions from Observation of Neutron Stars 60

3.4 Summary & Conclusions 62

4 Mergers as a Probe of Particle DM 65

4.1 Formation of Low Mass Transmuted Black Holes 65

4.2 Identifying the Origin of Low Mass Black Holes 69

4.3 Summary & Conclusions 75

5 Constraining Ultralight PBHs using Neutrino & Positron Emission 77

5.1 Particle Emission from Ultralight Evaporating PBHs 77

5.1.1 Constraints using Neutrino Emission 80

5.1.2 Constraints using Positron Emission 83

5.2 Summary & Conclusions 86

6 Constraining Asteroid mass PBHs using Photon Emission 89

6.1 Projected Constraints using Photon Emission 89

6.2 Summary & Conclusions 98

7 21-cm Cosmology Constrains Ultralight PBHs as DM 101

7.1 21-cm Cosmology: Preliminaries 101

7.2 Excess Radio Background 106

7.3 Constraining Ultralight PBHs as DM via 21-cm Cosmology 106

7.3.1 Heating and Ionization due to PBHs 106

7.3.2 Inference Procedure 108

7.3.3 Results 113

7.4 Constraints on the Primordial Curvature Power Spectrum 119

7.5 Summary & Conclusions 123

8 Summary and Conclusions 127

A Thermalization timescale 133

B Chandrasekhar Limit for Dark Core Collapse 137

C DM Density Profiles 139

List of Figures

1.1 Galactic rotation curve as an evidence for DM 2

1.2 Observations of the merging galaxy clusters as an evidence for DM . . . 3

1.3 Temperature fluctuation of CMB as an evidence for DM 4

1.4 Mass scale of DM 7

1.5 Three broad avenues to search for particle DM 11

1.6 Consolidated constraints on WIMP-nucleon interaction strength from underground searches 13

1.7 Consolidated constraints on WIMPs annihilating into neutrinos 15

1.8 Consolidated constraints on WIMPs annihilating into photons and other charged SM particles 16

1.9 Constraints on particle DM interactions from collider searches 17

1.10 Consolidated constraint on non-rotating PBHs as DM for a monochromatic mass distribution 21

2.1 Schematic diagram of particle DM accretion in a compact star 27

2.2 Maximum number of collisions that a DM particle encounters inside a stellar object while getting captured 32

2.3 Comparison of the total mass capture rate in single and multiple scattering regime 33

2.4 Comparison of the dark heating due to annihilation of the captured DM particles to the observed luminosity of the white dwarfs in our nearest globular cluster 35

2.5 Constraint on annihilating DM interactions from the non-observation of dark heating in a cold and old white dwarf residing in our nearest globular cluster 37

3.1 Schematic diagram of DM-nucleon scattering in the rest frame of the nucleon and in the center of mass frame 42
3.2 Energy loss distribution of DM for interactions mediated via arbitrary mass mediators 43
3.3 Total number of captured DM particles inside a neutron star for DM-nucleon interactions and DM self interactions 47
3.4 Projected constraints on annihilating DM interactions from the non-observation of dark heating in a neutron star residing in the solar neighborhood with a surface temperature of 1950 K 50
3.5 Estimation of the dark heating for DM interactions mediated by arbitrary mass mediators 51
3.6 Constraints on non-annihilating DM interactions from the existence of a 7 Gyr old pulsar in the solar neighborhood 55
3.7 Total number of captured DM particles inside a 7 Gyr old pulsar for DM interactions mediated by arbitrary mass mediators 56
3.8 Impact of repulsive self-interactions among the dark matter particles on the DM-nucleon interactions 59
3.9 Constraint on DM self-interaction strength from the existence of a 7 Gyr old pulsar in the solar neighborhood 61

4.1 Formation of sub-Chandrasekhar mass non-primordial black holes via gradual accumulation of non-annihilating particle DM in neutron stars 67
4.2 Redshift dependence of the binary merger rates can shed light on particle DM properties 70
4.3 Mass distribution of the compact stars can test the origin of low mass black holes 71

5.1 Spectrum of the Hawking emitted neutrinos from a non-rotating PBH of mass 10^{15} g 78
5.2 Constraints on ultralight evaporating PBHs as DM from non-observation of Hawking emitted neutrinos at Super-Kamiokande 82
5.3 Constraints on ultralight evaporating PBHs as DM from precise measurement of the GC 511 keV gamma-ray line by INTEGRAL 83

5.4 Impact of astrophysical uncertainties on the constraint derived from GC 511 keV gamma-ray line measurement by INTEGRAL 85

6.1 Flux of the Hawking emitted photons for Galactic and extra-Galactic primordial black holes 91

6.2 Comparison of the astrophysical photon fluxes to the photon fluxes from evaporating PBHs 93

6.3 Projected constraint on asteroid mass PBHs as DM from observation of Galactic Center photons in an upcoming soft gamma ray telescope AMEGO for a monochromatic mass distribution 95

6.4 Projected constraint on asteroid mass PBHs as DM from observation of Galactic Center photons in an upcoming soft gamma ray telescope AMEGO for an extended mass distribution 96

6.5 Confidence ellipses for astrophysical background parameters and PBH parameters for the AMEGO analysis 97

7.1 Expected cosmic evolution of the 21-cm brightness temperature from the dark ages to the end of the re-ionization 105

7.2 Time evolution of the gas kinetic temperature in the IGM and the 21-cm brightness temperature in the redshift range of 15 to 28 110

7.3 Marginalized posterior probability distributions for the astrophysical background parameters and the PBH parameters in the absence of any X-ray heating 114

7.4 Best fitting to the EDGES measurement of the global 21-cm signal in the absence of any X-ray heating 115

7.5 Best fitting to the EDGES measurement of the global 21-cm signal in the presence of an X-ray background 117

7.6 Marginalized posterior probability distributions for the astrophysical background parameters and the PBH parameters in the presence of an X-ray background 118

7.7 Constraints on ultralight PBHs as DM from the EDGES measurement of the global 21-cm signal 120

7.8 Constraints on primordial curvature power spectrum from EDGES measurement of the global 21-cm signal assuming a spherical collapse scenario of the primordial black holes 121

List of Tables

4.1 Possible detection rate of TBH mergers in current as well as upcoming GW detectors 74

7.1 Range of the astrophysical parameters that can affect the 21-cm brightness temperature 109

Chapter 1

Introduction

In 1933, the Swiss astronomer, Fritz Zwicky, first conjectured the existence of DM by using an application of the virial theorem to the observations of the Coma Cluster [1]. In this seminal work, he inferred that the total visible mass in this cluster can make up only about 1% of the total mass, which is needed to keep the galaxies in this cluster stable. However, the reality of this missing mass remained in question for a few decades, and the first unambiguous proof of its existence came from the precise measurements of the stellar rotation curve of the Andromeda galaxy in the 1970s [2]. Since then, the existence of DM has been confirmed by several cosmological observations. This includes multi-wavelength observations of the merging galaxy clusters [3], baryon acoustic oscillations and imprints in the CMB spectrum [4], gravitational lensing of the light from distant galaxies and galaxy clusters [5], and observed large scale structure of our Universe [6], etc.

In the current cosmological paradigm, the DM abundance is $\Omega_{\rm DM} = 0.265$, implying 85% of the matter in our Universe is in the form of DM [4]. Despite its enormous abundance, the microscopic identity of this non-baryonic form of matter still remains unknown, and one of the major mystery in modern day science. In this thesis, we aim to unravel this mystery with two fascinating objects in our Universe: Stars & Black Holes. We focus on two types of DM candidates: *i*) elementary particles as DM and *ii*) compact stellar objects such as black holes as DM. More particularly, we explore: *i*) Weakly interacting massive particles (WIMPs) in the mass range of GeV $-$ PeV and *ii*) Primordial black holes (PBHs) in the mass range of $10^{-18} - 10^{-15}\,M_{\odot}$. We show that electromagnetic and GW observation of the compact stars can probe properties of particle DM via particle DM accretion in compact stars and ultralight evaporating PBHs can not be a viable DM

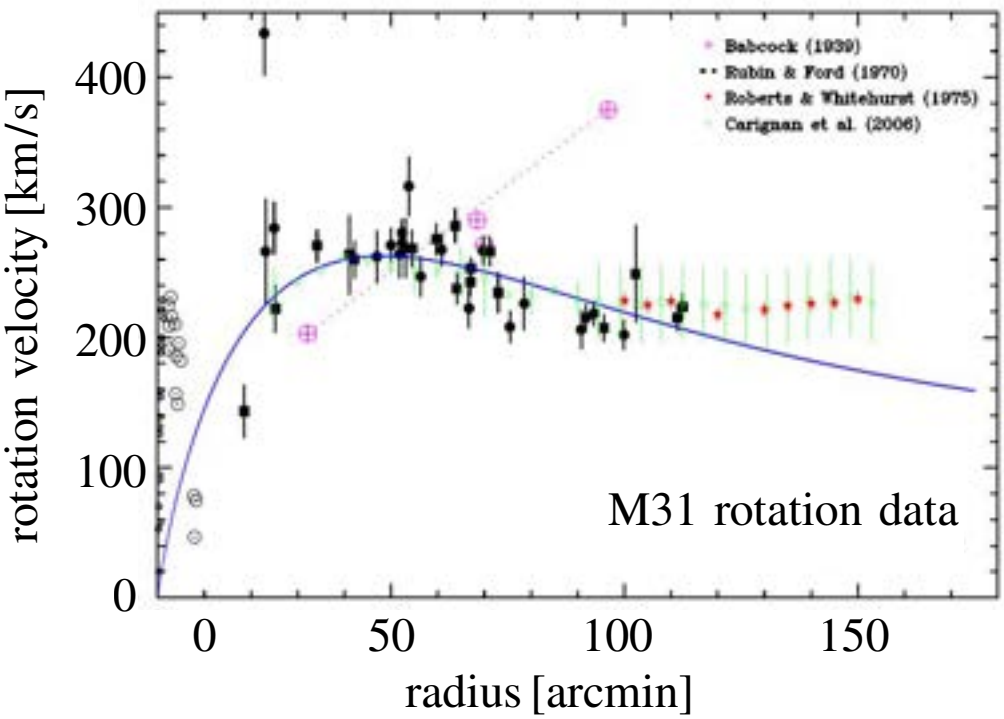

Figure 1.1: Circular velocity of the stars as a function of the distance from the Galactic Center, for Andromeda galaxy. The discrepancy between theory and observation reveals the existence of a missing mass in the form of non-baryonic matter. This figure is taken from Ref. [13].

candidate from non-observation of their Hawking emitted products in several detectors. The results presented in this thesis can be found in the Refs. [7, 8, 9, 10, 11, 12].
In the following, we give a brief overview of several DM candidates, focusing primarily on WIMPs and PBHs, along with discussing some evidences and properties of DM.

1.1 Evidences for Dark Matter

The first incontrovertible proof for DM comes from the measurement of the galactic rotation curve. If the luminous baryonic matter is the sole component of mass in a galaxy, Newtonian dynamics predicts that the circular velocity of the stars follows $v(r) \sim r^{-1/2}$, where r is the radial distance from the Galactic Center. Whereas, from observation, most galaxies show $v(r) \sim$ constant towards their outer radius. This implies existence of a "missing mass" in the form of non-baryonic matter that surrounds the galaxies, and commonly known as DM. In the 1970s, the seminal work of V. Rubin [2] made a decisive

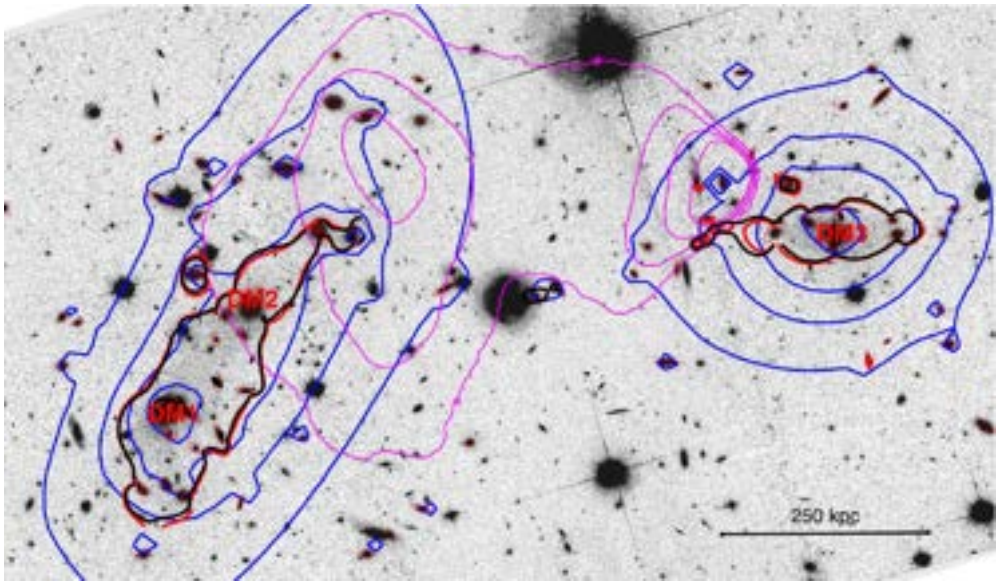

Figure 1.2: Image of the galaxy cluster 1E 0657-56 [14]. The blue contours trace the mass distribution of the galaxy cluster, and are determined from the lensing observations, whereas, the pink contours follow the distribution of the X-ray light. Since the mass is located far away from the center of the X-ray emission, it is considered as one of the best evidence for the existence of DM.

confirmation of this idea by measuring the galactic rotation curves of the Andromeda galaxy through observations of the Doppler shift of the Hydrogen 21-cm line as depicted in Fig. 1.1.

Gravitational lensing of the light from distant galaxies and galaxy clusters provide independent evidence for DM. The images of galaxy clusters captured by Hubble Space Telescope demonstrate the lensing effect due to matter in the intermediate region between the source and the observer. Since, the ordinary baryonic matter is unable to produce such large lensing effect, such effects can be understood to be caused by gravitational lensing by DM halos [5]. Gravitational micro-lensing of the stars in a nearby galaxy, i.e., simultaneously monitoring a large number of stars to detect variations in their brightness, also provides an observational evidence for DM [15, 16]. This strategy has been used to monitor the stars in the Large Magellanic Cloud and the Small Magellanic Cloud to search for DM in the form of massive astrophysical compact halo objects by the MACHO, EROS, and OGLE collaboration.

Multi-wavelength observations of the merging galaxy clusters provided a very strong ob-

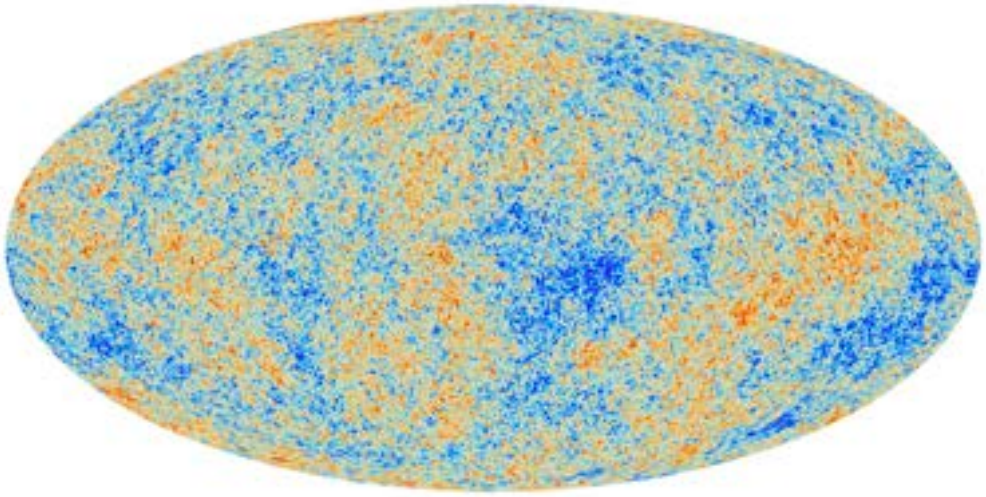

Figure 1.3: Temperature fluctuations of the cosmic microwave background, as measured by the Planck satellite. Orange (blue) regions correspond to high (low) temperatures. Image credit: ESA and the Planck Collaboration.

servational evidence for DM. Observations of the galaxy cluster 1E 0657-56, commonly known as the "Bullet Cluster", reveals that DM does not interact much with the ordinary baryonic matter, or with itself, and holds the majority of mass in a galaxy cluster [3, 17]. The Bullet Cluster, located at 3.8 billion light-years away from us, consists of two separate galaxy clusters that have collided and passed through each other. While the luminous galaxies have continued on their trajectories unimpeded, the intergalactic gas has been slowed down and heated up, emitting an observed flux of X-rays. The mass distribution of this system is traced by weak gravitational lensing where a diffuse matter distribution has been observed enveloping the luminous galaxies, and is shown in Fig. 1.2. This is a very strong evidence for collisionless dark matter, as the diffuse matter distribution has collided and passes through without interacting.

At the cosmological scale, the cosmic microwave background (CMB) is a novel probe to determine the matter content in our Universe. The CMB photons were emitted at the epoch of last scattering, when the Universe was 380,000 years old, and the spectrum of these photons is close to a perfect black-body spectrum. In particular, the CMB spectrum can be described as a black-body spectrum with a present day temperature of 2.7255 K with fluctuations which are of the order 10^{-5} K. These tiny temperature fluctuations, shown in Fig. 1.3, have been measured by surveys like the Cosmic Background Explorer (COBE), the Wilkinson Microwave Anisotropy Probe (WMAP), and the Planck Satellite.

From the measurement of this tiny temperature fluctuations, the Planck collaboration has inferred the DM content of our Universe, $\Omega_{\rm DM} = 0.265$ [4], implying 85% of the matter in our Universe is in the form of DM.

The large-scale structure formation of the Universe, where baryonic matter collapses to form galaxies and galaxy clusters in gravitational potential wells of the dark matter halos, is yet another evidence for DM [6]. Without the gravitational collapse of cold dark matter, small density perturbations of the baryonic matter would be washed out by radiation, delaying galaxy formation. Supercomputer simulations of the cold dark matter are also able to reproduce the observed large-scale structure of our Universe at the right time and on the correct scales to remarkable accuracy, further supporting the DM paradigm.

1.2 Properties of Dark Matter

DM is omnipresent in our Universe, from the Galactic scales to the cosmological scales. In the following, we discuss several properties of DM that can be discerned from the above observations.

- It is cold (non-relativistic) now, and at least since the epoch of structure formation. The mean velocity of the DM particles in the solar neighborhood is 300 km/s. This non-relativistic nature of DM can simply be inferred from the structure formation. If DM was relativistic, then the DM particles would have traveled longer distances because of their high velocity. As a consequence, the mean free path would be longer, and all the structures at length scales smaller than its mean free path, would not have formed. The fact that we observe such structures around us today tells us that DM has to be non-relativistic.

- It does not interact much with the light and other baryonic matter. The weakly interacting nature of DM is inferred from several experimental searches, which can be classified into three broad avenues - direct detection, indirect detection, and collider searches. In direct detection, we look for DM scattering with the SM particles, in indirect detection we look for DM annihilation or decay to the SM particles, and in the collider searches, we look for possible production of DM via scattering among the SM particles.

- It is essentially collisionless. The collisionless nature of DM stems from the weak lensing maps of the DM halos in several galaxy cluster mergers. It tells us that self-interaction among the DM particles has to be tiny, otherwise, it would cause significant lag between the colliding DM halos. Comparison of data with the N-body simulations predicts that in galaxy clusters DM has to satisfy $\sigma_{\chi\chi}/m_{\chi} < 1\,\mathrm{cm}^2/\mathrm{g}$, where m_{χ} denotes the mass of DM and $\sigma_{\chi\chi}$ denotes the self-interaction cross-section among the DM particles.

- It is stable. The lifetime of DM has to be greater than the age of our Universe (~ 10 times than the age of our Universe).

- It can have a wide range of masses. The mass range of DM spans more than 80 orders of magnitude, starting from 10^{-20} eV (for fermionic DM, the minimum mass is $\mathcal{O}(10)$ eV) to $\mathcal{O}(100)M_{\odot}$ and beyond. Depending on its mass, DM can be particle like, wave-like, and can even be compact object-like.

Given these properties of DM, it is widely held that DM must be a new fundamental particle or a very compact object formed before Big Bang Nucleosynthesis[1].

1.3 DM Candidates and Searches

"What makes up DM?" – is one of the most pressing questions in modern day science. This question is very difficult to answer, and one of the difficulties stem from the fact that DM candidates have an enormously large mass window, and they do not interact much with us as well as with themselves. Quantitatively, for bosonic DM, the mass range initiates from 10^{-20} eV [22, 23, 24], and goes beyond $\mathcal{O}(100)M_{\odot}$, implying a mass window that covers more than 80 orders of magnitude. The minimum mass for bosonic DM simply arises from the fact that the corresponding de-Broglie wavelength, which is inversely proportional to its mass, can not exceed the smallest structure observed in our Universe. Whereas, the maximum mass is due to existence of several globular clusters

[1]MOdified Newtonian Dynamics (MOND) is a framework for modified gravity on galactic scales [18], which was proposed as an alternative to DM. These theorized modifications of Newtonian gravity only affect the long-range behavior of gravity, but keep the dynamics on shorter distances intact. However, MOND can not explain the observed CMB anisotropies as well as the behavior of the galaxy clusters [19], and hence, is disfavored. Furthermore, the fact that GWs propagate at the speed of light and a recent analysis of the MW rotation curve rules out the majority of MOND theories [20, 21].

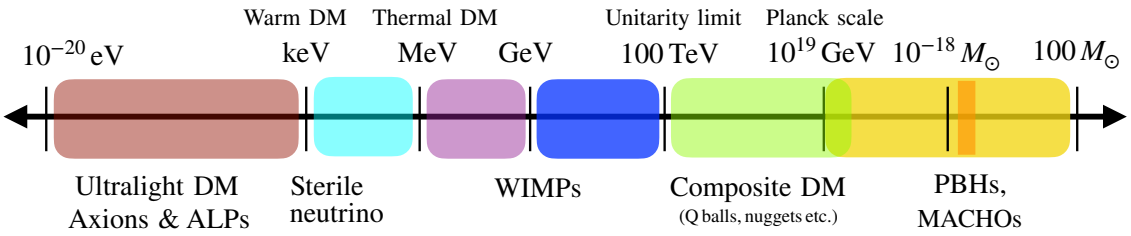

Figure 1.4: The allowed mass range of DM candidates, comprising both particle like candidates and compact object like candidates. The dark yellow shaded region corresponds to the mass range where PBHs can make up all of the DM. The figure is adapted from Ref. [32].

that are supposed to be disrupted in the presence of such heavy DM. For fermionic DM, the allowed mass window is also huge, but a bit smaller than its bosonic counterpart. Here, the minimum mass initiates from $\mathcal{O}(0.1)$ keV, and this simply comes from the fact that fermions have to obey the Pauli exclusion principle [25, 26, 27]. To illustrate this point furthermore, with decrease in mass, the number density of fermionic DM particles increases, and as a consequence, they come closer to each other, increasing the phase-space density. The requirement that the phase-space density of the fermionic DM does not exceed that of the degenerate Fermi gas leads to this lower mass bound, and is commonly known as Tremaine-Gunn bound. This lower mass bound is usually derived from the DM phase-space distribution in dwarf spheroidal galaxies, which are DM dominated spherical objects.

We schematically show the allowed mass ranges of DM in Fig. 1.4. However, this mass range can be narrowed down further if DM are produced thermally. For thermally produced DM, the minimum mass is $\sim 10\,\text{MeV}$ and the maximum mass is $\sim 100\,\text{TeV}$. The arguments are as follows. For thermally produced DM, it has to be compatible with the CMB anisotropy measurements and the observed light element abundances produced during Big Bang Nucleosynthesis [28, 29], and for masses lighter than 10 MeV, this does not occur. On the other hand, the maximum mass comes from the fact that obtaining the observed relic density via thermal freeze-out would require an unitarity violating DM cross-section for DM masses $\geq 100\,\text{TeV}$ [30, 31].

In this enormously large mass window, there exist numerous DM candidates. These include particle like DM such as WIMPs [33, 34, 35, 36, 37, 38, 39, 40], QCD axions and axion-like particles (ALPs) [41, 42, 43, 44, 45, 46, 47, 48], sterile neutrinos [49, 50, 51, 52, 53, 54, 55, 56, 57], and super-symmetric DM such as neutralino, higgsino, photino, etc [58, 59, 60, 61, 62, 63, 64]. Apart from this particle like DM, DM can be of composite states, such as dark quark nuggets [65, 66, 67, 68, 69, 70], super-symmetric Q-balls [71, 72, 73], massive compact halo objects (MACHOs) [15, 16, 74, 75, 76], primordial black holes (PBHs) [77, 78, 79, 80, 81, 82, 83, 84, 85], etc. In the following, we briefly describe some of the DM candidates before we elaborate on two particular DM candidates that we consider in this thesis.

Weakly interacting massive particles (WIMPs): WIMPs are a class of stable particles that interact with the SM particles via weak interactions and typically produced via thermal freeze-out in the early Universe. They are one of the favorite DM candidate because a mass of $\mathcal{O}(100)\,\mathrm{GeV}$ and an annihilation cross-section of $3 \times 10^{-26}\,\mathrm{cm}^3/\mathrm{s}$, which are typical for the SM electroweak sector, would naturally yield the observed DM abundance via thermal freeze-out. WIMPs are typically searched in three broad avenues: *i*) through missing transverse momentum searches at colliders, *ii*) through searches for their annihilation/decay products at various particle physics detectors, and *iii*) through looking at their energy transfer via elastic scattering with nuclei and electrons at various underground laboratory based experiments.

Axions and Axion-like particles (ALPs): Axions and Axion-like particles are hypothetical pseudo-scalar bosons. In the late 1970s, they were introduced in order to solve the strong CP problem in QCD. The strong CP problem is related to the fact that why the observed neutron electric dipole moment is so small compared to its theoretical prediction, and axions provide an elegant dynamic solution to this problem (see the recent review [86] on this topic for more details). Axions are viable DM candidates with very low masses, i.e., masses of meV or lighter. They are searched in a variety of ways, most notably through microwave cavity experiments, stellar cooling, and their conversion to photons in magnetic fields.

Sterile neutrinos: While SM neutrinos have proven to be too light, there is the possibility that heavy, right-handed neutrinos, commonly known as sterile neutrinos, can constitute a significant fraction of the present day DM density. They are typically pro-

duced in freeze-in scenarios and generically appear in models that explain the smallness of SM neutrino masses. The preferred mass range of sterile neutrino DM is in the keV scale, and can be probed via searching their radioactive decay to photons ($\nu_s \to \nu + \gamma$) in various X-ray telescopes, effects on structure formation, etc.

Primordial black holes (PBHs): Primordial black holes, possibly formed due to collapse of large over-densities in the very early Universe, are one of the earliest proposed DM candidates. They have a wide range of masses depending on their time of formation, and the preferred mass range of PBH DM initiates from $10^{-18}\,M_\odot$, and extends up to $\mathcal{O}(100)\,M_\odot$. The minimum mass for PBH DM simply comes from their survival till present day, whereas, the maximum mass comes from non-observation of their accretion signatures in CMB as well as from existence of the globular clusters that are supposed to be disrupted by PBHs. This wide mass window of PBHs can be probed in a variety of ways, such as through searching their Hawking evaporation products in various detectors, gravitational lensing, observation of GW mergers, accretion signatures, etc.

In this thesis, we primarily focus on two DM candidates: Weakly interacting massive particles (WIMPs) and Primordial black holes (PBHs). In terms of the mass range, we focus on: *i*) Weakly interacting massive particles (WIMPs) in the mass range of GeV $-$ PeV and *ii*) Primordial black holes (PBHs) in the mass range of $10^{-18} - 10^{-15}\,M_\odot$. We aim to address the following questions: *i*) Can interactions of WIMPs in the mass range of GeV $-$ PeV with the ordinary baryonic matter be probed from astrophysical observations? and *ii*) Can ultralight evaporating PBHs in the mass range of $10^{-18} - 10^{-15}\,M_\odot$ form a significant fraction of DM?. In short, our results indicate that: *i*) electromagnetic and GW observations of the compact stars can severely constrain the interaction of WIMPs in the GeV $-$ PeV mass range with the ordinary baryonic matter and *ii*) PBHs in the mass range of $10^{-18} - 10^{-15}\,M_\odot$ can not comprise a significant fraction of DM from non-observation of their Hawking products in several detectors. In the following, we discuss some preliminary of these two DM candidates before elaborating on the main results in the subsequent Chapters.

Weakly Interacting Massive Particles

Weakly interacting massive particles (WIMPs) are a class of stable particles that possess gravitational as well as weak interactions, and are defined by their production via thermal

freeze out in the early universe [35, 36, 37]. Historically, the study of WIMPs in cosmology, and the evolution of the Universe started with SM neutrinos [87, 88]. After that, in a series of papers in 1977, it was realized that a relic density of weakly interacting particles with masses above a few GeV could be produced thermally in the early Universe, and can survive until today [33, 38, 89, 90, 91, 92]. The best motivation for WIMPs came from the observation that thermal freeze out in the early universe provides a mechanism for producing DM with the relic density that we observe today, using weak-scale masses and annihilation cross-sections. The freeze-out story is as follows. In the hot early universe, the DM was in thermal equilibrium with the SM particles, being produced and annihilated at equal rates. With the expansion of the Universe, the temperature falls off, and once the temperature falls below the DM mass m_χ, the production of the DM particles is energetically blocked. As a consequence, DM particles can only annihilate among themselves, producing an exponential Boltzmann suppression of their number density. Eventually, the universe expands so much, the DM particles could not find each other to annihilate, and hence, the co-moving number density reached the constant relic density which we observe today. The relic abundance of the DM particles of mass m_χ via thermal freeze out can be expressed as [93]

$$\Omega_{\rm DM} \sim \frac{n_\gamma(x_*)}{\rho_c} x_* \frac{H(m_\chi)}{m_\chi^2 \langle \sigma_a v \rangle} \,, \tag{1.1}$$

where $H(m_\chi)$ is the Hubble expansion rate at $T = m_\chi$ and $n_\gamma(x_* = m_\chi/T_*) \sim T_*^3$ is the photon density at freeze out, where T_* denotes the freeze-out temperature. ρ_c denotes the present day critical density of the Universe and $\langle \sigma_a v \rangle$ is the thermally averaged annihilation cross-section of the DM particles. For DM masses in the range of 1 GeV to 100 TeV, x_* lies within 20 to 30 [93]. Therefore, at the time of thermal freeze out, WIMPs are always non-relativistic, and in order to match the cosmological observation, i.e., $\Omega_{\rm DM} = 0.265$, the annihilation cross-section of the WIMPs has to be $\sim 2.2 \times 10^{-26}\,{\rm cm}^{-3}\,{\rm s}^{-1}$ [94].

Detection Strategies

WIMPs are typically searched in three broad avenues: *i*) direct detection, *ii*) indirect detection, and *iii*) collider searches, as shown in Fig. 1.5.

Direct detection: In direct detection, we typically look for scattering between DM and

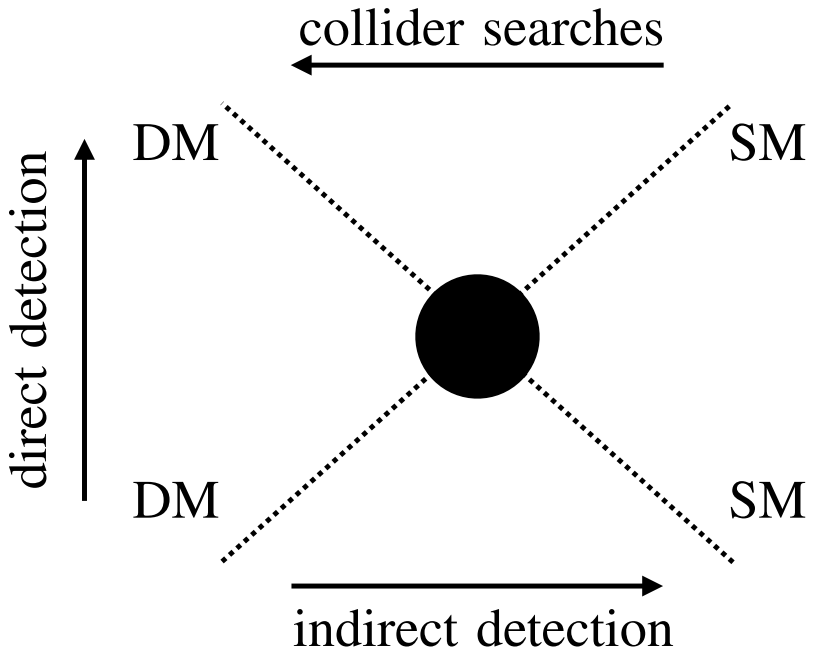

Figure 1.5: An illustration of the three main ways of searching for particle DM. The blob represents the interaction that connects DM and the SM particles and the arrow represents the direction of the time. In direct detection, we try to look for scatterings between the DM and SM particles (DM+SM $\rightarrow$ DM+SM), whereas, in indirect detection, we look for annihilation or decay of the DM particles (DM+DM $\rightarrow$ SM+SM). In the collider searches, we look for possible production of DM via scattering of SM particles (SM+SM $\rightarrow$ DM+DM).

the SM particles. Here, we aim to measure the recoil energy of the target nuclei, which arises due to the WIMP-nuclei collision in the underground detectors. The detectors are typically placed deep in underground to minimize any effects due to background. The idea of using such sensitive detectors to search for WIMP recoil was first developed in the seminal work by Goodman and Witten [95]. Since then, there are numerous experiments are searching for WIMP recoils, with no convincing detection so far. As a consequence, the exclusion limits on WIMP-nucleon scattering cross-section become more and more stringent over time. Currently, the best exclusion limit on WIMP-nucleon scattering cross-section comes from the XENON1T experiment, and it maximally excludes WIMP-nucleon scattering cross-section of 4.1×10^{-47} cm^2 for a DM mass of 30 GeV and probes DM masses above 6 GeV [96]. See Fig. 1.6 for a bird's-eye view of the available constraints on WIMP-nucleon interaction strength from several underground experiments

that are designed to measure very feeble push by the DM particles. From Fig. 1.6, it is evident that these underground detectors can not probe WIMPs with sub-GeV masses. This is simply because the nuclear recoil due to sub-GeV WIMP scattering is too low to measure, and this sub-GeV mass window of WIMPs is typically probed via some novel techniques such as the measurements of the electron recoil, phonon excitation, etc. For an in-depth study on direct detection of sub-GeV WIMPs using condensed matter systems, interested readers can go through the recent review [97], and references there in. From Fig. 1.6, it is also evident that the constraints on WIMP-nucleon interaction strength weaken linearly for heavier WIMP masses. This is simply because the number density of WIMPs is inversely proportional to its mass, and hence, the scattering rate as well as the constraints fall off as $1/m_\chi$.

Another form of direct detection is to search for the annual modulation of the WIMP-nucleon scattering rate [98]. This is expected due to the fact that the solar system is not at rest with respect to the Galactic DM halo combined with the revolution of the Earth around the Sun. The movement of our solar system through the Galactic DM halo results in a constant wind of WIMPs impinging on the Earth, and the rotation of the Earth around the Sun implies that the Earth is approximately moving towards this wind, one half of the year and away from it in the another half. As a consequence, the WIMP velocity at a point on Earth oscillates around the mean value, given by the velocity of the solar system around the Galactic Center. Since, the rate of WIMP scattering in a detector depends on the velocity of the WIMPs, this leads to an oscillation in the WIMP scattering rate over the course of one year. Measurement of such annually modulating signal provides a direct evidence for WIMPs. Recently, DAMA/LIBRA experiment has reported a clear signal of annual modulation caused by WIMPs [99], however, the inferred WIMP mass and WIMP-nucleon scattering cross-section are already excluded by many other direct detection experiments, and is shown in Fig. 1.6. Apart from this annual modulation signal reported by the DAMA/LIBRA experiment, there also exist several intriguing direct detection excesses, which could potentially have a DM origin, such as, the XENON-1T excess [100], the low-threshold excesses in the solid state detectors [101, 102], etc. For more details on this topic, see the recent review [103], and references there in.

Stellar objects can also be used as a direct detection probe for WIMPs. Accumulation

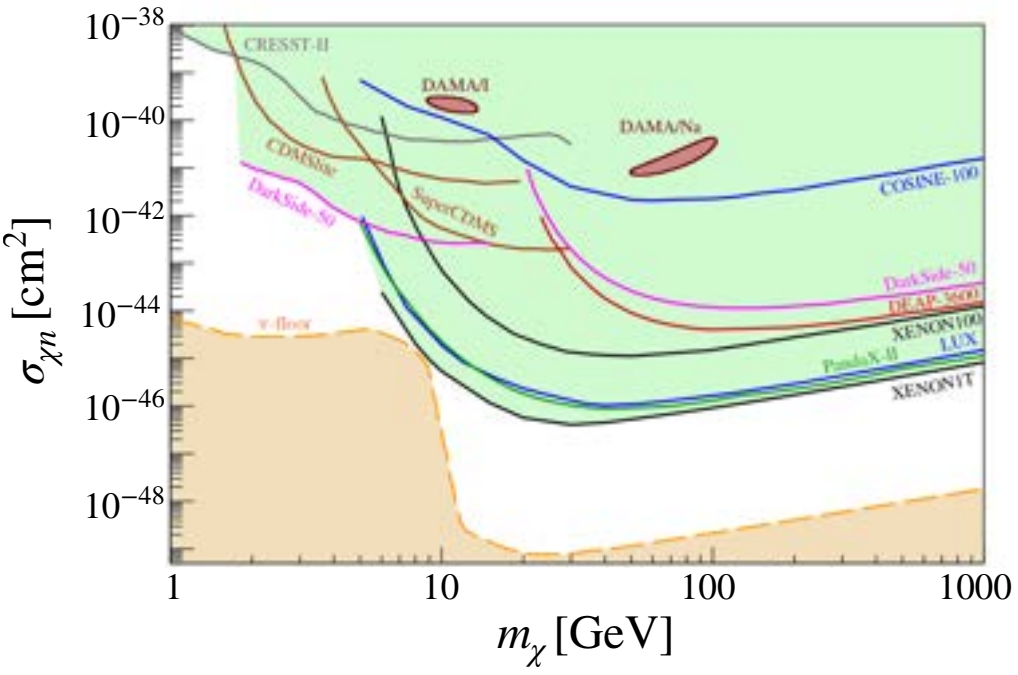

Figure 1.6: Consolidated constraints on spin-independent WIMP-nucleon scattering cross-section from various underground direct detection experiments for WIMP masses of 1−1000 GeV. The orange shaded region in the bottom indicates the "neutrino floor" where any signal due to WIMP-nucleus collision can not be distinguished from neutrino-nucleus coherent scattering, implying the underground searches become ineffective in this region. Note that, these exclusion limits do not exclude all cross-sections above the lines. For sufficiently large WIMP-nucleon scattering cross-sections, WIMPs scatter too much in the surface of the Earth, can not reach to the underground detectors, and hence, can not be probed. The figure is taken from Ref. [32].

of WIMPs in the stellar objects, followed by the electromagnetic and GW observation of the stellar objects, is considered to be a novel astrophysical probe of WIMP-nucleon interactions. Because of the finite WIMP-nucleon scattering cross-section, WIMPs from the galactic halo can down-scatter inside a stellar object to energies below the local escape energy, become gravitationally bound, re-scatter, and rapidly settle into a stable configuration near the core. Such captured WIMPs have several interesting phenomenological consequences. For annihilating WIMPs, the captured WIMPs annihilate among themselves, either heating up the stellar core or produce detectable fluxes of SM particles. Non-observation of any anomalous heating via luminosity measurements of the stellar objects or non-detection of any SM particles in various particle detectors provide

stringent exclusion on WIMP-nucleon interaction strength. For non-annihilating WIMPs, the captured WIMPs gradually accumulate inside the stellar core with time, and eventually destroys the host stellar object via gravitational collapse. Existence of the host stellar objects provide stringent exclusions on WIMP-nucleon interaction strength over a wide range of WIMP masses. Here, it is important to mention that these astrophysical constraints are significantly stronger than the corresponding constraints from the underground laboratory based experiments for both heavy and light DM. Furthermore, because of the enormously large mass and long lifetime of the stellar objects, these constraints can even reach up to super-heavy DM (DM mass of $\sim 10^{12}$ GeV) which is entirely inaccessible to any underground laboratory based experiments. In this thesis, we have explored this aspect in-depth, and made a few key improvements.

Indirect detection: In indirect detection, we typically look for DM annihilation or decay to the SM particles. Here, we aim to measure an excess flux of the SM particles over an astrophysical background via sensitive particle detectors. These searches are typically performed in a region where DM density is high, such as in the Galactic Center or in the satellite galaxies, as the signal is quadratically (linearly) proportional to the DM density for DM annihilation (decay). This idea of looking for gamma rays from the annihilation of the WIMPs was first studied in the Refs [104, 105], and later it was extended to other final state particles, such as antiprotons and positrons [106, 107, 108, 109]. Indirect searches are often challenged by the presence of backgrounds from ordinary astrophysical processes that are very difficult to estimate. One particularly interesting case is therefore the case of dwarf spheroidal galaxies, satellite galaxies to the Milky Way, that are expected to have very little astrophysical backgrounds. A recent analysis of the dwarf spheroidal galaxies using a combination of data from the Fermi-LAT and MAGIC experiments indeed presents some of the toughest constraints on WIMP annihilation rate, especially for WIMP masses below about 100 GeV [110].

Here, it is important to mention that for the charged final state particles, there is always a propagational uncertainty on the indirect direct constraints because of the presence of the galactic magnetic field. The gamma ray signal is not affected much by the propagation, but absorption causes some uncertainties to the flux, especially at high energies. On the other hand, the neutrino signals from DM annihilation or decay is free from any such uncertainties, except at very high energies. See Fig. 1.7 for a consolidated view

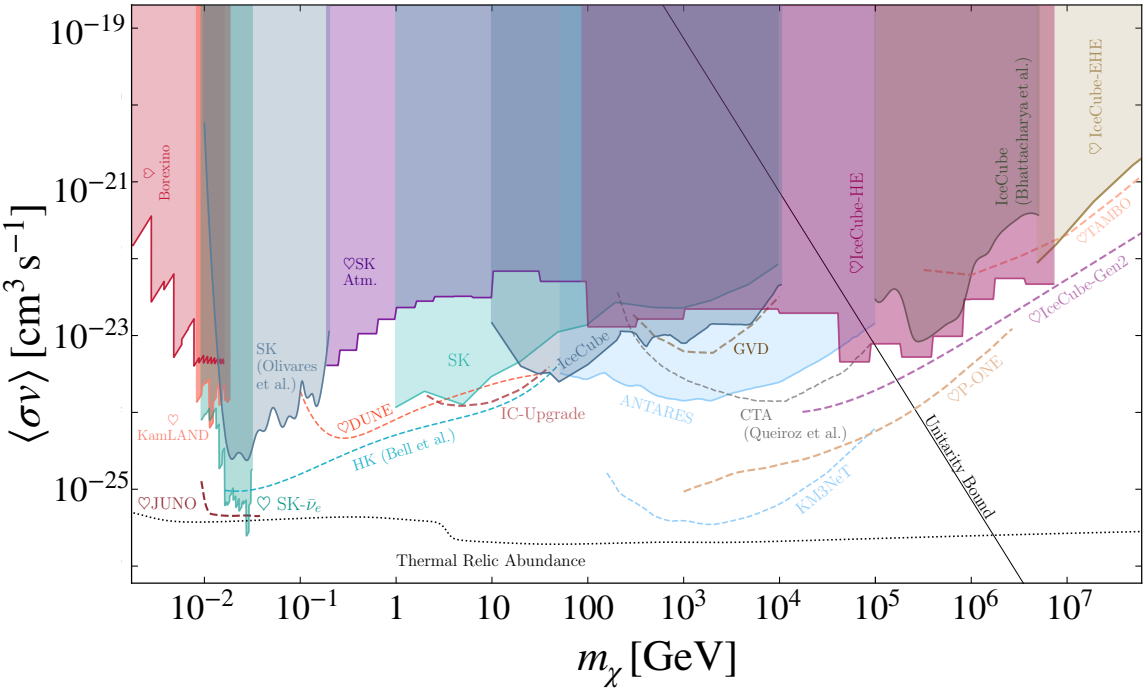

Figure 1.7: Consolidated constraints on WIMP annihilation cross-section into neutrinos for WIMP masses of 10 MeV $-$ 10^8 GeV. Solid and dashed lines represent 90% C.L. limits and sensitivities, respectively, and an s-wave annihilation is assumed. Projected sensitivities assume five years of data taking for the neutrino experiments. The dotted line corresponds to the thermal relic cross-section [94], whereas, the solid black line, labeled as "Unitarity Bound", gives the maximum allowed cross-section for a non-composite DM particle. Annihilation of WIMPs via $2 \to 2$ s-wave scattering is assumed for the thermal relic cross section as well as for the "Unitarity Bound". The figure is taken from Ref. [111].

of the available constraints on WIMP annihilation cross-section into SM neutrinos, by assuming an s-wave annihilation. See also Fig. 1.8 for constraints on WIMP annihilation cross-section to various other final states.

In indirect detection, we also search for excess fluxes of the SM particles near the surface of the stellar objects, such as in Sun, Earth, compact stars like neutron stars, white dwarfs, etc. It includes searching for the annihilation products that arises due to the annihilation of the captured WIMPs inside the stellar objects, followed by their escape from the stellar core. This escape can occur naturally or through any long-lived mediators. For example, the neutrinos that are produced in the core of the Sun via annihilation of WIMPs can naturally escape, whereas, photons can only escape in the presence of a long-

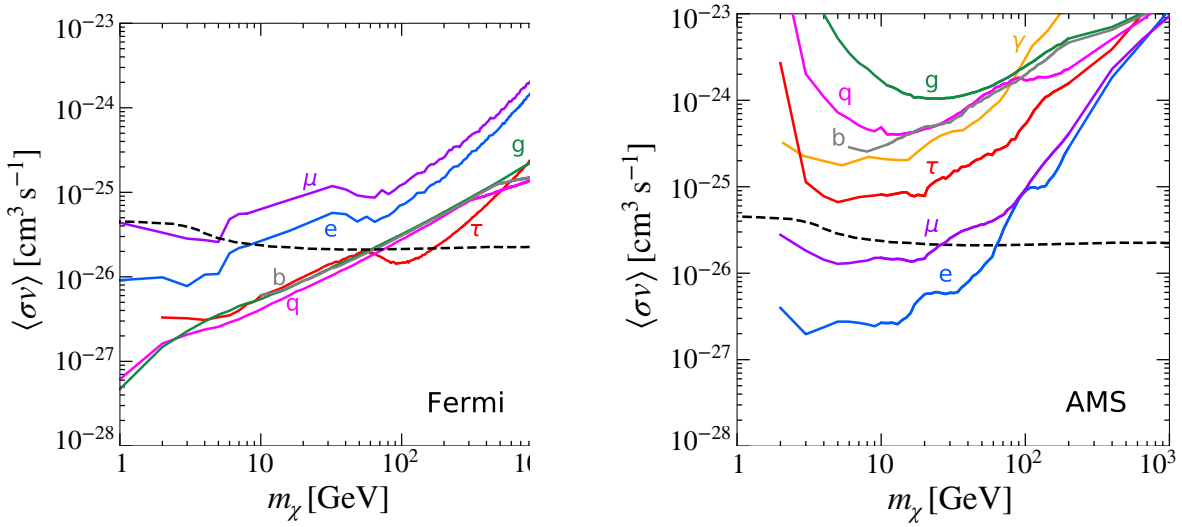

Figure 1.8: Constraints on WIMP annihilation cross-section into various final states (as labeled) for WIMP masses of 1−1000 GeV. s-wave $2 \to 2$ annihilation of WIMPs are assumed. In the left panel, constraints from Fermi measurements of gamma-rays in the dwarf spheroidal galaxies are shown, whereas, in the right panel, constraints from positron flux measurements with AMS-02 are shown. Thermal relic cross-section is denoted by the black dashed lines [94], and the figure is taken from Ref. [40].

lived mediator. Non-detection of such anomalous neutrinos and photons from the Sun provide stringent constraint on WIMP annihilation rate [112, 113, 114, 115, 116, 117]. It is also worth remembering that the indirect detection constraints are not limited to WIMPs, and applicable for other DM candidates also. Resonant conversion of axions to photons in the presence of galactic as well as stellar magnetic fields, evaporation of ultralight primordial black holes, decay of sterile neutrinos to SM neutrinos and photons, followed by the non-detection of those SM particles provide world-leading exclusions on the non-WIMP DM candidates. Besides these exclusions, indirect searches has also revealed some intriguing excess of SM particles which could potentially have a DM origin. These include GC GeV gamma-ray excess detected by the Fermi gamma-ray space telescope [118, 119, 120], the antiproton and positron excesses detected by the space-based telescope AMS-02 [121, 122, 123], measurement of the GC 511 keV gamma-ray line by the space-based telescope INTEGRAL [124], and detection of the 3.5 keV X-ray line by the XMM-Newton and Chandra telescopes [125, 126]. For a detailed study on each of these anomalous signals, the interested readers can go through the recent review, and references there in [103].

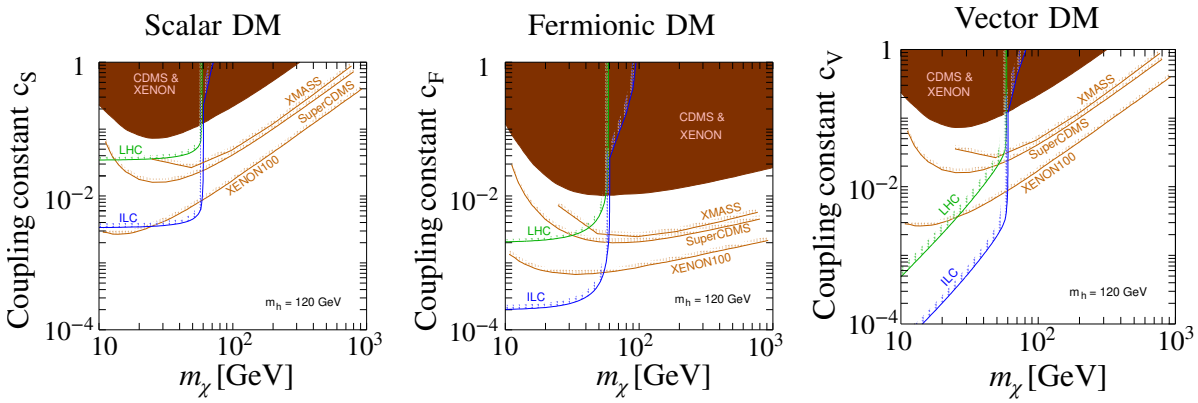

Figure 1.9: Constraints on particle DM coupling with Higgs boson from collider searches. The mass of the Higgs boson (m_h) is taken as 120 GeV. Left panel corresponds to scalar DM, middle panel corresponds to fermionic DM, and the right panel corresponds to vector DM. In each panel, green line indicates the result obtained from Large Hadron Collider (LHC) and the blue line is the projection from International Linear Collider (ILC). The figure is taken from Ref. [127].

Collider searches: In collider searches, we look for DM production via scattering of the SM particles. Here, we use particle accelerators to accelerate SM particles to very high energies, collide them, and aim to observe signatures of DM production as a form of the "missing energy" in the collisions [128, 129]. Currently, the highest energy collider is the Large Hadron Collider (LHC) at CERN, which collides protons with a center-of-mass energy of 13 TeV, and it is relevant for various super-symmetric DM searches. The basic idea of the collider searches of DM is as follows. If the DM particle has a very long lifetime, it escapes the detector entirely, and as a consequence, it leaves a signature in the form of missing energy. Similar to the approach of neutrino detection, energy-momentum conservation is applied to all the visible channels, and if there is any energy-momentum non-conservation in a given process, it indicates an evidence for DM. Here it is important to mention that, in these missing energy searches, the major SM backgrounds arise from the processes that include neutrinos and events with undetected leptons or mis-measured hadronic jets, which are very hard to distinguish. We show the collider constraints on particle DM interactions for scalar, fermionic, and vector DM in Fig. 1.9.

Primordial Black Holes

Primordial black holes (PBHs), possibly formed via gravitational collapse of large over-densities in the very early universe [77, 78, 79, 80, 130], can explain several cosmic mysteries. This includes mergers that give rise to the GW events detected by LIGO-VIRGO, providing seeds for the supermassive black holes observed at the center of galaxies, and more importantly, can be all of the DM over a wide mass range, ranging from 10^{15} g to well over 10^{50} g. PBHs has also been invoked to explain generation of large-scale structure through Poisson fluctuations, some short-period gamma-ray bursts, non-repeating fast radio bursts, solution to the core-cusp problem, etc. For more details on this topic, interested readers can go through Ref. [82], and references there in.

Despite its immense success of explaining several cosmic mysteries, PBHs do not have any compelling formation mechanisms. Collapse of large density perturbations, generated by a period of inflation in the very early Universe, is one of the most widely assumed formation mechanism for PBHs. In this scenario, a density perturbation $\delta = \delta\rho/\rho$ ($\delta\rho$ denotes the density of the over-dense regions and ρ denotes the average background density) can grow with time if the gravitational instability overcomes the pressure resistance, and eventually leads to a PBH formation once the density perturbation crosses its threshold value. The time evolution of δ is essentially determined by the metric perturbations in General Relativity, however, if the wavelength of the density perturbation is contained within the Hubble horizon (sub-horizon modes), it can be treated with a Newtonian approximation. In the regime of Newtonian approximation, i.e, $\lambda \leq r_{\rm horizon}(t)$, where, $\lambda = 2\pi/k$ denotes the co-moving wavelength of the density perturbation with wave-number k and $r_{\rm horizon}(t) = c/a(t)H(t)$ denotes the size of the co-moving Hubble horizon, respectively, the density perturbations exceeding the Jeans length ($\lambda_J = c_s\sqrt{\pi/G\rho}$, c_s denotes the sound speed), grow with time as the pressure resistance is not sufficient enough against the gravitational instability, and eventually leads to the formation of PBHs. Whereas, in the opposite regime, i.e., the density perturbations with $\lambda < \lambda_J$, oscillate with time, and are stabilized by the gravitational pressure. For super-horizon modes, i.e., wavelength of the density perturbation larger than the Hubble horizon, the Newtonian approximation breaks down, and the evolution of the density perturbations is governed by the metric perturbations in General Relativity. In this regime, the density perturbations evolve in a gauge dependent way (for example, in the conformal Newtonian gauge, density pertur-

bations remain constant, whereas, they grow with time in the synchronous gauge) [131]. However, the gravitational potential is constant, and remains same in all gauges.

The critical value of the density perturbation for PBH formation (δ_c) was first estimated in Ref. [132] by considering the Jean's length argument in Newtonian gravity, obtaining $\delta_c = c_s^2 = 1/3$, where c_s is the sound speed of the cosmological radiation fluid. Later, this analytical estimate of δ_c is refined by relativistic numerical simulations as well as further analytic improvements [133, 134, 135, 136], and the numerical value of δ_c lies within the range of $0.4 - 0.7$ depending on the shape of the density perturbation [82].

The characteristic mass of PBHs is essentially given by the mass contained in the horizon at the time of formation t, and can be expressed as [82]

$$M_{\rm PBH} \sim M_H \sim \frac{c^3 t}{G}\,. \tag{1.2}$$

From Eq. (1.2) it is evident that, PBHs can have a wide range of masses depending on their time of formation. For example, PBHs that are formed before the QCD phase transition ($t = 10^{-6}\,\mathrm{s}$), are naturally sub-Solar. Here, it is worthwhile to stress that the mass range of the PBHs is vastly different from the mass range of the astrophysical black holes, as in the latter case, the minimum mass is bounded by the Chandrasekhar limit, $M_{\rm BH} \geq 1.4\,M_\odot$.

Since, PBHs are formed due to collapse of large density perturbations in the very early Universe, we can estimate the characteristic scale of the perturbations that leads to the PBH formation. To illustrate this point furthermore, if PBHs are formed at $t = t_i$, when a mode of wave number k enters the Hubble horizon, the condition $a(t_i)\,H(t_i) = k$ holds. During the radiation dominated era, we have $a(t_i) \propto H(t_i)^{-1/2}$, and hence, $H(t_i) = k^2$. Since the mass of a PBH is essentially the mass contained in the horizon, i.e., $M_{\rm PBH} = c^3/2GH(t_i)$, the perturbation wave number k can be expressed in terms of the PBH mass [137]

$$k = \left(\frac{c^3}{2GM_{\rm PBH}}\right)^{1/2} = 2.9\times10^5\,\mathrm{Mpc}\,\left(\frac{\mathrm{M_{PBH}}}{30\,\mathrm{M_\odot}}\right)^{-1/2}\,. \tag{1.3}$$

Given that we have estimated the perturbation amplitude and the perturbation scale which produces a PBH population of mass $M_{\rm PBH}$, we now need to estimate their abundance. The initial abundance of PBHs at their time of formation, i.e., the fraction of the Universe's mass which is in the form of PBHs, is usually computed in the Press-

Schechter theory, and is simply given by the probability that a density contrast δ exceeds its threshold value [138]

$$\beta(M_{\rm PBH}) = 2\int_{\delta_c}^{\infty} \Pi(\delta) d\delta \,, \tag{1.4}$$

where $\Pi(\delta)$ denotes the probability density of the density contrast and δ_c denotes its threshold value. Assuming that $\Pi(\delta)$ is Gaussian with a mass variance σ, the initial abundance of PBHs can be estimated as

$$\beta(M_{\rm PBH}) = {\rm erfc}\left(\frac{\delta_{\rm c}}{\sqrt{2}\sigma}\right) \,, \tag{1.5}$$

For the standard cosmological scenario, the mass variance σ is around 10^{-5}, whereas, the threshold for collapse δ_c is around $\mathcal{O}(0.1)$. In this regime ($\delta_c \gg \sigma$), we can use the asymptotic expansion of the complementary error function (${\rm erfc}(x) = \exp[-x^2]/\sqrt{\pi}x$), and the initial abundance of PBHs can be expressed as

$$\beta(M_{\rm PBH}) = \sqrt{\frac{2}{\pi}}\frac{\sigma}{\delta_c}\exp\left[\frac{-\delta_c^2}{2\sigma^2}\right] . \tag{1.6}$$

Hence, for $\sigma = 10^{-5}$ and $\delta_c = \mathcal{O}(0.1)$, $\beta \sim 10^{-4}\exp[10^{-8}]$ is completely negligible. So, in order to have a cosmologically relevant population of PBHs, much larger values of the initial power spectrum are required. Besides, the assumption of a Gaussian probability distribution for the density perturbations may not be consistent with enhanced fluctuations and the presence of PBHs. Therefore, deviations from the Gaussian probability distribution are inevitable [139], and non-gaussianities can have a great impact on the initial abundance of PBHs, leading to a larger PBH population [140].

The present-day abundance of PBHs is typically expressed as a ratio between the mean energy density of the PBHs and the mean energy density of the DM

$$f_{\rm PBH} = \frac{\Omega_{\rm PBH}}{\Omega_{\rm DM}} \tag{1.7}$$

where $\Omega_{\rm DM} = 0.265$ is determined by the recent Planck measurement [4]. In other words, $f_{\rm PBH}$ denotes what fraction of the DM is in the form of PBHs, and $f_{\rm PBH} = 1$ signifies the fact that PBHs can make up all of the DM. The initial abundance of PBHs $\beta(M_{\rm PBH})$ can be expressed in terms of the present-day PBH abundance via the following

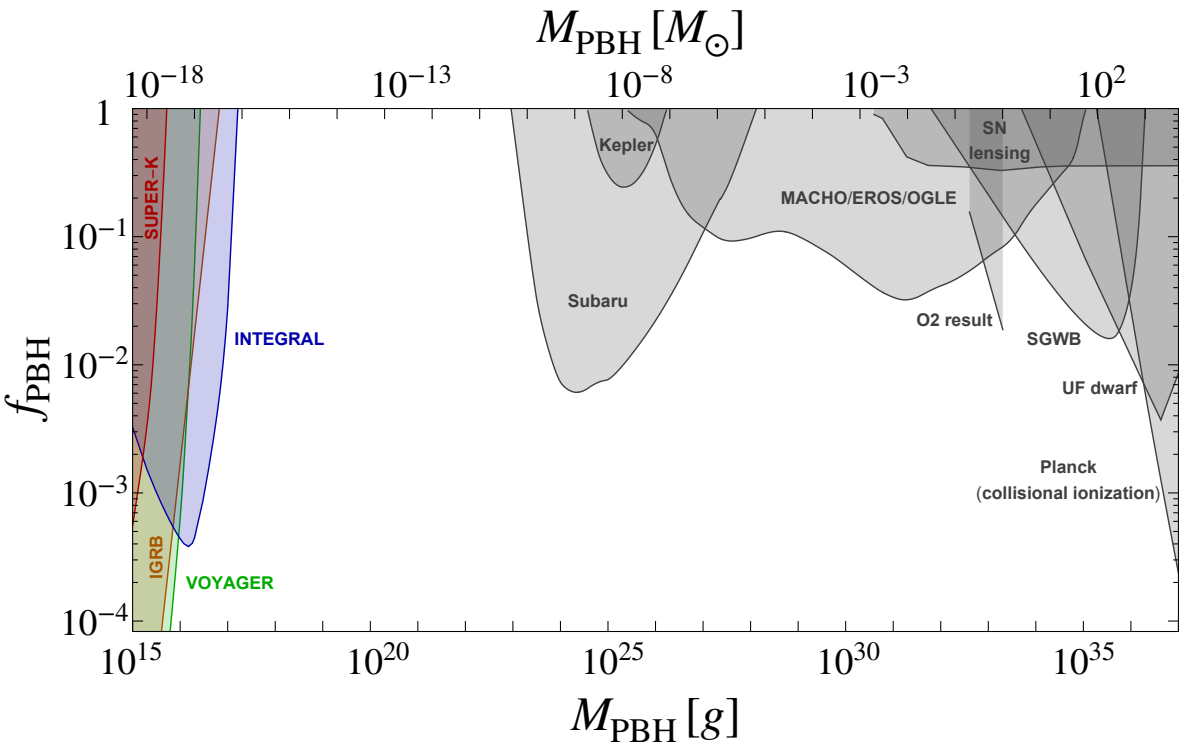

Figure 1.10: Constraints on non-rotating primordial black hole as a dark matter candidate with a monochromatic mass distribution over the entire viable mass range. This plot is taken from Ref. [10], and the constraints that are shown in this plot are taken from Refs. [10, 83, 141, 142, 143, 144, 145, 146, 147, 148, 149, 150, 151].

relation [82, 132]

$$f_{\rm PBH} = \frac{\Omega_r}{\Omega_{\rm DM}}(1+z_i)\beta(M_{\rm PBH}) \sim 10^6\beta\left(\frac{t}{1\,\rm sec}\right)^{-1/2} \sim 10^9\beta\left(\frac{M_{\rm PBH}}{M_\odot}\right)^{-1/2}, \tag{1.8}$$

where $\Omega_r = 5\times10^{-5}$ is the present day radiation density of the Universe, z_i denotes the redshift of PBH formation, and the factor $(1+z_i)$ arises because of the matter and radiation density scale as $(1+z_i)^3$ and $(1+z_i)^4$, respectively. Here it is important to stress that, although the initial fraction β is a very small quantity, the PBH contribution to DM can become relevant at the present time. For example, for initial mass fractions as low as $\beta \sim 10^{-9}$ of solar mass PBHs, PBH contribution to DM can be of order unity. In the following, we discuss several observational constraints on the present day abundance of PBHs ($f_{\rm PBH}$) over the entire viable mass range.

Observational Constraints on PBHs as DM

Extremely light PBHs lose their mass via Hawking evaporation, and emit particles which follow a blackbody like distribution. PBHs lighter than $\sim 10^{15}$ g have already evaporated by now because of their efficient Hawking emission, setting a lower limit on their mass if they can comprise DM. PBHs in the ultralight mass window, i.e., $10^{15} - 10^{17}$ g, are still evaporating, acting as a decaying DM, and can be probed via searching these Hawking emitted particles in several space as well as ground based detectors. Non-observations of such Hawking evaporated photons [83, 152, 153, 154, 155, 156, 157, 158, 159, 160, 161], neutrinos [10, 162, 163, 164, 165], and electrons/ positrons [10, 141, 166, 167] provide the leading constraints on ultra-light PBHs. PBHs in the ultralight mass range can also be constrained via precise measurements of the cosmic microwave background [168, 169, 170, 171, 172, 173], dwarf galaxy heating [174, 175], radio observations [176, 177], and 21-cm cosmology [12, 178, 179, 180, 181, 182, 183].

Slightly heavier PBHs, i.e., PBHs in the mass range of $10^{17} - 10^{23}$ g, often known as asteroid mass window, are particularly interesting as they can make up the entirety of the present day DM density. The exclusion limits in this mass window from capture on celestial objects as well as from gravitational femtolensing have been refuted by several recent studies [142, 184, 185, 186]. PBHs heavier than 10^{23} g are typically constrained via lensing observations, dynamics of galaxies, GW observations, and their accretion signatures. For an overview of the observational constraints on PBHs as DM, the interested readers can go through the recent reviews [82, 137, 84, 85].

Finally, in Fig. 1.10 we show a bird's-eye view of the available constraints on PBHs as DM. In this plot, PBHs are assumed to be non-rotating and a monochromatic mass distribution of the PBHs are considered. The Hawking evaporation constraints are shown by the colored (non-gray) shaded regions and all the other constraints are shown by the gray shaded regions.

1.4 Our Contributions & Outline of the Thesis

In the first half of the thesis (Chapter 2 to Chapter 4), we have explored astrophysical direct detection of particle DM, and demonstrated that interactions of particle DM (more particularly, WIMPs in the mass range of GeV − PeV) with the ordinary baryonic matter

can be constrained from electromagnetic and GW observation of the compact stars. For this purpose, we have comprehensively studied particle DM accretion in the compact stars, and our results are following:

1. For heavy DM capture, or capture in compact stars, the effect of multiple collisions is pronounced. We provide an exact analytical treatment for multi-scatter stellar capture and put stringent constraint on DM-nucleon interaction strength via luminosity measurements of several cold white dwarfs in our nearest globular cluster (Chapter 2).

2. We generalize the treatment of DM capture in compact stars to account for interactions mediated via arbitrary mass mediators. We show that the astrophysical constraints on DM-nucleon interaction strength, which are obtained either from luminosity measurements of the cold neutron stars or existence of old neutron stars, weaken significantly for interactions mediated via light mediator, and can even be voided for light enough mediators (Chapter 2).

3. We discuss a novel formation mechanism of sub-Chandrasekhar mass black holes via gradual accumulation of non-annihilating particle DM in compact stars. This low mass black holes, commonly known as transmuted black holes (TBHs), is a viable alternative to PBHs, and can be tested in the upcoming GW detectors (Chapter 6).

In the second half of the thesis (Chapter 5 to Chapter 7), we demonstrate that ultralight evaporating PBHs in the mass range of $10^{-18} - 10^{-15}\, M_\odot$ can not make up a significant fraction of DM. We have comprehensively searched the Hawking emitted particles from these evaporating PBHs in several detectors that are designed for particle physics and cosmological observations, and non-observation of those Hawking emitted particles lead to such conclusion. Our results can be summarized in the following:

1. Non-observation of the Hawking radiated neutrinos (positrons) in the diffuse supernova neutrino background searches at Super-Kamiokande (measurement of the 511 keV gamma-ray line by INTEGRAL) provide stringent exclusion on ultralight PBHs as DM (Chapter 5).

2. Non-observation of the Hawking radiated Galactic Center photons with the imminent soft gamma-ray telescope AMEGO can exclude asteroid mass PBHs to make up a significant fraction of DM (Chapter 6).

3. EDGES measurement of the global 21-cm signal can be translated to set a world-leading exclusion on ultralight PBHs as DM (Chapter 7).

Finally, we summarize and conclude the thesis in Chapter 8.

Chapter 2

White Dwarfs as DM Detectors: Effect of Multiple Collisions

In this Chapter, we demonstrate the relevance of multiple collisions in the context of particle DM accretion in stellar objects. We provide an *exact* formalism for multi-scatter stellar capture, and show that white dwarfs can be used to probe particle DM interactions. The results presented in this chapter can be found in [7].

2.1 Particle DM accretion in Stellar Objects

Accumulation of particle DM in stellar objects is a novel astrophysical probe of DM-nucleon interactions. Because of the finite DM-nucleon scattering cross-section, DM particles from the galactic halo can down-scatter inside a stellar object to energies below the local escape energy, become gravitationally bound, re-scatter, and rapidly settle into a stable configuration near the core [187, 188, 189]. Such captured DM particles have several interesting phenomenological consequences. For annihilating DM, such captured DM particles annihilate among themselves and produce SM Particles. If these SM Particles can not escape the stellar core, they re-scatter, and eventually heat up the stellar core. Non-observation of any such anomalous heating project stringent exclusions on DM interactions with the ordinary baryonic matter. This has been extensively studied in the context of the neutron stars/white dwarfs [7, 8, 190, 191, 192, 193, 194, 195, 196, 197, 198, 199, 200, 201, 202, 203, 204, 205, 206, 207, 208, 209, 210, 211, 212, 213], Earth [214, 215, 216, 217], Moon [218], Solar system planets such as Mars, Jupiter,

Uranus, & Neptune [217, 219, 220, 221], and Exoplanets [222]. On the other hand, if these SM Particles escape from the stellar core, either naturally or through any long-lived mediator, non-observation of them in several ground based detectors provide stringent constraint on DM interactions [112, 113, 114, 115, 116, 117, 223, 224, 225, 226, 227, 228, 229, 230, 231, 232, 233, 234, 235, 236, 237, 238, 239, 240, 241, 242, 243, 244, 245]. For non-annihilating DM, captured DM particles gradually accumulate inside the stellar object, form a tiny black hole via dark core collapse, and destroys the host. Existence of the host stellar body provide stringent exclusions on DM-nucleon interaction strength over a wide range of DM masses [8, 190, 193, 202, 246, 247, 248, 249, 250, 251, 252, 253, 254, 255, 256, 257, 258, 259, 260, 261, 262].

Particle DM accretion in stellar objects can also be used to determine DM self-interaction strength. Given nonzero self-interaction among the DM particles, an incoming DM particle can also collide with previously captured dark matter particles inside the stellar core. This additional contribution is known as the self-capture of DM particles. The accretion of DM particles with non-negligible self-interaction and its related phenomenology is extensively studied in [200, 250, 251, 263, 264, 265, 266, 267, 268]. For non-annihilating DM capture in compact stars, repulsive self-interactions among the DM particles have a significant impact on the gravitational collapse, and hence, it can be constrained via existence of the compact stars, complementary to the constraints obtained from the observations of colliding galaxies.

2.1.1 Motivations for Multi-scatter Stellar Capture

Most of the prior treatments of DM capture in stellar objects assume that the DM is captured either after a single collision or not at all. However, this single-collision approximation fails in two distinct ways, as pointed out by Bramante et al. [196].

i) DM that is much heavier than the targets loses a tiny amount of energy per collision, and hence, heavier DM requires multiple collisions to lose enough energy to be captured. This is simply because the fractional energy loss per collision, $\Delta E/E$, is inversely proportional to the DM mass, and it gradually decreases for higher DM masses

$$\frac{\Delta E}{E} = \frac{4 m_\chi m_t}{(m_\chi + m_t)^2} \cos^2\theta \sim \frac{m_t}{m_\chi}\,, \tag{2.1}$$

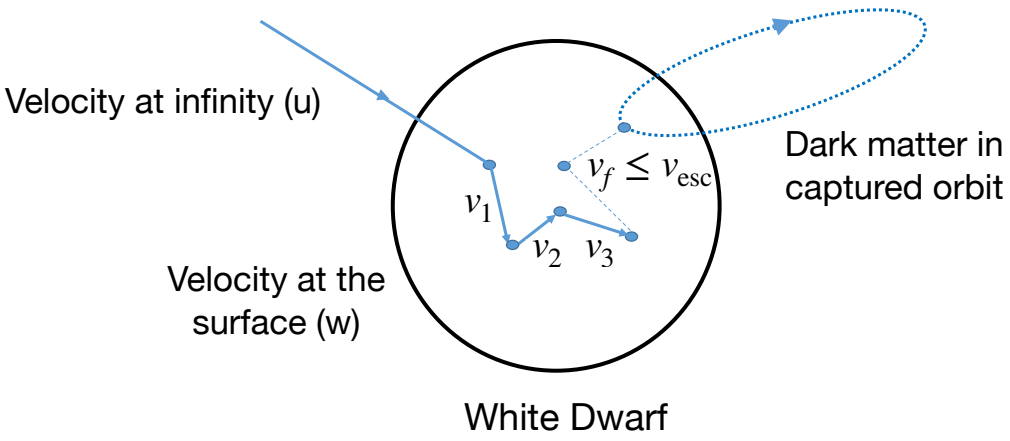

Figure 2.1: A dark matter particle coming in from infinity with velocity u enters the celestial object, *e.g.*, a white dwarf, with velocity w. After this, it undergoes single or multiple collisions with the stellar targets, loses energy, and ultimately when its final velocity falls below the escape velocity of the celestial object, it enters a closed orbit. During its subsequent passages through the celestial object, it loses more and more energy before finally being captured.

where m_χ is the mass of the DM particle, m_t is the target mass, and θ denotes the recoil angle in the rest frame of the target.

ii) For stellar objects with larger compactness (more precisely, larger M/R^2 ratio), the effect of multiple scattering is pronounced. This is because the typical number of scatterings inside a stellar object of mass M and radius R scales as

$$N = \frac{R}{\lambda_{mfp}} = n\sigma R \sim \frac{\sigma M}{m_n R^2}\,, \tag{2.2}$$

where $\lambda_{mfp} = 1/n\sigma$ is the mean free path and σ is the DM-nucleon interaction strength. Quantitatively, for a solar mass neutron star (white dwarf), the expected number of DM-nucleon scattering is $\sim 10^8(10^4)$ times higher than the Sun.

In summary, a) for very heavy DM capture *and* b) for DM capture in compact stars, incorporating the effects of multiple collisions are necessary. In the following section, we will provide an exact formalism of DM capture in the multiple collision regime.

2.2 DM Capture: Effect of Multiple Collisions

Far away from the stellar body, the dark matter particle has a velocity u, and when it approaches the surface of the stellar body, its velocity becomes w, given by

$$w^2 = u^2 + v_{\rm esc}^2 \,. \tag{2.3}$$

It undergoes one or more scatterings as it transits through the stellar object. As a result of these collisions with essentially static stellar constituents, the incoming dark matter particle can lose energy. If eventually its final velocity v_f becomes less than the escape velocity $v_{\rm esc}$ of the stellar object, it is considered to be captured. A schematic diagram of such a scenario is shown in Fig. 2.1.

The capture rate of DM particles inside a stellar object depends not only on the size of the stellar object and the flux of DM particles, but also on the probability of collisions and the probability of incurring sufficient energy loss after a given collision. Therefore, the capture rate after a given collision (say N^{th} collision) takes the form

$$C_N = \pi R^2 \, \frac{\rho_\chi}{m_\chi} \int \frac{f(u)du}{u} \, (u^2 + v_{\rm esc}^2) \, p_N(\tau) \, g_N(u) \,, \tag{2.4}$$

where $p_N(\tau)$ denotes the probability of a dark matter particle with optical depth τ to undergo N scatterings and $g_N(u)$ denotes the probability of incurring sufficient energy after N^{th} collision. The optical depth $\tau = {\rm Min}\,[\frac{3\sigma}{2\sigma_{\rm sat}}, \frac{3}{2}]$ is normalized such a way that $\tau = 1$ corresponds to DM particle typically scatters *once* as it transits through the stellar object. σ denotes the scattering cross-section between DM and the stellar target and $\sigma_{\rm sat} = \pi R^2/N_t$ denotes its geometrical saturation value, where N_t is the total number of stellar targets. The probability of occurring N^{th} collision, $p_N(\tau)$, is given a Poisson (τ, N). However, this expression can be improved by taking into account of all the incidence angles of the incoming DM particle [196]

$$p_N(\tau) = 2 \int_0^1 dy \, \frac{y e^{-y\tau} (y\tau)^N}{N!} \,, \tag{2.5}$$

where y denotes the cosine of the incidence angle.

The capture probability, g_N, denotes the probability that the final velocity of the DM particle after N^{th} collision (v_f) falls below the escape velocity of the stellar object ($v_{\rm esc}$),

and is given by

$$g_N(u) = \int_0^1 dz_1 \int_0^1 dz_2 ... \int_0^1 dz_N \, s_1(z_1) s_2(z_1, z_2) ... s_N(z_1, z_2 ... z_N) \times \Theta \left(v_{\rm esc} - \underbrace{\left(u^2 + v_{\rm esc}^2\right)^{1/2} \prod_{i=1}^{N} \left(1 - z_i \frac{4 m_\chi m_t}{(m_\chi + m_t)^2}\right)^{1/2}}_{v_f} \right) . \quad (2.6)$$

Here, $z = \cos^2\theta = \sin^2(\theta_{\rm CM}/2)$ is a kinematic variable which takes values between 0 and 1, and encodes the fractional energy loss of the DM particle in a given scattering. More specifically, z is proportional to the fractional energy loss of the DM particle, and can be written as $\Delta E/E = \beta z$, where $\beta = (4 m_\chi m_t)/(m_\chi + m_t)^2$. $s(z)$ denotes the probability distribution of the kinematic variable z, and is dictated by the differential scattering cross-section of the relevant scattering process. For an isotropic differential scattering cross-section, i.e., for interactions mediated by infinitely massive mediators, $s(z)$ reduces to unity.

In the following subsection, we provide an exact analytical expression of $g_N(u)$ in the regime of $s(z) = 1$, i.e., for interactions mediated via infinitely massive mediators. Note that, the estimation of $g_N(u)$ for interactions mediated by arbitrarily massive mediators has not been done yet. This is simply because the N-dimensional integral in Eq. (2.6) can not be solved analytically for arbitrary $s(z)$. However, we have computed the generalized capture probability in the single-collision regime, and the calculation is given in chapter 3. Qualitatively, in a given collision, if the mediator mass is smaller than the typical energy transfer, i.e., $m_\phi^2 \ll \mu^2 v_{\rm rel}^2$, forward scattering dominates, reducing the energy loss rate, and hence, the capture rate.

2.2.1 Capture Probability for N^{th} Collision

We compute the N dimensional integral in Eq. (2.6) analytically to find

$$g_N(u) = \frac{1}{\beta} \frac{v_{\rm esc}^2}{u^2 + v_{\rm esc}^2} \left[\frac{1}{\beta} \log \frac{1}{1-\beta}\right]^{N-1} - \left(\frac{1}{\beta} - 1\right) . \quad (2.7)$$

We interpret $g_N(u)$ as the probability that a DM particle with velocity u at infinity gets captured at its N^{th} collision. To ensure that g_N is positive, we write it as

$$g_N(u) = \left[\frac{1}{\beta}\frac{v_{\rm esc}^2}{u^2+v_{\rm esc}^2}\left[\frac{1}{\beta}\log\frac{1}{1-\beta}\right]^{N-1} - \left(\frac{1}{\beta}-1\right)\right]\times \\ \Theta\left(\left[\frac{1}{\beta}\frac{v_{\rm esc}^2}{u^2+v_{\rm esc}^2}\left[\frac{1}{\beta}\log\frac{1}{1-\beta}\right]^{N-1} - \left(\frac{1}{\beta}-1\right)\right]\right) . \quad (2.8)$$

This exact expression is a non-trivial improvement over the previous work [196], where z was replaced by its average value of 1/2, which instead gave [196]

$$g_N^{\rm approx}(u) = \Theta\left(v_{\rm esc} - \left(u^2+v_{\rm esc}^2\right)^{1/2}\left(1-\frac{1}{2}\frac{4m_\chi m_t}{(m_\chi+m_t)^2}\right)^{N/2}\right) . \quad (2.9)$$

The Θ function in Eq.(2.8) sets an upper limit to the halo velocity u given by

$$u_{\rm max}^2 \leq v_{\rm esc}^2\left[\frac{1}{1-\beta}\left(\frac{1}{\beta}\log\frac{1}{1-\beta}\right)^{N-1} - 1\right] . \quad (2.10)$$

This upper limit on u indicates that DM particles with arbitrarily large velocity cannot typically be trapped by the celestial object after N scatterings. Furthermore, as $g_N(u)$ is a probability, it should also satisfy the condition $g_N(u) \leq 1$. This imposes a lower limit on u that was not apparent in the single scattering case, where it is trivially satisfied. Here, $g_N(u) \leq 1$ gives rise to the condition

$$u_{\rm min}^2 \geq v_{\rm esc}^2\left[\left(\frac{1}{\beta}\log\frac{1}{1-\beta}\right)^{N-1} - 1\right] . \quad (2.11)$$

This lower limit encodes that if the velocity of the incoming DM particle is below this threshold, then it is more likely to be captured already *before* the $N^{\rm th}$ collision.

2.2.2 Capture Rate for N^{th} Collision

We use the analytical expression for $g_N(u)$ in Eq. (2.8), to evaluate the capture rate for N^{th} scattering. Using energy per unit mass $\zeta = u^2/2$ along with the definition of capture

rate in Eq. (2.4), we find

$$C_N = \pi R^2 \, p_N(\tau) \, \frac{\rho_\chi}{m_\chi} \int_{\zeta_{\rm min}}^{\zeta_{\rm max}} \frac{f(\zeta) d\zeta}{\zeta} (\zeta + \zeta_{\rm esc}) \, g_N(\zeta) \,, \tag{2.12}$$

where $\zeta_{\rm max}$ and $\zeta_{\rm min}$ can be obtained from Eq.(2.10) and Eq.(2.11), respectively and is given by

$$\zeta_{\rm max} = \zeta_{\rm esc} \left[\frac{1}{1-\beta} \left(\frac{1}{\beta} \log \frac{1}{1-\beta} \right)^{N-1} - 1 \right] , \tag{2.13}$$

and

$$\zeta_{\rm min} = \zeta_{\rm esc} \left[\left(\frac{1}{\beta} \log \frac{1}{1-\beta} \right)^{N-1} - 1 \right] . \tag{2.14}$$

with $\zeta_{\rm esc} = v_{\rm esc}^2/2$.

We use the Maxwell Boltzmann velocity distribution to estimate the capture rate for N^{th} collision

$$C_N = \left(\frac{8}{\pi} \right)^{\frac{1}{2}} \pi R^2 \, p_N(\tau) \, \frac{1}{\sqrt{\bar{\zeta}}} \frac{\rho_\chi}{m_\chi} \left[\frac{\zeta_{\rm esc}}{\beta^N} \left(\log \frac{1}{1-\beta} \right)^{N-1} p - \left(\frac{1}{\beta} - 1 \right) q \right] , \tag{2.15}$$

where p and q are given as

$$p = \exp \left[\frac{-\zeta_{\rm min}}{\bar{\zeta}} \right] - \exp \left[\frac{-\zeta_{\rm max}}{\bar{\zeta}} \right] , \tag{2.16}$$

and

$$q = \left(\bar{\zeta} + (\zeta_{\rm esc} + \zeta_{\rm min}) \right) \exp \left[\frac{-\zeta_{\rm min}}{\bar{\zeta}} \right] - \left(\bar{\zeta} + (\zeta_{\rm esc} + \zeta_{\rm max}) \right) \exp \left[\frac{-\zeta_{\rm max}}{\bar{\zeta}} \right] , \tag{2.17}$$

with $\bar{\zeta} = \bar{v}^2/3$, where $\bar{v}$ is the average velocity of the Maxwell Boltzmann distribution. We have verified that in the limit of $N = 1$, the capture rate in Eq. (2.15) matches the familiar expression of single collision capture rate.

2.2.3 Maximum Number of Scatterings

Total capture rate is essentially a sum of the capture rate over the possible values of N

$$C_{\rm tot} = \sum_{N=1}^{N_{\rm max}} C_N \,, \tag{2.18}$$

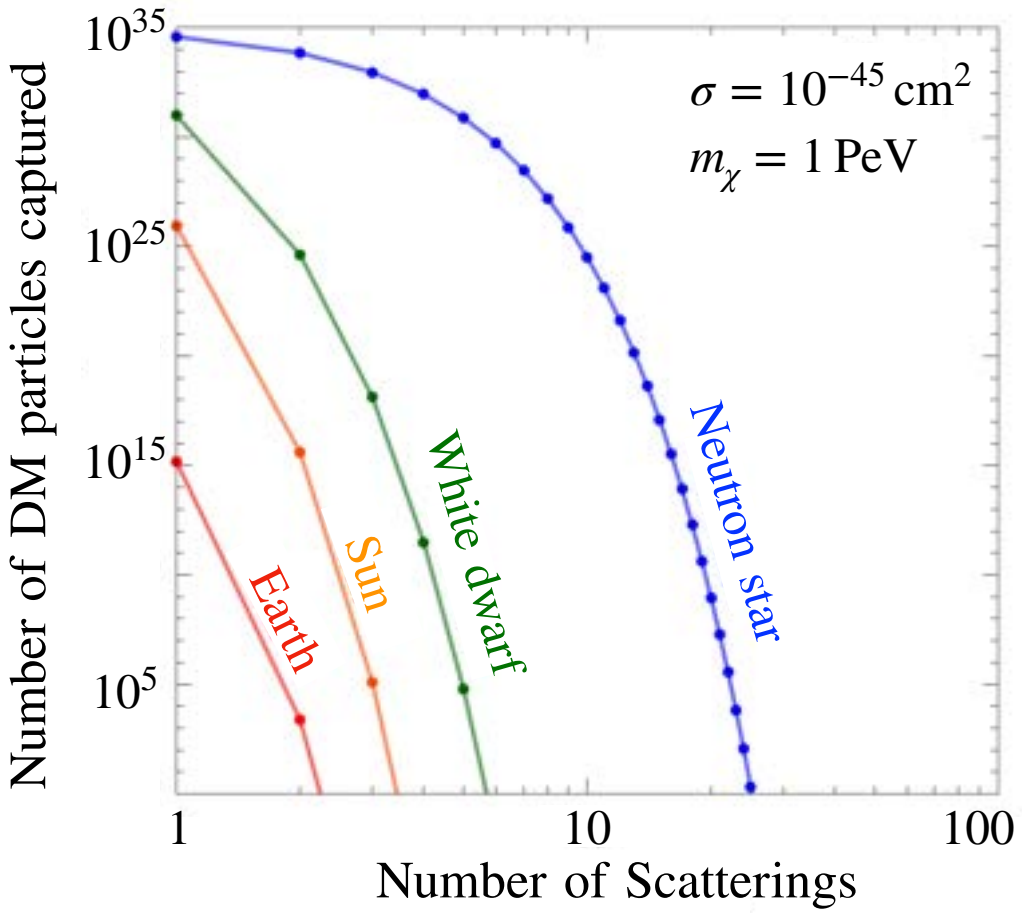

Figure 2.2: Number of particles captured after N collisions during the lifetime of the different celestial objects plotted against the number of collisions N. Note that, here, σ denotes the interaction cross-section with the relevant target. For example, in Earth the target nucleus is taken to be that of iron while for neutron stars it is simply a neutron. The density of DM, for simplicity, has been taken to be the that around the solar system, *i.e.*, 0.3 GeV cm^{-3}. We also consider very heavy DM (DM mass of 1 PeV) to emphasize the effect of multiple collisions.

where, $N_{\rm max}$ denotes the maximum number of scattering. The determination of $N_{\rm max}$ is arbitrary in the previous literature [196]. In the previous literature, $N_{\rm max}$ is determined from the criterion that $p_{N_{\rm max}}(\tau) = \epsilon$, where ϵ is an arbitrary small number. So depending on the smallness of ϵ, $N_{\rm max}$ can be quite high. We determine $N_{\rm max}$ from the physical criterion that the number of captured DM particles at $N_{\rm max}$ reduces to unity, i.e., $t_{age}\, C_{N_{\rm max}} = 1$. In other words, we will truncate the sum in Eq. (2.18) when $t_{age}\, C_{N_{\rm max}} = 1$ is satisfied. This is possible because the capture rate at N^{th} collision, C_N, decreases monotonically with increase in N as the probability of occurring N^{th} collision,

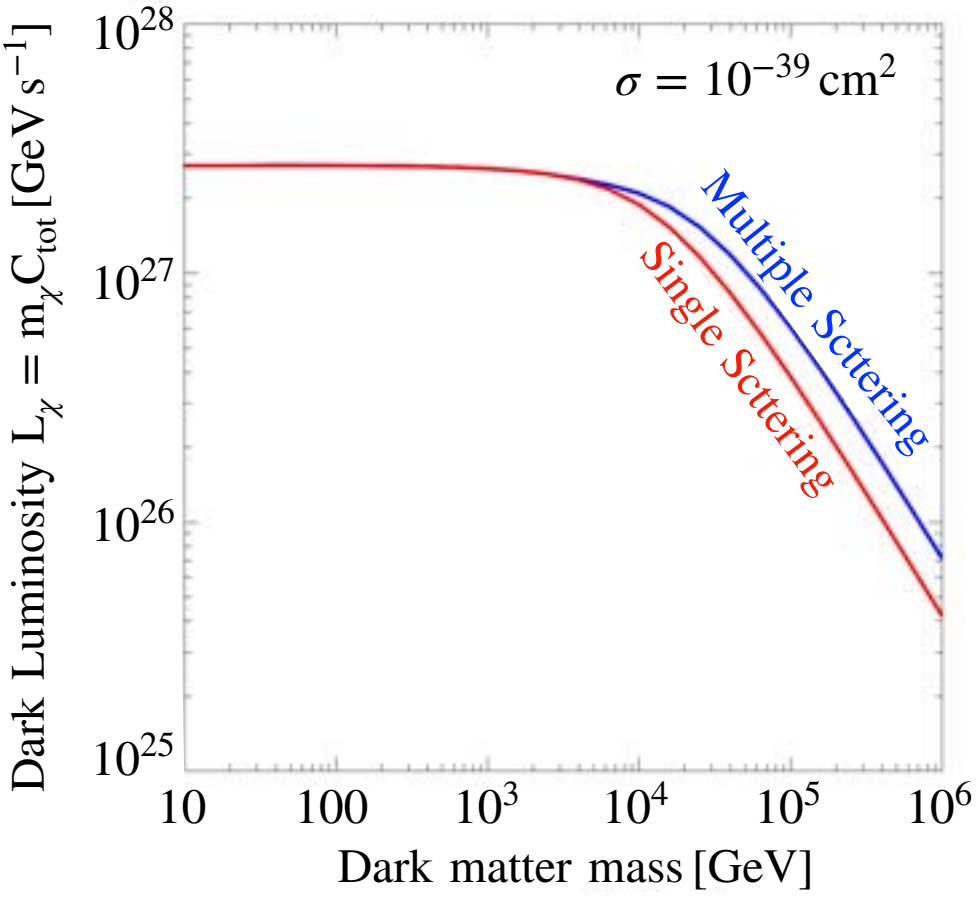

Figure 2.3: Dark luminosity from annihilation of captured DM particles are shown for various DM masses. The red line corresponds to the single scattering approximation and the blue line correspond to the multiple collision (using the formalism developed in the previous section). $\sigma = 10^{-39}$ cm^2 denotes the interaction cross-section of DM with the carbon nucleus.

$p_N(\tau)$, is suppressed for higher values of N.

In Fig. 2.2, we show the maximum number of scatterings ($N_{\rm max}$) that can occur in various stellar objects such as Earth, Sun, White dwarf, and Neutron Star. We find that for non-compact objects, capture always almost occur after single collision. For compact objects like neutron stars, the maximum number of scatterings can at most be $\mathcal{O}(10)$. However, the captured number of DM particles for a given collision is significantly suppressed for higher values of N. The results shown in Fig. 2.2 demonstrate the overestimate of $N_{\rm max}$ in the previous literature [196], where $N_{\rm max}$ is taken as high as $\mathcal{O}(10^3)$.

2.3 White Dwarfs as DM Detectors

We now consider the capture of annihilating DM particles inside a white dwarf to probe DM interactions with the baryonic matter. For annihilating DM, the captured DM particles annihilate among themselves, and produce SM particles. Because of the very high baryonic density of the white dwarf, the mean free path of these SM particles is quite high, and they (even neutrinos) can not come out of the white dwarf. As a result, these SM particles re-scatter, eventually heat up the white dwarf, and thereby increase the luminosity of the white dwarf. Non detection of such anomalous heating via luminosity measurement of the white dwarfs provide stringent constraint on DM interactions with the baryonic matter, as detailed in the following sections.

The process by which DM heats up a white dwarf involves several steps. First, each captured DM particle must thermalize with the host through successive scattering with the targets. This is ensured by checking that the thermalization timescale [201, 248, 269, 270] is less than the age of the white dwarf under consideration. In fact, the thermalization timescale is instantaneous with respect to the age of the white dwarf ($\sim$ Gyr) for the values of DM mass and scattering cross-section that we are considering. See Appendix A for a detailed derivation of the thermalization timescale. The next step is to understand how the number of captured DM particles, $N_{\rm cap}$, evolves with the time inside the stellar core. This can be phrased as a simple differential equation

$$\frac{dN_{\rm cap}}{dt} = C_{\rm tot} - A N_{\rm cap}^2 \,, \tag{2.19}$$

where $C_{\rm tot}$ is the total capture rate given in Eq. (2.18) and $A = \langle \sigma_a v \rangle / V_{\rm th}$ is the self-annihilation rate. $\langle \sigma_a v \rangle$ denotes the thermally-averaged annihilation cross-section of the DM particles and $V_{\rm th}$ denotes the volume of the thermalization sphere[1].

The differential equation in Eq. (2.19) attains its equilibrium solution if the equilibration time, $t_{\rm eq} \sim \sqrt{\frac{V_{\rm th}}{C_{\rm tot}\langle \sigma_a v \rangle}}$, is shorter than the age of the white dwarf. We have verified that for DM annihilation cross-section larger than $10^{-56}\,{\rm cm}^3\,{\rm s}^{-1}$, this condition is always satisfied for typical white dwarf parameters. As a consequence, the dark luminosity (L_χ)

[1]The DM particles thermalize and settle into a spherical region of radius $r_{\rm th} = \sqrt{\frac{9 k_B T_{\rm WD}}{4\pi G \rho_{\rm WD} m_\chi}}$ in the stellar core, where $T_{\rm WD}$ ($\rho_{\rm WD}$) denotes the core temperature (density) of the white dwarf. Quantitatively, $r_{\rm th} = 30\,{\rm m} \left(\frac{10^6\,{\rm GeV}}{{\rm m}_\chi}\right)^{1/2} \left(\frac{10^7\,{\rm K}}{{\rm T}_{\rm WD}}\right)^{-1/2} \left(\frac{10^9\,{\rm g/cm^3}}{\rho_{\rm WD}}\right)^{1/2}$, and is much smaller than the radius of the white dwarf for the DM masses that we are interested in.

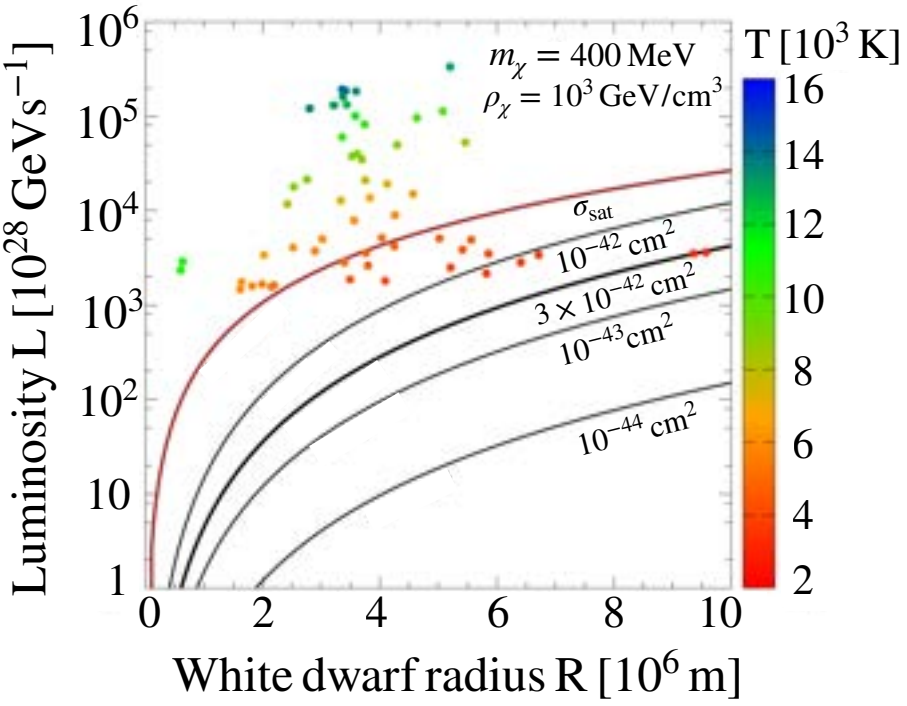

Figure 2.4: Dark luminosity arising from annihilation of captured DM particles compared with the observed WD luminosities. DM mass is taken as 400 MeV, and five benchmark DM-nucleon cross-sections are shown. The topmost curve corresponds to the luminosity when DM-nucleon cross-section takes its geometrical saturation value, i.e, σ_{sat}. The lower curves correspond to smaller cross-sections, with the curve marked by $\sigma_{\chi n} = 3\times10^{-43}\,\mathrm{cm}^2$ being just excluded. The local dark matter density in the M4 cluster is taken to be $\sim 10^3\,\mathrm{GeV\ cm^{-3}}$ [195] and the dispersion velocity to be ~ 20 km s^{-1} [195].

which arises solely from the annihilation of the captured DM particles is essentially given by the total mass capture rate, i.e., $L_\chi = m_\chi C_{\mathrm{tot}}$.

In Fig. 2.3, we show the dark luminosity in a typical white dwarf as a function of the DM mass for single collision approximation as well as for multiple collisions. For low DM masses, the dark luminosity is constant as the capture rate is inversely proportional to the DM mass, and the effect of the multiple collision is also negligible. For higher DM masses, the dark luminosity is inversely proportional to the DM mass as the capture rate scales as $1/m_\chi^2$ due to the kinematic suppression. The impact of multiple collisions also becomes important for heavier DM, i.e., for DM masses ≥ 10 TeV.

We now compare the dark luminosity, L_χ, to the observed luminosities of several white dwarfs to probe DM interactions with the nucleons. We consider the white dwarfs in

the M4 globular cluster, the closest globular cluster to the Earth, which is about 1.9 kpc from us [271]. The luminosity ($L_{\rm obs}$) and the temperature ($T_{\rm obs}$) of these white dwarfs are adapted from [195]. These white dwarfs are particularly interesting because *i*) they are old (age $\sim$ Gyr) so that they can capture DM particles for a much longer time and *ii*) White dwarfs in the M4 globular cluster are very cold so that any anomalous heating signature is easy to observe. Furthermore, if DM is present in M4, the expected DM density is very large compared to the DM density in the Solar neighborhood, which enhances the DM capture rate. We assume an ambient DM density of $\rho_\chi = 1000$ GeV/cm^3 and the velocity dispersion of $\bar{v} = 20$ km/s for this analysis [195].

In the absence of a dominant burning mechanism inside these white dwarfs, they are assumed to be nearly perfect black body emitters. Under this assumption, if the luminosity and temperature of the white dwarfs are independently measured, we can infer their radius to be $R = \sqrt{\frac{L_{\rm obs}}{4\pi\sigma_0 T_{\rm obs}^4}}$, where σ_0 is the Stefan-Boltzmann constant. We next calculate the dark luminosity, which is essentially the total mass capture rate by using their derived radius. Demanding that the dark luminosity should not exceed the observed luminosity ($L_{\rm obs}$) of the white dwarfs, we impose an exclusion limit on DM mass and scattering cross-section with the baryonic matter

$$L_\chi = m_\chi \sum_{N=1}^{N_{\rm max}} C_N \leq L_{\rm obs}\,. \tag{2.20}$$

White dwarfs are dominantly made up of carbon (C^{12}) nuclei, which we take to be the target particle. For the range of DM masses that are of interest to us, we can treat the relevant collisions to be coherent and elastic. This is simply because the typical momentum transfer to a carbon nucleus is always *smaller* than the inverse of the de-Broglie wavelength of the nuclei. To illustrate this point further, the typical momentum transfer to a carbon nuclei in a given collision is μv, where μ is the reduced mass of the DM and the carbon nuclei, and v is the relative velocity of the DM particle with respect to the target. For heavy DM masses (say $m_\chi \gg 10\,\text{GeV}$), μ is given by the mass of the carbon nuclei, i.e., $\mu \sim 10\,\text{GeV}$, whereas, for light DM masses (say $m_\chi \ll 10\,\text{GeV}$), μ is essentially the DM mass. Due to the steep gravitational potential of the white dwarfs, v is essentially given by the escape velocity of the white dwarfs, i.e., $v \sim \mathcal{O}(0.01)$ for white dwarfs. Hence, for heavy DM masses, the typical momentum transfer to a carbon

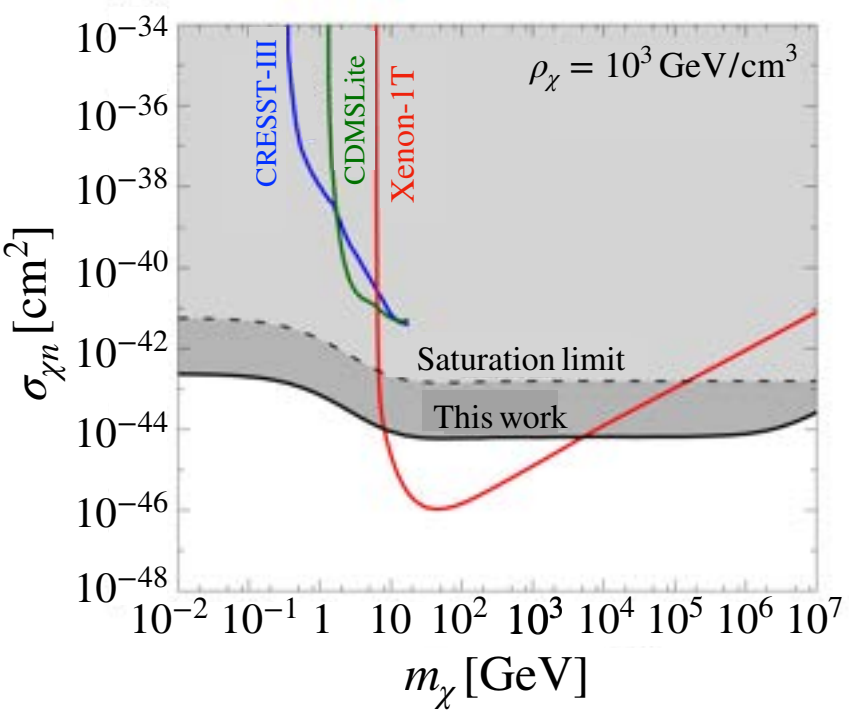

Figure 2.5: Upper bound on the DM-nucleon cross-section (solid black line) from the observed luminosity of 2.5×10^{31} GeV s^{-1} and a derived radius of $\sim 9\times10^6$ m from a white dwarf in the M4 globular cluster. Related exclusion limits from the underground direct detection experiments, CRESST-III [273] and SuperCDMS [274] in the low mass regime and XENON-1T [96] in the high mass regime are also shown for comparison. Note that, XENON-1T limit has been linearly extrapolated beyond 10^3 GeV. The dashed black line corresponds to the saturation cross-section $\sigma_{\rm sat}$ (translated to nucleonic cross-sections). Above this, in the light gray shaded region, any cross-section is essentially equivalent to $\sigma_{\rm sat}$, and ruled out alike. The minimum DM mass is taken as 10 MeV because below this mass the evaporation of DM particles becomes important [275].

nuclei is 100 MeV. This is always *smaller* than the inverse of the de Broglie wavelength of the nucleus, which is $1\,\text{fm}^{-1} \sim 200\,\text{MeV}$, explaining the coherent approximation for heavier DM. Similarly, for lighter DM, the typical momentum transfer to a carbon nuclei is always smaller than 200 MeV, explaining the coherence approximation. We have also included a Helm form factor ($F^2_{\rm Helm}$) [272] to account for any loss of coherence. However, it remains unity for the all DM masses that we are interested in.

To compare with the present direct detection limits, we translate the DM-carbon cross-section σ to DM-nucleon cross-section $\sigma_{\chi n}$. As we are in the regime of coherent scattering,

for spin-independent interactions, and by assuming equal contributions from protons and neutrons, this translation is simply given by

$$\sigma = \frac{\mu_t^2}{\mu_n^2} A^2 \sigma_{\chi n} \,. \tag{2.21}$$

Here, μ_t (μ_n) denotes the reduced masses of the DM-carbon (DM-nucleon) system and $A = 12$ corresponds to the total number of the nucleons in a carbon nucleus. For light DM particles, this ratio of μ_t^2/μ_n^2 reduces to unity, whereas, for heavier DM masses, this ratio reduces to A^2, giving rise to the A^4 scaling from Eq. (2.21).

Fig. 2.4 compares the dark luminosity from the annihilation of the captured DM particles to the observed luminosity of the white dwarfs in the M4 globular cluster. The solid lines denote the estimated dark luminosity, L_χ, as a function of the white dwarf radius, for several values of the DM-nucleon scattering cross-sections, and for a fixed value of the DM mass ($m_\chi = 400$ MeV). The position of each colored dot denotes the observed luminosities of the white dwarfs ($L_{\rm obs}$), and their radius inferred through an independent measurement of its temperature, as explained before. The observed temperature ($T_{\rm obs}$) is encoded in color, as per the shown color-bar. The topmost solid line, marked by $\sigma_{\rm sat}$ denotes the maximum attainable dark luminosity when the cross-section reaches its saturation limit. Since, L_χ must be smaller than the $L_{\rm obs}$, we find that DM-nucleon cross-section of $\sigma_{\chi n} \sim 10^{-42}$ cm^2 is in tension with the lower luminosity white dwarfs.

Fig. 2.5 demonstrates an upper bound on the DM-nucleon scattering cross-section obtained from the non-observation of dark heating in a white dwarf residing in the M4 globular cluster. The observed luminosity of this white dwarf is $2.5 \times 10^{31}\,{\rm GeV\,s^{-1}}$, and its radius is inferred to be 9×10^6 m. This conservative constraint is obtained by demanding that the dark luminosity can not exceed the observed luminosity. Exclusion limits obtained from several underground direct detection experiments are also shown for comparison. Note that, this constraint is practically independent of the DM mass, and differs from the corresponding direct detection constraints which linearly weaken at high DM masses, and cuts off at low DM masses. The mass independence of this constraint stems from the fact that DM capture rate is inversely proportional to the DM mass, and hence, the dark luminosity, which is essentially the total mass capture rate, is independent of the DM mass. However, the weak mass-dependence of the constraint, especially in the low mass regime, is due to the presence of the Helm form factor, and the ratio of the

reduced masses, both of which depend on DM mass, as described in Eq. (2.21).

The constraint obtained here is very stringent. In the approximation of DM over-density in the M4 globular cluster, it is the strongest constraint for DM masses below ~ 10 GeV. For such light DM masses, this constraint is nearly 3–7 orders of magnitude stronger than the corresponding direct detection constraints. Crucially, because of the signature mass-independence, one finds stringent exclusions for DM particles less than 350 MeV that are below the sensitivity of typical direct detection experiments. Likewise, in the high-mass regime, say above a few TeV, these constraints are also the strongest. In this regime, the improvement due to multiple scattering is important.

2.4 Summary & Conclusions

We have revisited the formalism of DM capture in the multiple collision regime, and made several key improvements. We provide an exact analytical expression of the capture probability as well as the capture rate for multi-scatter stellar capture, as given in Eq. (2.8) & Eq. (2.15). We also estimate the maximum number of scatterings ($N_{\rm max}$) that can actually take place inside a stellar object, as shown in Fig. 2.2. Our estimation of $N_{\rm max}$ significantly improves over the previous estimate [196], and demonstrate that the effect of multiple collision on the DM capture rate is actually modest.

By using our formalism, we provide stringent constraint on DM interactions with the baryonic matter from annihilating DM capture in white dwarfs, as shown in Fig. 2.5. This constraint is simply derived from the fact that annihilation of captured DM particles does not over-heat the white dwarfs in our nearest globular cluster. Our constraint on DM-nucleon interaction strength is significantly stronger than the corresponding constraints from the underground direct detection experiments. For light DM ($10\,\text{MeV} \leq m_\chi \leq 10\,\text{GeV}$), this constraint is 3$-$7 order of magnitude stronger than the direct detection constraints, whereas, for heavy DM ($10^7\,\text{GeV} \geq m_\chi \geq 10^4\,\text{GeV}$), it is 1$-$2 order of magnitude stronger. It is important to mention that this astrophysical constraint can probe very low DM masses, which is currently inaccessible to the terrestrial direct detection experiments. Quantitatively, the astrophysical constraint probe DM masses as low as $m_\chi = 10\,\text{MeV}$ (below which DM particles evaporate from the stellar core while getting thermalized [275]), whereas, the underground direct detection experiments typically probe up to DM mass

of 350 MeV.

It is also worth-noting that, the constraint shown in Fig. 2.5 hinges over the DM over-density in the M4 globular cluster, which is not yet well-established. Further simulations of galaxy formation and evolution, together with observations, will shed light on this topic, and can even improve the limits estimated here.

Note added: Recently, Ref [202] appeared, and it improves our constraint on DM-nucleon interaction strength by taking into account the inner structure of the white dwarfs as well as a more realistic treatment of the response function in the DM-nuclei interactions.

Chapter 3

Neutron Stars as DM Detectors: Effect of Mediator Masses

In this Chapter, we generalize the formalism for DM capture in stellar objects to account for arbitrary mediator masses, and demonstrate that the astrophysical constraints on DM-nucleon interaction strength, obtainable from neutron star heating or collapse, significantly weaken for lighter mediators, and can even be voided for light enough mediators. We further show the impact of repulsive self-interactions among the DM particles on the corresponding constraints on DM-nucleon interaction strength. The results presented in this chapter can be found in [8].

3.1 DM Capture: Effect of Mediator Mass

In the previous chapter, we have derived the DM capture rate in a stellar object in the multiple collision regime, as given in Eq. (2.4). So, in the single-collision approximation, the DM capture rate simply takes the form

$$C = \pi R^2 \frac{\rho_\chi}{m_\chi} \int \frac{f(u)du}{u} (u^2 + v_{\rm esc}^2)\, {\rm Min}\left[\frac{\sigma_{\chi n}}{\sigma_{\chi n}^{\rm sat}}, 1\right] g_1(u)\,, \tag{3.1}$$

where $p_1(\tau) = {\rm Min}\left[\frac{\sigma_{\chi n}}{\sigma_{\chi n}^{\rm sat}}, 1\right]$ denotes the probability of occurring *first* collision, and $g_1(u)$ is the capture probability in the single-collision approximation (the subscript 1 refers to the single-collision approximation). $g_1(u)$ is determined by the fact that the final velocity of the DM particles has to be less than the escape velocity of the stellar object, and is

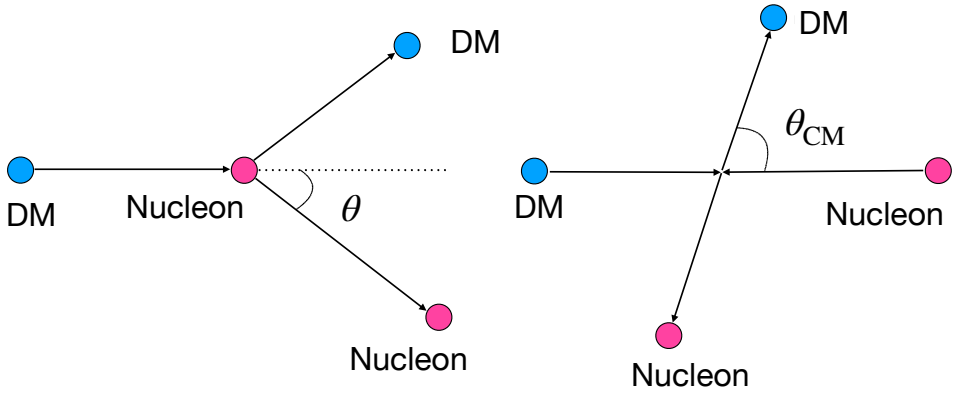

Figure 3.1: DM-nucleon scattering is schematically illustrated in the rest frame of nucleon (left) as well as in the center of mass frame (right). The recoil angle in the rest frame of nucleon is denoted as θ and the scattering angle in the center of mass frame as $\theta_{\rm CM}$. The probability distribution function of either of these angles determines the energy loss distribution.

given by

$$g_1(u) = \int_0^1 dz\, \Theta\left(v_{\rm esc} - \underbrace{\left(u^2 + v_{\rm esc}^2\right)^{1/2} \left(1 - z\frac{4m_\chi m_n}{(m_\chi + m_n)^2}\right)^{1/2}}_{v_f} \right) s(z)\,. \tag{3.2}$$

Here, $z = \cos^2\theta = \sin^2(\theta_{\rm CM}/2)$ is a kinematic variable which takes values between 0 and 1, and encodes the fractional energy loss of the DM particle ($\Delta E/E$) in a given scattering. More specifically, z is proportional to the fractional energy loss of the DM particle, and can be written as $\Delta E/E = \beta z$, where $\beta = (4m_\chi m_n)/(m_\chi + m_n)^2$. $s(z)$ denotes the probability distribution of the kinematic variable z, and it is *assumed* to be unity, in the prior treatments. We show that $s(z)$ is intimately related to the differential scattering cross-section of the relevant scattering process. For interactions mediated via infinitely massive mediators, the assumption of $s(z) = 1$ only holds true. However, in general, the differential cross section may involve lighter mediators, and the distribution is not guaranteed to be uniform. In the following subsection, we derive the general form of $s(z)$ for DM interactions mediated by a Yukawa potential with a mediator mass of m_ϕ.

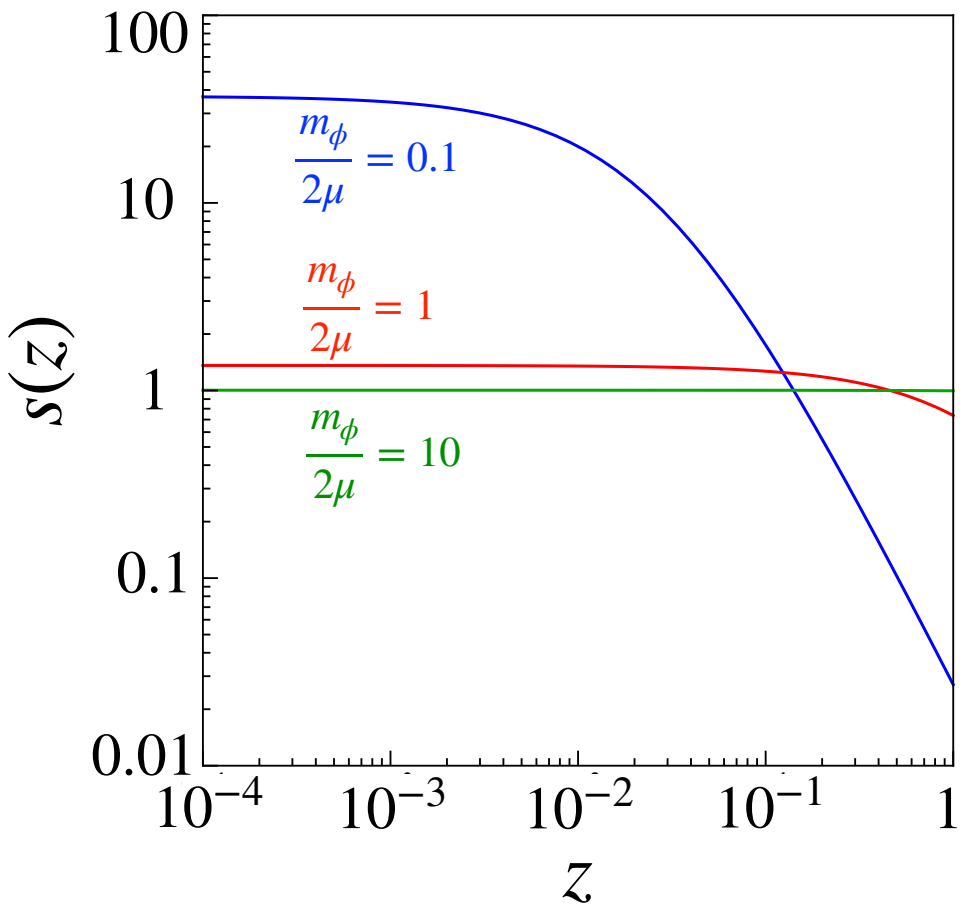

Figure 3.2: Energy loss distribution, $s(z)$, with z for three representative values of $m_\phi/2\mu$. When the mediator is lighter than the reduced mass, the deviation from uniform energy loss distribution becomes significant.

3.1.1 General Form of $s(z)$

For DM-nucleon interaction via a Yukawa potential,

$$V = \frac{\alpha}{r} e^{-m_\phi r}\,, \tag{3.3}$$

where α denotes the interaction strength and m_ϕ denotes the mediator mass, the differential scattering cross-section in non-relativistic Born approximation is given by

$$\frac{d\sigma}{d\Omega_{\rm CM}} = \frac{4\mu^2\alpha^2}{\left(4\mu^2 v_{\rm rel}^2 \sin^2(\theta_{\rm CM}/2) + m_\phi^2\right)^2}\,. \tag{3.4}$$

Here μ is the reduced mass of the system, $v_{\rm rel}$ is the relative velocity between DM and nucleon made dimensionless in units of the speed of light and $\theta_{\rm CM}$ denotes the scattering

angle in the center of mass frame. The fractional loss in kinetic energy in DM-nucleon scattering, as shown in Fig. 3.1, is given by

$$\frac{\Delta E}{E} = \frac{4 m_\chi m_n}{(m_\chi + m_n)^2} z = \beta\, z\,, \tag{3.5}$$

where m_χ, m_n are the mass of DM and nucleon, respectively. The scattering kinematics determines $z = \cos^2\theta = \sin^2(\theta_{\rm CM}/2)$, with $z \in [0,1]$.

The *energy loss distribution* $s(z)$, a key quantity to estimate the capture rate precisely, is determined by the distribution of $\Omega_{\rm CM}$, which is in turn dictated by the differential scattering cross-section of the relevant scattering process,

$$s(\Omega_{\rm CM}) = \frac{1}{\sigma}\frac{d\sigma}{d\Omega_{\rm CM}} = \frac{1}{4\pi} s(z)\,. \tag{3.6}$$

For DM-nucleon scattering via a Yukawa potential, to consider a widely applicable example, the energy loss distribution $s(z)$ is given by

$$s(z) = \frac{m_\phi^2\left(4\mu^2 v_{\rm rel}^2 + m_\phi^2\right)}{\left(4\mu^2 v_{\rm rel}^2 z + m_\phi^2\right)^2}\,. \tag{3.7}$$

For DM self scattering via a Yukawa potential, the reduced mass $\mu = m_\chi/2$, and energy loss distribution $s^{\rm self}(z)$ simplifies to

$$s^{\rm self}(z) = \frac{m_\phi^2\left(m_\chi^2 v_{\rm rel}^2 + m_\phi^2\right)}{\left(m_\chi^2 v_{\rm rel}^2 z + m_\phi^2\right)^2}\,. \tag{3.8}$$

In the limit $m_\phi \to \infty$, we recover the familiar expressions for uniform distribution, $s(z) = 1$ and $s^{\rm self}(z) = 1$, which have been used extensively in the previous treatments. Variation of $s(z)$ with mediator mass is shown in Fig. 3.2 for DM-nucleon interaction mediated via a Yukawa potential. From Fig. 3.2 it is evident that the assumption of uniformity in energy loss distribution, i.e., $s(z) = 1$, is a poor approximation when the mediator is lighter than either of the scattering particles.

We use the general form of $s(z)$ from Eq. (3.7) to estimate the generalized capture prob-

ability, $g_1(u)$, in Eq. (3.2). The generalized capture probability simplifies to

$$g_1(u) = \frac{m_\phi^2 \left(1 - \frac{1}{\beta}\frac{u^2}{u^2+v_{\rm esc}^2}\right)}{\left(m_\phi^2 + \frac{4\mu^2 u^2}{\beta c^2}\right)} \Theta\left(v_{\rm esc}\sqrt{\frac{\beta}{1-\beta}} - u\right) . \tag{3.9}$$

Note that, in the limit of $m_\phi \to \infty$, we again recover the familiar expression for capture probability [188]. From this generalized analytical expression of the capture probability, one can easily estimate the capture rate of DM particles inside a stellar body, as given in Eq. (3.1), by considering a suitable velocity distribution of the dark matter particles.

3.2 DM Self-Capture: Effect of Mediator Mass

In the previous section, we have estimated the baryonic capture rate for DM-nucleon scattering via a Yukawa potential. If the dark matter particles have appreciable self-interaction strength, an incoming dark matter particle can also lose its energy by colliding with previously captured DM particles within the celestial core. This is known as *self-capture* of DM particles. In this section, we estimate the generalized self-capture rate for DM self-interactions mediated by a Yukawa potential.

For self-capture, the incoming dark matter particle has to lose enough energy so that its final velocity v_f falls below the escape velocity $v_{\rm esc}$ of the stellar body. The target dark matter particle, on the other hand, gains energy from these collisions but its final velocity v_f' should also remain less than $v_{\rm esc}$. Therefore, the *self-capture probability* is given by

$$g_1^{\rm self}(u) = \int_0^1 dz\, \Theta(v_{\rm esc} - v_f)\, \Theta(v_{\rm esc} - v_f')\, s^{\rm self}(z)\,, \tag{3.10}$$

where $v_f = \sqrt{(u^2 + v_{\rm esc}^2)(1-z)}$ denotes the final velocity of the incoming DM particle and $v_f' = \sqrt{(u^2 + v_{\rm esc}^2)z}$ denotes the final velocity of the target DM particle.

Using the expression for $s^{\rm self}(z)$ from Eq. (3.8), the generalized self-capture probability for DM self-interactions mediated by a Yukawa potential simplifies to

$$g_1^{\rm self}(u) = \frac{m_\phi^2 \left(m_\phi^2 + m_\chi^2 \frac{u^2+v_{\rm esc}^2}{c^2}\right)}{\left(m_\phi^2 + m_\chi^2 \frac{v_{\rm esc}^2}{c^2}\right)\left(m_\phi^2 + m_\chi^2 \frac{u^2}{c^2}\right)} \left(\frac{v_{\rm esc}^2 - u^2}{v_{\rm esc}^2 + u^2}\right) \Theta(v_{\rm esc} - u)\,. \tag{3.11}$$

Note that, in the limit of $m_\phi \to \infty$, we recover the familiar expression for self-capture probability [263].

Self-capture rate of dark matter particles in the stellar body depends on the number of already captured DM particle N_χ, DM self scattering cross-section $\sigma_{\chi\chi}$, the flux of incoming dark matter particles and most importantly on the probability of incurring energy loss $g_1^{\rm self}(u)$ which depends on the energy loss distribution. Hence, the self-capture rate takes the form

$$C^{\rm self} = \frac{\rho_\chi}{m_\chi} \int \frac{f(u)du}{u} \left(u^2 + v_{\rm esc}^2\right) N_\chi \, {\rm Min}\left[\sigma_{\chi\chi}, \sigma_{\chi\chi}^{\rm sat}\right] \, g_1^{\rm self}(u)\,. \tag{3.12}$$

Using the analytical expression of the self-capture probability from Eq. (3.11), one can easily estimate the generalized self-capture rate for a given velocity distribution of dark matter particles. The self-capture rate depends linearly on the number of captured dark matter, N_χ, so the number of captured particle due to self-capture grows exponentially with time. In general, the equation governing the number of captured DM in presence of self-interaction is given by

$$\frac{dN_\chi}{dt} = C + C^{\rm self}. \tag{3.13}$$

However, this exponential growth due to self-capture cuts off when DM self-interaction strength reaches its geometric saturation value $\sigma_{\chi\chi}^{\rm sat}$ [200, 251], determined by the radius of the thermalization sphere $r_{\rm th}$ inside the stellar body

$$N_\chi \sigma_{\chi\chi}^{\rm sat} = \pi r_{\rm th}^2\,. \tag{3.14}$$

Once the number of captured dark matter particles inside the stellar object attains its saturation value, self-capture rate becomes time-independent, i.e., $N_\chi \sigma_{\chi\chi} \to \pi r_{\rm th}^2$. Therefore, after the saturation, number of captured dark matter particles due to self-interactions grows only linearly with time. Note that, for self-capture of fermionic DM, the effect of Pauli blocking has to be taken into consideration and hence the self-capture rate of fermionic DM is additionally suppressed by Pauli blocking efficiency $\zeta = [\Delta p/p_F, 1]$, where Δp is the momentum transfer and p_F is the Fermi momentum [249, 259]. However, in case of bosonic DM, there is no such suppression in the self-capture rate.

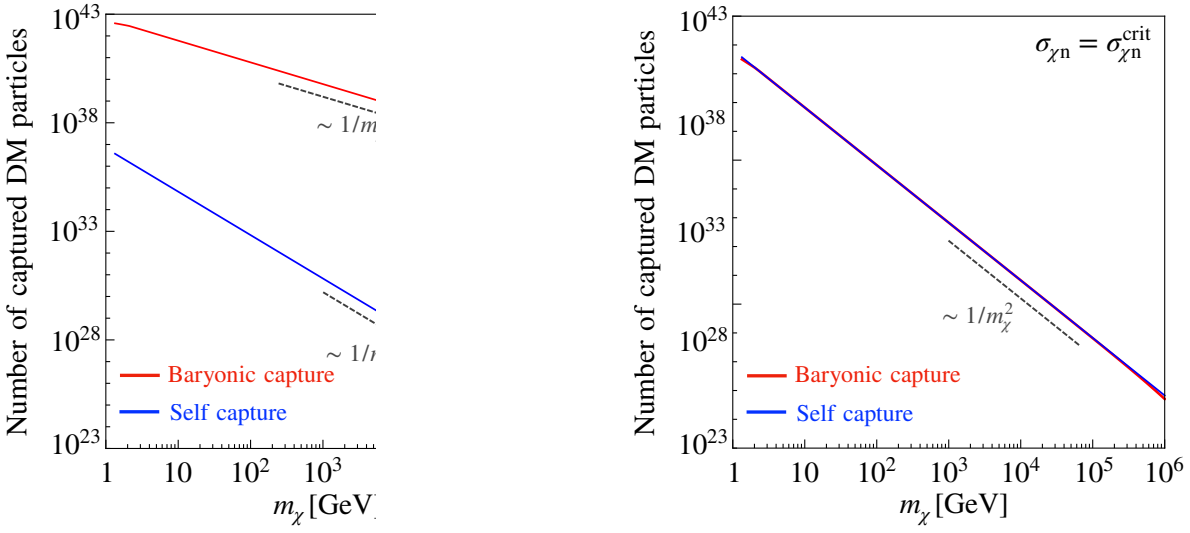

Figure 3.3: Number of DM particles captured inside a neutron star is shown with DM mass, assuming uniform energy loss distribution. In the left panel, DM-nucleon scattering cross-section is taken to its largest possible value, i.e., the geometrical saturation value, $2 \times 10^{-45}\,\mathrm{cm}^2$. In the right panel, the scattering cross-section is taken to its critical value, $\pi r_{\rm th}^2/N_n$, such that self-capture and baryonic capture are equally efficient. In each plot, the red lines correspond to baryonic capture and the blue lines correspond to the maximum allowed self-capture. The local DM density around the neutron star is taken as 0.4 GeV/cm^3 and age of the neutron star is taken as 6.69×10^9 years. The core temperature of the neutron star is taken as 2.1×10^6 K and all the other neutron star parameters are described in the text. We restrict our study to $m_\chi < 10^6$ GeV to ensure multiple scattering is not relevant.

3.3 Neutron Stars as DM Detectors

We now consider capture of annihilating as well as non-annihilating DM particles inside a neutron star to probe DM interactions with the baryonic matter. We first compute the capture rate of DM particles, inside a neutron star, by considering the velocity distribution of incoming DM particles as Maxwell-Boltzmann with halo velocity dispersion 220 km/s. We take typical values for neutron star parameters [249], such as, mass $M_{\rm NS} = 1.44 M_\odot$, radius $R_{\rm NS} = 10.6$ km and the central density $\rho_{\rm NS} = 1.4 \times 10^{15}$ g/cm^3 for the analysis. We have not considered the effect of multiple scatterings in the capture rate, because, for DM particles lighter than a few 100 TeV, capture almost always occurs after a single scattering, as shown in the previous chapter.

While considering DM capture rate in a neutron star, two corrections, gravitational blueshift of the initial kinetic energy and general relativistic enhancement of the number of dark matter particles crossing the stellar surface, have to be considered [196]. For the gravitational blueshift effect, in the rest frame of the neutron star, the incoming DM particle has a relativistic correction in kinetic energy $\sim \mathcal{O}(v_{\rm esc}^2/c^2)$, and it modifies the capture probability. As the lower limit of the capture probability integral is proportional to $v_{\rm esc}^2/w^2$, this can be accounted for by substituting

$$v'_{\rm esc} \to \frac{v_{\rm esc}}{\left(1+\frac{3}{4}\left(\frac{v_{\rm esc}}{c}\right)^2\right)^{1/2}} \,. \tag{3.15}$$

For the general relativistic enhancement of the gravitational potential of the stellar body, the number of dark matter particles which traverse the stellar surface increases. Therefore, this effect modifies the capture rate by [191, 196]

$$C \to \frac{C}{1-\left(\frac{v'_{\rm esc}}{c}\right)^2} \,. \tag{3.16}$$

We have explicitly examined that the gravitational blueshift effect can reduce the capture rate up to $\sim 20\%$, whereas, the general relativistic correction can enhance the capture rate by as far as a factor of two.

We have also neglected the contribution from self-capture in the estimation of the total capture rate. Self-interactions among the DM particles can lead to an additional contribution to the capture rate. For the not too small values of $\sigma_{\chi n}$ that we can probe, baryonic capture always dominates over the self-capture even if we take the maximum allowed value of the DM self-interaction strength. This can be understood easily, because in neutron stars, the extremely large nucleon density increases the baryonic capture rate and also shrinks the thermalization sphere[1] as $r_{\rm th} = \sqrt{9k_{\rm B}T_{\rm NS}/(4\pi G\rho_{\rm NS}m_\chi)}$. Since the self-capture rate scales quadratically with the radius of the thermalization sphere $r_{\rm th}$, self-capture rate falls off significantly. However, if the DM-nucleon scattering cross-section is extremely small, at some point, self-capture dominates over the baryonic capture. This

[1]For typical neutron star parameters, i.e., $M_{\rm NS} = 1.44 M_\odot$ and $\rho_{\rm NS} = 1.4\times10^{15}$ g/cm^3, the radius of the thermalization sphere $r_{\rm th} = 24\,{\rm cm}\left(\frac{100\,{\rm GeV}}{m_\chi}\right)^{1/2}\left(\frac{10^5\,{\rm K}}{T_{\rm WD}}\right)^{-1/2}$, and is always smaller than the radius of the neutron star ($R_{\rm NS} = 10.6$ km) for the range of DM masses that we are interested in.

is what we call the *critical cross-section*, $\sigma_{\chi n}^{\rm crit}$, which is given by $\sigma_{\chi n}^{\rm crit} \sim \pi r_{\rm th}^2/N_n$. Quantitatively, we can estimate that for a neutron star with core temperature of 2.1×10^6 K and for DM mass of 100 GeV, this limiting cross-section turns out to be $\sim 2.5 \times 10^{-53}$ cm^2. For heavier dark matter, this limiting cross-section further reduces linearly with DM mass, as $r_{\rm th}^2$ is inversely proportional to the DM mass. Of course, thermalization requires $\sigma_{\chi n}$ to not become smaller than the minimum value required for thermalization. For $m_\chi \gtrsim 1$ TeV, the critical cross-section falls below the minimum thermalization cross-section, and self-capture never exceeds baryonic capture for even moderately large DM masses.

Total number of captured DM particles due to baryonic and self-interactions is shown in Fig. 3.3, for a neutron star with a core temperature of 2.1×10^6 K. From Fig. 3.3, it is evident that self-capture can contribute significantly to the total capture rate only when the DM-nucleon interaction strength is lowered past its critical value, which is really small compared to the parameter space of contemporary interest. Note that baryonic capture scales as $1/m_\chi$, as the number density of incoming DM particles is inversely proportional to the DM mass. In the right panel, the additional $1/m_\chi$ suppression in the baryonic capture simply comes from the mass dependence of DM-nucleon scattering cross-section, as $\sigma_{\chi n}^{\rm crit} \sim 1/m_\chi$. However, number of captured DM particles due to self-capture always scales as $\sim 1/m_\chi^2$, because self-capture rate is quadratically proportional to the thermalization radius, and $r_{\rm th}^2$ scales inversely to the DM mass, in addition to the $1/m_\chi$ suppression from the number density of the incoming DM particles.

3.3.1 Annihilating DM & Dark Kinetic Heating

For annihilating DM, the number of captured dark matter particles inside the stellar object follows

$$\frac{dN_\chi}{dt} = C - C_a N_\chi^2 \,, \tag{3.17}$$

where, C is the total capture rate and C_a is the annihilation rate. The annihilation rate is simply given by $C_a = 3\langle\sigma_a v\rangle/4\pi r_{\rm th}^3$, where $\langle\sigma_a v\rangle$ denotes the thermally averaged annihilation cross-section of the DM particles.

For annihilating DM, the captured dark matter particles after being thermalized can annihilate among themselves, and heat up the neutron star. For such heating to be

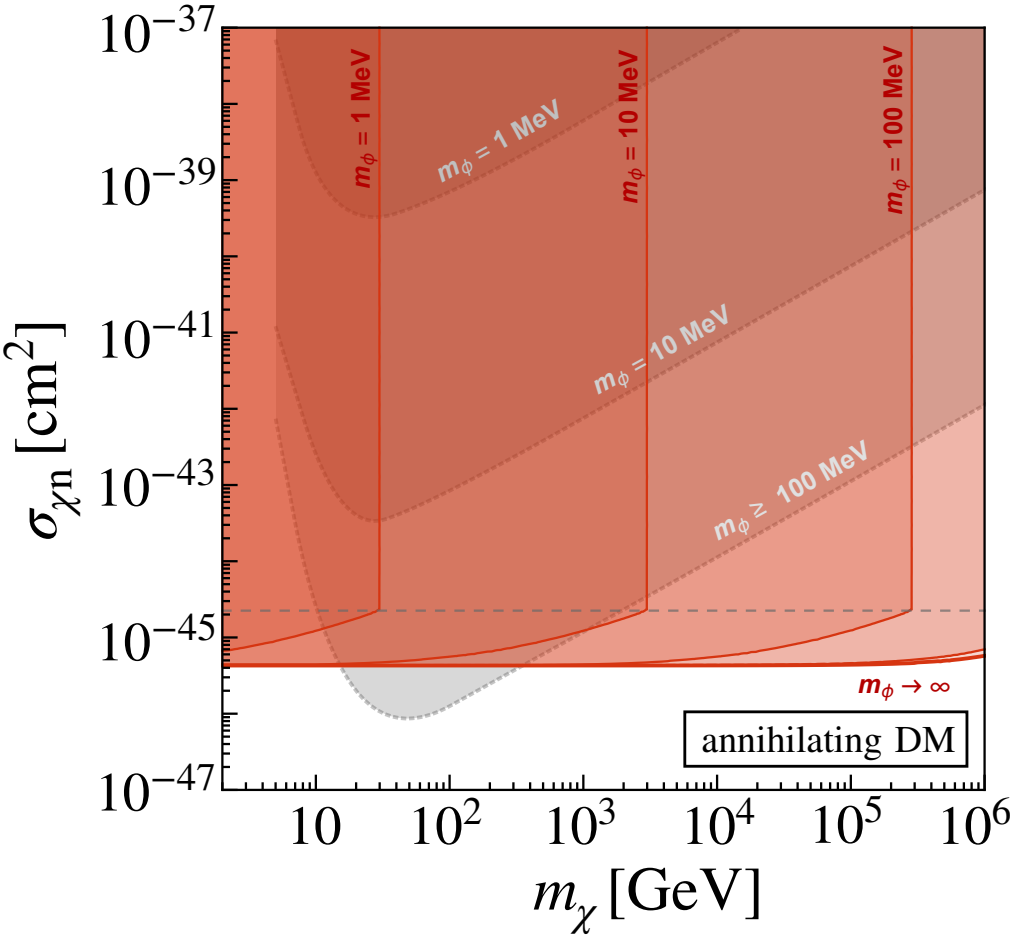

Figure 3.4: Projected upper limits on DM-nucleon scattering cross-section for annihilating DM, obtainable from dark heating of a neutron star with surface temperatures of 1950 K, shown for different mediator masses. Red shaded regions above the solid red lines are excluded; lines corresponding to mediator masses of $m_\phi = 1$ MeV, $m_\phi = 10$ MeV, $m_\phi = 100$ MeV, respectively, from left to right. For $m_\phi = 1$ GeV, the constraint is close to the case with $m_\phi \to \infty$. Related spin-independent exclusion limits from the underground detector PandaX-II [276] are shown in the gray shaded regions above dotted gray lines. For mediators heavier than 100 MeV, exclusion limits from direct detection experiments are close to those obtained assuming an infinitely massive mediator. The dashed gray horizontal line corresponds to the geometrical saturation cross-section, above which any cross-section is essentially equivalent to the saturation cross-section and therefore ruled out with the same confidence. As evident, the dark heating constraints weaken significantly with lighter mediators, being washed out for $m_\phi \leq 0.25$ MeV. However, the astrophysical limits and the terrestrial limits weaken in a complementary fashion.

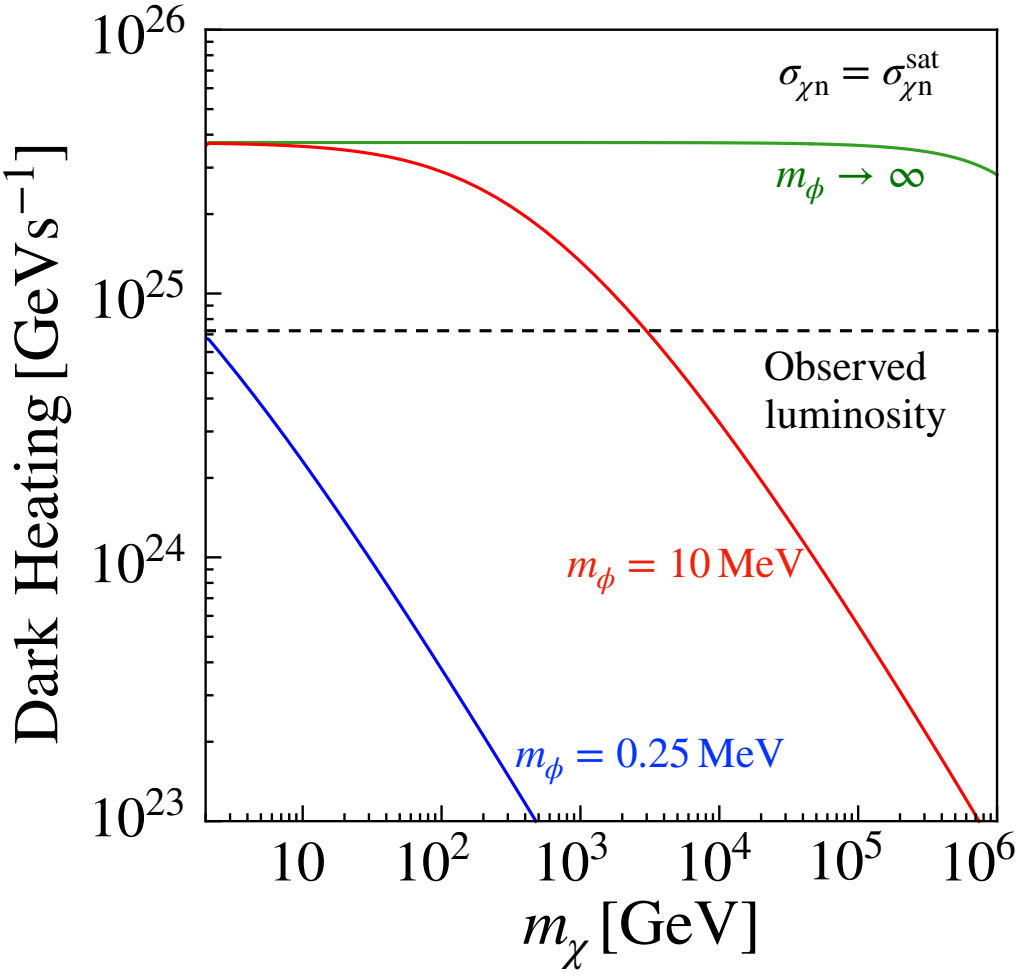

Figure 3.5: Dark heating from annihilation of captured DM particles & kinetic heating is shown with dark matter mass for a neutron star, $\sigma^{\rm sat}_{\chi n}$ denotes the geometrical saturation value of DM-nucleon scattering cross-section. The dashed black line corresponds to the luminosity of the neutron star with surface temperature of 1950 K. Green, red, and blue lines correspond to mediator masses of $m_\phi \to \infty$, $m_\phi = 10$ MeV, and $m_\phi = 0.25$ MeV, respectively. For mediators lighter than 0.25 MeV, dark heating can not exceed the observed luminosity. As a consequence, constraints on DM-nucleon scattering cross-section from dark heating are completely washed out for mediators lighter than 0.25 MeV.

efficient, the annihilation products must have mean free paths smaller than the size of the neutron star. Because of the very high baryonic density of the neutron star, *all* SM final states satisfy this criterion. The additional *dark luminosity*, $L_{\rm ann}$, is then simply given by the total mass capture rate inside the neutron star, provided that the equilibration timescale is less than the age of the neutron star. We have verified that within the

parameter space of interest, the equilibration time [196] is extremely small compared to the typical neutron star lifetime and, as a consequence, dark luminosity simplifies to

$$L_{\rm ann} = m_\chi C_a N_\chi (t_{\rm age})^2 = m_\chi C \,. \tag{3.18}$$

In addition to the dark luminosity, DM-nucleon scattering can also kinematically heat up the neutron star. DM particles acquire immense kinetic energies while falling into the steep gravitational potential of the neutron star, can transfer the kinetic energy to the nucleons during collisions, and as a consequence, can heat up the neutron star. This is known as *dark kinetic heating*, $L_{\rm kin}$ [197, 198]. For the neutron star parameters used in this work, the dark kinetic heating is given by $L_{\rm kin} \sim 0.3 L_{\rm ann}$.

Therefore, a conservative constraint on DM-nucleon interaction strength can simply be obtained by requiring that the total dark heating not exceed the observed luminosity

$$L_{\rm ann} + L_{\rm kin} \leq L_{\rm obs} \,. \tag{3.19}$$

In order to put stringent constraints on DM-nucleon interaction strength, observations of neutron stars with low enough surface temperatures or observations of neutron stars in DM rich environments are required. This is because the low surface temperature, $T_{\rm obs}$, of neutron star significantly reduces the observed luminosity as $L_{\rm obs} \sim T_{\rm obs}^4$, and the large DM density in DM rich environments increases the total dark heating $(L_{\rm ann} + L_{\rm kin})$, as it is proportional to the ambient DM density. Right now, even with the coldest observed neutron star, PSR J2144–3933 [277], one can not probe DM-nucleon scattering cross-sections by using Eq. (3.19) . But, as discussed in [197], radiation from a neutron star of surface temperature $\sim 1750\,\mathrm{K}$ near the Earth can be detected by the upcoming telescopes, JWST [278], TMT [279], and E-ELT [280]. Possible detection of such neutron stars with imminent telescope technology, or alternatively detection of neutron stars with surface temperatures $\sim \mathcal{O}(10^4)\,\mathrm{K}$ in DM rich environments, typically project extremely stringent constraints on DM-nucleon scattering cross-section [196, 197].

However, such strong upper limits entirely rely on the assumption of contact interaction between DM & the nucleon, i.e., for interactions via infinitely massive mediators, and weaken significantly with lighter mediators, as shown in Fig. 3.4. From Fig. 3.4, it is also evident that, in the contact interaction approximation, constraints from anomalous

heating are significantly stronger than terrestrial direct detection experiments for heavier DM mass. The reason behind this is also simple; constraints obtained from dark heating is essentially mass independent in the contact interaction approximation, whereas, constraints from direct detection experiments weaken proportionally to the DM mass for heavier DM. However, for interactions mediated via light mediators, the capture probability, and thereby the dark heating, decreases with lighter mediator.

The upper limits on DM-nucleon interaction strength, as shown in Fig. 3.4, can be understood qualitatively. The flux of incoming DM particles scales as $1/m_\chi$, the capture rate of DM particles is inversely proportional to the DM mass. As a consequence, dark heating becomes independent of DM mass being essentially the total mass capture rate, explaining the m_χ independence of the upper limits. For higher DM mass, due to the kinematic suppression of a light mediator, the capture rate begins to scale as $\sim 1/m_\chi^2$, and as a consequence, dark heating scales as $\sim 1/m_\chi$, explaining the departure from m_χ independence. Eventually, once the DM-nucleon scattering cross-section reaches the geometrical saturation value the constraints become independent of $\sigma_{\chi n}$, explaining the sharp vertical cutoff. For a general energy loss distribution, constraints weaken with lighter mediators simply because the cutoff mass decreases as $\sim m_\phi^2$, which is evident from the generalized capture probability in Eq. (3.9).

The astrophysical exclusion limits weaken for mediators lighter than 1 GeV as shown in Fig. 3.4, in contrast to those from underground detector that weaken for mediators lighter than 100 MeV. This has to do with the typical relative velocity in each case. For underground detectors, the average velocity of the DM particles is $\mathcal{O}(10^{-3})$ and the typical momentum transfer is in the range of 1-100 MeV for DM mass of $1\,\text{GeV} - 1\,\text{PeV}$. As a consequence, the contact interaction approximation holds for mediators heavier than 100 MeV. For astrophysical constraints, the velocity of the DM particles is significantly enhanced while falling into the steep gravitational potential of the neutron star. Thus, the typical momentum transfer is ~ 1 GeV for DM mass above 1 GeV, thereby, invalidating the contact interaction approximation for much higher mediator mass compared to the underground direct detection experiments.

Fig. 3.5 illustrates why capture constraints on DM-nucleon scattering cross-section of annihilating DM are significantly weakened for light mediators. For mediators lighter than 0.25 MeV, dark heating can not exceed the observed luminosity as shown in Fig. 3.5, re-

sulting in a complete washout of the constraints on DM-nucleon scattering cross-section.

3.3.2 Non-annihilating DM & Dark Core Collapse

For non-annihilating DM, the number of dark matter particles captured inside the stellar object follows

$$\frac{dN_\chi}{dt} = C\,. \tag{3.20}$$

Therefore, the number of DM particles accumulating inside the neutron star increases linearly with time. If the total number of captured DM particles inside the neutron star becomes self-gravitating, collapse ensues and if the zero point energy is not sufficient to prevent the gravitational collapse, a black hole forms inside the neutron star. So, the *collapse criterion* is simply given by [249, 259]

$$N_\chi(t_{\rm age}) \geq {\rm Max}\left[N_\chi^{\rm self}, N_\chi^{\rm cha}\right]\,, \tag{3.21}$$

where $N_\chi^{\rm self}$ denotes the required number of particles for initiating the self-gravitating collapse and $N_\chi^{\rm cha}$ denotes the Chandrasekhar limit, beyond which the core collapse is not sustainable.

The black hole formed inside the neutron star, due to the gradual accretion of DM particles followed by a subsequent collapse, can swallow the host neutron star in a very short timescale [281, 282, 283, 284]. Therefore, the upper limits on DM-nucleon interaction strength from gravitational collapse, arise simply from the existence of the neutron star and are shown in Fig. 3.6. We have used the observation of a relatively old neutron star, PSR J0437-4715, in this analysis. The core temperature and age of PSR J0437-4715 is discussed in [249] and are given by 2.1×10^6 K and 6.69×10^9 years, respectively. PSR J0437-4715 is located at a distance of about 139 ± 3 pc from the solar system, and therefore, the local DM density around the neutron star is assumed as 0.4 GeV/cm^3.

The collapse condition in Eq. (3.21) essentially implies that the density of DM particles within the thermalized sphere has to be larger than the baryonic density within that volume. In order to satisfy this criterion, DM particles have to obey

$$\rho_\chi = \frac{m_\chi N_\chi^{\rm self}}{\left(\frac{4}{3}\pi r_{\rm th}^3\right)} \geq \rho_{\rm NS}\,. \tag{3.22}$$

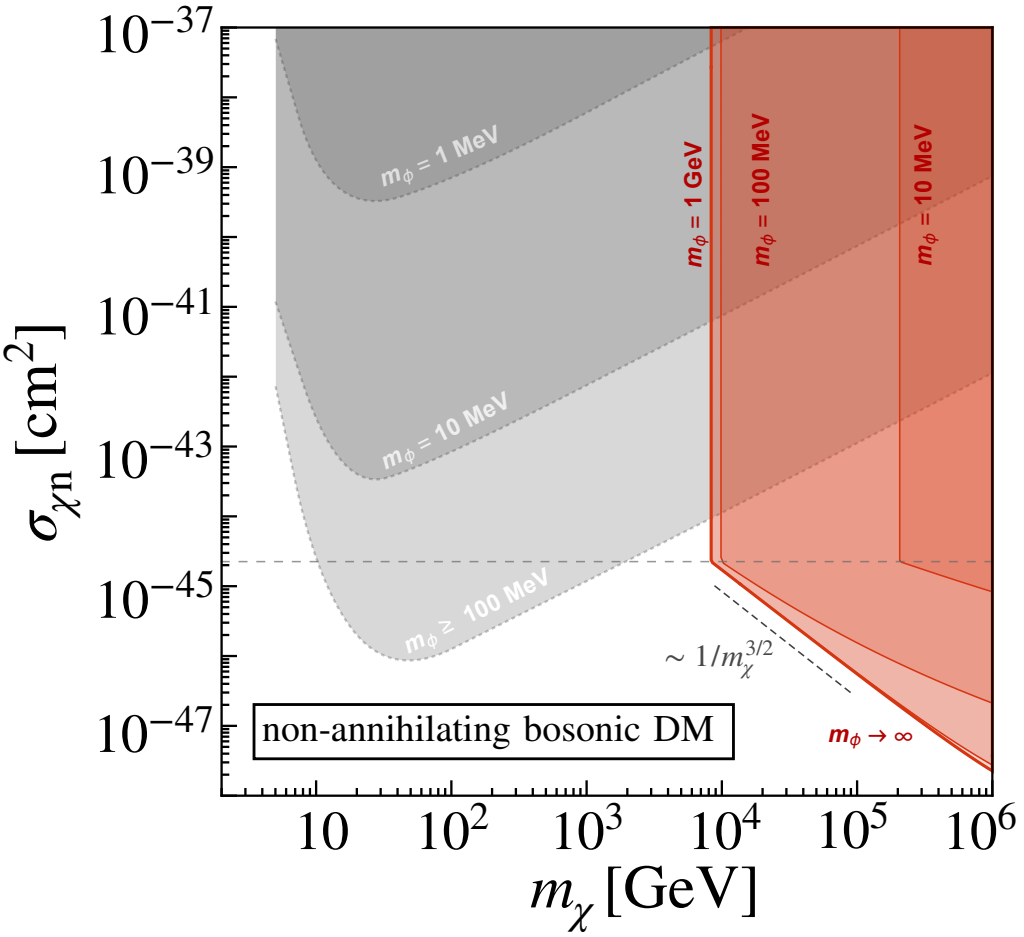

Figure 3.6: Upper limits on DM-nucleon scattering cross-section for a bosonic non-annihilating DM, obtained from existence (i.e., non-collapse) of an old neutron star, PSR J0437-4715, shown for different mediator masses. Regions above the solid red lines are excluded. The lines correspond to mediator masses of $m_\phi = 1$ GeV, $m_\phi = 100$ MeV, and $m_\phi = 10\,\text{MeV}$, respectively, from left to right. For $m_\phi = 1$ GeV, the constraint is close to the case with $m_\phi \to \infty$. Related spin-independent exclusion limits from the underground detector PandaX-II [276] are shown in the gray shaded regions above dotted gray lines. For mediators heavier than 100 MeV, exclusion limits from direct detection experiments remain unaltered. The dashed gray horizontal line corresponds to the geometrical saturation cross-section, above which any cross-section is essentially equivalent to the saturation cross-section and therefore ruled out alike. Constraints on DM-nucleon scattering cross-section obtained from gravitational collapse weaken significantly for lighter mediators, being washed out for $m_\phi \leq 5\,\text{MeV}$. Terrestrial limits also weaken, but in a complementary fashion. Astrophysical constraints extend only up to 30 PeV due to efficient Hawking evaporation.

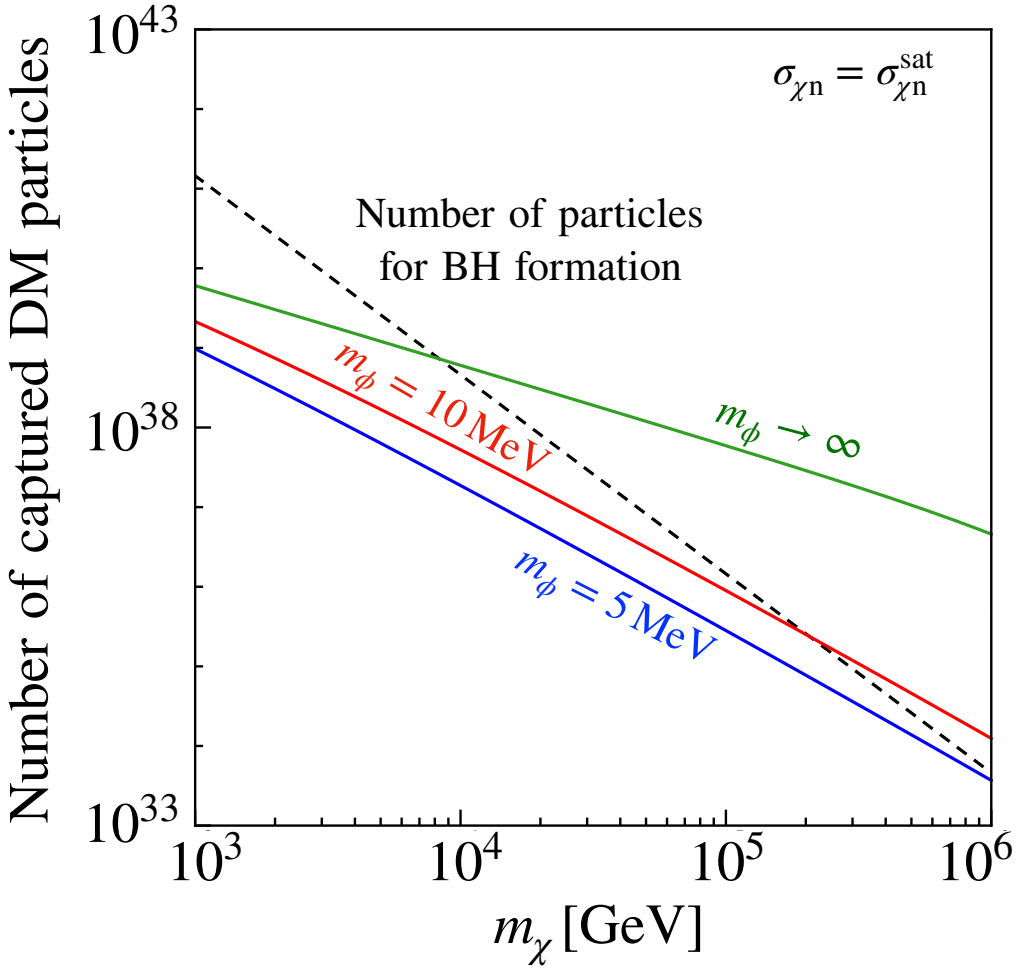

Figure 3.7: Total number of captured DM particles is shown with dark matter mass for a relatively old neutron star, PSR J0437-4715. $\sigma^{\rm sat}_{\chi n}$ denotes the geometrical saturation value of DM-nucleon scattering cross-section. Dashed black line corresponds to the number of DM particles required for black hole formation, which is simply given by Max $\left[N^{\rm self}_\chi, N^{\rm cha}_\chi\right]$. Green, red, and blue lines correspond to mediator masses of $m_\phi \to \infty$, $m_\phi = 10$ MeV, and $m_\phi = 5$ MeV, respectively. For mediators lighter than 5 MeV, the total number of captured DM particles cannot exceed the number of DM particles required for black hole formation. As a consequence, constraints on DM-nucleon scattering cross-section from gravitational collapse completely wash out for mediators lighter than 5 MeV.

For typical neutron star parameters, this implies [249]

$$N^{\rm self}_\chi \sim 4.8 \times 10^{41} \left(\frac{100\,{\rm GeV}}{m_\chi}\right)^{5/2} \left(\frac{T}{10^5\,{\rm K}}\right)^{3/2} \tag{3.23}$$

and is same for bosonic and fermionic DM. However, the Chandrasekhar limit, $N_\chi^{\rm cha}$, depends on the spin-statistics of DM particles. For bosonic DM, the zero point energy is supported by the uncertainty principle, whereas, for fermionic DM, it is supported by the Pauli exclusion principle. In the absence of any repulsive self-interactions among the dark matter particles, the Chandrasekhar limit for bosonic dark matter, $\sim 1.5 \times 10^{34}\,(100\,{\rm GeV}/m_\chi)^2$, is much less than that for fermionic dark matter, $\sim 1.8 \times 10^{51}\,(100\,{\rm GeV}/m_\chi)^3$ [249]. Therefore, it is obvious that in the absence of any repulsive DM self-interactions, bosonic DM experiences gravitational collapse much more easily than fermionic DM. As a consequence, the corresponding constraints on DM-nucleon interaction strength from gravitational collapse are much more stringent for bosonic DM compared to that for fermionic DM. See Appendix B for a detailed derivation of the Chandrasekhar limit for bosonic and fermionic DM.

The upper limits shown in Fig. 3.6 can also be qualitatively understood. The total number of captured DM particles inside the neutron star is proportional $1/m_\chi$, and in the collapse criterion, $N_\chi(t_{\rm age}) \geq {\rm Max}[N_\chi^{\rm self}, N_\chi^{\rm cha}]$, the right hand side is essentially dominated by self-gravitation, $N_\chi^{\rm self}$, which has a $1/m_\chi^{5/2}$ dependence. This explains the $1/m_\chi^{3/2}$ dependence of the upper limits shown in Fig. 3.6. When the scattering cross-section reaches its geometrical saturation value, the constraints become independent of $\sigma_{\chi n}$, which explains the sharp vertical cutoff. For lighter mediators, the capture probability and the total number of captured DM particles, decreases, explaining the weakening of the constraints compared to the upper limit obtained from a contact interaction approximation.

From Fig. 3.6, it is clear that even in the absence of any repulsive self-interactions among the DM particles the astrophysical upper limits on DM-nucleon scattering cross-section weaken appreciably with lighter mediators. For mediators lighter than 5 MeV, the total number of captured DM particles is not sufficient to form a black hole, as shown in Fig. 3.7. Hence, such astrophysical constraints are completely washed out.

Note that if the newly formed black hole evaporates faster than it mass accretion rate, the host neutron star can still survive. As a consequence, the constraints obtained from gravitational collapse can be alleviated [248, 249, 254, 259]. The mass accretion rate of the newly formed black hole is usually assumed as a spherical Bondi-Hoyle accretion, and is given by

$$\frac{dM_{\rm acc}}{dt} = \frac{4\pi\lambda\rho_{\rm NS}\,G_N^2\,M_{\rm BH}^2}{c_{\rm s}^3}\,, \tag{3.24}$$

where $\lambda = 0.25$, $c_s = 0.17c$ is the speed of sound inside the neutron star, G_N denotes gravitational constant, and $M_{\rm BH}$ is the initial mass of the newly formed black hole [254]. On the other hand, the newly formed black hole evaporates via Hawking evaporation, and the mass loss rate is simply given by

$$\frac{dM_{\rm evap}}{dt} = -\frac{\hbar\, c^4}{74\pi G_N^2 M_{\rm BH}^2}\,. \tag{3.25}$$

This mass loss rate is derived by summing over contributions from all SM particles, and takes into account the greybody factor of the Hawking emission. This is a significant improvement (increases the mass loss rate by a factor $\sim$ 200) over the earlier treatments [248, 249, 259], where the mass loss rate is estimated by treating the newly formed black hole as a blackbody.

Constraints on DM-nucleon cross-section get alleviated when the Hawking evaporation rate exceeds the mass accretion rate, i.e., if $dM_{\rm acc}/dt \geq dM_{\rm evap}/dt$. For a relatively cold neutron star, PSR J0437-4715, with core temperature of 2.1×10^6 K, we estimate that such astrophysical constraints on DM-nucleon interaction strength obtained from gravitational collapse vanish at $m_\chi \geq 3 \times 10^7$ GeV for bosonic DM and $m_\chi \geq 8 \times 10^9$ GeV for fermionic DM. Therefore, the constraints shown in Fig. 3.6 can only extend up to 3×10^7 GeV.

3.3.3 Effect of DM Self-interactions on the DM-nucleon Interactions

For annihilating DM, constraints on DM-nucleon scattering cross-section are simply obtained by comparing the dark heating with the observed luminosity. The estimation of dark heating solely depends on the total capture rate. In principle, self-interactions among the DM particles can lead to an additional contribution to the total capture rate. However, due to the extremely large baryonic density in neutron stars, self-interactions have an insignificant impact on the total capture rate. Therefore, the upper limits shown in Fig. 3.4 remain unaltered even with the inclusion of maximally allowed repulsive self-interactions among the DM particles.

For non-annihilating DM, the inclusion of repulsive self-interactions among the DM particles has a prominent impact on the corresponding upper limits on the DM-nucleon

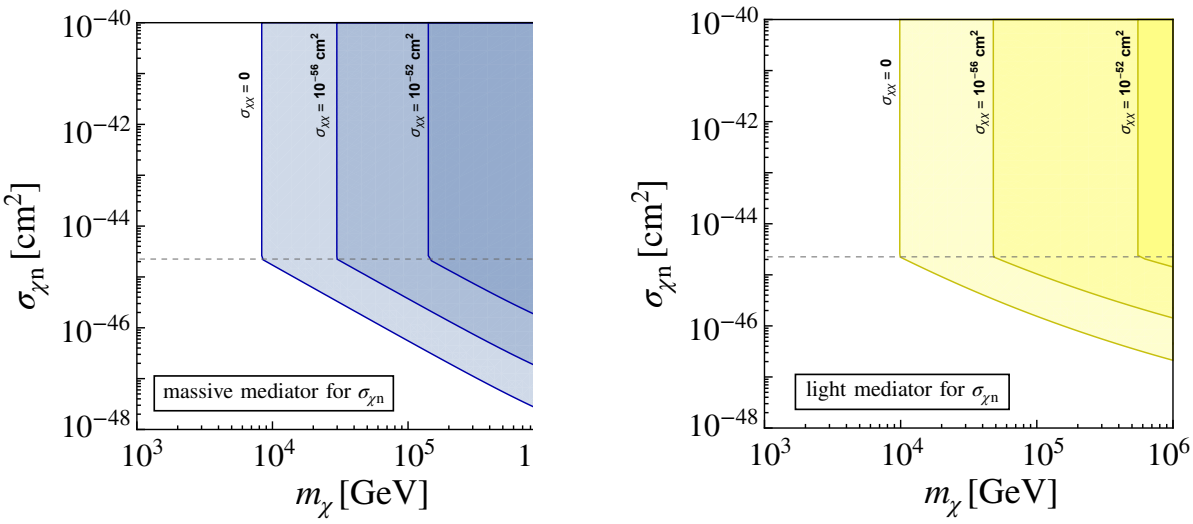

Figure 3.8: Upper limits on DM-nucleon scattering cross-section of non-annihilating self-repelling bosonic DM, obtained from non-observation of gravitational collapse of PSR J0437-4715. In the left panel, a uniform energy loss distribution is assumed and in the right panel the DM-nucleon interaction is taken to be mediated via a Yukawa potential with a mediator mass of 100 MeV. In each panel, different lines correspond to $\sigma_{\chi\chi} = 0$, $\sigma_{\chi\chi} = 10^{-56}\,\mathrm{cm}^2$, and $\sigma_{\chi\chi} = 10^{-52}\,\mathrm{cm}^2$, respectively, from left to right. The values of the DM self-interaction cross-section, shown in the plots, are not ruled out by the Bullet Cluster observation [285]. The dashed gray line corresponds to the geometrical saturation cross-section, above which any cross-section is essentially equivalent to the saturation cross-section and therefore ruled out at the same confidence. Constraints on DM-nucleon scattering cross-section weaken and eventually washout, with increase of the strength of repulsive self-interactions.

scattering cross-section. In neutron stars, self-interactions among the DM particles do not enhance the capture rate but repulsive self-interactions among the dark matter particles significantly enhance the Chandrasekhar limit, thereby, increasing the number of DM particles required for black hole formation. For a repulsive self-interaction of contact type, the Chandrasekhar limit for bosonic DM modifies to [254]

$$N_\chi^{\mathrm{cha}} = \frac{2}{\pi}\frac{M_{\mathrm{pl}}^2}{m_\chi^2}\left(1 + \frac{\lambda}{32\pi}\frac{M_{\mathrm{pl}}^2}{m_\chi^2}\right)^{1/2}, \tag{3.26}$$

where λ is the dimensionless self-interaction coupling among the DM particles, which is given by $\lambda = (64\pi\sigma_{\chi\chi})^{1/2}\, m_\chi$. Note that, the second term in the expression of N_χ^{cha}

always dominates over unity for any reasonable value of DM self scattering cross-section. As a consequence, the corresponding constraints on DM-nucleon interaction strength further weaken with inclusion of repulsive DM self-interactions [254, 255]. We show the impact of repulsive DM self-interactions on the corresponding upper limits on DM-nucleon scattering cross-section in Fig. 3.8. From Fig. 3.8, it is evident that with increase of the self-interaction strength, the Chandrasekhar limit significantly enhances and as a consequence, the black hole formation criterion becomes stricter. This explains the further weakening of the constraints. However, inclusion of attractive self-interactions among bosonic DM particles ($\lambda < 0$) requires a different analysis involving bound state formation, which is beyond the scope of this work. For fermionic DM, the impact of attractive self-interactions among the DM particles on the DM-nucleon scattering cross-section have been extensively discussed in [257, 260].

3.3.4 Constraining DM Self-interactions from Observation of Neutron Stars

Gravitational collapse of neutron stars, due to continued accumulation of non-annihilating particle DM, can also be used as an astrophysical probe of DM self-interaction strength. As discussed in the previous subsection, strong self-interactions make the black hole formation criterion stricter, while its impact on the total capture rate is negligible. Therefore, strong self-interactions among DM particles inhibits collapse. However, very feeble self-interactions among the dark matter particles do not alter the Chandrasekhar limit appreciably, and collapse can occur. Thus, observation of collapse rules out strong self-interactions. In Fig. 3.9, the red or blue shaded regions correspond to parameter spaces where the DM core in a neutron star can collapse, for $\sigma_{\chi n}$ being $\sigma_{\chi n}^{\rm sat}$ or $10^{-47}\,{\rm cm}^2$, respectively. We show these regimes for a uniform energy loss distribution. Evaporation of the newly formed black hole faster than its mass accretion rate invalidates the above-stated astrophysical constraints on DM self-interaction strength. This region is shown by the green hatched region in Fig. 3.9. Assuming a blackbody spectrum, instead of the correct Hawking spectrum we have used, leads to the hatched region under the dashed green line, underestimating the efficacy of Hawking evaporation.

Even if we do not know $\sigma_{\chi n}$, a collapse observation will conservatively exclude enormous swathes of parameter space in Fig. 3.9. The entire white unhatched unshaded region is

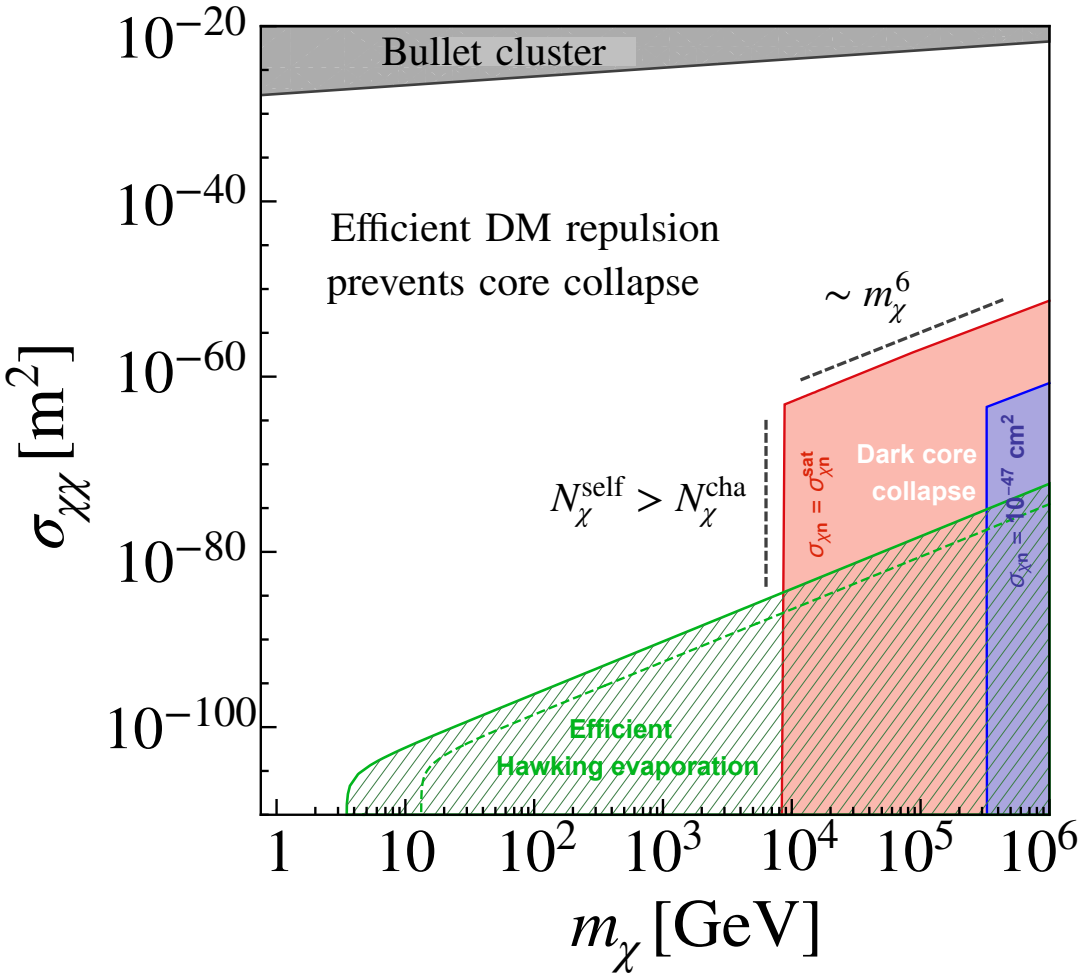

Figure 3.9: Constraints on DM self scattering cross-section for non-annihilating bosonic dark matter, obtained from a nearby old neutron star, PSR J0437-4715. The shaded regions denote parameter space where the DM core can collapse; red region for $\sigma_{\chi n} = \sigma_{\chi n}^{\rm sat} = 2 \times 10^{-45}\,{\rm cm}^2$ and blue shaded region for $\sigma_{\chi n} = 10^{-47}\,{\rm cm}^2$. Hatched region under the solid green line corresponds to the alleviation of the constraints due to rapid Hawking evaporation of the newly formed black hole. Assuming a blackbody spectrum, instead of the correct Hawking spectrum, leads to the hatched region under the dashed green line. The exclusion limit from Bullet Cluster observation [285] is shown in the gray shaded region at the top. The local DM density around the neutron star is taken as 0.4 GeV/cm^3 and all the other neutron star parameters are described in the text. For a given $\sigma_{\chi n}$, the existence of PSR J0437-4715 rules out the corresponding shaded but unhatched region.

disfavored by the observed collapse of a star such as PSR J0437-4715, assuming that we can separately constrain the accretion of gas etc. If on the other hand, the value of $\sigma_{\chi n}$ is known, one can obtain bounds from non-observation of collapse. For illustration, if it is known that $\sigma_{\chi n} = 10^{-47}\,\mathrm{cm}^2$, the existence of PSR J0437-4715 rules out the blue region that does not overlap with the hatched Hawking constraint.

The upper limits shown in Fig. 3.9 can also be understood qualitatively. The black hole formation criterion is $N_\chi(t_{\rm age}) \geq \mathrm{Max}[N_\chi^{\rm self}, N_\chi^{\rm cha}]$. The left hand side scales as $1/m_\chi$ and has no dependence on $\sigma_{\chi\chi}$, whereas for heavier DM the right hand side is dominated by the Chandrasekhar limit, which scales as $\sim \sigma_{\chi\chi}^{1/4}/m_\chi^{5/2}$, so that the constraint scales as $\sigma_{\chi\chi} \sim m_\chi^6$. For lighter DM, $N_\chi^{\rm self}$ dominates over $N_\chi^{\rm cha}$ on the right hand side, and both $N_\chi^{\rm self}$ and $N_\chi(t_{\rm age})$ are independent of $\sigma_{\chi\chi}$, explaining the $\sigma_{\chi\chi}$ independence of the upper limit, i.e., the sharp vertical cutoff in Fig. 3.9. These two regimes meet almost discontinuously at the corner of the red or blue shaded regions, where $N_\chi^{\rm self} = N_\chi^{\rm cha}$, identifying a minimum DM mass below which collapse cannot occur for a chosen $\sigma_{\chi n}$ and other fixed parameters. Note that, since the total number of captured DM particles is proportional to the DM-nucleon scattering cross-section, lower values of DM-nucleon scattering cross-section reduce the total number of captured DM particles, and as a consequence, enfeeble the upper limits on DM self-interaction strength as shown in Fig. 3.9.

3.4 Summary & Conclusions

Dark matter capture in celestial objects is believed to be one of the most sensitive astrophysical probes of interactions between the dark and visible sector. However, all such previously obtained astrophysical constraints on DM-nucleon scattering cross-section depend crucially on the assumption of a uniform energy loss distribution. This assumption of uniformity, tantamount to assuming an infinitely massive mediator, does not always hold true, and the constraints must be updated for lighter mediators, self-interactions, and to better codify the effect of Hawking evaporation. Here we summarize our main results:

1. We pointed out that the assumption of uniformity in energy loss distribution only holds true for isotropic differential cross-section, which occurs only for an infinitely massive mediator. For DM interactions via light mediators, the deviation from

uniformity becomes prominent and is shown in Fig. 3.2.

2. We generalized the treatment of DM capture inside celestial objects for arbitrary mediator masses, in Eqs. (3.2 – 3.11), and updated the existing and projected astrophysical upper limits on DM-nucleon interaction strength.

3. We found that for non-annihilating bosonic DM, the existing constraints obtained from an old nearby neutron star, PSR J0437-4715, and for annihilating DM, the projected constraints obtainable from a neutron star with surface temperature of 1950 K, depend firmly on mediator masses, weaken appreciably for lighter mediators, and are not generally superior to terrestrial detectors as shown in Fig. 3.4 and Fig. 3.6, respectively. Such astrophysical constraints are completely washed out for mediators lighter than 5 MeV for asymmetric DM, and for mediators lighter than 0.25 MeV for annihilating DM as shown in Fig. 3.5 and Fig. 3.7, respectively.

4. We showed in Fig. 3.8 that the constraints on DM-nucleon interaction strength obtained from gravitational collapse further weaken with inclusion of repulsive self-interactions among the DM particles. As repulsive DM self-interactions have a significant impact on the black hole formation criterion, constraints can even be completely washed out for strong enough repulsive self-interactions among the DM particles. However, constraints obtained from dark heating remain unaltered with the inclusion of DM self-interactions, due to their insignificant contribution to the total capture rate.

5. Gravitational collapse of captured DM particles acts as an astrophysical probe of DM self scattering cross-section. Self-interactions among the DM particles have an insignificant impact on the total capture rate, but repulsive DM self-interactions have a significant impact on the black formation criterion. Strong repulsive DM self-interactions can prevent the black hole formation inside a stellar object, and black hole formation criterion can only be achieved with very feeble repulsive DM self-interaction strength. Thereby, from collapse of a stellar object the white region shown in Fig. 3.9 is ruled out. If $\sigma_{\chi n}$ is known, then the existence of such stellar objects rule out shaded but unhatched regions therein.

6. In all the previous treatments, the Hawking evaporation rate from the newly formed

black hole was calculated in a blackbody radiation approximation. This is not completely correct. We correct the Hawking evaporation estimate by taking into the greybody factor of the emission spectrum, which leads to a stronger alleviation of the constraints on DM self-interaction strength, compared to what would be obtained using a blackbody approximation.

We have not attempted to treat multiple scattering, light mediators, and self-capture within a single framework; it can be relevant for $m_\chi > 10^6\,\mathrm{GeV}$ and remains to be addressed.

Chapter 4

Mergers as a Probe of Particle DM

In this Chapter, we demonstrate that continued accumulation of non-annihilating particle DM in compact stars can lead to sub-Chandrasekhar ($\leq 1.4\,M_\odot$) mass black hole formation, providing a viable alternative to the primordial black hole scenario. We point out several avenues to test the origin of low mass black holes, focusing on the cosmic evolution of the binary merger rates. We demonstrate that measurement of the binary merger rates, especially in the high-redshift, by the imminent GW detectors can conclusively determine the origin of low mass black holes. The results presented in this chapter can be found in [9].

4.1 Formation of Low Mass Transmuted Black Holes

Unusual masses of black holes being discovered by GW experiments [286, 287, 288] pose fundamental questions about their origin. More interestingly, black holes with masses smaller than the Chandrasekhar limit ($1.4\,M_\odot$) are essentially impossible to produce through *any* standard stellar evolution, and often considered as a smoking gun evidence of its primordial origin. In this section, we demonstrate that possible detection of a sub-Chandrasekhar mass black hole is *not* a smoking gun evidence of its primordial origin. Non-annihilating particle DM with non-zero interaction strength with the stellar nuclei, a universal feature of the DM models, is sufficient to produce sub-Chandrasekhar or $\mathcal{O}(1)M_\odot$ mass non-primordial black holes. In the following, we briefly describe their formation mechanism, and answer a few basic questions, such as, what particle physics parameter space can they explore, how to test their origin, and especially, how to distin-

guish them from primordial black holes?

The formation of sub-Chandrasekhar mass non-primordial black holes has previously been studied in the context of exotic cooling of an atomic dark matter cloud [290] and accretion of fermionic asymmetric DM with non-negligible self-interactions inside a neutron star [291]. However, the previously proposed models employing a fermionic asymmetric DM with non-negligible self-interactions or dark quantum electrodynamics are not generic, and appeal to fairly baroque DM models. Transit of tiny PBHs (PBHs in the mass range of $10^{18}-10^{24}$ g) through a compact star, and subsequent conversion of the host to a black hole is also thought to be a novel mechanism to produce sub-Chandrasekhar mass non-primordial black holes [292, 293]. However, the recent estimates [184, 185] suggest that the capture rate of a tiny PBH by a neutron star has been over-estimated in the previous literature, and the actual capture rate is quite small, $\sim 10^{-17}\,\mathrm{yr}^{-1}$ for a neutron star residing in a Milky-Way-like galaxy. In short, tiny PBHs just pass through the neutron star rather than being captured. Hence, this mechanism is now ineffective for transmutation. Here it is important to mention that the capture rate scales linearly with the ambient DM density and has a strong dependence on the velocity dispersion, $(\bar{v}^{-3})$, so an $\mathcal{O}(1)$ Gyr old neutron star in a DM dense region ($\rho_\chi = 10^3\,\mathrm{GeV\,cm}^{-3}$) inside a globular cluster ($\bar{v} \sim 10^{-5}$) can, in principle, implode due to a PBH transit. However, such over-dense DM cores in a globular cluster are quite speculative and not yet well established. It has, in fact, been shown that globular clusters do not have any DM over-densities[294, 295, 296]. Hence, the explanation of a sub-Chandrasekhar or $\mathcal{O}(1)\,M_\odot$ black hole due to a tiny PBH transit is either ineffective or hinges on the contentious assumption of a high DM density in globular clusters, and remains uncertain until the provenance of globular clusters is settled. Below we propose a very simple production mechanism of sub-Chandrasekhar black holes which can be a viable alternative to primordial black holes.

Non-annihilating DM [297, 298] scatters with stellar nuclei, gets captured via single [187, 188] or multiple scattering[7, 196, 209], and accumulates inside a stellar object linearly with time. Once the total number of captured DM particle satisfy the collapse criterion, i.e., $N_\chi|_{t_{\rm age}} \geq \max\left[N_\chi^{\rm cha}, N_\chi^{\rm self}\right]$, a small black hole forms in the stellar core [249, 248, 259]. Here, $N_\chi|_{t_{\rm age}}$ denotes the total number of DM particles accumulated within a celestial object throughout its age $t_{\rm age}$. A precise estimation of $N_\chi|_{t_{\rm age}}$ in the contact in-

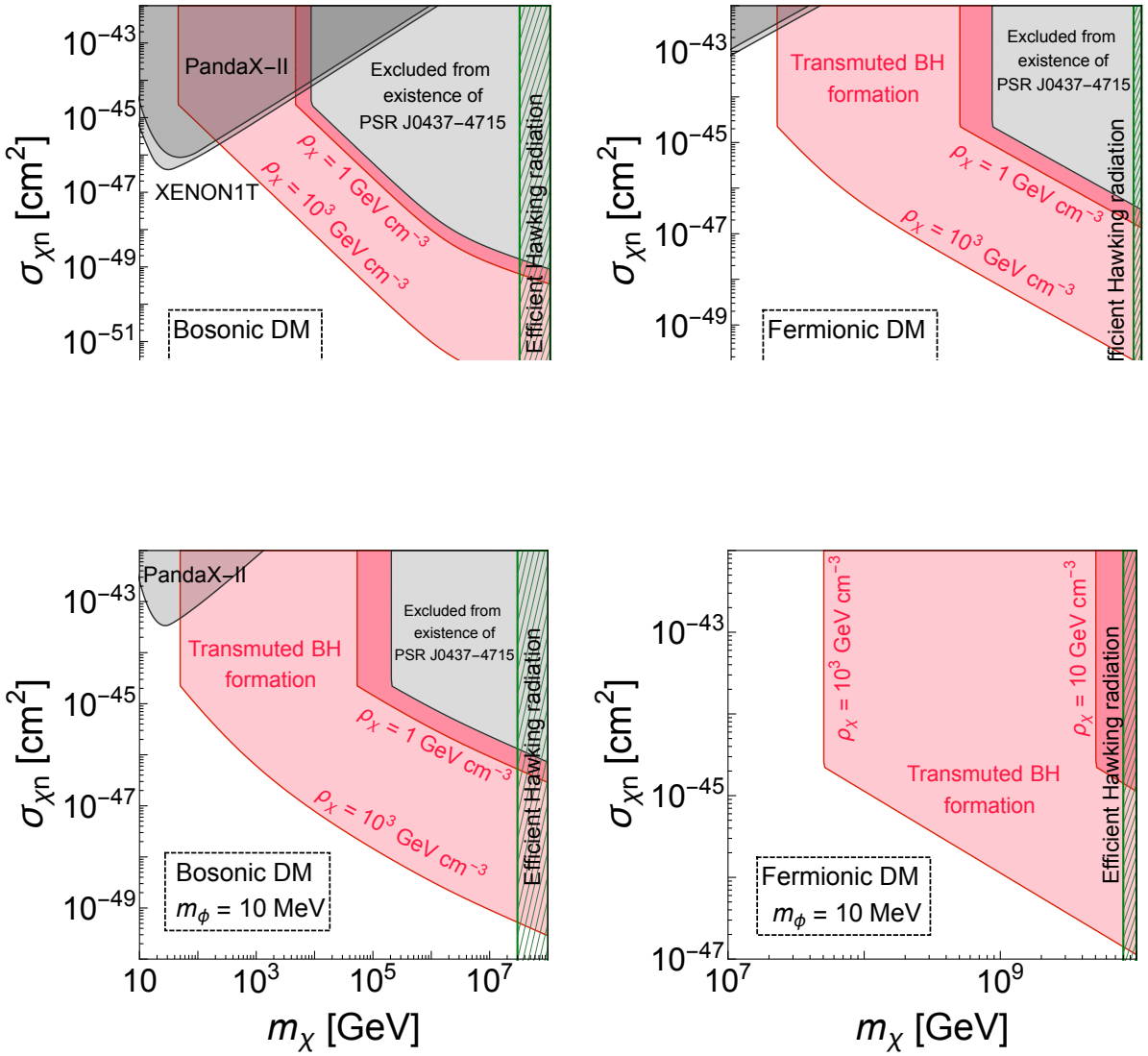

Figure 4.1: DM mass and scattering cross-section required for a dark core collapse and subsequent transmutation of a 1.3 $M_\odot$ neutron star to a comparable mass black hole are shown in the red shaded regions. The two panels on the left (respectively, right) correspond to interaction between DM and stellar nuclei mediated by an infinitely heavy mediator, i.e., $m_\phi \gg$ recoil momentum (resp. 10 MeV scalar). Scenarios with non-annihilating bosonic or fermionic DM are marked. Two representative values of ambient DM density, $\rho_\chi = 1$ and 10^3 GeV cm^{-3} (only for the right panel, $\rho_\chi = 10$ and 10^3 GeV cm^{-3}), are considered. Exclusion limits from underground direct detection experiments PandaX-II [276] and XENON1T [96] as well as from existence of an $\sim$ 7 Gyr old [289] nearby pulsar PSR J0437-4715 [8, 249, 259] are also shown by the gray shaded regions. Green hatched regions mark the parameter space where efficient Hawking evaporation stops the implosion of the neutron star. The region of no thermalization is many orders of magnitude below [259], and is not shown for clarity.

teraction approximation as well as for interactions mediated via arbitrary mass mediators can be found in the previous two chapters. $N_\chi^{\rm self}$ denotes the required number of DM particles for initiating the self-gravitating collapse, and $N_\chi^{\rm cha}$ denotes the Chandrasekhar limit, the number of DM particles beyond which gravitational collapse is no longer sustainable. Chandrasekhar limit, $N_\chi^{\rm cha}$, depends on the spin-statistics of the DM particles, and is different for bosonic and fermionic DM. In the absence of any repulsive self-interactions among the DM particles, the Chandrasekhar limit for bosonic dark matter is $\sim 1.5 \times 10^{34} \, (100\,{\rm GeV}/m_\chi)^2$, and for fermionic dark matter is $\sim 1.8 \times 10^{51} \, (100\,{\rm GeV}/m_\chi)^3$ [249], explaining an easier transmutation for the bosonic DM. See Appendix B for a detailed derivation of the Chandrasekhar limit for bosonic and fermionic DM. The required number of DM particles for self-gravitation, $N_\chi^{\rm self}$, does not depend on the spin statistics of the DM particles, and is set by the condition that DM density has to exceed the baryonic density within the stellar core [249].

Once the number of captured DM particles satisfies the collapse criterion, dark core collapse ensues, and a tiny black hole forms inside the stellar object. This tiny black hole accumulates matter from the host, and eventually swallows the host in a very short timescale [281, 282, 283, 284] to a comparable mass black hole − transmuted black hole. So, depending on the mass of the progenitors, TBHs can naturally be sub-Chandrasekhar, or even sub-solar. However, note that, if the nascent black hole that forms via dark core collapse is sufficiently light, it quickly evaporates due to its efficient Hawking emission, ceasing the transmutation. For typical neutron star parameters, if the initial mass of the black hole is lighter than $\sim 10^{-20}\, M_\odot$ (see Ref. [284] for a quantum correction to this evaporation mass), Hawking evaporation dominates over the swallowing process, and the transmutation ceases [8, 248]. For non-annihilating bosonic and fermionic DM, it corresponds to DM masses $\gtrsim \mathcal{O}(10^7)$ and $\gtrsim \mathcal{O}(10^{10})$ GeV, respectively, providing an upper limit on the DM mass for transmutation.

Fig. 4.1 shows the DM parameter space where a neutron star with mass $1.3\, M_\odot$ can transmute to a low mass black hole for either bosonic or fermionic DM, for two choices of ambient DM density. DM-nucleon interactions mediated by an infinitely heavy mediator (light mediator of mass 10 MeV) is assumed in the first (last) two panels. In the contact interaction approximation, asymmetric bosonic (fermionic) DM of mass $\mathcal{O}(100)$ GeV ($\mathcal{O}(1)$ PeV) in a DM dense environment can lead to a sub-Chandrasekhar mass

black hole. For DM-nucleon interaction mediated via lighter mediators, transmutation of compact objects is easier, as exclusion limits weaken and implosions can be achieved with a wider range of parameters. Similar analysis can also be performed for a solar mass white dwarf. However, because of the lower baryonic density compared to a neutron star, the implosion criterion is harder to achieve for a white dwarf. For transmutation of a solar mass white dwarf with ambient DM density 10^3 GeV cm^{-3}, the scattering cross-section has to be $\gtrsim 10^{-44}$ cm^2 for a 10 PeV asymmetric bosonic DM, whereas, the corresponding cross-section for a neutron star with the same ambient DM density is $\sim 10^{-48}$ cm^2. The transmutation does not happen for small DM masses, causing the cutoff on the left side of the red shaded region in Fig. 4.1. This is because the number of DM particles required for initiating self-gravitation ($N_\chi^{\rm self}$), as well as the Chandrasekhar limit ($N_\chi^{\rm cha}$), increases for lighter DM [$N_\chi^{\rm self} \sim 1/m_\chi^{5/2}$, $N_\chi^{\rm cha} \sim 1/m_\chi^2$ $\left(1/m_\chi^3\right)$ for bosonic (fermionic) DM] and the number of captured DM particles is not sufficient to satisfy the dark core collapse criterion. Note that, we do not consider the possibility of Bose-Einstein condensate (BEC) formation because the temperature required for BEC formation, $T_{\rm BEC} \approx (2\pi/m_\chi)\,(n_\chi/2.612)^{2/3}$ [249] is almost always less than the core temperature of the neutron star ($T = 2.1 \times 10^6\,{\rm K}$) that we consider.

4.2 Identifying the Origin of Low Mass Black Holes

Formation of sub-Chandrasekhar mass non-primordial black holes via gradual accumulation of non-annihilating DM in compact stars demand a critical investigation to pinpoint the origin of the low mass black holes. In this section, we briefly describe several avenues to identify the origin of low mass black holes, focusing on the cosmic evolution of the binary merger rates.

The merger rate of PBH binaries keeps rising with higher redshift as the PBH binaries can form efficiently in the early Universe [301, 302, 305, 306, 307]. It has a universal time dependence of $R_{\rm PBH} \propto t^{-34/37}$, where t is the coalescence time at formation. On the other hand, the merger rate of binary neutron stars, $R_{\rm NS}(t)$ [308], as shown in Fig. 4.2, traces the cosmic star formation rate [299, 309]

$$R_{\rm NS}(t) = \int_{t_f=t_*}^{t} dt_f \frac{dP_m}{dt}(t-t_f)\lambda\frac{d\rho_*}{dt}(t_f)\,. \tag{4.1}$$

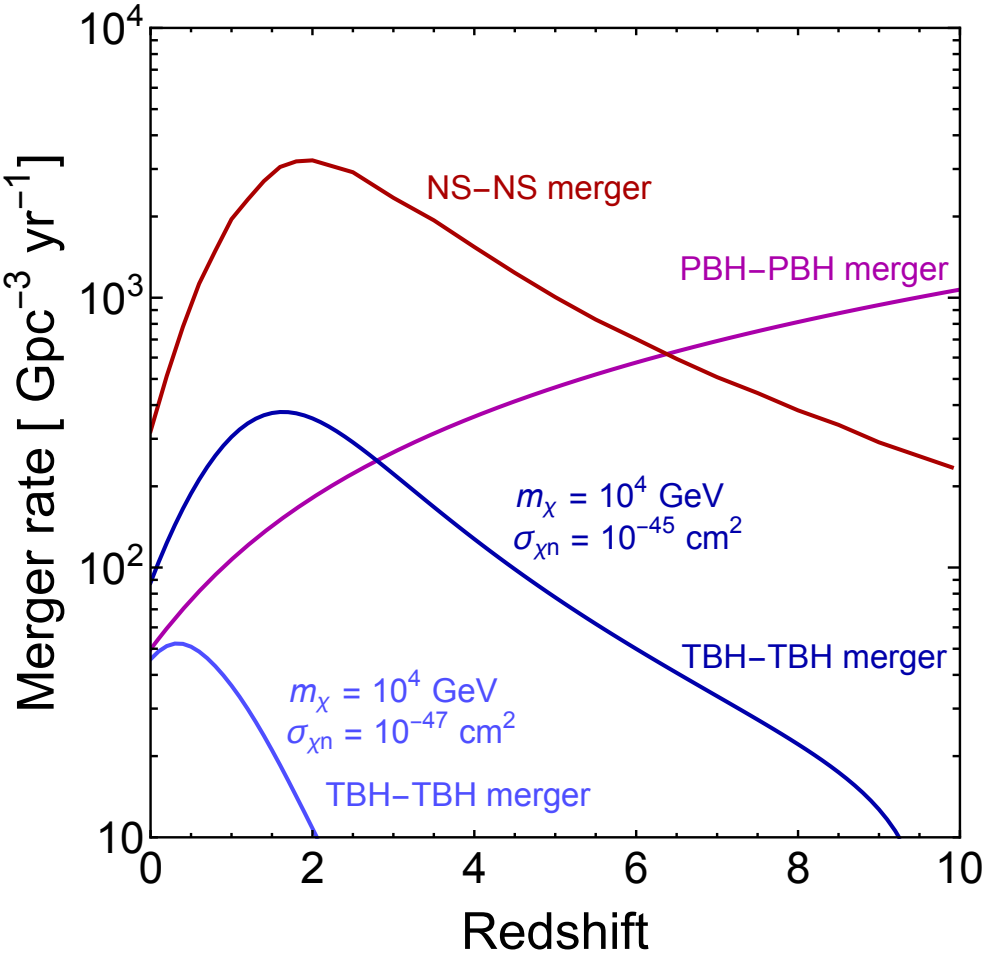

Figure 4.2: Cosmic evolution of the binary merger rates provides a simple yet novel technique to determine the stellar or primordial origin of black holes. Cosmic evolution of the binary PBH, neutron star, and TBH merger rates are shown in the redshift range of 0 to 10. For the binary neutron star and TBH merger rate, cosmic star formation rate is adopted from [299] and they are normalized to the recent LIGO-VIRGO measurement [300]. Non-annihilating bosonic DM with mass of 10 TeV and DM-nucleon scattering cross-section of 10^{-45} and 10^{-47} cm^2 in the contact approximation are assumed for the estimation of binary TBH merger rate. The PBH merger rate is estimated by considering 1.3 $M_\odot$– 1.3 $M_\odot$ PBH binary and a dark matter fraction $f_{\rm PBH} = 10^{-3}$, which enters as $f_{\rm PBH}^{53/37}$ [301, 302]

It peaks at an $\mathcal{O}(1)$ redshift when the star formation rate is maximal. In Eq. (4.1), $\frac{d\rho_*}{dt}(t_f)$ denotes the cosmic star formation rate at binary formation time t_f, λ is the number of coalescing neutron star binaries per unit star forming mass, and $\frac{dP_m}{dt}(t - t_f)$ is the probability density distribution of binary neutron stars merging within the time interval

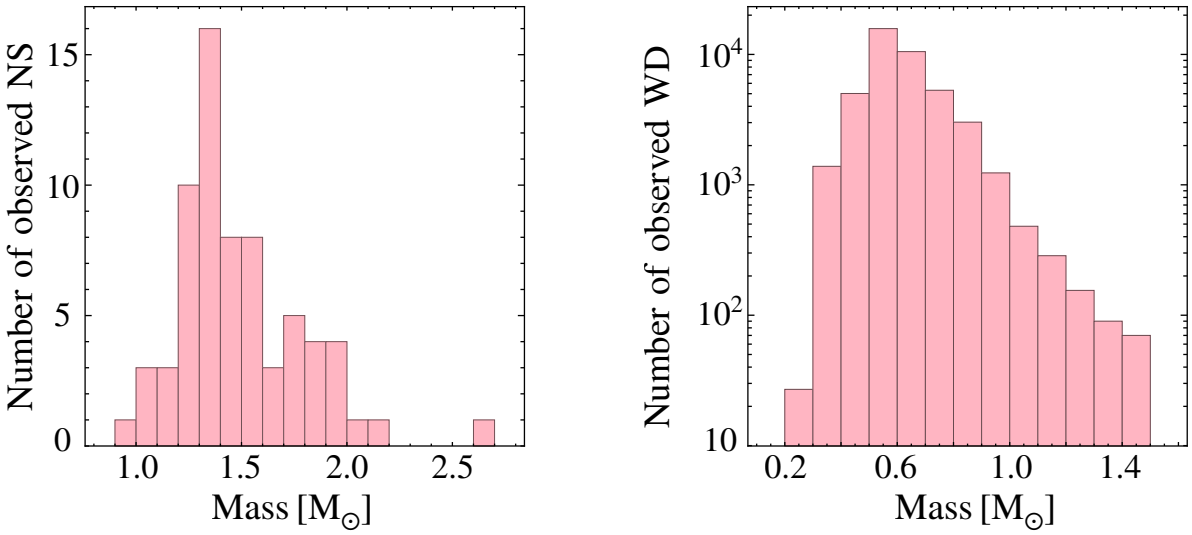

Figure 4.3: Mass distribution of the compact stars provide yet another probe to test the origin of low mass black holes. The mass distribution of all the observed neutron stars and white dwarfs [303, 304] are shown in this plot. The mass distributions of these progenitors can be compared against some well-motivated PBH mass distributions to examine the origin of low mass black holes.

$(t - t_f)$ after formation. For this analysis, we have used $\lambda = 10^{-5} M_\odot^{-1}$, the earliest star formation time $(t_*) = 4.9 \times 10^8$ year which corresponds to $z = 10$, $\frac{dP_m}{dt} \propto (t - t_f)^{-1}$ [308], and adopted the cosmic star formation rate from [299].

The merger rate of TBH binaries, $R_{\rm TBH}(t)$, is systematically lower than of neutron star binaries, $R_{\rm NS}(t)$, as only a fraction of them transmute depending on the time required for transmutation. This fraction depends on the binary neutron star population in the galaxies, as well as evolution of the DM density in the galaxies, and it gradually decreases with higher redshifts as neutron binaries at higher redshift do not have the sufficient time to accumulate enough DM required for implosion. Hence, $R_{\rm TBH}(t)$ takes the form

$$R_{\rm TBH}(t) = \sum_i f_i \int_{t_f=t_*}^{t} dt_f \frac{dP_m}{dt}(t - t_f)\lambda \frac{d\rho_*}{dt}(t_f) \times \Theta\left\{t - t_f - \tau_{\rm trans}\left[m_\chi, \sigma_{\chi n}, \rho_{{\rm ext},i}(t)\right]\right\} , \tag{4.2}$$

where $\tau_{\rm trans}$ denotes the transmutation time, which is essentially a sum of the two timescales: *i*) time required for the micro black hole formation via dark core collapse and *ii*) time required by the micro black hole to swallow the host star. We note that the swallowing time [281, 282, 283] is almost instantaneous with respect to the black hole formation time

inside the stellar core, and hence, $\tau_{\rm trans}$ is always dominated by the first timescale.

In Eq. (4.2), we assume that the neutron star binaries live in Milky-Way-like galaxies, and are distributed uniformly in $r = (0.01, 0.1)$ kpc, where r denotes the distance from the Galactic Center. Binning r into K bins and denoting the fraction of neutron star binaries in the $i^{\rm th}$ bin as f_i one has $f_i = 1/K$. We further assume that f_i do not evolve with time, but the ambient DM density in the $i^{\rm th}$ bin, $\rho_{{\rm ext},i}$, does evolve with time. We assume that the DM density in each halo is given by the Navarro-Frenk-White profile $\rho_{\rm ext}(r) = \rho_s/\left[(r/r_s)(1+r/r_s)^2\right]$ [310, 311], such that the average density within the virial radius $r_{\rm vir}$ is $200\rho_c(z)$. The two parameters in the Navarro-Frenk-White profile, ρ_s and r_s, are expressible in terms of the critical density of the Universe $\rho_c(z)$, the concentration parameter $c_{200} = r_{\rm vir}/r_s$, and the mass inside the virial radius M_{200}. For Milky Way like galaxies we take $c_{200} = 13.31$ and $M_{200} = 0.82 \times 10^{12}\, M_\odot$ [312], and the time evolution of $\rho_{{\rm ext},i}$ is solely determined by evolution of $\rho_c(z) = \rho_c(0)\left[\Omega_\Lambda + \Omega_m(1+z)^3\right]$, where Ω_m, Ω_Λ are the present day density parameters for matter and dark energy, respectively [4]. For a detailed discussion on DM density profiles, see Appendix C.

From the expression for the merger rate, it is evident that $R_{\rm TBH}(t)$ decreases with increase in transmutation time. Therefore, for a fixed DM mass and DM-nucleon scattering cross-section, the merger rate of TBH binaries decreases with higher redshift. This is simply because neutron star binaries at higher redshift do not have the time for accumulating sufficient amount of DM required for implosion. Of course, given a DM mass, decrease in DM-nucleon scattering cross-section leads to higher $\tau_{\rm trans}$, and, hence, lower merger rate. This distinct redshift dependence of the binary merger rates, especially at higher redshifts, can be measured with the upcoming third generation GW detectors like Cosmic Explorer [313], Einstein Telescope (ET) [314] and space-based GW detector Pre-DECIGO [315] which will distinguish the transmutation scenario from PBHs. In Table 4.1, we also estimate the possible detection rates of TBH mergers for several GW detectors.

The expected detection rate of TBH mergers, N_D, is simply given by [308, 316]

$$N_D = \int_{z=0}^{\infty} dz \frac{4\pi D_c^2(z)}{(1+z)H(z)} R_{\rm TBH}(z) \times C_\theta \left[\frac{\rho_0}{8}\frac{D_L(z)}{r_0}\left(\frac{1.2 M_\odot}{(1+z)\mathcal{M}_c}\right)^{5/6}\right], \tag{4.3}$$

where $D_c(z) = \int_0^z \frac{dz'}{H(z')}$ denotes the co-moving radial distance and $D_L(z) = (1+z)\, D_c(z)$ denotes the luminosity distance respectively. $H(z)$ is the Hubble rate at redshift z, and we use the cosmological parameters determined by the latest Planck observations [4]. The angular dependence of the signal-to-noise-ratio (SNR) is encoded within the variable θ, and the cumulative distribution of θ is denoted by C_θ, and is given by [316]

$$C_\Theta(x) = \begin{cases} 1, & \text{if } x \leq 0 \\ \frac{(1+x)(4-x)^4}{256}, & \text{if } 0 \leq x \leq 4 \\ 0, & \text{if } x > 4. \end{cases} \tag{4.4}$$

The chirp mass of the coalescing binary is denoted by $\mathcal{M}_c$. ρ_0, r_0 are the SNR threshold for GW detection, and the characteristic distance sensitivities of the GW detectors. For this analysis, we have considered $\rho_0 = 8$ and $r_0 = 80$ Mpc for advanced LIGO, and $\rho_0 = 8$ and $r_0 = 1591$ Mpc for Einstein Telescope [308].

The possible detection rate of TBH binaries for present and upcoming GW detectors, such as advanced LIGO and Einstein Telescope, are tabulated in Table 4.1. From this tabulated values, we find that advanced LIGO is already sensitive to DM parameters that are not ruled out by *any* other data at present, e.g., $m_\chi = 10^4\,\text{GeV}$ and $\sigma_{\chi n} = 10^{-45}\,\text{cm}^2$. Hence, LIGO can act as a direct detection experiment for non-annihilating particle DM by observing the binary merger rates of the transmuted black holes. From Table 4.1, we can also discriminate the TBH/PBH events using the shape-information of the binary merger rates. Suppose $N_D = 5916\ \text{yr}^{-1}$ in the low redshift bin ($0 \leq z \leq 1$), which could be due to mergers of 1.3 $M_\odot$ PBH binaries with $f_{\text{PBH}} = 0.0019$ or $1.3\,M_\odot$ TBH binaries with $m_\chi = 10^4$ GeV, $\sigma_{\chi n} = 10^{-45}\,\text{cm}^2$. 1 ET-yr worth of high redshift data can discriminate between these two model points using the shape-information alone (i.e., with same normalization at low redshift). The PBH binaries will have 787 events in the high redshift bin ($z \geq 1$), whereas TBH binaries will have 880, indicating putatively $\geq 3\sigma$ discrimination between said TBH and PBH model points, with statistical errors only.

Apart from the cosmic evolution of the binary merger rates, we point out several avenues to test the transmuted origin of low mass black holes, and are detailed below

- The ambient DM density around a sub-Chandrasekhar or $\mathcal{O}(1)\,M_\odot$ black hole is a

$M_{\rm NS}$ $[M_\odot]$	m_χ [GeV]	$\sigma_{\chi n}$ [cm^2]	aLIGO [yr^{-1}]	ET [yr^{-1}]
1.0	10^4	10^{-47}	0.2; 0; 0.2	672; 3; 675
1.0	10^4	10^{-45}	0.3; 0; 0.3	2982; 32; 3014
1.3	10^4	10^{-47}	0.4; 0; 0.4	1451; 84; 1535
1.3	10^4	10^{-45}	0.8; 0; 0.8	5916; 880; 6796

Table 4.1: Possible detection rates of TBH binaries for advanced LIGO (aLIGO) and Einstein Telescope (ET), estimated using the procedure in the text, for representative choices of neutron star mass $M_{\rm NS}$, dark matter mass m_χ and DM-nucleon scattering cross-section $\sigma_{\chi n}$. The radius of the progenitors are taken to be 10.6 km. The three numbers in the last two columns are for low redshift ($z \leq 1$); high redshift ($z > 1$); and total, respectively.

simple yet powerful probe to test its origin. Since a DM rich environment favors implosion of stellar objects, detection of a low mass black hole in a DM deficient region will prefer a primordial origin. Coexistence of a low mass black hole and a companion neutron star of similar age can also be a strong evidence of its primordial origin, as the required parameter space for such transmutation will be disfavored by the existence of the companion neutron star. Since the DM dense inner regions potentially contain a large number of neutron stars [317], possible detection of an $\sim \mathcal{O}(1)$ Gyr old NS by the radio telescopes like FAST [318] and SKA [319] will significantly strengthen the exclusion limits on DM-nucleon interaction strength. As a consequence, the allowed parameter space for dark core collapse-induced transmutation of a stellar object will shrink.

- Mass distributions of the compact objects provide yet another powerful way to distinguish TBHs from PBHs. Since, the TBHs track the mass distribution of their progenitors, it can be compared against well-motivated PBH mass distributions to statistically determine the stellar or primordial origin of BHs. The last two panels of Fig. 4.3 correspond to the mass distribution of all observed neutron stars and white dwarfs, progenitors of the TBHs. It would take a striking coincidence for the PBH mass distribution to coincide with these distributions. Ref. [320], that appeared as our paper was being readied, establishes this technique in more detail.

- With imminent ground and space-based GW detectors, about one binary neutron star merger event is expected per week [321]. Considering the huge number of

expected events, the greatly improved sky localization of the GW events with a multi-detector network [321], as well as the GW lensing [322], the implosion scenario can easily be tested in the near future. Observationally, there also exist several ways to distinguish a TBH binary from a binary neutron star. The peak signal frequency of a binary neutron star merger is much lower than that of a binary black hole merger due to the less compact nature of neutron stars compared to the similar mass black holes [291]. Also, the amount of ejected neutron star material during a merger is much larger if one of the components is a black hole, and therefore, an unusually bright transient would favor a low mass TBH-neutron star merger [323]. Besides, the dimensionless tidal deformability parameter, which is zero for a black hole and ~ 100 for a typical neutron star, and the strength of tidal heating can also be used to probe this implosion scenario [324, 325]. More importantly, possible detection of an associated electromagnetic counterpart from radio wavelengths to gamma rays can also distinguish binary black holes from binary neutron stars or black hole-neutron star merger.

4.3 Summary & Conclusions

Sub-Chandrasekhar mass black holes cannot be explained by any standard stellar evolution and will herald new physics. PBHs are the most discussed explanation of these objects. The notable existing alternative proposals [290, 291, 292] are either not effective or appeal to baroque DM models. Here, we study a simple yet novel production mechanism for sub-Chandrasekhar mass non-primordial black holes. Continued accumulation of non-annihilating particle DM inside compact stars can lead to transmutation of compact stars via dark core collapse, and that can produce low mass black holes without fine-tuning. Non-zero interactions of DM with stellar nuclei, which is a universal feature of DM models, is sufficient for such transmutations, and is shown in Fig. 4.1. For sub-Chandrasekhar mass progenitors, the transmuted black holes are viable alternative to PBHs, whereas, for heavier mass progenitors, they can also possibly explain the recent anomalous GW events. Cosmic evolution of the binary merger rates (Fig. 4.2) and the mass distributions of the progenitors (Fig. 4.3) are simple yet powerful probes of our proposal. More specifically, we estimate the binary merger rates of TBHs (Eq. 4.2), and compare it with the binary merger rates of PBHs and neutron stars, demonstrating that

measurement of the high-redshift binary merger rates by the imminent GW detectors can conclusively test this transmutation scenario. We also estimate the expected detection rate of TBH mergers in present as well as upcoming GW detectors (Eq. 4.3), and illustrate that advanced LIGO is already sensitive to the DM parameters that are not probed otherwise. Observation of an associated electromagnetic counterpart along with a GW event, as well as a precise measurement of the tidal deformability parameter, can differentiate merger of such TBHs from a binary neutron merger or a black hole-neutron star merger. Importantly, possible detection of any low mass black hole in a DM deficient environment or accompanied by an old neutron star can falsify our proposal. Improved sky localization with multi-detector networks as well as sub-arc-second precision of a GW event from GW lensing can also shed light on this topic in the near future.

Chapter 5

Constraining Ultralight PBHs using Neutrino & Positron Emission

In this Chapter, we demonstrate that non-observations of Hawking radiated neutrinos & positrons in the diffuse supernovae neutrino background searches at the existing neutrino detectors such as Super-Kamiokande and measurement of the GC 511 keV gamma-ray line by the space based telescope INTEGRAL provide world-leading exclusions on ultralight PBHs as DM. We also explore the impact of PBH rotation on the corresponding exclusions. The results presented in this chapter can be found in [10].

5.1 Particle Emission from Ultralight Evaporating PBHs

PBHs Hawking radiate, act as a decaying DM, and emit particles which follow a blackbody like distribution. An uncharged, rotating PBH of mass $M_{\rm PBH}$, and dimensionless spin parameter a_* emits particles of spin s with ($c = \hbar = k_B = 1$) [326, 327, 328, 329, 330]

$$\frac{d^2N}{dEdt} = \frac{1}{2\pi}\frac{\Gamma_s(E, M_{\rm PBH}, \mu, a_*)}{\exp[-E'/T_{\rm PBH}] - (-1)^{2s}}\,, \tag{5.1}$$

where μ is the rest mass of the emitted particles and E' is the effective energy of the emitted particles, including the rotational velocity of PBHs. Γ_s denotes the greybody factor, and non-unity of the greybody factor in Hawking emission accounts for the departure from an ideal blackbody emission. In the high energy regime ($GM_{\rm PBH}E \gg 1$),

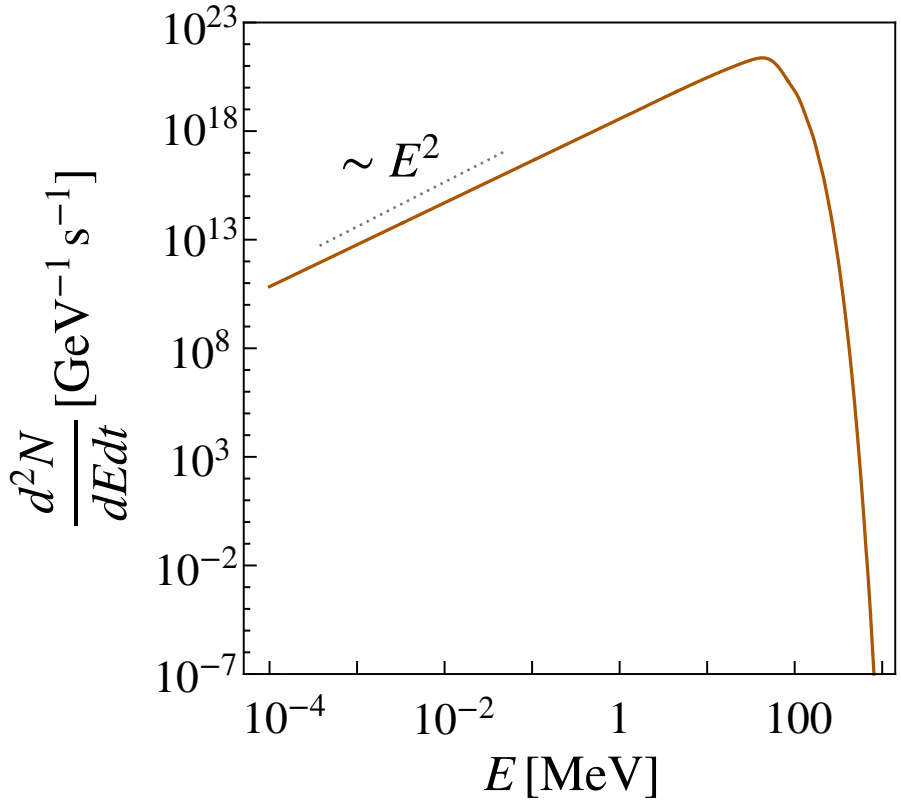

Figure 5.1: Spectrum of the emitted neutrinos from an uncharged and non-rotating PBH of mass 10^{15} g. The temperature of the PBH is 10 MeV, and hence, the emission peaks at $\sim$ 40 MeV. The emission is exponentially suppressed for $E \gg 40$ MeV, and falls off as $\sim E^2$ for energies lower than 40 MeV because of the E^2 dependence of the greybody factor in the low energy regime.

the greybody factor becomes independent of the spin of the emitted particle species, and it reaches its geometric saturation value, i.e., $\Gamma = 27G^2M_{\rm PBH}^2(E^2-\mu^2)$ for an uncharged and non-rotating PBH. Whereas, in the opposite regime ($GM_{\rm PBH}E \ll 1$), greybody factor depends strongly on the spin of the emitted particle species, and scales as E^2 for $s = 0, 1/2$ emission and as E^4 for $s = 1$ emission [328]. $T_{\rm PBH}$ denotes the temperature which is inversely proportional to its mass [326, 327, 328, 329, 330]

$$T_{\rm PBH} = \frac{1}{4\pi G M_{\rm PBH}} \frac{\sqrt{1-a_*^2}}{1+\sqrt{1-a_*^2}}\,. \tag{5.2}$$

For a given PBH mass, temperature can decrease by several orders of magnitude when the dimensionless spin parameter, a_*, approaches to unity, and Hawking emission ceases at $a_* = 1$. From Eq.(5.1), it is evident that the emission of particles is exponentially

suppressed for energies exceeding the temperature of a PBH, i.e., $E \gg T_{\rm PBH}$. In the opposite regime, i.e., $E \ll T_{\rm PBH}$, the emission falls off as a power law because of the energy dependence of the greybody factor. Hence, Hawking emission becomes significant for energies comparable to the temperature of a PBH, and peaks at $E_{\rm peak} = 2.81\,T_{\rm PBH}$ for $s = 0$ emission, $E_{\rm peak} = 4.02\,T_{\rm PBH}$ for $s = 1/2$ emission, and $E_{\rm peak} = 5.77\,T_{\rm PBH}$ for $s = 1$ emission[330]. We use BlackHawk [331, 332] to compute the spectra of the emitted particles, and we have verified these numerically obtained emission rates against semi-analytical emission rates from [326, 327, 328].

Fig. 5.1 demonstrates the spectrum of the emitted neutrinos from an uncharged, non-rotating PBH of mass $10^{15}\,\mathrm{g}$, calculated using the publicly available package BlackHawk, explaining all the relevant features in the spectrum.

The mass loss rate of an evaporating PBH is essentially determined by summing over all the emission channels. By assuming SM particle emission, the mass loss rate of an evaporating black hole can be expressed as [329]

$$\frac{dM_{\rm PBH}}{dt} = -5.34 \times 10^{25} f(M_{\rm PBH}) M_{\rm PBH}^{-2}\ \ \mathrm{g\,s^{-1}}\,, \tag{5.3}$$

where $f(M_{\rm PBH})$ is a measure of the number of emitted particle species, and it is normalized to unity for PBHs with $M_{\rm PBH} \gg 10^{17}\,\mathrm{g}$. Integrating Eq. (5.3) over time, one can also obtain the lifetime of an evaporating PBH

$$\tau \sim 407 \left(\frac{f(M_{\rm PBH})}{15.35}\right)^{-1} \left(\frac{M_{\rm PBH}}{10^{10}\,\mathrm{g}}\right)^{3}\ \mathrm{s}\,. \tag{5.4}$$

Since the lifetime of an evaporating PBH scales at $M_{\rm PBH}^3$, where $M_{\rm PBH}$ denotes its initial mass, extremely light PBHs have a lifetime less than the current age of our Universe, and hence, can not exist till the present day. We denote the threshold mass of the PBHs as M_*, i.e., $\tau(M_*) = t_0$, where t_0 is the current age of our Universe. Using the recent measurement of $t_0 = 13.797\,\mathrm{Gyr}$ [4], we find, $M_* \approx 5 \times 10^{14}\,\mathrm{g}$ for non-rotating PBHs and $M_* \approx 7 \times 10^{14}\,\mathrm{g}$ for maximally rotating PBHs, respectively. Therefore, non-rotating (maximally rotating) PBHs lighter than $5 \times 10^{14}\,\mathrm{g}$ ($7 \times 10^{14}\,\mathrm{g}$) can not survive till the present day.

In the following subsections, we derive stringent exclusions on fraction of DM that is in the form of ultralight PBHs by considering neutrino and positron emissions.

5.1.1 Constraints using Neutrino Emission

The diffuse supernova neutrino background (DSNB) is the accumulation of all $\sim$ MeV energy neutrinos emitted by core-collapse supernovae over the history of the Universe [333, 334, 335]. Ultralight PBHs in the mass range of $10^{15} - 10^{16}$ g emit $\mathcal{O}(1-10)$ MeV neutrinos, and these low energy Hawking radiated neutrinos can be searched in the DSNB searches at the existing neutrino detectors such as Super-Kamiokande [336], KamLAND [337], Borexino [338], etc. Non-observations of such Hawking evaporated neutrinos in those searches provide stringent constraint on PBH fraction of DM.

As the temperature of a PBH becomes comparable to the energy of the neutrino, emission occurs in significant amount. The emission has two contributions: *i*) contribution from Galactic PBHs and *ii*) Contribution from extra-Galactic PBHs, and for a monochromatic mass distribution of PBHs, the fluxes are respectively

$$F_{\rm gal,mono} = \int \frac{d\Omega}{4\pi} \int dE \frac{d^2N}{dEdt} \int dl \, \frac{f_{\rm PBH}\, \rho_{\rm MW}\left[r(l,\psi)\right]}{M_{\rm PBH}} \,, \tag{5.5}$$

$$F_{\rm eg,mono} = \int \int dt \, d\tilde{E} \, \left[1+z(t)\right] \frac{f_{\rm PBH}\rho_{\rm DM}}{M_{\rm PBH}} \frac{d^2N}{dEdt}\Big|_{E=[1+z(t)]\tilde{E}} \,. \tag{5.6}$$

In the Galactic neutrino flux ($F_{\rm gal,mono}$), r is the Galactocentric distance, $\rho_{\rm MW}$ denotes the DM profile of the Milky Way (MW), l is the distance from the observer, and ψ is the angle between the line of sight and the observer. Ω denotes the solid angle under consideration and the fraction of DM composed of ultralight evaporating PBHs is denoted by $f_{\rm PBH}$. The upper limit of the line of sight integral, $l_{\rm max}$, depends on the MW halo size ($r_{\rm max}$) and the angle ψ

$$l_{\rm max} = r_\odot \cos\psi + \left(r_{\rm max}^2 - r_\odot^2 \sin^2\psi\right)^{1/2} \,, \tag{5.7}$$

where $r_\odot$ is the Galactocentric distance of the Sun. It is important to mention that the DM profile of the Milky Way, $\rho_{\rm MW}$, is uncertain, and for a detailed discussion on DM density profiles, see Appendix C .

In the extra-Galactic neutrino flux ($F_{\rm eg,mono}$), the time integral runs from $t_{\rm min} = 1\,$s, to the neutrino decoupling time, to $t_{\rm max}$, the smaller of the PBH lifetime and age of the Universe. Although the ultralight PBHs are formed much earlier than the neutrino decoupling time, we have taken it as a lower limit of the time integral $t_{\rm min}$ because neutrinos emitted from

PBHs can free stream only after the neutrino decoupling. Note that, changing this lower limit to smaller values has very little effect on the corresponding upper limit. The average DM density of the Universe at the present time is denoted by $\rho_{\rm DM}$, and we use the cosmological parameters determined by the recent Planck observations [4].

In addition to a monochromatic mass distribution for the PBHs, we also consider a log-normal mass distribution, as predicted by various inflationary models [132, 339, 340, 341]

$$\frac{dN_{\rm PBH}}{dM_{\rm PBH}} = \frac{1}{\sqrt{2\pi}\sigma M_{\rm PBH}} \exp\left[-\frac{\ln^2\left(M_{\rm PBH}/\mu_{\rm PBH}\right)}{2\sigma^2}\right], \tag{5.8}$$

where $\mu_{\rm PBH}$ and σ are the average mass and width of the distribution, respectively. For an extended mass distribution of PBHs, the fluxes can be obtained by integrating the monochromatic fluxes over the underlying mass distribution

$$F_{\rm gal/eg,ext} = \int dM_{\rm PBH} \frac{dN_{\rm PBH}}{dM_{\rm PBH}} F_{\rm gal/eg,mono}\,. \tag{5.9}$$

For non-rotating PBHs, the mass integral runs from the minimum evaporation mass $M_{\rm min} = 5\times10^{14}\,{\rm g}$ to $M_{\rm max} = \infty$, whereas, for maximally rotating PBHs, it runs from $M_{\rm min} = 7\times10^{14}\,{\rm g}$ to $M_{\rm max} = \infty$, as the maximal rotation increases the minimum evaporation mass by enhancing the Hawking emission rate.

The upper limit on $f_{\rm PBH}$ is obtained by comparing the total Galactic and extra-Galactic flux due to PBHs, with the current upper limit on the neutrino flux ($F_{\rm DSNB}$) from the DSNB searches at various neutrino detectors

$$F_{\rm gal} + F_{\rm eg} \leq F_{\rm DSNB}\,. \tag{5.10}$$

Current best upper limits on the DSNB flux ($F_{\rm DSNB}$) come from Super-Kamiokande (KamLAND), and the upper limits are 2.9 $\bar{\nu}_e\,{\rm cm}^{-2}\,{\rm s}^{-1}$ (139 $\bar{\nu}_e$ ${\rm cm}^{-2}\,{\rm s}^{-1}$) in the energy ($E_{\bar{\nu}_e}$) range of 17.3 to 91.3 MeV (8.3 to 31.8 MeV) respectively [336, 337]. We find that both the Super-Kamiokande and the KamLAND data help us probe the physical region of $f_{\rm PBH} < 1$. However, we only show the upper limit obtained using the Super-Kamiokande data, as it is stronger at all PBH masses we consider.

Fig. 5.2 shows the upper limits on $f_{\rm PBH}$ that can be derived from DSNB searches, for various PBH mass distributions and spins. The left panel shows the constraints for the

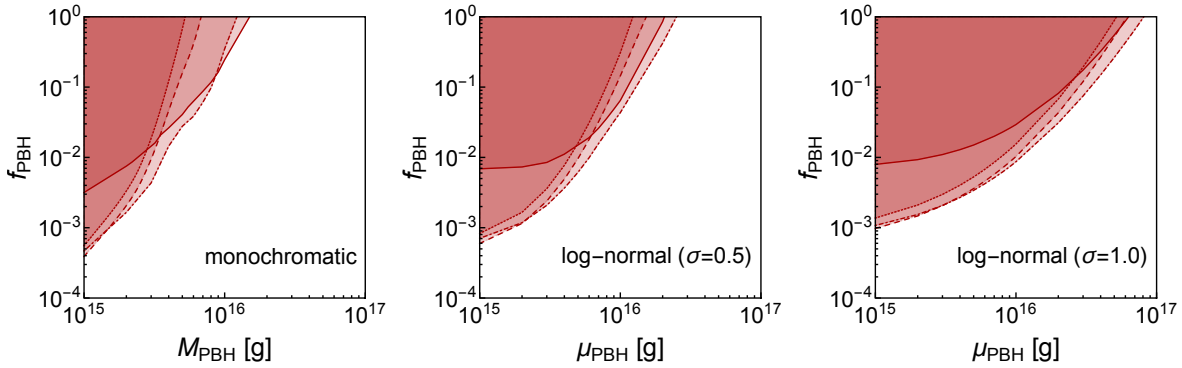

Figure 5.2: Upper limit on PBH fraction of DM, $f_{\rm PBH}$, from DSNB searches at Super-Kamiokande. The left, middle, and right panel corresponds to a monochromatic PBH mass function, and log-normal PBH mass functions with $\sigma = 0.5$ and 1.0, respectively. In each plot, four different lines correspond to four different dimensionless spin parameters ($a_* = 0, 0.5, 0.9, 0.9999$) of PBHs. Tiny dotted, dashed, dot-dashed, and solid lines correspond to $a_* = 0, 0.5, 0.9$, and 0.9999, respectively. These constraints are derived using an NFW DM profile of the Milky Way. However, the results are sensitive to the other choices of DM profiles.

monochromatic mass distribution, whereas the middle and the right panels show the constraints for a log-normal distribution with $\sigma = 0.5$ and 1, respectively. For all these cases, we choose $a_* = 0$, 0.5, 0.9, and 0.9999 and the NFW profile to derive our limits. The constraints shown in Fig. 5.2 have a non-trivial dependence on the rotation of the PBHs, and typically probe more mass window for PBHs that have maximal rotation. The constraints also weaken for higher PBH masses because: *i*) PBHs become less abundant for higher masses and *ii*) the temperature decreases with higher $M_{\rm PBH}$, and as a result, the emission of particles in the considered energy range falls off. For example, the temperature of uncharged, non-rotating PBHs of mass 10^{15} g is 10 MeV, and therefore they emit $\sim$ 40 MeV neutrinos maximally which fall in the correct energy window for DSNB searches. Whereas, for PBHs of mass 10^{16} g, the temperature is 1 MeV, and the emission occurs significantly at $\sim$ 4 MeV which falls well-outside the energy ranges of DSNB searches (17.3 to 91.3 MeV), explaining the weakening of the exclusion limits.

The exclusions from DSNB searches are somewhat weaker than the existing exclusions from diffuse gamma-ray background searches [153]. However, they are very robust to the astrophysical uncertainties such as choice of DM density profiles, as well as to a variety of propagational uncertainties that are inevitably associated with photons or any other

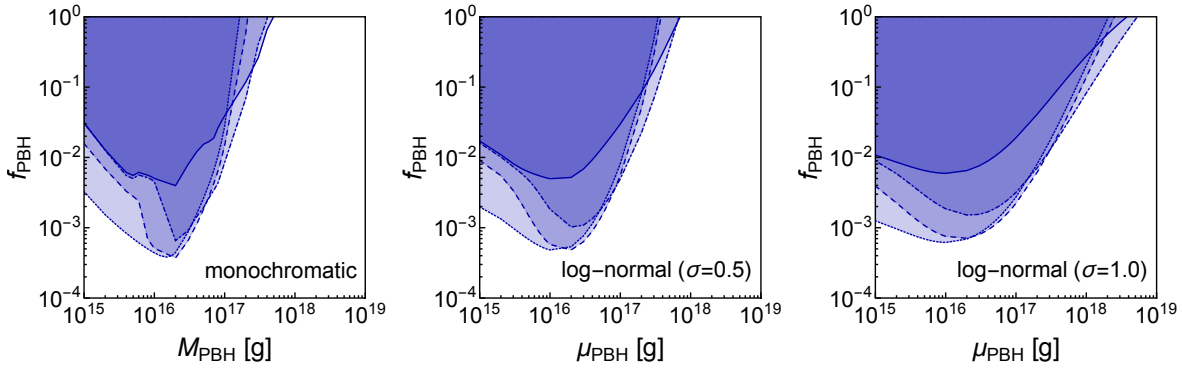

Figure 5.3: Upper limit on DM fraction of PBHs, $f_{\rm PBH}$, from INTEGRAL measurement of the 511 keV gamma-ray line flux. The left, middle, and right panels correspond to a monochromatic PBH mass function and log-normal PBH mass functions with $\sigma = 0.5$ and 1.0, respectively. In each plot, four different lines correspond to four different reduced spin parameters ($a_* = 0, 0.5, 0.9, 0.9999$) of PBHs. Tiny dotted, dashed, dot-dashed, and solid lines correspond to $a_* = 0, 0.5, 0.9$, and 0.9999, respectively. These constraints are derived using an NFW DM profile of the Milky Way and assume that 80% of positrons within 3.5 kpc of the GC annihilate to produce the 511 keV signal.

charged particles. The minimal uncertainty to the constraints can be due to matter effect, and uncertainties in the oscillation parameters. With loading of gadolinium in Super-Kamiokande [342] and with Hyper-Kamiokande [343], the constraints will soon be improved.

5.1.2 Constraints using Positron Emission

The origin of the 511 keV gamma-ray line from the Galactic Center is one of the enduring mysteries of astrophysics. This line has been observed by a number of observatories over the last few decades, and a detailed study has been made by the SPI/INTEGRAL observatory. Despite the intense scrutiny of this signal, we do not yet know the origin of this signal. Many viable astrophysical models, including PBH evaporation have been proposed as a solution to the origin of the 511 keV gamma-ray line [344, 345, 346, 347, 348]. Here, we present a very conservative exclusion limit on ultralight evaporating PBHs as DM from the precise measurement of the 511 keV gamma-ray line by INTEGRAL. This possibility has also been explored recently in Refs. [166, 167] in the context of non-rotating PBHs, and we extend this idea for rotating PBHs which have a significant effect

on the PBH evaporation rate.

The observed flux of the 511 keV gamma-ray line by INTEGRAL indicates that the total production rate of positrons within the Galactic bulge is $\sim 10^{50}\,\mathrm{yr}^{-1}$ [124, 349, 350]. This measurement can be translated to set world-leading exclusion limits on PBH fraction of DM in the mass range of $10^{15} - 10^{17}$ g. The most conservative limit on the PBH fraction of DM can simply be obtained by requiring that the total positron injection rate from PBHs has to be less than this inferred rate, i.e.,

$$f_{\rm PBH} \leq \frac{10^{50}\ \mathrm{yr}^{-1}}{\int dE \int dM_{\rm PBH} \frac{dN_{\rm PBH}}{dM_{\rm PBH}} \frac{d^2N}{dEdt} \int \frac{d^3r\,\rho_{\rm MW}(r)}{M_{\rm PBH}}}\,. \tag{5.11}$$

In the above Eq., the energy integral runs from $m_e = 0.511$ MeV to 3 MeV. This is because for energies below 3 MeV, the probability for in-flight annihilation is negligible, and hence, the majority of the positrons come to rest before undergoing annihilation, and contributes to the 511 keV gamma-ray line [351]. Note that, here, we simply demand that the positron injection luminosity is less than what is measured by SPI/ INTEGRAL. This is the most conservative option. If we model the contributions of some astrophysical source(s) to this gamma-ray observation, then the corresponding upper limit on the fraction of DM that is in the form of ultralight PBHs become more stringent. Quantitatively, it can even be improved by more than an order of magnitude [167].

Fig. 5.3 shows the upper limit on $f_{\rm PBH}$, from the GC positron observation for various PBH mass functions and reduced spin parameters. The left, middle, and right panels display the constraints for the monochromatic PBH mass function and the log-normal mass distribution with $\sigma = 0.5$ and 1, respectively. In each panel, constraints are shown for four different reduced spin parameters, $a_* = 0$, 0.5, 0.9, and 0.9999. For monochromatic, non-rotating PBHs, the strongest constraint arises for $M_{\rm PBH} \sim 10^{16}\,\mathrm{g}$ because these PBHs can emit $\mathcal{O}(1)$ MeV positrons maximally which can contribute to the 511 keV gamma-ray line flux. For higher (lower) mass PBHs, the peak of the emission occurs at lower (higher) energies, explaining the weakening of the exclusion limits. The constraints also probe higher mass windows for PBHs that have rotation or which follow an extended mass distribution.

Unlike the neutrino derived results, the GC positron derived results depend on several astrophysical uncertainties. The major astrophysical uncertainties stem from i) choice of

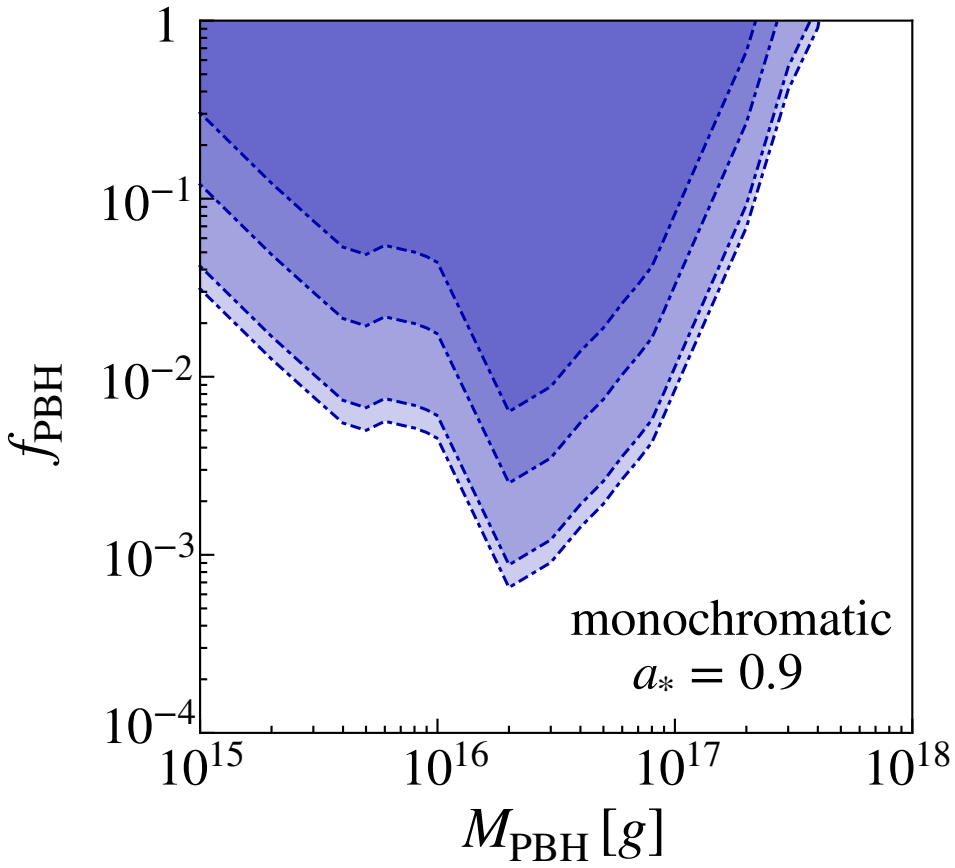

Figure 5.4: Variation in the upper limit on dark matter fraction of PBHs for monochromatic mass distribution from INTEGRAL 511 keV gamma-ray line measurement, due to dark matter density profiles and unknown positron propagation distance. This plot considers a PBH with $a_* = 0.9$. The lines from top to bottom correspond to isothermal with 1.5 kpc, NFW with 1.5 kpc, isothermal with 3.5 kpc, and NFW with 3.5 kpc region of interest, respectively.

DM density profiles and *ii*) unknown propagation distance of the low energy GC positrons. We bracket the first source of uncertainty by assuming two different DM density profiles: cuspy (NFW) and cored (isothermal). Because of the cusp present in the NFW profile, the constraints derived using this input are stronger than the results obtained from the isothermal profile. For a detailed discussion on DM density profiles, see Appendix C. The second source of uncertainty comes from the fact that propagation of non-relativistic positrons in the GC region is not precisely known. The positron propagation distance in the GC region depends strongly on various parameters, such as ionization fraction, temperature, and density of the GC region, the structure of the Galactic magnetic field, the scale of magnetic turbulence, etc., and all of these parameters have uncertainties.

There are scenarios via which positrons can be advected up to a distance of ~ 1 kpc [352, 353]. So in order to include this propagation uncertainty, we assume that: *i*) 80% of the PBH-produced positrons within a 3.5 kpc radius of the GC can annihilate to produce the 511 keV signal and *ii*) all (100%) of the PBH-produced positrons within a 1.5 kpc radius of the GC can annihilate to produce the 511 keV signal [352].

Fig. 5.4 shows the variation of the positron-derived constraints for $a_* = 0.9$, for different DM profiles and propagation distance of low-energy positrons in the GC. Since this variation is a multiplicative constant, as evident from Eq. (5.11), this uncertainty is the same for PBHs with different spins. The strongest constraint arises when we consider that the DM profile is NFW and 3.5 kpc region of interest around the GC. The weakest constraint arises with the isothermal DM profile and a 1.5 kpc region of interest around the GC. In short, the GC positron derived constraints can vary by an order of magnitude depending on the astrophysical uncertainties that are discussed above.

5.2 Summary & Conclusions

PBHs can have substantial spin – a fundamental property that has a strong effect on their evaporation rate. There has been a recent surge of interest in rotating PBHs, and it is necessary to fully explore the parameter space of these exotic objects. Using DSNB searches at the existing neutrino detectors such as Super-Kamiokande & KamLAND, and precise measurement of the GC 511 keV gamma-ray line by the space based telescope INTEGRAL, we constrain the fraction of DM that is in the form of uncharged (non)-rotating PBHs (Fig. 5.2 and Fig. 5.3). For a monochromatic mass distribution of PBHs, the neutrino (positron)-derived constraints demonstrate that non-rotating PBHs in the mass range of $10^{15} - 5 \times 10^{15}\,\mathrm{g}$ ($10^{15} - 10^{17}\,\mathrm{g}$) can not make up the solitary component of DM. The constraints probe much higher mass windows for PBHs that have rotation or which follow an extended mass distribution.

The neutrino-derived constraints are inferred by requiring that the total neutrino flux from PBHs can not exceed the current DSNB flux upper limits (Eq. 5.10). These constraints are somewhat weaker than the existing constraints in the ultralight mass window, but they are complementary and very robust to a variety of propagational uncertainties that are inevitably associated with photons or any other charged particles. Apart from

this, the neutrino-derived constraints are minimally dependent on choice of DM density profiles, and remains almost same for cored or cuspy DM profiles, implying them one of the cleanest constraint in the ultralight mass window. With near-future loading of gadolinium in Super-Kamiokande and Hyper-Kamiokande, the capability to search for the DSNB will enhance [342, 343], and as a consequence, the neutrino-derived constraints will improve further.

The positron-derived constraints are simply derived from the fact that positron injection rate from PBHs can not exceed the same from the 511 keV gamma-ray line measurement (Eq. 5.11). These conservative constraints are one of the leading constraints in the ultralight mass window, and can vastly be improved with a proper identification of the astrophysical sources that are responsible for the 511 keV gamma-ray line emission. Unlike the neutrino derived constraints, these constraints depend very strongly on the astrophysical uncertainties, such as, choice of DM density profiles and unknown propagation distance of the low energy Hawking emitted positrons, and can vary by an order of magnitude based on these uncertainties (Fig. 5.4).

Note added: Recently, Ref [162, 163, 165] appeared, and it extends our analysis (also improving it with the spectral analysis of the neutrino spectrum) for the upcoming neutrino detectors such as JUNO, DUNE, THEIA, and Hyper-Kamiokande.

Chapter 6

Constraining Asteroid mass PBHs using Photon Emission

In this Chapter, we demonstrate that future observation of low energy Galactic Center photons by the imminent soft gamma-ray telescopes, such as AMEGO, can probe asteroid mass PBHs. We also study the impact of PBH rotation and PBH mass distributions on the corresponding projections. The results presented in this chapter can be found in [11].

6.1 Projected Constraints using Photon Emission

PBHs emit significant number of photons via Hawking evaporation when the energy of the emitted particle becomes comparable to the temperature of the PBHs. More specifically, photon emission peaks at an energy $E \sim 5.77\, T_{\rm PBH}$ [328, 330] for an evaporating PBH with a temperature of $T_{\rm PBH}$. The emission of photons is exponentially suppressed for energies exceeding $T_{\rm PBH}$ ($E \gg T_{\rm PBH}$), and falls off as a power law in the opposite limit ($E \ll T_{\rm PBH}$).

For a monochromatic mass distribution of PBHs, the Galactic contribution to the differential flux from PBH evaporation is

$$\left.\frac{d\phi_{\rm gal}}{dE}\right|_{\rm mono} = \frac{f_{\rm PBH}}{4\pi M_{\rm PBH}} \frac{d^2N}{dEdt} \int_0^{s_{\rm max}} \rho\left[r(s,l,b)\right] ds\, d\Omega\,, \tag{6.1}$$

where $f_{\rm PBH}$ denotes the DM fraction of PBHs. DM profile of the Milky Way (MW) is denoted by $\rho\,[r(s,l,b)]$, where r is the Galactocentric distance, s is the distance from the observer, l and b denote the Galactic longitude and latitude respectively, and $d\Omega = \cos[b]\,dl\,db$ is the differential solid angle under consideration. The upper limit of the line of sight integral, $s_{\rm max}$, depends on the size of the MW DM halo, Galactic longitude, and Galactic latitude:

$$s_{\rm max} = r_\odot\,\cos[b]\,\cos[l] + \sqrt{r_{\rm max}^2 - r_\odot^2\,(1-\cos^2[b]\,\cos^2[l])}\,, \tag{6.2}$$

where $r_{\rm max}$ denotes the maximum size of the MW halo and $r_\odot$ is the Galactocentric distance of the Sun. See Appendix C for a detailed discussion on DM density profiles.

The extra-Galactic contribution to the differential flux for a monochromatic mass distribution of PBHs is

$$\left.\frac{d\phi_{\rm eg}}{dE}\right|_{\rm mono} = \frac{\Delta\Omega}{4\pi}\frac{f_{\rm PBH}\,\rho_{\rm DM}}{M_{\rm PBH}}\int_{z=0}^{\infty}\frac{dz}{H(z)}\left.\frac{d^2N}{dEdt}\right|_{E\to[1+z]E}\,, \tag{6.3}$$

where $\Delta\Omega$ denotes the total solid angle under consideration, $\rho_{\rm DM}$ is the average DM density of the Universe at the present epoch, and $H(z) = H_0\,\sqrt{\Omega_\Lambda + \Omega_m(1+z)^3 + \Omega_r(1+z)^4}$ is the Hubble expansion rate at redshift z. The Hubble expansion rate at the present epoch is H_0; Ω_Λ, Ω_m, and Ω_r denote the current dark-energy, matter, and radiation densities of the Universe, respectively. For numerical values of all cosmological parameters, we use the latest Planck 2018 measurements [4].

In addition to the monochromatic mass distribution, PBHs can also have extended mass distributions. For a log-normal mass distribution, as defined in Eq. (5.8), the Galactic/extra-Galactic contribution to the differential flux can be obtained by integrating the monochromatic flux with the underlying mass function

$$\left.\frac{d\phi_{\rm gal,eg}}{dE}\right|_{\rm ext} = \int dM_{\rm PBH}\,\frac{dN_{\rm PBH}}{dM_{\rm PBH}}\left.\frac{d\phi_{\rm gal,eg}}{dE}\right|_{\rm mono}. \tag{6.4}$$

For non-rotating PBHs, the mass integral runs from $M_{\rm min} = 5\times10^{14}$ g to $M_{\rm max} = \infty$. For PBHs approaching to their maximal rotation, the mass integral runs from $M_{\rm min} = 7\times10^{14}$ g to $M_{\rm max} = \infty$, as the maximal rotation increases the minimum evaporation mass $M_{\rm min}$ by enhancing the Hawking emission rate.

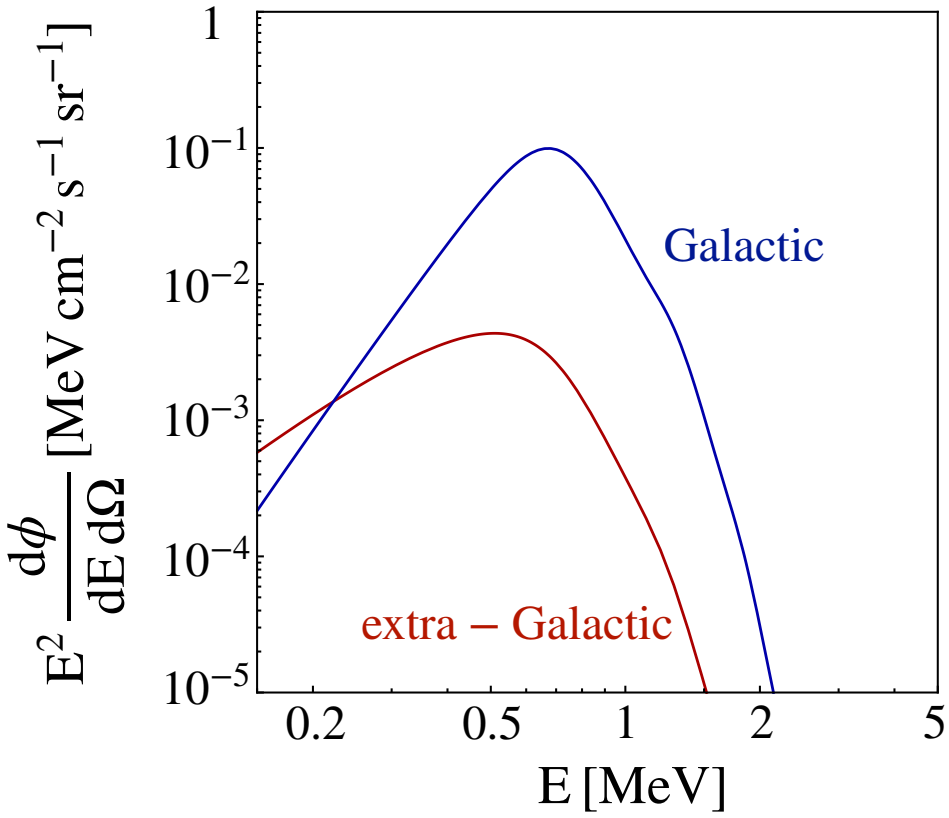

Figure 6.1: The Galactic and extra-Galactic photon contributions from Hawking evaporation off a non-rotating PBHs of mass 10^{17} g. It is assumed that PBHs make up the entirety of DM and follow an NFW density profile. The blue and red lines correspond to the Galactic and extra-Galactic contributions in the region of interest ($|l| \leq 5$ deg and $|b| \leq 5$ deg) respectively.

Fig. 6.1 shows the Galactic and extra-Galactic contributions to the total evaporation flux from PBHs of mass 10^{17} g in Galactic Center, defined to have: $|l| \leq 5$ deg and $|b| \leq 5$ deg. Since this region of interest resides in a DM-dominated environment, the extra-Galactic contribution to the evaporation signal is always subdominant. Galactic emission peaks at around ~ 0.6 MeV, as the temperature of a 10^{17} g PBH is 0.1 MeV. The extra-Galactic signal peaks at a slightly lower energy as it is redshifted.

Of course, PBHs are not the only possible source of gamma-rays in the cosmos. In particular, there are well-known astrophysical backgrounds, which we ought to marginalize over to unearth a possible PBH signal. Fig. 6.2 shows the Galactic and extra-Galactic astrophysical backgrounds used in this analysis. We have adapted the Galactic astrophysical

background $\phi^{\rm bkg}_{\rm gal}$ from Ref. [354]

$$\phi^{\rm bkg}_{\rm gal}(E) = A_{\rm bkg}\left(\frac{E}{1\,{\rm MeV}}\right)^{-\alpha}\exp\left[-\left(\frac{E}{E_c}\right)^{\gamma}\right], \tag{6.5}$$

in units of ${\rm MeV}^{-1}\,{\rm cm}^{-2}\,{\rm s}^{-1}{\rm sr}^{-1}$, which contains four parameters: an amplitude ($A_{\rm bkg}$), power-law index (α), exponential cut-off energy (E_c), and the index within the exponential (γ). Their best fit values are $A_{\rm bkg} = 0.013\,{\rm MeV}^{-1}\,{\rm cm}^{-2}\,{\rm s}^{-1}{\rm sr}^{-1}$, $\alpha = 1.8$, $E_c = 20\,{\rm MeV}$, and $\gamma = 2$, respectively. We have verified that this formula provides an adequate fit to the data obtained by COMPTEL [355, 356, 357].

For the extra-Galactic background, $\phi^{\rm bkg}_{\rm eg}$, we have considered a single power law which fits the cosmic X-ray background spectrum measured by various experiments [358, 359, 360, 361, 362] in the energy range 150 keV to 5 MeV [154]

$$\phi^{\rm bkg}_{\rm eg}(E) = A^{\rm eg}_{\rm bkg}\left(\frac{E}{1\,{\rm MeV}}\right)^{-\alpha^{\rm eg}}, \tag{6.6}$$

also in ${\rm MeV}^{-1}\,{\rm cm}^{-2}\,{\rm s}^{-1}{\rm sr}^{-1}$. Our power-law model for the extra-Galactic background contains two parameters, its amplitude ($A^{\rm eg}_{\rm bkg}$) and the power law index ($\alpha^{\rm eg}$), with best-fit values of $A^{\rm eg}_{\rm bkg} = 0.004135\,{\rm MeV}^{-1}\,{\rm cm}^{-2}\,{\rm s}^{-1}{\rm sr}^{-1}$, and $\alpha^{\rm eg} = 2.8956$.

We consider photons in the energy range $0.15 - 5$ MeV for this analysis. The lower end of the energy range is determined by the sensitivity of AMEGO, whereas, the higher end of the energy range is determined by the evaporation signal. For PBHs of mass 2×10^{16} g (minimum mass considered for this analysis), the evaporation signal peaks at around 3 MeV, and falls off exponentially with increase in photon energy. Moreover, the single power-law fit to the extra-Galactic background in Eq.(6.6) is valid only up to ~ 5 MeV [154].

We have applied Fisher forecasting [363, 364, 365] with marginalization over all astrophysical background parameters to compute the projected upper limits at 95% C.L. The exclusion limits are derived by assuming no evaporation signal is present in the data. The Fisher information matrix ($\mathcal{F}$) is a $N \times N$ matrix, where N denotes the total number of parameters $\vec{p} = \{p_1, p_2, ..., p_N\}$ and is defined as [354]

$$\mathcal{F}_{ij} = \int_E\int_\Omega \frac{\partial_i\phi(E,\Omega)\,\partial_j\phi(E,\Omega)}{\phi(E,\Omega)}\,T_{\rm obs}\,A_{\rm eff}(E)\,d\Omega\,dE\,, \tag{6.7}$$

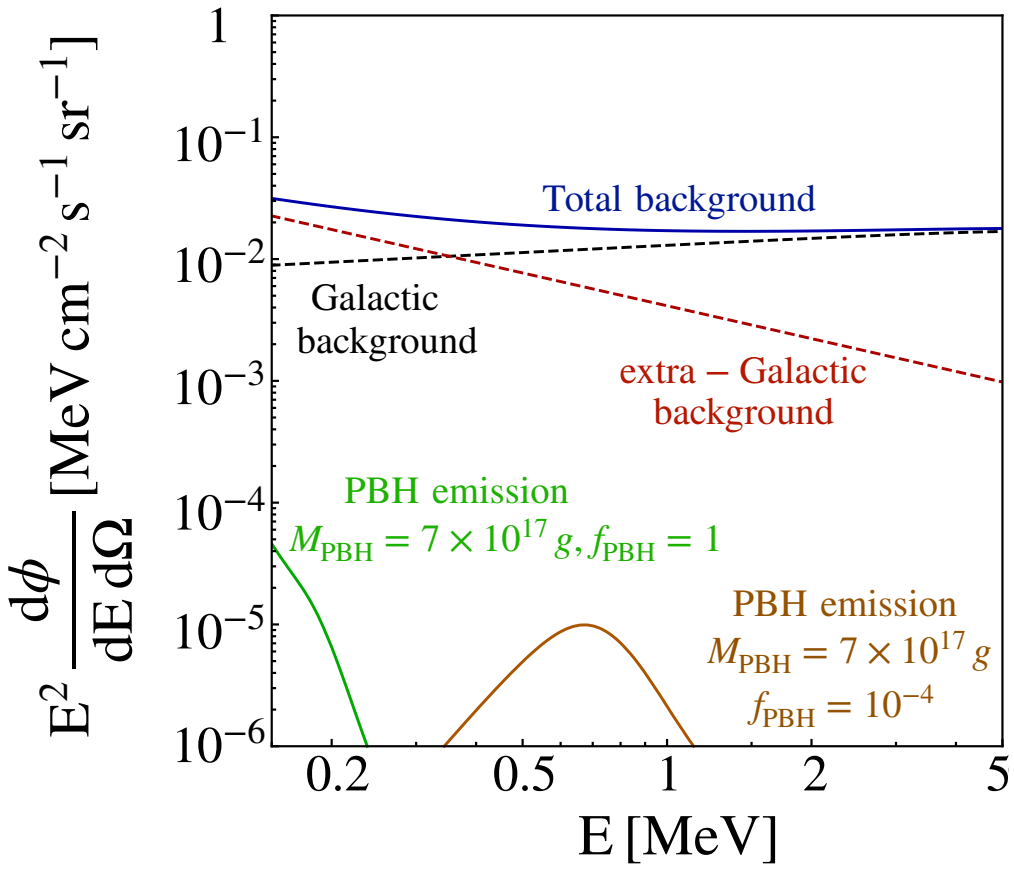

Figure 6.2: Galactic and extra-Galactic astrophysical backgrounds are shown as a function of the emitted photon energy. Dashed black line corresponds to the Galactic background, which is adapted from Ref. [354]. Dashed red line corresponds to the extra-Galactic background, which is a single power law fit to the Cosmic X-ray background measurements. Total background, the sum of the Galactic and extra-Galactic backgrounds, is shown by the solid blue line. Evaporation signals from non-rotating PBHs of mass 10^{17} g with dark matter fraction of 10^{-4} and a non-rotating PBH of mass 7×10^{17} g with dark matter fraction of unity are shown for comparison.

where $\phi(E, \Omega) = \left(\phi_{\rm gal} + \phi_{\rm eg} + \phi_{\rm gal}^{\rm bkg} + \phi_{\rm eg}^{\rm bkg}\right)$ is the total flux, $T_{\rm obs}$ is the observation time, and $A_{\rm eff}(E)$ is the effective area. We conservatively ignore the extra-Galactic PBH emission, as it is subdominant in our region of interest. The effective area for AMEGO is adapted from Ref. [366][1] and a uniform sky coverage $T_{\rm obs}$ of 1 year is considered for this analysis. We use a sufficiently dense binning in order to capture all the spectral variations in the Fisher information matrix. We have considered 2000 logarithmically spaced bins

[1] https://asd.gsfc.nasa.gov/amego/technical.html

between the energy interval of $0.15 - 5$ MeV.

For this work, there is only one signal parameter, the fraction $f_{\rm PBH}$ of the DM that is composed of PBHs for each mass we study, plus the 6 astrophysical parameters introduced in Eqs. (6.5) and (6.6). Hence, the Fisher information matrix ($\mathcal{F}$) used in our analysis is a 7×7 symmetric matrix. The projected upper limit on the signal parameter $f_{\rm PBH}$ at 95% C.L. is [354]

$$f_{\rm PBH}^{\rm UL} = 1.645 \sqrt{(\mathcal{F}^{-1})_{11}}\,, \tag{6.8}$$

where 1.645 represents the percent-point function for 95% C.L.

Because of the relatively large region of interest, our results are almost insensitive to different choices of DM density profiles. For this work, we assume that the density distribution of ultra-light PBHs in MW halo follows a Navarro-Frenk-White (NFW) profile [311]. However, we have tested our results with other density profiles, such as with a cored isothermal profile [367] and with a cored NFW profile with a core radius of 2 kpc [155]. We find that due to the different choices of DM density profiles, our results alter by as far as a factor of two (degrades by a factor of ~ 1.69 for a cored isothermal profile and by a factor of ~ 1.55 for a cored NFW profile with a core radius of 2 kpc). We have also checked that a somewhat larger region of interest around the Galactic Center, say $|l| \leq 30\,\text{deg}$ and $|b| \leq 10\,\text{deg}$, increases the Hawking evaporated photons as well as background photons by a factor of 6.81 and 12 respectively, indicating a putative improvement of the projections by a factor of $(S/\sqrt{N}) \sim 1.96$ (which, however, may be reduced by marginalization with the Fisher matrix).

Fig. 6.3 shows the projected upper limits (at 95% C.L.) on DM fraction of PBHs, $f_{\rm PBH}$, that can be derived from future AMEGO observations by assuming that no DM signal is present in the data. Monochromatic mass distribution of the PBHs is assumed in this plot. The solid (dashed) lines correspond to non-rotating, $a_* = 0$ (approaching maximal rotation, $a_* = 0.9999$) PBHs. Note that, we take the maximum value of spin as 0.9999 because BlackHawk can not go beyond that. The limits are derived by assuming an NFW density profile of the PBHs. As the PBHs become maximally rotating, their temperatures as well as the effective energy of the emitted photons fall off rapidly, and as a result, maximally rotating PBHs probe a higher mass window than their non-spinning counterparts. Because of the lower energy reach and larger effective area, AMEGO is able to probe into asteroid-mass windows compared to the previous gamma-ray observatories

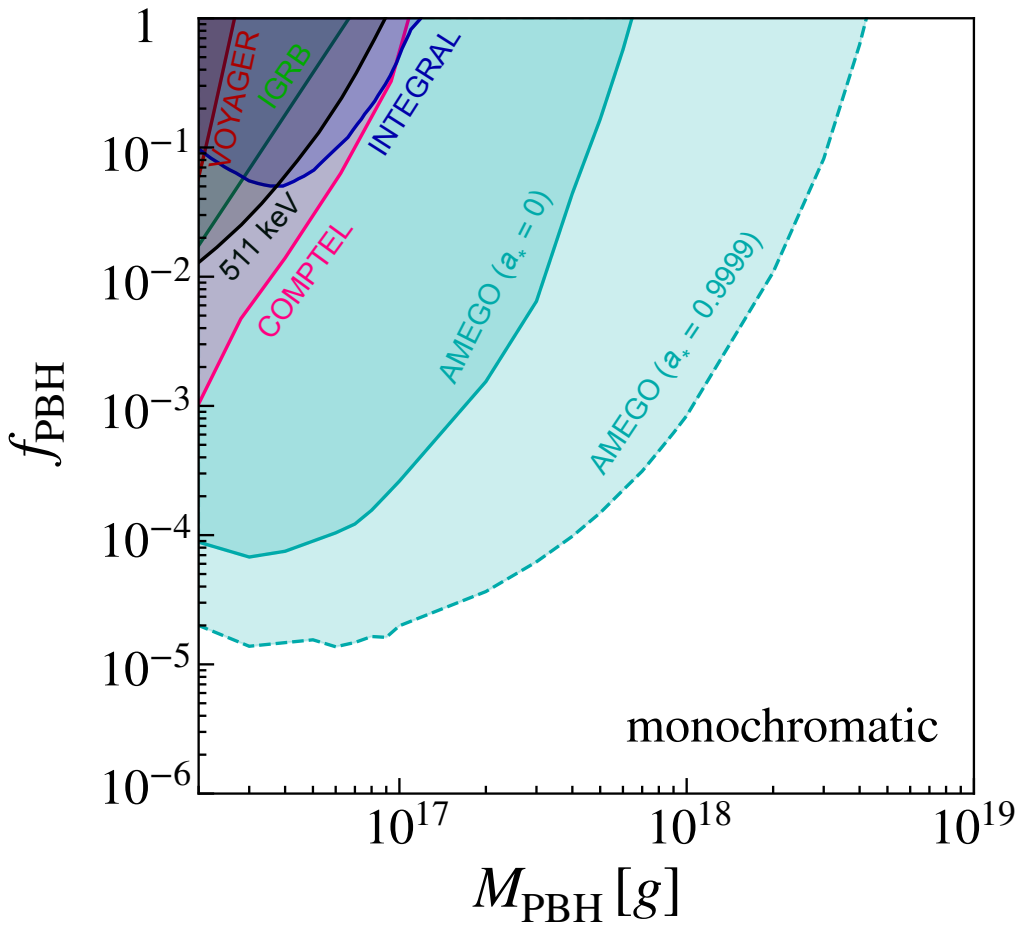

Figure 6.3: Projected upper limit (95% C.L.) on the DM fraction of PBHs, $f_{\rm PBH}$, from near future MeV telescope AMEGO. The plot corresponds to a monochromatic mass distribution of PBHs. Results for non-rotating PBHs ($a_* = 0$) and PBHs approaching to their maximal spin ($a_* = 0.9999$) are shown by the solid line and the dashed line, respectively. The constraints are derived by considering an NFW density profile of the ultra-light PBHs. The existing exclusions on ultra-light non-spinning PBHs from Voyager-1 measurement of positron flux (shaded red) [141], extra-Galactic gamma ray emission (shaded green) [83, 153, 154], SPI/INTEGRAL 511 keV emission line with 1.5 kpc positron annihilation region & isothermal DM profile (shaded black) [10, 166, 167] and INTEGRAL, COMPTEL Galactic Center MeV flux (shaded blue, shaded magenta) [155, 156] are also shown for comparison. For reference, there are no existing exclusion limits to the right of the plot until $M_{\rm PBH} \sim 10^{23}$ g [142, 184, 186].

such as INTEGRAL [368], Fermi [369], and CRGO [370] for both non-rotating and maximally rotating PBHs. The projected upper limit from AMEGO excludes non-rotating (maximally rotating, $a_* = 0.9999$) PBHs as the sole component of DM up to 7×10^{17}

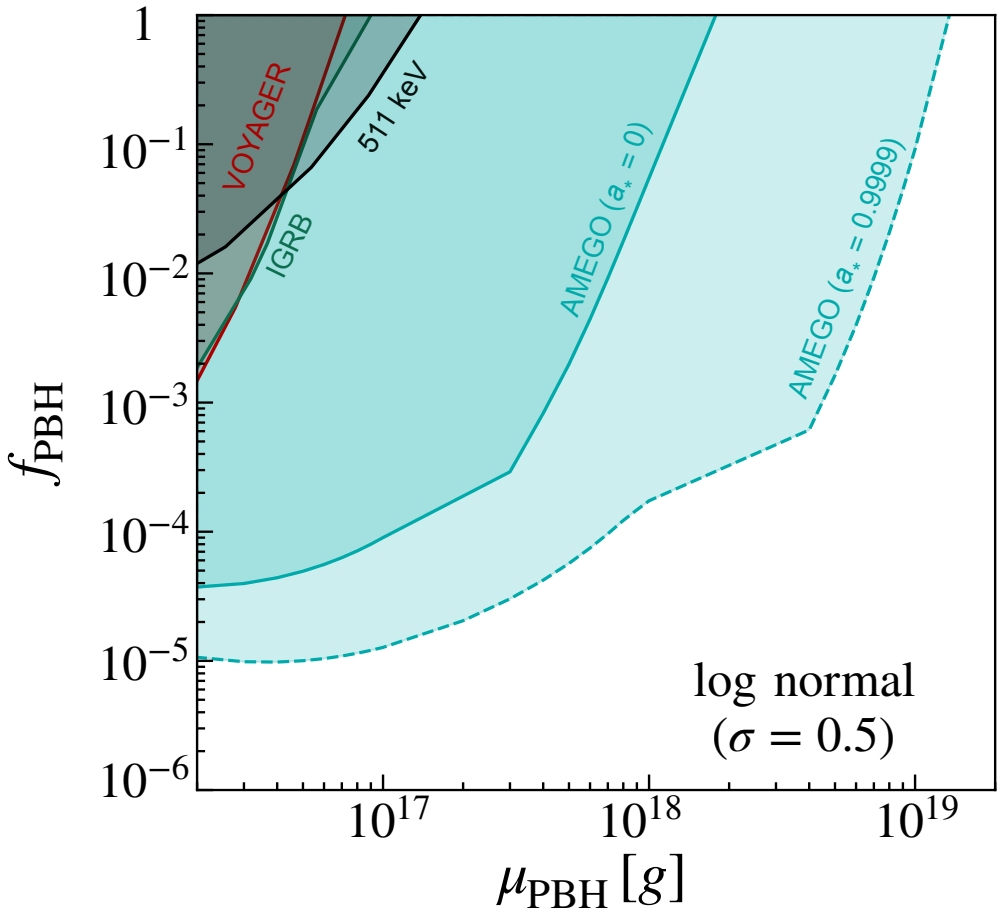

Figure 6.4: Projected upper limit (95% C.L.) on the DM fraction of PBHs, $f_{\rm PBH}$, from near future MeV telescope AMEGO. Log-normal mass distribution with a width $\sigma = 0.5$ is considered in this plot. Results for non-rotating PBHs ($a_* = 0$) and maximally rotating PBHs ($a_* = 0.9999$) are shown by the solid line and the dashed line respectively. The constraints are derived by considering an NFW density profile of the ultra-light PBHs. The existing constraints on ultra-light non-spinning PBHs from Voyager-1 measurement of positron flux (shaded red) [141], extra-Galactic gamma ray emission (shaded green) [83, 153, 154], and SPI/INTEGRAL 511 keV emission line with 1.5 kpc positron annihilation region & isothermal DM profile (shaded black) [10, 166, 167] are also shown for comparison.

g (4×10^{18} g). The kinks in the exclusion limits for both non-rotating and maximally rotating PBHs are due to finite number of mass point samplings. Our exclusion limits start from 2×10^{16} g as lighter PBHs mostly evaporate to higher-energy photons, outside our considered energy range. Quantitatively, for a non-rotating PBH of mass 10^{16} g (2×10^{16} g), $\sim 30\%$ ($\sim 97\%$) of the evaporation spectrum resides in our considered energy

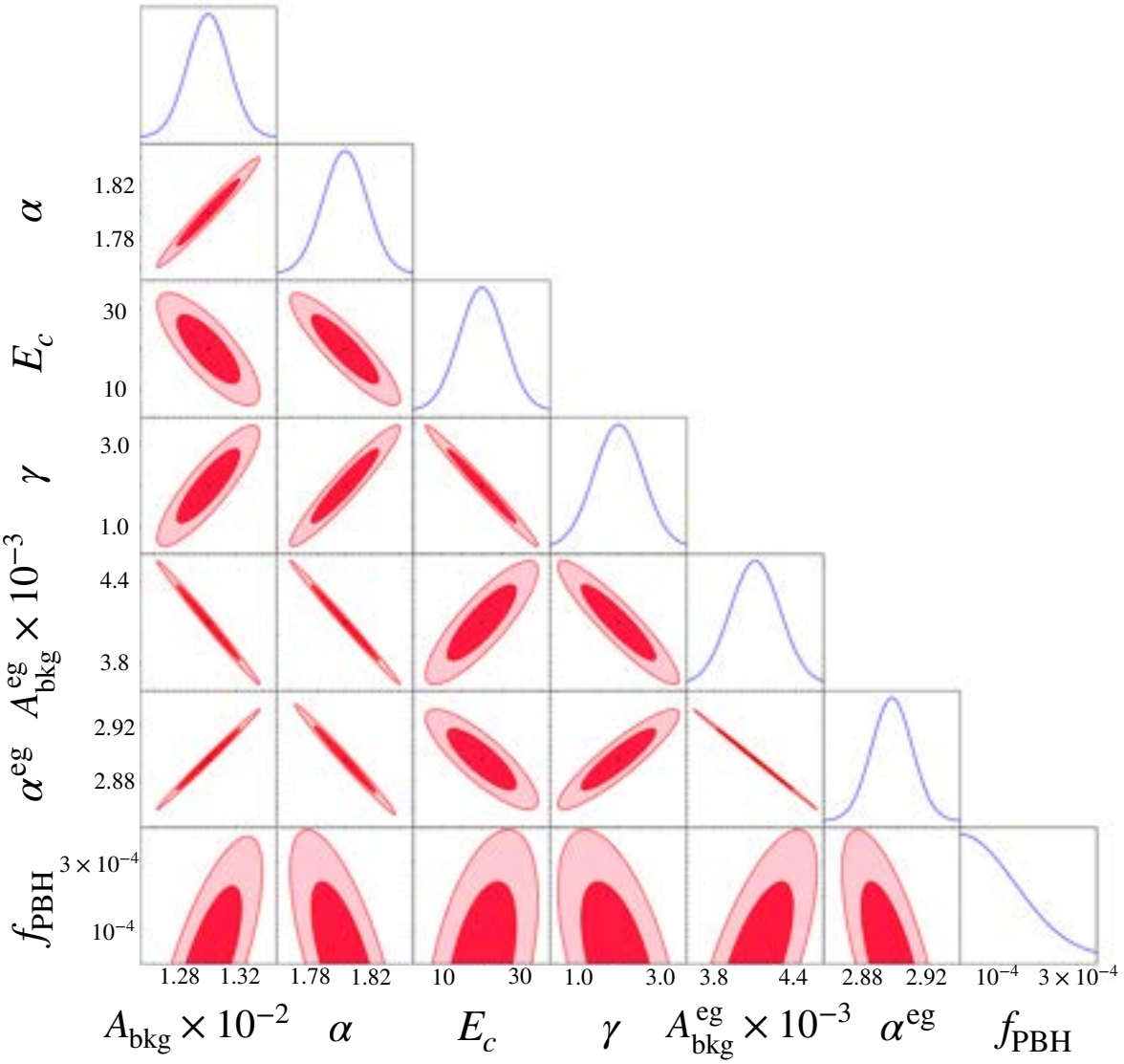

Figure 6.5: Confidence ellipses at 68.3% C.L. (1-σ, dark red) and 95% C.L. (2-σ, light red) for all background and signal parameters. A larger correlation between parameters appears as a more tilted confidence ellipse. For this corner plot we have assumed non-rotating and uncharged PBHs with a monochromatic mass distribution centered at 10^{17} g, following a NFW density profile. Black dots represent best-fit (i.e., our chosen fiducial) values of the background parameters, and we assume a fiducial $f_{\rm PBH} = 0$. The predicted posteriors for all parameters are shown by the Gaussian curves in blue.

interval, explaining the choice of 2×10^{16} g as the minimum PBH mass for this analysis. Fig. 6.4 shows the projected upper limits (95% C.L.) on DM fraction of PBHs, $f_{\rm PBH}$, that can be derived from future MeV telescope AMEGO by assuming no signal present in the data for an extended mass distribution. Log-normal mass distribution of PBHs,

a motivated scenario from several inflationary models, with a width of $\sigma = 0.5$ is considered to derive the exclusion limits. The density profile of PBHs are assumed to be NFW, however, the result degrades by at most a factor of two for cored density profiles. The solid (dashed) lines correspond to non-rotating (maximally rotating) PBHs. For this particular mass distribution, our projections exclude up to $\sim 2 \times 10^{18}$ g ($\sim 10^{19}$ g) for non-rotating (approaching maximal rotation $a_* = 0.9999$) PBHs. Similar to the monochromatic mass distributions, here also, AMEGO probes better than other proposed MeV telescopes because of its lower energy reach and larger effective area. Similar to Fig. 6.3, here also, the kinks in the exclusion limits at around 3×10^{17} g for non-rotating PBHs, and at $\sim 3 \times 10^{18}$ g for maximally rotating PBHs are due to finite number of mass point samplings.

Fig. 6.5 shows the confidence ellipses at 68.3% C.L. and 95% C.L. for all signal and background parameters. Non-rotating PBHs with a monochromatic mass distribution centered at 10^{17} g and an NFW density profile is assumed for this plot. The confidence ellipses show degeneracies among all of the parameters, and the parameters of the ellipses are computed from [371]. For example, amplitude of the Galactic background ($A_{\rm bkg}$), amplitude of the extra-Galactic background ($A^{\rm eg}_{\rm bkg}$), and the exponential cutoff energy for the Galactic background ($E_{\rm cut}$) are correlated with the signal parameter, DM fraction of PBHs ($f_{\rm PBH}$). However, power law index of the Galactic background (α), power law index of the extra-Galactic background ($\alpha^{\rm eg}$), and index of the exponential cutoff energy in the Galactic background (γ) are anti-correlated with $f_{\rm PBH}$. From the confidence ellipses, it is also evident that the correlation coefficient $r_{ij} (= \mathcal{F}^{-1}_{ij}/\sqrt{\mathcal{F}^{-1}_{ii}\mathcal{F}^{-1}_{jj}})$ between $A^{\rm eg}_{\rm bkg}$ and $f_{\rm PBH}$ ($r = 0.697$) is much stronger than the correlation between $E_{\rm cut}$ and $f_{\rm PBH}$ ($r = 0.468$). In Fig. 6.5, we also show the best fit values of all background parameters as well as their corresponding error bars by the mean and variance of the blue Gaussian curves.

6.2 Summary & Conclusions

PBHs in the asteroid-mass range, $\sim 10^{17}$ – 10^{23} g, can make up the entire DM density as the exclusion limits in this mass window are now shown to be ineffective. We propose a strategy to decisively probe a part of this parameter space. At the lower end of this mass

range, i.e., PBHs with masses $\sim 10^{17}$ g $- 10^{18}$ g have temperatures in the range of 0.01 MeV to 0.1 MeV, implying that substantial Hawking evaporated photons are produced by them around these energy scales. Near-future soft gamma-ray telescopes like AMEGO, with its large effective area and improved background rejection capabilities, can search for these photons, and investigate this hard-to-probe parameter space. The most efficient search strategy involves observations of the region around the Galactic Center. We include the Galactic astrophysical background produced by cosmic-rays and the measured extra-galactic gamma-ray background in our projected search strategy. Our projections show that AMEGO can exclude non-rotating PBHs as the sole component of DM up to $\sim 7 \times 10^{17}$ g (Fig. 6.3), and maximal rotation as well as extended mass distribution of the PBHs can explore larger PBH masses (Fig. 6.4). Here it is important to mention that the projections obtained from AMEGO not only cover the unexplored mass window where PBHs can make up the entirety of DM($> 10^{17}$ g), but also provide more stringent exclusion in the ultralight mass range of PBHs as compared to the existing exclusions. For much heavier PBHs, the Hawking radiation flux gets smaller and therefore, much larger instruments need to be built in order to detect the evaporation signature. In the absence of much larger telescopes, other techniques need to be developed in order to probe the entire asteroid-mass window of PBHs.

Note added: Ref. [156], which appeared as our work was near completion, performs a similar study for non-rotating PBHs with a monochromatic mass distribution. Our analysis differs from Ref. [156] in several key aspects (e.g., the inclusion of the extra-Galactic astrophysical background and a different region of interest in the Galactic Center), chief among them is our usage of more robust statistical treatment (Fisher analysis) to derive the projected exclusion limits on the DM fraction of ultra-light PBHs including marginalization over the astrophysical parameters. Also, very recently, Ref. [372] appeared which extends our analysis for another upcoming soft gamma-ray telescope XGIS-THESEUS.

Chapter 7

21-cm Cosmology Constrains Ultralight PBHs as DM

In this Chapter, we demonstrate that EDGES measurement of the global 21-cm signal can be translated to set a world-leading exclusion on ultralight PBHs as DM. We also derive stringent constraint on the primordial curvature power spectrum at extremely small scales under the assumption of a spherical gravitational collapse based on the Press-Schechter formalism. The results presented in this chapter can be found in [12].

7.1 21-cm Cosmology: Preliminaries

The global 21-cm signal has been proposed as a probe of Cosmic Dawn & the Epoch of Re-ionization, and is an important tool in modern cosmology. This signal arises from the hyperfine energy split between parallel and anti-parallel spin states of a hydrogen atom, and the hyperfine energy split occurs due to the interaction between proton and electron magnetic moments. The energy difference between these hyperfine energy levels corresponds to a photon of frequency 1420 MHz or wavelength of around 21 cm. The global 21 cm signal is usually represented by the differential brightness temperature measured against the background (usually cosmic microwave background, however in this analysis it is cosmic microwave background + an excess radio background) [373, 374, 375]

$$\Delta T_{\rm b} = 27 \bar{x}_{\rm HI} \left(\frac{1-Y_{\rm p}}{0.76}\right) \left(\frac{\Omega_{\rm b} h^2}{0.023}\right) \sqrt{\frac{0.15}{\Omega_{\rm m} h^2} \frac{1+z}{10}} \left(1 - \frac{T_{\rm r}}{T_{\rm s}}\right) {\rm mK}\,, \tag{7.1}$$

where $x_{\rm HI}$ is the neutral hydrogen fraction, $T_{\rm s}$ is the spin temperature, and $T_{\rm r}$ is the net background temperature (CMB temperature + an excess radio background). The spin temperature, also known as 21-cm excitation temperature, is not a real thermodynamic quantity, and is defined as the ratio of the number densities of hydrogen atoms in the two hyperfine levels

$$\frac{n_1}{n_0} = \frac{g_1}{g_0} e^{-T_*/T_{\rm s}}\,, \tag{7.2}$$

where the subscripts 0 and 1 are for 1S singlet and triplet states, respectively. g_1/g_0 denotes the ratio of the statistical degeneracy factors of the two hyperfine levels and $T_* = hc/k_B\lambda_{21} = 0.068\,{\rm K}$. Spin temperature can also be expressed as [374]

$$T_{\rm s}^{-1} = \frac{T_{\rm r}^{-1} + x_\alpha T_\alpha^{-1} + x_{\rm c} T_{\rm k}^{-1}}{1 + x_\alpha + x_{\rm c}}\,, \tag{7.3}$$

where $x_{\rm c}, x_\alpha$ are the coupling coefficients due to atomic collisions and scattering of Ly α photons, respectively. T_α denotes the color temperature of the Ly α radiation field at the Ly α frequency, and is closely coupled to the gas kinetic temperature $T_{\rm k}$. From Eq. (7.1), it is evident that an absorption signal occurs when the background temperature exceeds the spin temperature, i.e., $T_{\rm r} > T_{\rm s}$.

In the following, we briefly describe the coupling coefficients x_c and x_α.

Collisional Coupling ($x_{\rm c}$)

Atomic collisions can cause hyperfine transition in a neutral hydrogen atom and dominate the coupling in the early Universe where the gas density is high. Three main channels are available: collisions between two hydrogen atoms, collisions between a hydrogen atom and an electron, and collisions between a hydrogen atom and a proton. The collisional coupling can be written as [373]

$$x_{\rm c} = \frac{T_*\, C_{10}}{T_{\rm r} A_{10}} \tag{7.4}$$

where C_{10} is the de-excitation rate by collisions and $A_{10} = 2.85 \times 10^{-15}\,{\rm Hz}$ is the Einstein coefficient of spontaneous emission for the hyperfine transition [376]. Collisional de-excitation rate is expressed as

$$C_{10} = n_{\rm HI}\kappa_{\rm HH} + n_{\rm e}\kappa_{\rm eH} + n_{\rm p}\kappa_{\rm pH}\,, \tag{7.5}$$

where n_i is the number density of species i and $\kappa_{i\mathrm{H}}$ is the reaction rate between the species i and neutral hydrogen atom. We use the following values of $\kappa_{i\mathrm{H}}$ for this analysis

$$\kappa_{\mathrm{HH}} = 3.1 \times 10^{-17} T_{\mathrm{k}}^{0.357} e^{-32/T_{\mathrm{k}}}\,, \tag{7.6a}$$

$$\log_{10}\kappa_{\mathrm{eH}} = \begin{cases} -15.607 + \frac{1}{2}\log_{10} T_{\mathrm{k}} \cdot \exp\left[-(\log_{10} T_{\mathrm{k}})^{4.5}/1800\right] \text{ if } T_{\mathrm{k}} < 10^4 \\ -14.102 \text{ if } T_{\mathrm{k}} \geq 10^4\,, \end{cases} \tag{7.6b}$$

$$\kappa_{\mathrm{pH}} = 10^{-16}\left[4.28 + 0.24\log_{10} T_{\mathrm{k}} - 1.37\log_{10}^2 T_{\mathrm{k}} + 0.53\log_{10}^3 T_{\mathrm{k}}\right]\,, \tag{7.6c}$$

where T_{k} denotes the gas kinetic temperature.

Ly α Coupling (x_{k})

The Ly α photons produced by the first galaxies indirectly affect the spin temperature through a process known as the Wouthuysen-Field effect [377, 378]. Accurate modeling of this coupling is essential at Cosmic Dawn because it is the Ly α coupling that makes the 21-cm signal observable. The expression for the Ly α coupling can be written as

$$x_\alpha = (1 - \delta_\alpha)\frac{J_\alpha}{J_0}\,, \tag{7.7}$$

where δ_α represents a distortion in the Ly α background due to its interaction with the neutral hydrogen atom. It is given by [379]

$$\delta_\alpha = {}_3F_0(1/3, 2/3, 1; 0; -\xi_1)\,, \tag{7.8}$$

where

$$\xi_1 = \frac{9\pi}{4a\tau_\alpha\eta^3}\,, \tag{7.9}$$

and ${}_3F_0$ being the $(3,0)-$hyper-geometric function. The parameters in ξ_1 are [380, 381]

$$a = \frac{A_\alpha}{4\pi\nu_\alpha}\sqrt{\frac{m_{\mathrm{H}}c^2}{2k_{\mathrm{B}}T_{\mathrm{k}}}}\,, \tag{7.10a}$$

$$\tau_\alpha = \frac{3}{8\pi}\frac{A_\alpha}{H} n_{\mathrm{HI}}\lambda_\alpha^3\,, \tag{7.10b}$$

$$\eta = \frac{h/\lambda_\alpha}{\sqrt{2m_{\mathrm{H}}k_{\mathrm{B}}T_{\mathrm{k}}}}\,, \tag{7.10c}$$

respectively. Here $A_\alpha = 6.25 \times 10^8\,\mathrm{Hz}$ is the Einstein spontaneous emission coefficient of Ly α transition, m_H is the mass of hydrogen, and $\lambda_\alpha(\nu_\alpha)$ is the wavelength (frequency) of the Ly α photon.

$J_0 = 5.54 \times 10^{-8}\,(T_\mathrm{r}/2.725\,\mathrm{K})$ is a combination of fundamental constants and background temperature, and J_α denotes the undisturbed Ly α specific intensity. It can be written as [382]

$$J_\alpha(z) = \frac{c}{4\pi}(1+z)^2 \sum_{n=2}^{23} P_n \int_z^{z_\mathrm{max}} \frac{\epsilon_\alpha(E'_n, z')}{H(z')}\, dz'\,, \tag{7.11}$$

where ϵ_α denotes the co-moving emissivity. The n^th term in the sum accounts for the finite probability P_n with which a photon in the upper Lyman line will redshift to Ly α wavelength. The values of P_n are computed in an iterative fashion using the selection rule and the decay rates. A detailed procedure and table of values for P_n can be found in [383, 384]. The red-shifted energy of n^th Lyman series line is given by

$$E'_n = E_n \frac{1+z'}{1+z}\,, \tag{7.12}$$

where E_n is the energy of the photon released in transition from n^th state to ground state. The maximum redshift from which this photon could have been received is given by

$$1 + z_\mathrm{max} = \frac{E_{n+1}}{E_n}(1+z) = \frac{1-(1+n)^{-2}}{1-n^{-2}}(1+z)\,. \tag{7.13}$$

Next we describe the time evolution of the 21-cm signal, as shown in Fig. 7.1

- $200 \leq z \leq 1100$: The residual free electron fraction left after recombination allows Compton scattering to maintain thermal coupling of the gas to the CMB, implying $T_\mathrm{r} = T_\mathrm{k}$. On the other hand, the high gas density leads to effective collisional coupling so that $T_\mathrm{s} = T_\mathrm{k}$, and hence $\Delta T_\mathrm{b} = 0$, no detectable 21 cm signal.

- $40 \leq z \leq 200$: In this regime, the gas cools adiabatically, $T_\mathrm{k} \propto (1+z)^2$, thus falling faster than the background temperature as $T_\mathrm{r} \propto (1+z)$. This implies that $T_\mathrm{k} < T_\mathrm{r}$. Collisional coupling still prevailed, and as a result we get $T_\mathrm{s} = T_\mathrm{k} < T_\mathrm{r}$, and hence $\Delta T_\mathrm{b} < 0$. We have the first absorption trough.

- $z_* \leq z \leq 40$: As the Universe expands, gas density decreases, and collisional

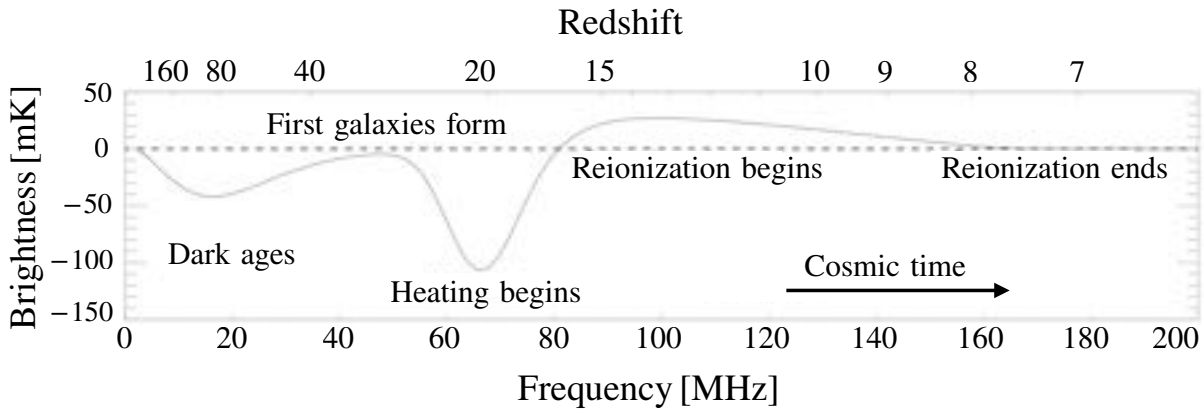

Figure 7.1: Expected evolution of the sky-averaged 21-cm brightness temperature $\Delta T_{\rm b}$ from the "dark ages" (at $z \sim 200$) to the end of re-ionization ($z \sim 6$). Solid curve indicates the 21-cm signal, and the dashed curve indicates zero signal, i.e., $\Delta T_{\rm b} = 0$. This figure is taken from Ref. [374].

coupling becomes no longer effective. It implies $T_{\rm s} = T_{\rm r}$, and hence $\Delta T_{\rm b} = 0$, no detectable 21 cm signal.

- $z_\alpha \leq z \leq z_*$: Once the first stars are formed at z_* ($z_* \sim 30$), they emit Ly α photons, heating up the gas, and creates 21-cm transition. Because of this Ly α coupling, the spin temperature tracks the gas kinetic temperature, $T_{\rm s} \sim T_{\rm k} < T_{\rm r}$. This results in the second absorption trough, and its depth depends on various uncertain astrophysical parameters. Recently, EDGES collaboration has reported the first, and till date the only measurement of this absorption trough [385]. The key features of this absorption signal are its location (78.2 MHz, corresponding to $z = 17.2$), amplitude ($\Delta T_{\rm b} = -500\,{\rm mK}$), and the full width at half maximum (19 MHz). The most interesting part of this detected signal is the amplitude, which is found to be more than double the prediction of even the most optimistic theoretical models.

- $z \leq z_\alpha$: After the second absorption trough, Ly α coupling saturates. By this point, heating becomes significant, and the gas is heated everywhere so that $T_{\rm k} = T_{\rm r}$, and we do not have any further 21-cm absorption signal. However, due to X-ray heating, there is 21-cm emission signal which eventually end after re-ionization because the neutral hydrogen fraction ($x_{\rm HI}$) after re-ionization vanishes.

In the following sections, we utilize the recent measurement of the global 21-cm signal (the second absorption trough) by the EDGES collaboration [385] to set a stringent exclusion on ultralight PBHs as DM.

7.2 Excess Radio Background

In order to match the EDGES measurement of the global 21-cm signal, we have considered an excess radio background. This excess radio background is uniformly distributed in the sky, and fits very well by a power law as observed by ARCADE 2 and LWA1 [386, 387]. Because of this excess radio background, the net background temperature is essentially a sum of the CMB temperature and an excess radio measured today at frequency ν

$$T_{\rm r}(\nu) = T_0 + T_{\rm R}\left(\frac{\nu}{\nu_0}\right)^{\beta} . \tag{7.14}$$

In Eq. 7.14, $T_0 = 2.725\,\mathrm{K}$ denotes the CMB temperature measured today, $T_{\rm R} = 24.1\,\mathrm{K}$, $\beta \approx -2.6$, and reference frequency $\nu_0 = 310\,\mathrm{MHz}$ [387].
Generalizing the above for an earlier epoch at redshift z and measurement made for the frequency corresponding to 21-cm line (red-shifted to z, i.e., $\nu = \nu_{21}/(1+z)$) we get [388, 389]

$$T_{\rm r}(z) = 2.725(1+z)\left[1 + 0.169\,\zeta_{\rm ERB}(1+z)^{2.6}\right] , \tag{7.15}$$

where we have parameterized the amplitude of excess radio background by $\zeta_{\rm ERB}$. We vary $\zeta_{\rm ERB}$ between 0.01 and 1. Note that, $\zeta_{\rm ERB} = 1$ represents the base value corresponding to the excess observed by ARCADE 2.

7.3 Constraining Ultralight PBHs as DM via 21-cm Cosmology

7.3.1 Heating and Ionization due to PBHs

Ultralight PBHs, i.e., PBHs in the mass range of $10^{15} - 10^{17}\,\mathrm{g}$, emit particles via Hawking evaporation, and the spectrum of the emitted particles follow a blackbody like distribution, as detailed in Section 5.1. These Hawking radiated particles (photons, neutrinos,

and electrons/positrons) can interact with the ordinary baryonic matter in the intergalactic medium (IGM), providing an additional heating and ionization in the IGM. Since, the amplitude of the global 21-cm signal depends on the temperature and ionization of the IGM, Hawking emission from ultralight PBHs causes a damping in the global 21-cm signal, and hence, can be probed via 21-cm observations. Note that, unlike the other probes that are mentioned in the previous chapters, this cosmological probe uses all emission channels from PBHs simultaneously, making it a particularly interesting one.

The energy deposition by the Hawking emitted particles typically occurs through five different channels which include hydrogen ionization, helium ionization, hydrogen excitation, IGM heating and sub-10.2 eV continuum photons [390, 391]. However, for this analysis, only hydrogen ionization and IGM heating are relevant. For a monochromatic mass distribution of PBHs, the deposited energy per unit volume per unit time in a particular channel c (where, $c \in$ Heating, Ionization) can be written as

$$\left.\frac{d^2E}{dVdt}\right|_c = \frac{f_{\rm PBH}\rho_{\rm DM}}{M_{\rm PBH}} \int dE \left[f_c\left(E_\gamma, z\right) E_\gamma \frac{d^2N_\gamma}{dEdt} + 2 f_c\left(E_e - m_e c^2, z\right)\left(E_e - m_e c^2\right) \frac{d^2N_e}{dEdt} \right], \tag{7.16}$$

where $f_c(E_K, z)$ denotes the ratio of the energy deposited into channel c to the injected energy as a function of the kinetic energy of the emitted particle E_K and redshift z. We use the numerical data table of f_c corresponding to DM decay from Ref. [390] which are in close agreement with that of Ref. [391]. The neutrino emission is not included in the analysis as it is negligible, and the factor of 2 counts the contributions from electron and positron emission. $\rho_{\rm DM}$ denotes the average DM density of the Universe, and is taken from [4]. Note that, $\left.\frac{d^2E}{dVdt}\right|_c$ is almost independent of the redshift because for $M_{\rm PBH} > 10^{15}\,$g, the mass loss of PBHs due to Hawking emission is negligible, and f_c has a very weak dependence on z for the range considered in this work.

We use BlackHawk to compute the particle spectrum from evaporating PBHs, and by using the spectrum, we estimate the additional heating and ionization of the IGM from Eq. (7.16). We then utilize the full shape information of the recent measurement of the global 21-cm signal by EDGES collaboration [385] to set the constraint on ultralight PBHs as DM.

Here, it is important to mention that the previously published analysis on this topic [178] only used a central location of the 21-cm absorption feature ($z = 17$), whereas, in this

analysis we use the full spectral shape of the EDGES data ($28 \geq z \geq 14$), thus capturing *all* the relevant features of the observed signal. Besides, we improve upon the previously published analysis [178] by considering a more detailed model of the known astrophysical phenomena that affect the global 21-cm signal. We use an MCMC-enabled Bayesian analysis to derive our constraints. This also allows us to study the covariance of PBH parameters with other astrophysical processes affecting the 21-cm signal.

7.3.2 Inference Procedure

We now describe the inference procedure that is being used in our analysis. Here, we follow a Bayesian procedure with a Gaussian likelihood. We use the full information content in the EDGES data[1] by using their measurements at all of 123 redshift points, rather than focusing on some specific features of the signal.

Let $\Delta T_{\rm b}^{\rm exp} = \Delta T_{\rm b}^{\rm exp}(z)$ and $\Delta T_{\rm b}^{\rm theo} = \Delta T_{\rm b}^{\rm theo}(\theta, z)$ represent the data and the model values, respectively, of the 21-cm signal at redshift z. θ denotes the set of n parameters that describe our model. Our likelihood is then

$$\mathcal{L}(\Delta T_{\rm b}^{\rm exp}|\theta) = \prod_{i=1}^{123} \frac{1}{\sqrt{2\pi}\varepsilon_i} \exp\left[-\frac{\left(\Delta T_{\rm b}^{\rm exp} - \Delta T_{\rm b}^{\rm theo}\right)_i^2}{2\varepsilon_i^2}\right], \tag{7.17}$$

where ε_i are the $1\,\sigma$ uncertainties in the data for the redshift bin i. The label i in the above equation runs over the 123 data points corresponding to the different redshift bins. We take a constant uncertainty for all the redshift bins, i.e., $\varepsilon_i = 0.05\,\mathrm{K}$ for $i = 1, ..., 123$. Some remarks are in order about this. In the result presented by the EDGES collaboration [385], the uncertainty is presented only for $z = 17$. This uncertainty estimate is not useful if one intends to infer constraints using the full frequency range of the EDGES data. This problem has been noted before, and in response, several works have inferred the uncertainties for the entire frequency range of the EDGES data. For example, Ref. [392] provide an uncertainty estimate of $0.025\,\mathrm{K}$ at all frequencies within the EDGES band. See also Ref. [393], where a frequency-independent $0.025\,\mathrm{K}$ uncertainty is considered, or Ref. [394], where a frequency-independent $0.01\,\mathrm{K}$ uncertainty throughout the EDGES band is considered. Since an important motivation in our work is to use the full spectral information of the EDGES data, we follow the same approach, albeit with a slightly more

[1] http://loco.lab.asu.edu/edges/edges-data-release/

Parameter	Description	Min	Max
$\log_{10} f_\alpha$	Controls the strength of Ly α background	-2	2
$\log_{10} T_{\rm vir,4}$	Minimum virial temperature of dark matter halos	-0.75	1.25
$\log_{10} f_{\rm X}$	Controls the strength of X-ray background	-1	1
$\log_{10} \zeta_{\rm ERB}$	Controls the strength of excess radio	-2	0
$\log_{10} f_{\rm PBH}$	Fraction of DM in the form of PBHs	–	–

Table 7.1: Model parameters used in this work, with the ranges of values over which uniform prior probability distribution functions are used. The range of values for $\log_{10} f_{\rm PBH}$ depends on the mass of PBH under consideration (see text for more detail).

conservative estimate, setting all $\varepsilon_i = 0.05\,\mathrm{K}$. Note that, by choosing all $\varepsilon_i = 0.025\,\mathrm{K}$ will not change any of our constraints, except to slow down the MCMC convergence.

We choose uniform priors on our model parameters in the ranges mentioned in Table 7.1. Note that, the prior on $\log_{10} f_{\rm PBH}$ changes with PBH mass. For example, in the presence of X-ray heating, the prior required for a PBH of mass $10^{15}\,\mathrm{g}$ is $[-11.0, -9.0]$, while that for a PBH of mass $10^{16}\,\mathrm{g}$ is $[-6.5, -3.0]$. This choice of a mass-dependent prior might appear odd, but it merely reflects the fact that large values of $\log_{10} f_{\rm PBH}$ are obviously ruled out due to the enormous heating rates. One could in principle choose a wide prior, such as $[-11, 0]$, for all masses. But this would waste considerable computational effort. For example, for a $10^{15}\,\mathrm{g}$ PBH, the best-fit value of $f_{\rm PBH}$ is $\sim 10^{-9}$, so exploring $f_{\rm PBH}$ up to 1 for this mass would imply heating rate higher by nine orders of magnitude which is clearly ruled out by the EDGES observation.

In Fig. 7.2, we qualitatively demonstrate the impact of five model parameters that are tabulated in Table 7.1 on the global 21-cm signal.

(a) Ly α photons affect the 21-cm signal via two effects, heating and coupling. A higher value of f_α implies a stronger background, which in turn means more heating but also a stronger coupling. Heating reduces the absorption feature, whereas, stronger

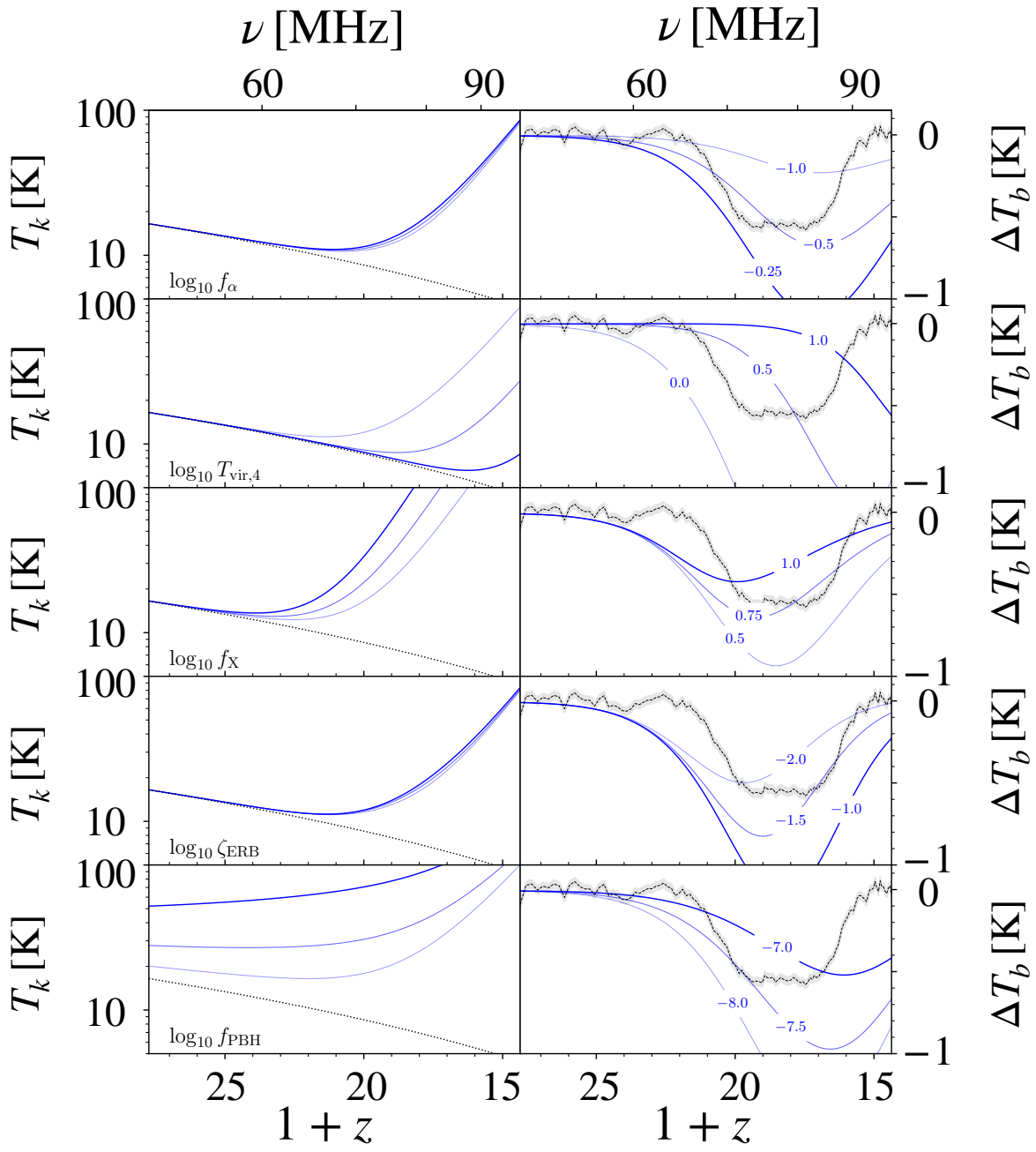

Figure 7.2: Gas temperature $T_{\rm k}$ evolution (left column), and the corresponding 21-cm signal $\Delta T_{\rm b}$ (right column) for a range of parameter values. For reference, we show the adiabatic thermal evolution in all panels of the left column, and the EDGES measurement of the 21-cm signal in all panels of the right column. In each row, a single parameter is varied, while the remaining parameters are held fixed at 0, unless one of these fixed parameters is $\log_{10} f_{\rm PBH}$. When $\log_{10} f_{\rm PBH}$ is held fixed, it is assigned a value of -10, and a PBH mass of 10^{15} g is assumed.

coupling produces a deeper absorption feature. However, the latter dominates since Ly α heating is not a very efficient heating mechanism, and is evident from the first panel.

(b) When the minimum virial temperature is smaller, more star forming halos are allowed, and thus more star formation rate density (SFRD). This results in a stronger Ly α coupling, resulting in a deeper 21-cm signal. But the more important role of this parameter is to change the timing of the first drop in the signal without affecting the shape.

(c) As $f_{\rm X}$ takes higher values, the X-ray background gets stronger which implies more X-ray heating. This in turn raises the gas temperature $T_{\rm k}$, and hence the spin temperature $T_{\rm s}$, thus reducing $\Delta T_{\rm b}$.

(d) When we increase the excess radio background strength, $\zeta_{\rm ERB}$, we allow more excess radio background, and hence, a stronger contrast between the 21-cm brightness and the background, thus producing a deeper absorption signal.

(e) Higher $f_{\rm PBH}$ imply more number of PBHs, and therefore, more heating, which in turn reduces the 21-cm signal. We take the PBH mass of $10^{15}\,$g for this plot.

With the likelihood and priors, we can construct the posterior distribution by using the Bayes theorem

$$P(\theta|\Delta T_{\rm b}^{\rm exp}) \propto \mathcal{L}(\Delta T_{\rm b}^{\rm exp}|\theta)\mathcal{P}(\theta)\,, \tag{7.18}$$

where $\mathcal{P}(\theta)$ represents the prior distribution. Since we use a MCMC implementation [395] for sampling $P(\theta|\Delta T_{\rm b}^{\rm exp})$, the normalization of the above is unnecessary. To explore the nD parameter space, we use the publicly available code `emcee`[2] [396]. We run 64 Markov chains (number of 'walkers'), and 5000 steps for each parameter, which is a reasonable length since the auto-correlation time for any parameter is not more than ~ 50. We obtain the initial guess for parameters by maximizing $\mathcal{L}(\Delta T_{\rm b}^{\rm exp}|\theta)$ when treated as a function of θ. The thermalization time (number of burn-in steps) is less than 100. Once we have obtained the parameter set, $\theta_{\rm BF}$, which best explain the model, we test the goodness-of-fit by the reduced chi-squared statistics given by $\chi^2/{\rm dof}$. The standard definition of χ^2 is

[2] https://github.com/dfm/emcee.

given by

$$\chi^2 = \sum_{i=1}^{123} \frac{\left[\Delta T_{\rm b}^{\rm exp}(z_i) - \Delta T_{\rm b}^{\rm theo}(\theta_{\rm BF}, z_i)\right]^2}{\varepsilon_i^2}\,, \tag{7.19}$$

where 'dof' stands for degrees of freedom, and is equal to the number of data points minus the number of free parameters employed in the model.

Note that calculating $\Delta T_{\rm b}^{\rm theo}$ for any set of parameters during an MCMC simulation can be time-consuming and expensive. To overcome this difficulty, we prepare our $\Delta T_{\rm b}^{\rm theo}$ at some specific grid points in the nD space of parameters before running MCMC sampler. With these pre-calculated $\Delta T_{\rm b}^{\rm theo}$s we can then estimate $\Delta T_{\rm b}^{\rm theo}$ at the desired intermediate parameter set using multi-dimensional linear interpolation. If we have p number of evenly spaced points in each of the n dimensions, then we have a total of p^n number of models.

As the X-ray emissivity at Cosmic Dawn is unknown, it is interesting to consider PBHs as the sole heating mechanism that terminates the 21-cm absorption signal. We therefore consider two distinct scenarios for our inference: one without X-ray heating and the other with X-ray heating. In the following subsections, we give the details of our analysis for these two cases. We aim to probe the fraction of DM that is in the form of PBHs, $f_{\rm PBH}$, for several values of PBH masses for these two distinct scenarios.

Case 1: assuming X-ray heating is absent

In the absence of any X-ray heating, the four components that affect the global 21-cm signal are star formation rate density (SFRD), Ly α coupling, heating due to Hawking emission, and excess radio background (ERB). Therefore, the total number of degrees of freedom, dof, is $123 - 4 = 119$, and our model parameters are

$$\theta = \{\log_{10} f_\alpha,\ \log_{10} T_{\rm vir,4},\ \log_{10} \zeta_{\rm ERB},\ \log_{10} f_{\rm PBH}\}\,. \tag{7.20}$$

We choose $p = 9$ points for each of these parameters, so that we have a total of $9^4 = 6561$ models explored. However, note that an MCMC simulation with all the parameters varying is not required for each mass. We need to run the 4-parameter MCMC for just one mass, say $M_{\rm PBH} = 10^{15}$ g, to obtain the best-fitting parameters. Once this is done, we can fix all parameters other than $f_{\rm PBH}$, i.e., $T_{\rm vir}$, f_α and $\zeta_{\rm ERB}$ to their best-fitting values so that for the remaining masses we have only one parameter to vary. The reason for this

preferred method of analysis stems from the fact that the additional heating/ionization due to PBHs is almost redshift independent.

Case 2: allowing for X-ray heating

Four out of the five parameters are the same as before, and the new parameter is the strength of the X-ray background. The total number of degrees of freedom, dof, is $123 - 5 = 118$, and our models parameters are

$$\theta = \{\log_{10} f_\alpha,\ \log_{10} T_{\rm vir,4},\ \log_{10} f_{\rm X},\ \log_{10} \zeta_{\rm ERB},\ \log_{10} f_{\rm PBH}\}\,. \tag{7.21}$$

We choose $p = 5$ points for each of these parameters, so that we have a total of $5^5 = 3125$ models explored. Similar to case 1, we need not run the 5-parameter MCMC simulation for all PBH masses. Once we have obtained the best-fitting parameter values of the non-PBH parameters, we can set all of them to those values for the remaining PBH masses. Note that, in case 2, we only obtain an upper bound on $f_{\rm PBH}$. But in case 1, we obtain a best fit value of $f_{\rm PBH}$, implying a detection. This simply comes from the fact that, in case1, there are no alternative heating sources that can result in the low-redshift rising edge of the 21-cm absorption profile. Case 2 is arguably more conservative, as some X-ray emission is perhaps easily plausible at these redshifts. However, until such high-redshift X-ray sources are conclusively known to exist, case 1 remains a viable alternative.

7.3.3 Results

Case 1: assuming X-ray heating is absent

Our marginalized two-dimensional, and one-dimensional posterior distributions are shown in Fig. 7.3. The best-fitting parameter values with 90% confidence intervals, for a PBH of mass $M_{\rm PBH} = 10^{15}\,{\rm g}$, are respectively

$$\log_{10} f_\alpha = 0.9964^{+0.0057}_{-0.0164}\,, \tag{7.22}$$

$$\log_{10} T_{\rm vir,4} = 0.2526^{+0.0111}_{-0.0039}\,, \tag{7.23}$$

$$\log_{10} \zeta_{\rm ERB} = -0.9998^{+0.0189}_{-0.0187}\,, \tag{7.24}$$

$$\log_{10} f_{\rm PBH} = -6.8398^{+0.0199}_{-0.0192}\,. \tag{7.25}$$

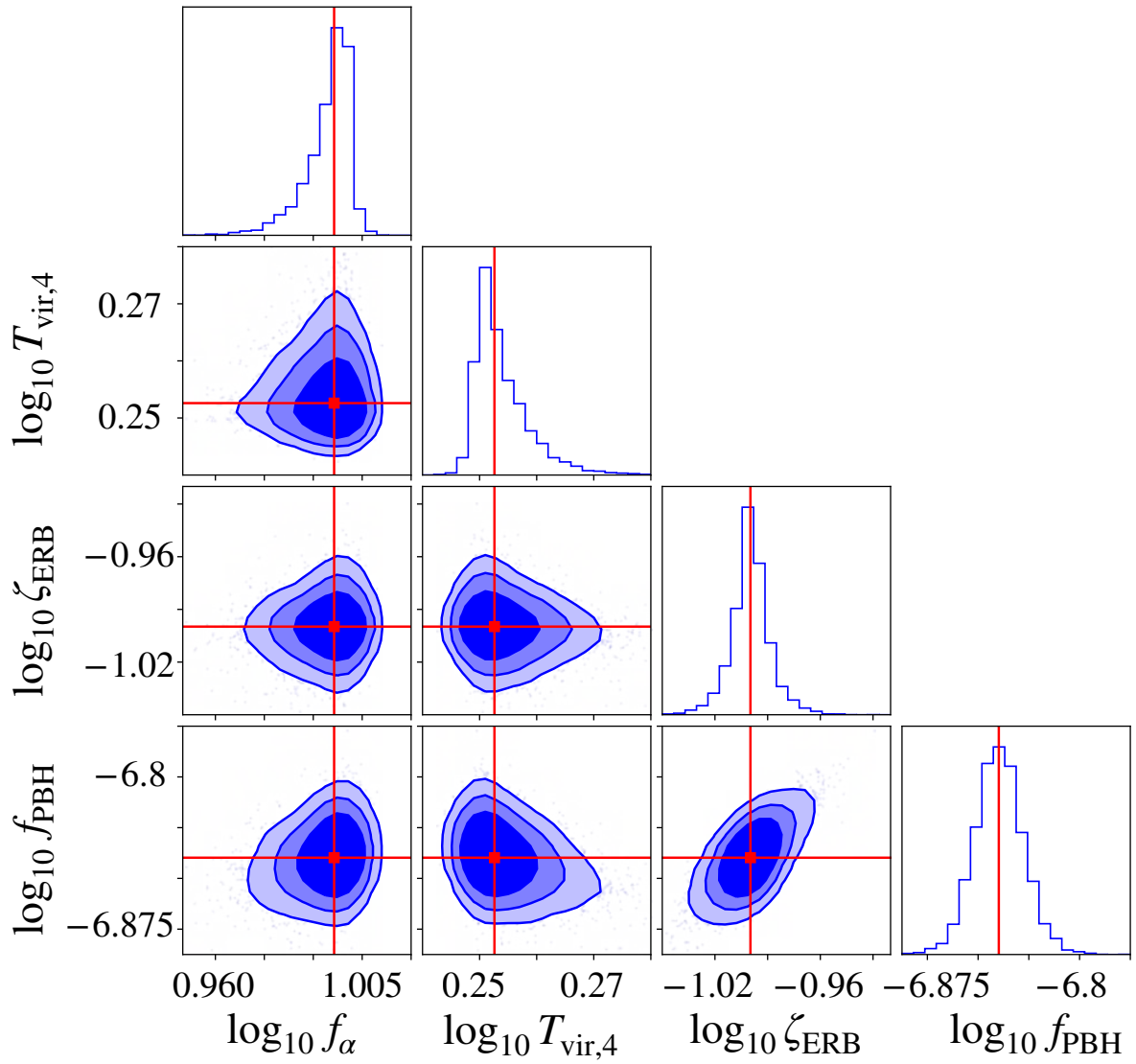

Figure 7.3: Two-dimensional and one-dimensional marginalized posterior probability distributions of parameters for a PBH of mass $M_{\rm PBH} = 10^{15}\,{\rm g}$ in a model with no X-ray heating. The contour lines show the 68.3%, 86.6% and 95.5% levels corresponding to 1-sigma, 1.5-sigma and 2-sigma, respectively. The red lines show the median values.

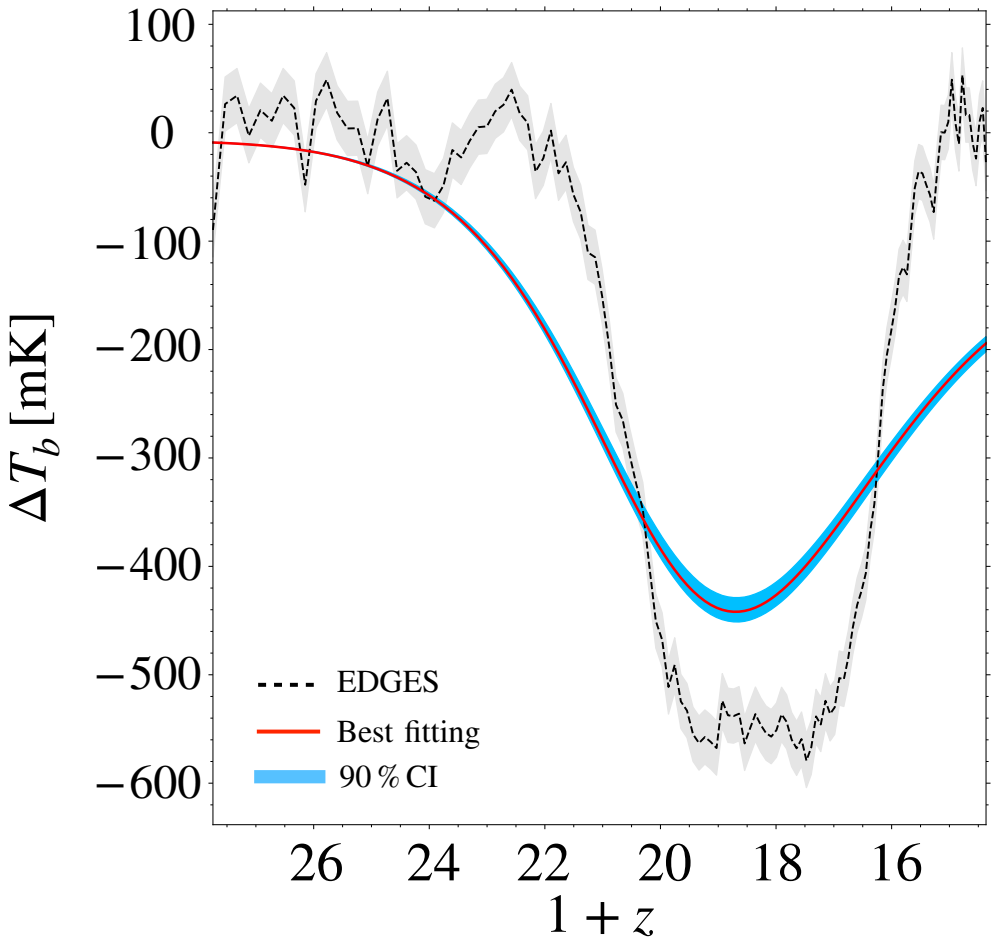

Figure 7.4: Red curve shows the derived posterior median 21-cm signal in the absence of an X-ray background. The blue shaded region shows the 90% confidence intervals. This is for PBH of mass 10^{15} g, and corresponds to $\log_{10} f_{\rm PBH} = -6.8398^{+0.0199}_{-0.0192}$. The EDGES measurement is shown by the black dashed curve, with the gray shaded region around it showing the uncertainty. The goodness-of-fit is $\chi^2/\text{dof} = 910.5/119$.

The best-fitting 21-cm signal, 90% confidence interval, and its comparison with the EDGES measurement are shown in Fig. 7.4 for PBHs of mass $10^{15}\,\mathrm{g}$. Using the definition of goodness-of-fit given in Eq. (7.19) we get $\chi^2/\mathrm{dof} = 910.5/119$. For discussion, we can divide the EDGES measurement of the global 21-cm signal into three regions: A, B and C. These three regions correspond to the regions on the left of the absorption, the absorption itself, and the right side of the absorption, respectively. We see that there is some residual gap in the best-fitting curve, and the measurement in all A, B and C. Other parameters being fixed, decreasing f_{PBH} may give the correct absorption depth but will increase the errors in regions A and C. On the other hand if we increase f_{PBH} we get better fits in A and C but with increased error in B. Thus, we see that there is an optimum value of f_{PBH} with best fits the signal given some uncertainty ε. A similar reasoning applies for other parameters as well.

Case 2: allowing for X-ray heating

We now discuss the case 2 results where X-ray heating is present. The best-fitting parameter values for a PBH of mass $M_{\mathrm{PBH}} = 10^{15}\,\mathrm{g}$, are respectively

$$\log_{10} f_\alpha = 0.0207^{+0.0073}_{-0.0071}\,, \tag{7.26}$$

$$\log_{10} T_{\mathrm{vir},4} = 0.2501^{+0.0018}_{-0.0016}\,, \tag{7.27}$$

$$\log_{10} f_{\mathrm{X}} = 0.5007^{+0.0076}_{-0.0069}\,, \tag{7.28}$$

$$\log_{10} \zeta_{\mathrm{ERB}} = -1.2666^{+0.0224}_{-0.0246}\,. \tag{7.29}$$

The best-fitting 21-cm signal corresponding to the parameters above, 90% confidence interval, and its comparison with the EDGES measurement of the global 21-cm signal are shown in Fig. 7.5 for PBHs of mass $10^{15}\,\mathrm{g}$. Using the definition of goodness-of-fit given in Eq. (7.19) we get $\chi^2/\mathrm{dof} = 295.3/118$. The data thus prefer the model in which X-ray heating is accompanied by the heating due to PBH evaporation. The marginalized two-dimensional and one-dimensional posterior distributions for PBH mass of $M_{\mathrm{PBH}} = 10^{15}\,\mathrm{g}$ is shown in Fig. 7.6. We see that in the presence of X-rays, only an upper bound is obtained on f_{PBH}, and we quantify our upper bound by choosing the 95% levels of the probability distribution of $\log_{10} f_{\mathrm{PBH}}$.

On comparing the best-fitting parameters for the two cases that are only related to setting

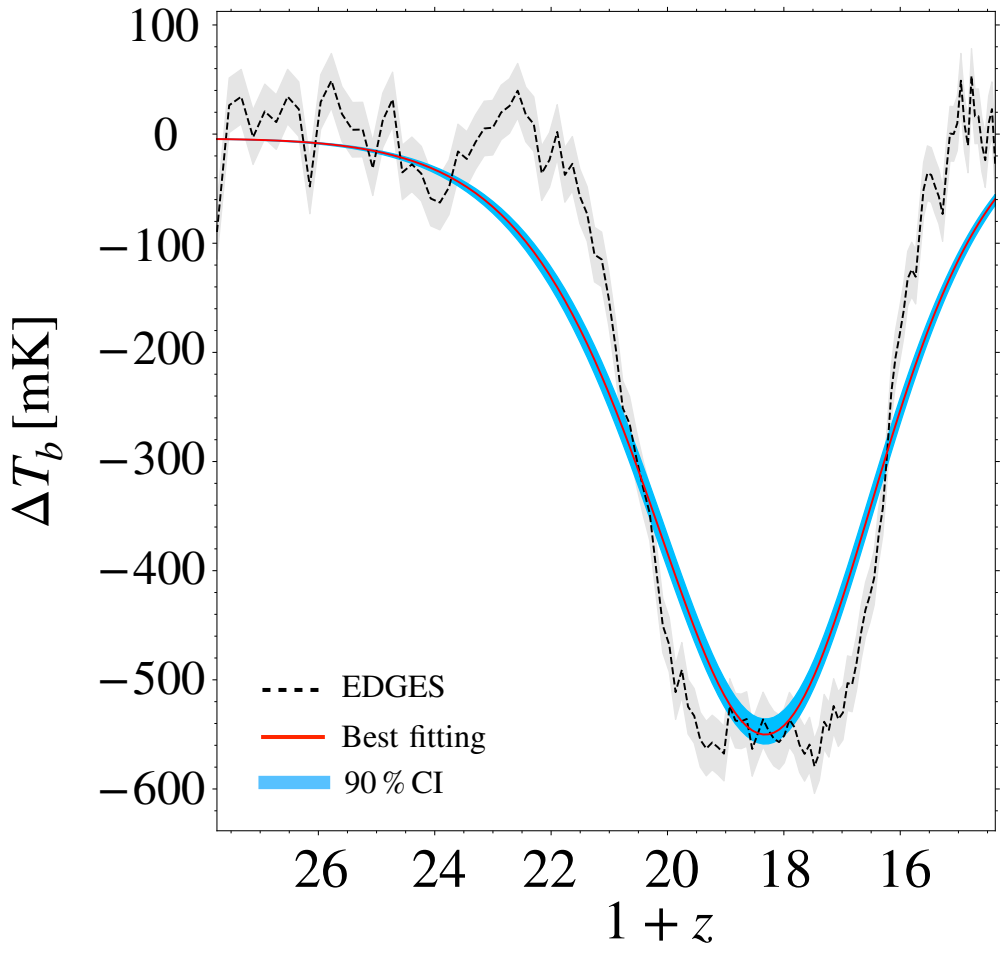

Figure 7.5: Red curve shows the derived posterior median 21-cm signal in the presence of an X-ray background. The blue shaded region shows the 90% confidence intervals. This is for PBH of mass 10^{15} g, and corresponds to $f_{\rm PBH} = 10^{-9.73}$ (95% level). The EDGES measurement is shown by the black dashed curve, with the gray shaded region around it showing the uncertainty. The goodness-of-fit is $\chi^2/{\rm dof} = 295.3/118$, which is much better compared to case I result.

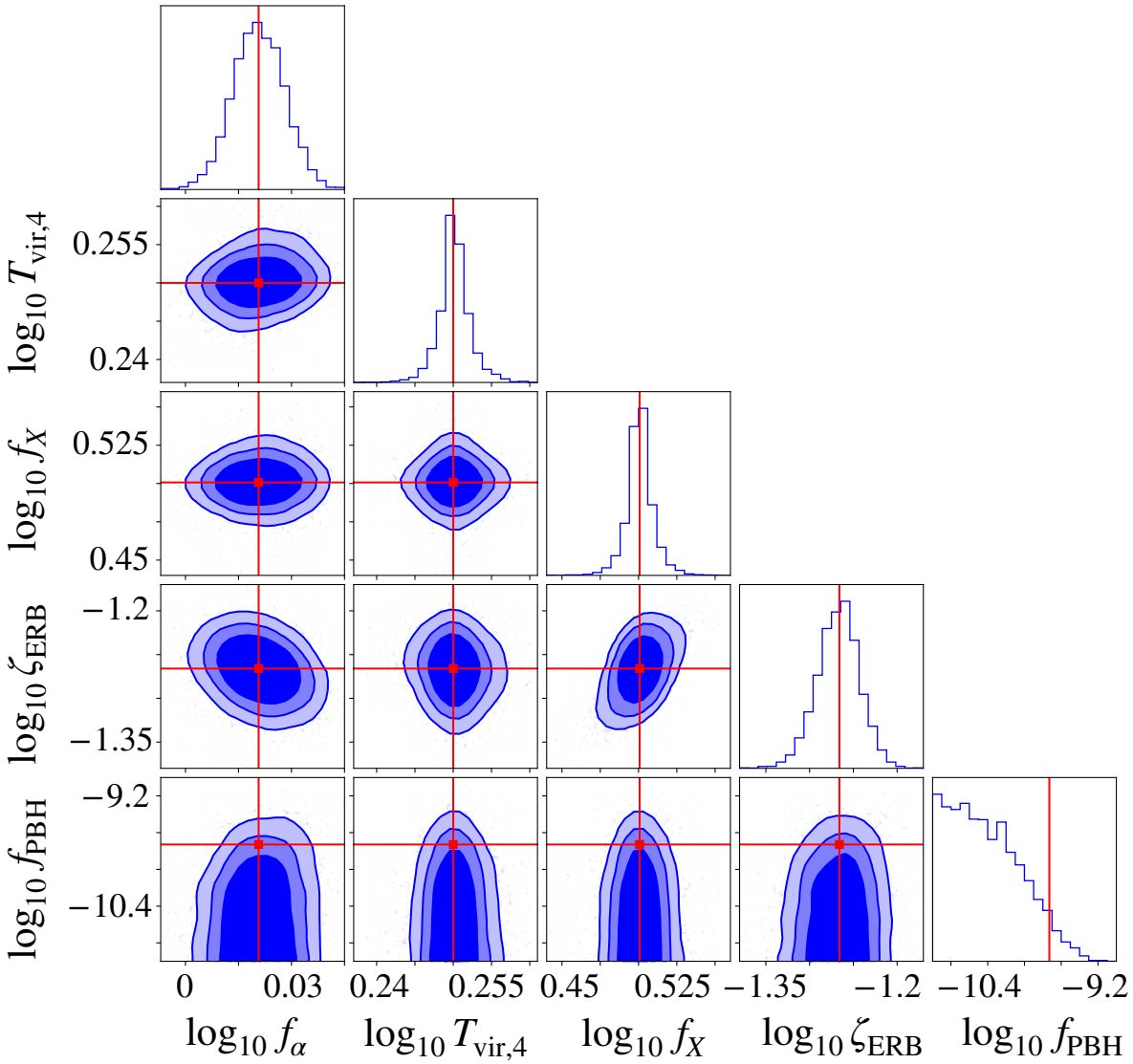

Figure 7.6: Marginalized posterior distributions of parameters for a PBH of mass $M_{\rm PBH} = 10^{15}$ g in the presence of an X-ray background. The contour lines show the 68.3%, 86.6% and 95.5% levels corresponding to 1-sigma, 1.5-sigma and 2-sigma, respectively. The red lines show the median of the probability distribution except in the case of $\log_{10} f_{\rm PBH}$, for which we show the 95% level.

the depth of the absorption, f_α and $\zeta_{\rm ERB}$, we find that in case 1, the values are higher. The Ly α background required in the absence of X-ray background is nearly 10 times higher in the presence of it. This is understandable, because in case 2, X-ray heating takes care of the shape, which then reduces the requirement of a stronger Ly α coupling or excess radio background. The minimum virial temperature is roughly the same in both the cases because it mainly sets the timing of the first drop in the signal.

Fig. 7.7 (left) shows our constraints on $f_{\rm PBH}$ as a function of PBH mass. For comparison, we also show the results from the previous literature on this topic [178] (black dashed and dotted lines) which are somewhat weaker than ours. In the absence of any X-ray heating, our constraint can be written as

$$f_{\rm PBH} = 10^{-6.84} \left(\frac{M_{\rm PBH}}{10^{15}\,{\rm g}} \right)^{3.75} , \tag{7.30}$$

whereas, in presence of X-ray heating

$$f_{\rm PBH} \leqslant 10^{-9.73} \left(\frac{M_{\rm PBH}}{10^{15}\,{\rm g}} \right)^{3.96} . \tag{7.31}$$

Fig. 7.7 (right) compares our constraint to the relevant constraints in the ultralight mass window. It provides a consolidated view of the existing constraints on the fraction of DM composed of ultralight PBHs in the mass range of $10^{15} - 10^{17}\,{\rm g}$.

7.4 Constraints on the Primordial Curvature Power Spectrum

If PBHs form due to the collapse of large density perturbations in the very early Universe, exclusion limits on the PBH abundance can be translated to the constraints on the primordial curvature power spectrum [397, 398, 399, 400]. This leads to constraints on the primordial curvature power spectrum at extremely small scales that are currently inaccessible to any other cosmological observable.

In gravitational collapse, a certain fraction of the horizon mass collapses to form PBHs. Now, if all the PBHs are formed at the same epoch, say in a radiation dominated epoch with a monochromatic mass distribution, we can relate their mass to the present day

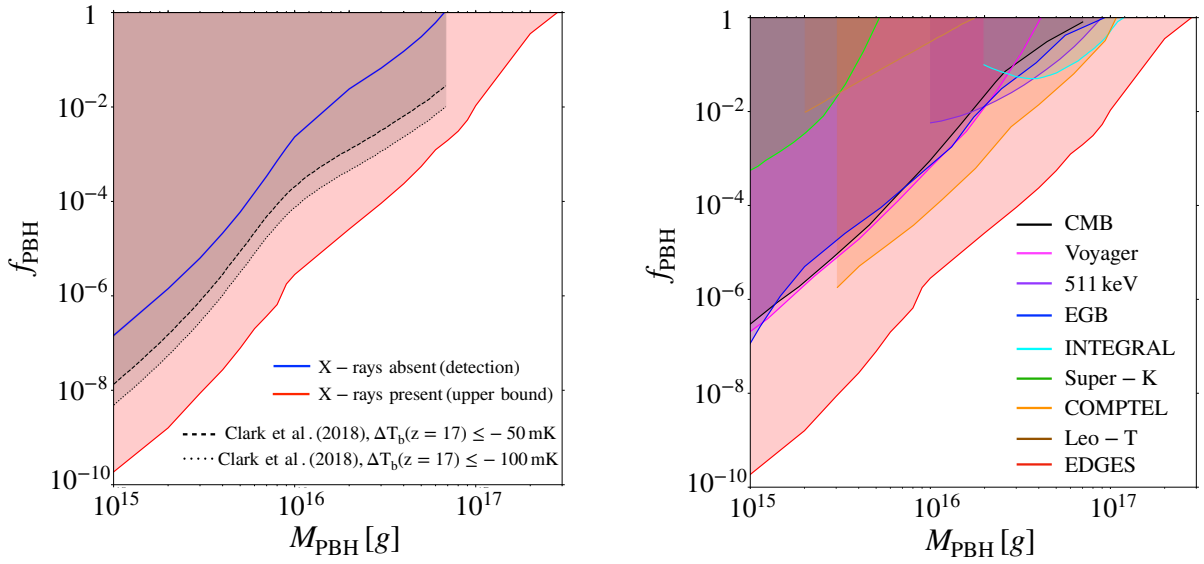

Figure 7.7: (Left) Our inferred constraints on the fraction of DM that is in the form of ultralight non-rotating PBHs. In the model with X-rays, the upper limit obtained from this analysis is shown by the shaded red region. In the model without X-rays, PBHs are the only heating mechanism, so the result formally represent a detection of PBHs. This is shown by the blue curve. The associated uncertainty is too small to be visible on this plot. For comparison, we also show the result from Ref. [178] for $\Delta T_{\rm b}(z = 17) \lesssim -50\,{\rm mK}$ and $\Delta T_{\rm b}(z = 17) \lesssim -100\,{\rm mK}$ by the black dashed and black dotted line, respectively. (Right) Our constraint, in the case of X-ray heating is present, is compared with the existing exclusion limits in the ultralight mass window.

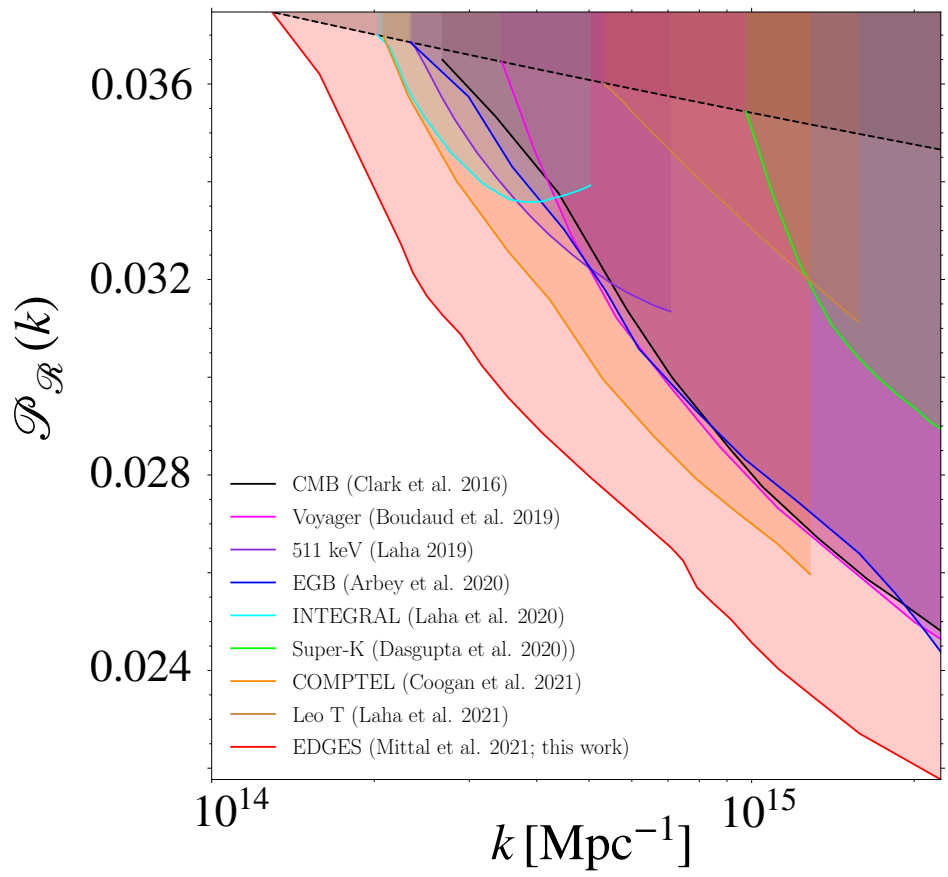

Figure 7.8: Upper limits (red curve) on the curvature power spectrum by translating our upper limits on $f_{\rm PBH}$ in the presence of X-ray heating. The red shaded region is ruled out. Constraints translated from the Planck measurement of CMB (black) [169], Voyager measurement of the positron flux (magenta) [141], SPI/INTEGRAL measurement of the 511 keV emission line (purple) [167], measurement of the extra-Galactic gamma-ray background (blue) [153], INTEGRAL (cyan) & COMPTEL (orange) measurements of the GC MeV gamma-ray flux [155, 156], diffuse supernovae neutrino background searches at Super-Kamiokande (green) [10] and Leo T heating (brown) [175] are also shown for comparison. The region above the black dashed line is ruled out because in that region the density of PBHs exceeds that of DM, i.e., $f_{\rm PBH} > 1$.

horizon mass, $M_0 = c^3/(2G_N H_0)$ [399]

$$M_{\rm PBH} = \gamma \sqrt{\Omega_r}\, M_0 \left(\frac{g_0}{g_i}\right)^{1/6} \left(\frac{H_0}{ck}\right)^2 , \tag{7.32}$$

where $\gamma \approx 0.2$ is the fraction of collapsed horizon mass [399]. Ω_r denotes the present day radiation density relative to critical density, k denotes the scale of horizon re-entry, and

$g_0 = 3.38$ ($g_i = 106.75$) denotes the total number of relativistic degrees of freedom at present day (at the time of PBH formation) [401].

The initial mass fraction of PBHs, i.e., the fraction of the Universe mass that is in the form of PBHs at their time of formation, is related to the present day PBH abundance $f_{\rm PBH}$, and is given by [399]

$$\beta(M_{\rm PBH}) = f_{\rm PBH} \left(\frac{g_i}{g_0}\right)^{1/4} \left(\frac{\Omega_{\rm DM}}{\Omega_r^{3/4}}\right) \sqrt{\frac{M_{\rm PBH}}{\gamma M_0}}\,, \tag{7.33}$$

where $\Omega_{\rm DM}$ denotes the present day DM density relative to critical density of our Universe. In Press-Schechter theory [138], the initial mass fraction of PBHs is equivalent to the probability that a smoothed density field exceeds its threshold value. Therefore, β can also be written as

$$\beta(M_{\rm PBH}) = 2\int_{\delta_c}^{\infty} \Pi(\delta) d\delta\,, \tag{7.34}$$

where $\Pi(\delta)$ denotes the probability density of the density contrast $\delta = \delta(R)$ for a co-moving length scale R. Assuming that the probability distribution of the smoothed density contrast at horizon crossing, $\Pi(\delta)$, is Gaussian with a mass variance σ, Eq. (7.34) simplifies to

$$\beta(M_{\rm PBH}) = {\rm erfc}\left(\frac{\delta_{\rm c}}{\sqrt{2}\sigma}\right)\,, \tag{7.35}$$

where the mass variance can be expressed in terms of the primordial curvature power spectrum $\mathcal{P}_{\mathcal{R}}$ as [398]

$$\sigma^2 = \frac{16}{3}\int_0^{\infty} (kR)^2 j_1^2\left(\frac{kR}{\sqrt{3}}\right) e^{-(kR)^2} \mathcal{P}_{\mathcal{R}}(k)\frac{dk}{k}\,. \tag{7.36}$$

Assuming that the integral in Eq.(7.35) is dominated at $kR \sim 1$, we can estimate the curvature power spectrum as

$$\mathcal{P}_{\mathcal{R}}(k) \approx \frac{3e}{16} j_1^{-2}\left(\frac{1}{\sqrt{3}}\right)\sigma^2\,, \tag{7.37}$$

where

$$j_1(x) = \frac{\sin x - x\cos x}{x^2}\,, \tag{7.38}$$

is the spherical Bessel function.

For a PBH of mass $M_{\rm PBH}$, we know $f_{\rm PBH}$, and therefore, by using Eq. (7.33) we can

estimate β. Now, by using this β in Eq. (7.35), we can find σ. Using σ in Eq. (7.37) we can obtain $\mathcal{P}_\mathcal{R}$. We now have $\mathcal{P}_\mathcal{R}$ as function of $M_{\rm PBH}$. To get $\mathcal{P}_\mathcal{R}$ as a function of k we finally use Eq. (7.32). Our resulting constraints on the primordial curvature power spectrum corresponding to case 2 (X-ray heating included) can be approximated as

$$\mathcal{P}_\mathcal{R}(k) \leq 2.46 \times 10^{-2} \left(\frac{k}{10^{15}\,\mathrm{Mpc}^{-1}} \right)^{n_\mathcal{R}-1}, \tag{7.39}$$

where $n_\mathcal{R} \approx 0.806$. In Fig. 7.8, we compare our result with the existing constraints on the primordial curvature power spectrum.

7.5 Summary & Conclusions

We inferred constraints on the abundance of non-rotating monochromatic PBHs in the mass range $10^{15} - 10^{17}\,\mathrm{g}$ by using the global 21-cm signal measured by EDGES collaboration. The contrast between our inferred constraints, as shown in Fig. 7.7, and the constraints previously reported in the literature [178] illustrate the importance of using the full information content in the EDGES data. Constraints reported in [178] were obtained by requiring that the value of the 21-cm brightness temperature ΔT_b remains below a somewhat arbitrarily chosen threshold of -50 or -100 mK at $z = 17$, which was taken to be the approximate mid-point of the absorption profile detected by EDGES. But the actual data are far more informative than this. In general, the three main features in the EDGES data are its location, depth, and width. If we use all available redshift points from the data, as we do in this analysis, there are more features to exploit, e.g., the steepness of the rise and fall of the absorption feature. Utilizing all of this information is particularly advantageous for heating mechanisms that evolve slowly, such as PBHs. This explains why the constraints from our analysis, shown in Fig. 7.7, are tighter than those previously reported in the literature.

Our main conclusions are as follows

1. In the absence of X-ray heating, PBH evaporation is the only major heating mechanism in our model. In this scenario, the EDGES measurement formally represents a detection of PBHs. For PBHs of mass $10^{15}\,\mathrm{g}$, we infer a best-fitting value of the fraction of DM that is in the form of PBHs as $\log_{10} f_{\rm PBH} = -6.84 \pm 0.02$, and

$f_{\rm PBH}$ changes as $\sim M_{\rm PBH}^{3.75}$ at higher PBH masses (Eq. 2.4 and Fig. 7.7). However, note that, the best-fitting values in this scenario are already ruled out by Voyager measurement of the positron flux, extra-Galactic gamma-ray background measurement by COMPTEL, and CMB measurements, thus favoring our model with X-ray heating.

2. When X-ray heating is present, we get only an upper bound on the fraction of DM that is in the form of PBHs. We find that the data prefers this scenario because the X-ray heating rate evolves much more rapidly than the heating rate induced by PBH evaporation. For PBHs of mass$10^{15}\,$g, we infer $\log_{10} f_{\rm PBH} \leqslant -9.73$ ($95^{\rm th}$ percentile), and $f_{\rm PBH}$ changes as $\sim M_{\rm PBH}^{3.96}$ towards higher PBH masses (Eq. 2.5 and Fig. 7.7).

3. Our constraints on $f_{\rm PBH}$ are the strongest constraint available in the entire ultra-light mass window. An important reason behind this is that we use the measured 21-cm signal values across the entire EDGES band. This tightens the limits on PBH evaporation because PBH-induced heating rate evolves very slowly across the redshift range covered by EDGES.

4. Our inferred values for the non-PBH astrophysical parameters are consistent with observations as well as with other analyses. For example, we require an excess radio background quantified by $\zeta_{\rm ERB} \approx 0.05$, where $\zeta_{\rm ERB} = 1$ corresponds to the maximum observed by the radio instruments such as ARCADE 2, and LWA1.

5. We also derived bounds on the primordial curvature power spectrum at extremely small scales under the assumption of a spherical gravitational collapse, based on the Press-Schechter formalism. We get an upper limit of $\mathcal{P}_{\mathcal{R}} = 2.46 \times 10^{-2}$ at $k = 10^{15}\,{\rm Mpc}^{-1}$, with a $\sim k^{-0.2}$ scaling at other values of k (Eq. 7.39 and Fig. 7.8).

This work highlights the usefulness of the global 21-cm signal for probing exotic physical processes. It also shows that global 21-cm measurements contain much more crucially useful information than just the redshift of absorption. The large number of experiments currently underway to probe the 21-cm signal add to the promise of this type of study in the future.

Author Contribution: I computed the particle spectra from ultralight evaporating PBHs,

and the additional heating/ionization in the IGM due to PBHs. Shikhar Mittal included this additional heating/ionization in the IGM to study its impact on the global 21-cm signal. He derived the constraints on ultralight PBHs as DM using an MCMC-enabled Bayesian analysis with the full spectral shape of the EDGES measurement, and performed the parameter estimations. I translated the constraints on PBH fraction of DM to constraints on primordial curvature power spectrum at extremely small scales, by assuming a spherical collapse scenario.

Chapter 8

Summary and Conclusions

Unambiguous evidences of a non-baryonic form of matter, commonly known as dark matter, constituting 26% of the total energy budget of our Universe have been established by a variety of observations. However, the microscopic identity of dark matter remains one of the most pressing problems in modern day science. Decades of experimental efforts and theoretical studies have been pursued in order to hunt for these mysterious non-baryonic form of matter. But, no evidence has shown up yet. In this thesis, we aim to decode the mystery of dark matter with two fascinating objects in our Universe: Stars, & Black Holes. More particularly, we try to address the following questions:

1. Can electromagnetic and GW observations of compact stars probe particle DM properties?

2. Can ultralight primordial black holes be a viable DM candidate?

We answer the first question by doing an in-depth study on particle DM accretion in compact stars. Accumulation of particle dark matter in compact stars, followed by the electromagnetic and GW observations of the compact stars, is a novel astrophysical probe to constrain the interactions between DM and the ordinary baryonic matter. The basic strategy is the following. For annihilating DM, captured dark matter particles annihilate among themselves, and heats up the stellar core. This heating has two contributions. Firstly, because of the very high baryonic density of the compact stars, the annihilation products can not escape from the stellar core. As a result, they scatter repeatedly in the stellar core, deposits energy, and heats up the stellar core. Secondly, DM particles acquire immense kinetic energies while falling into the steep gravitational potential of

the compact stars, and while getting captured, they can transfer part of their kinetic energy to the nucleons via collisions, resulting in another form of heating in the stellar core. Non-observation of any such anomalous heating via luminosity measurement of the cold compact stars project stringent exclusions on dark matter interactions. For non-annihilating DM, captured dark matter particles gradually accumulate inside the stellar core, and increases linearly with time. Once the total number of captured DM particles exceed the required number of particles for black hole formation, a dark core collapse ensues, and a tiny black hole forms at the center. If the nascent black hole is not sufficiently light, it swallows surrounding matter via accretion, and in very short time, it eats up the host star. Existence of the host stars provide stringent exclusions on dark matter interactions over a wide range of DM masses.

We have revisited the formalism of DM capture in compact stars, and made two key improvements. Firstly, we provided an exact analytical treatment of DM capture in the multiple collision regime (Eq. 2.4), and based on our formalism, we provide stringent constraint on annihilating dark matter interactions (Eq. 2.20). Our constraints are derived by using the luminosity measurement of several old and cold white dwarfs in our nearest globular cluster, and they are significantly stronger than the corresponding direct detection constraints for both heavy and light DM (Fig. 2.5). Secondly, we generalized the formalism of DM capture to account for arbitrary mediator masses (Eq. 3.1 & Eq. 3.9), and revisited the astrophysical constraints on DM-nucleon interaction strength from observations of old and cold neutron stars (Eq. 3.19 & Eq. 3.21). We demonstrated that for interactions mediated via light mediators, these astrophysical exclusions on DM-nucleon interaction strength significantly weaken (Fig. 3.4 & Fig. 3.6), and can even be completely alleviated for interactions mediated by very light mediators (Fig. 3.5 & Fig. 3.7). Furthermore, we showed the impact of repulsive self-interactions among the DM particles on the capture rate, and derived constraints on DM self-interaction strength from the existence of old neutron stars, complementary to the constraints obtained from merging galaxy clusters (Fig. 3.9).

We also discuss the possible formation mechanism of sub-Chandrasekhar mass black holes via continued accumulation of non-annihilating particle dark matter in the compact stars. We demonstrate that non-zero interactions between DM and the nuclei, which is a universal feature of DM models, is sufficient to produce such low mass black holes (Fig. 4.1).

These low mass black holes, which originate via transmuting the compact stars to comparable mass black holes, are particularly interesting. For sub-Chandrasekhar mass progenitors, these transmuted black boles are a viable alternative to PBHs, whereas, for heavier mass progenitors, they can also explain the recent GW events with unusually low masses. We pointed out several avenues to test the origin of low mass black holes, concentrating on the cosmic evolution of the binary merger rates. We demonstrated that measurement of the binary merger rates, especially at high redshifts, with the imminent GW detectors can conclusively identity this transmutation scenario, and therefore, can shed light on particle DM properties (Fig. 4.2).

We answer the second question via searching the Hawking evaporated particles from ultralight PBHs in a variety of probes. PBHs in the ultralight mass window, i.e., in the mass range of $10^{-18} - 10^{-15}\,M_\odot$, act as a decaying dark matter, and emit photons, neutrinos, and electrons/positrons via Hawking radiation. The spectrum of these emitted particles follow a blackbody like distribution (Eq. 5.1), and can be probed in various detectors that are designed for particle physics and cosmological observations.

We demonstrated that non-observation of such Hawking emitted neutrinos in the DSNB searches at the existing neutrino detectors, such as Super-Kamiokande and KamLAND, provide stringent exclusions on fraction of dark matter that is in the form of ultralight PBHs (Fig. 5.2). The neutrino-derived exclusions are inferred by requiring that the total neutrino flux from PBHs can not exceed the current DSNB flux upper limits (Eq. 5.10). These constraints are a bit weaker than the existing constraints in that mass window, but they are complementary and very robust to a variety of propagational uncertainties that are inevitably associated with other particles. These constraints are also minimally dependent on the choice of DM density profiles, making them one of the cleanest constraints in the ultralight mass window.

We also showed that recent measurement of the 511 keV gamma-ray line flux by the space based telescope INTEGRAL can be translated to set a world-leading exclusion on ultralight PBHs as DM (Fig. 5.3). The positron-derived constraints are simply derived from the fact that positron injection rate from PBHs can not exceed the same from the 511 keV measurement (Eq. 5.11). These conservative constraints are one of the leading constraints in the ultralight mass window, and can vastly be improved with a proper identification of the astrophysical sources that are responsible for the 511 keV gamma-

ray line emission. Unlike the neutrino derived constraints, these constraints depend very strongly on the astrophysical uncertainties, such as, choice of DM density profiles and unknown propagation distance of the low energy Hawking emitted positrons, and can vary by an order of magnitude based on these uncertainties (Fig. 5.4). Here, it is important to mention that the neutrino (positron)-derived constraints can probe much higher mass window for PBHs that have rotation or which follow an extended mass distribution.

We further illustrated that future observation of low energy ($0.15 - 5$ MeV) Galactic Center photons by the imminent soft gamma-ray telescopes, such as AMEGO, can project stringent exclusions on the fraction of DM that is in the form of ultralight PBHs (Fig. 6.3 & Fig. 6.4). By assuming no evaporation signal is present in the data, AMEGO can probe a mass window where PBHs can make up the entirety of DM. Quantitatively, for a monochromatic mass of distribution of PBHs, the projections can extend up to 7×10^{17} g for non-rotating PBHs, and 4×10^{18} g for maximally rotating PBHs.

21-cm cosmology provides yet another probe to constrain ultralight PBHs as dark matter. Hawking emitted particles from evaporating PBHs can interact with the ordinary baryonic matter in the intergalactic medium (IGM), providing an additional heating and ionization in the IGM. Since, the amplitude of the global 21-cm signal depends on the temperature and ionization of the IGM, Hawking emission from ultralight PBHs causes a damping in the global 21-cm signal, and hence, can be probed via 21-cm observations. We demonstrate that recent measurement of the global 21-cm signal by the radio telescope EDGES can be translated to set a leading constraint on ultralight PBHs as DM (Fig. 7.7). We also derive stringent constraints on primordial curvature power spectrum at extremely small scales under the assumption of a PBH formation via spherical gravitational collapse (Fig. 7.8).

Thus summarizing, the crux of this thesis broadly consists with the following results:

1. Electromagnetic and GW observations of the compact stars *can* shed light on particle DM properties. Particle DM interactions with the ordinary baryonic matter can be constrained via luminosity measurement of the cold compact stars (Fig. 2.5 & Fig. 3.4) and existence of the old compact stars (Fig. 3.6). For a contact interaction between the DM and the stellar target, these astrophysical constraints are the world-leading constraints on DM-nucleon interaction strength for both heavy and light DM. However, for interactions mediated via light mediators, these astrophysi-

cal constraints significantly weaken, and can even be voided (Fig. 3.4 and Fig. 3.6). GW observations of the compact stars, more particularly, cosmic evolution of the binary merger rates provide yet another novel probe to shed light on particle DM properties (Fig. 4.2).

2. Ultralight PBHs in the mass range of $10^{-18} - 10^{15}\, M_\odot$ *can not* be a viable dark matter candidate. The fraction of DM that is in the form of ultralight PBHs are severely constrained via non-observation of the Hawking emitted particles in a variety of probes. This includes: *i*) non-observation of Hawking radiated neutrinos in the DSNB searches at the existing neutrino detectors, such as Super-Kamiokande (Fig. 5.2), *ii*) precise measurement of the 511 keV gamma-ray line by the space based telescope INTEGRAL (Fig. 5.3), *iii*) observation of low energy Galactic Center photons by the imminent soft gamma-ray telescopes, such as AMEGO (Fig. 6.3 & Fig. 6.4), and *iv*) measurement of the global 21-cm signal by the radio telescope EDGES (Fig. 7.7).

We hope that the results obtained in this thesis will prove useful in our quest to unravel the mystery of dark matter using stars and black holes.

Appendix A

Thermalization timescale

Captured DM particles follow a closed orbit that intersects with the stellar object, lose more energy in successive scatterings, and eventually thermalize with the stellar constituents in a short timescale, which is known as the thermalization timescale [213, 248, 249, 269, 270]. Thermalization of the captured DM particles occurs in two stages: first thermalization and second thermalization. In the first thermalization, DM particles orbit outside the stellar object, whereas, in the second thermalization, they orbit entirely inside the stellar object. In the following, we estimate the timescales for the first and second thermalization, and the total thermalization timescale is therefore a sum of these two timescales.

First Thermalization

At the start of the thermalization process, the captured DM particles have orbits larger than the size of the stellar object, crossing it multiple times, and depositing a fraction of their kinetic energy in each crossing. The average energy loss of a DM particle of mass m_χ due to a scattering against a stellar target of mass m_t which resides at a distance $\tilde{r}$ from the center of the stellar object is given by ($m_\chi > m_t$)

$$\Delta E = 2\frac{m_t}{m_\chi}\left(E + GMm_\chi\frac{3R^2 - \tilde{r}^2}{2R^3}\right), \tag{A.1}$$

where M and R denotes the mass and radius of the stellar object under consideration, and E denotes the initial energy of the DM particle after getting captured, which can

also be written as $E = -GMm_\chi/r$, where r is the classical turning point. To obtain the average energy loss, we express E in terms of the classical turning point r, and average over the size of the stellar object

$$\Delta E = 2GMm_t \left(-\frac{1}{r} + \frac{1}{R} \int_0^R d\tilde{r}\, \frac{3R^2 - \tilde{r}^2}{2R^3} \right) = 2GMm_t \left(\frac{4}{3R} - \frac{1}{r} \right) . \tag{A.2}$$

On the other hand, the time takes by the DM particle to complete one orbit through the stellar object is approximately given by its orbital period

$$\Delta t = 2\pi r^{3/2} \frac{1}{\sqrt{GM}} . \tag{A.3}$$

The first thermalization timescale is then obtained by dividing Eq. A.2 by Eq. A.3 and multiplying by the optical depth of the stellar object τ [213]

$$\frac{dE}{dt} = \frac{(GM)^{3/2} \tau m_t}{\pi r^{3/2}} \left(\frac{4}{3R} - \frac{1}{r} \right) . \tag{A.4}$$

By substituting, $\epsilon = R/r$, the first thermalization timescale for the DM particles, i.e., the time for the DM particles to settle completely inside the stellar object is given by

$$t_1^{\rm th} = \frac{\pi m_\chi r^{3/2}}{\sqrt{GM} m_t} \int_{\epsilon_{\rm min}}^1 \frac{d\epsilon}{\tau \epsilon^{3/2} (4/3 - \epsilon)} , \tag{A.5}$$

where $\epsilon_{\rm min} \sim R/r_0$ and r_0 can be determined from the initial kinetic energy of the captured DM particles. For typical white dwarf parameters, the time to complete the first stage of thermalization is [213]

$$t_1^{\rm th} = 10^{-4}\,{\rm yrs} \left(\frac{10^{-40}\,{\rm cm}^2}{\sigma_{\chi n}} \right) \left(\frac{m_\chi}{10^6\,{\rm GeV}} \right) \left(\frac{1.4\,M_\odot}{M} \right)^{5/2} \left(\frac{R}{2500\,{\rm km}} \right)^{7/2} , \tag{A.6}$$

Second Thermalization

Once dark matter particles have lost sufficient energy via successive scatterings with the stellar targets, their orbits become completely contained within the stellar object, and they enter the second stage of thermalization. They continue to lose energy via repeated collisions, and finally shrinks their orbits to a "thermal radius", $r_{\rm th} = \sqrt{9 k_{\rm B} T/(4\pi G \rho m_\chi)}$, where they follow a thermal velocity distribution determined by the core temperature of

the stellar object T. To compute the energy loss rate, we first estimate the interaction time for dark matter-nucleus scattering

$$t_{\rm int} = \frac{1}{n_t \sigma v_{\rm rel}}\,, \tag{A.7}$$

where n_t is the number density of the target nuclei, σ is the DM-nuclei scattering cross-section, and $v_{\rm rel}$ is the relative velocity of the DM-nuclei system. The average energy loss per scattering is also given by ($m_\chi > m_t$)

$$\Delta E = \frac{2m_t}{m_\chi} E\,, \tag{A.8}$$

where E is the energy of the DM particle. Hence, the energy loss rate can be written as

$$\frac{dE}{dt} = \frac{2m_t n_t \sigma v_{\rm rel} E}{m_\chi}\,. \tag{A.9}$$

After completing the first thermalization phase, the initial energy of the DM particles is simply given by the binding energy at the surface of the stellar object $\sim GMm_\chi/R$. For energies higher than E_*, they are in an inertial regime, where $v_{\rm rel} = \sqrt{\frac{2E}{m_\chi}}$, and in such inertial regime, the energy loss rate is

$$\left(\frac{dE}{dt}\right)_{\rm in} \sim \frac{2\sqrt{2} m_t n_t A^4 \sigma_{\chi n} E^{3/2}}{m_\chi^{3/2}}\,. \tag{A.10}$$

When the energy is lower than E_*, dark matter particles enter the viscous regime where the scattering rate is driven by the thermal speed of nuclei, and therefore, $v_{\rm rel} = \sqrt{\frac{T}{m_t}}$. In the viscous regime, the energy loss rate is

$$\left(\frac{dE}{dt}\right)_{\rm vis} \sim \frac{2 m_t n_t A^4 \sigma_{\chi n} \sqrt{T} E^2}{m_\chi \sqrt{m_t}\, E_*}\,. \tag{A.11}$$

Finally, the energy of the DM particle attain its thermal value $E = 3T/2$ at the end of the second thermalization, and hence, the timescale for second thermalization is simply given by

$$t_2^{\rm th} = \frac{m_\chi \sqrt{m_t}\, E_*}{2 m_t n_t A^4 \sigma_{\chi n} \sqrt{T}} \int_{E_*}^{3T/2} \frac{dE}{E^2}\,. \tag{A.12}$$

For typical white dwarf parameters, the time to complete the second thermalization timescale is [213]

$$t_2^{\rm th} = 20\,{\rm yrs}\left(\frac{10^{-40}\,{\rm cm}^2}{\sigma_{\chi n}}\right)\left(\frac{m_\chi}{10^6\,{\rm GeV}}\right)^2\left(\frac{10^7\,{\rm K}}{T_{\rm WD}}\right)^{5/2}, \tag{A.13}$$

Given that we have estimated $t_1^{\rm th}$ and $t_2^{\rm th}$, we can obtain the total thermalization time ($t_{\rm th}$) by adding these two timescales. However, for the range of DM masses and DM-nucleon scattering cross-section that we are interested in, $t_1^{\rm th}$ is always negligible, and hence, the total thermalization timescale is given by the second thermalization timescale, i.e., $t_{\rm th} \approx t_2^{\rm th}$.

Appendix B

Chandrasekhar Limit for Dark Core Collapse

Here we review the derivation of the Chandrasekhar limit for both bosonic and fermionic DM, which is very crucial for estimating the dark core collapse criterion.

Let there are N number of fermionic DM of mass m_χ distributed in a sphere with a radius of R. So, the number density of the fermionic DM is $\sim N/R^3$, and because of the Pauli exclusion principle, average distance between two fermionic DM is $\sim R/N^{1/3}$. Now, from the uncertainty principle, each fermionic DM have momentum $\sim N^{1/3}/R$. Hence, the average energy per fermionic DM is

$$E \sim \frac{-GNm_\chi^2}{R} + \frac{1}{2m_\chi}\left(\frac{N^{1/3}}{R}\right)^2 . \tag{B.1}$$

The system can have a stable spherical configuration when the gravitational energy and Fermi energy reach equilibrium. It implies an equilibrium radius of $R = 1/\left(2GN^{1/3}m_\chi^3\right)$. As the number of fermionic DM increases, the equilibrium radius shrinks and Fermi energy increases, eventually they become relativistic with a total energy of

$$E \sim \frac{-GNm_\chi^2}{R} + \frac{N^{1/3}}{R} . \tag{B.2}$$

For gravitational collapse to occur, gravitational energy has to dominate over the Fermi energy, and hence, the Chandrasekhar limit for fermionic DM [249]

$$N_\chi^{\rm cha} \sim \left(\frac{1}{G m_\chi^2}\right)^{3/2} \sim 1.8 \times 10^{51} \left(\frac{100\,{\rm GeV}}{m_\chi}\right)^3 \tag{B.3}$$

Next, we discuss Chandrasekhar limit for bosonic DM. Similar to the fermionic case, the gravitational collapse occurs when the DM particles are relativistic. However, the bosonic system is substantially different from the fermionic system because they have no Fermi pressure to hinder gravity. If there are N number of bosonic DM contained inside a sphere with radius R, they have a momentum of $1/R$ which arises from the uncertainty principle. Therefore, in the relativistic limit, the total energy of the bosonic DM

$$E \sim \frac{-G N m_\chi^2}{R} + \frac{1}{R}\,. \tag{B.4}$$

For gravitational collapse to occur, gravitational energy has to dominate over the zero point energy, and hence, the Chandrasekhar limit for bosonic DM [249]

$$N_\chi^{\rm cha} \sim \left(\frac{1}{G m_\chi^2}\right) \sim 1.5 \times 10^{34} \left(\frac{100\,{\rm GeV}}{m_\chi}\right)^2 \tag{B.5}$$

From Eq. B.5, it is evident that Chandrasekhar limit for bosonic DM is much lower than the Chandrasekhar limit for fermionic DM, unless the DM particles are sufficiently heavy ($m_\chi > 1.2 \times 10^{19}\,{\rm GeV}$).

Appendix C

DM Density Profiles

N-body simulations of cold DM indicate that halo density profiles have a universal shape, known as the Navarro–Frenk–White (NFW) profile [310, 311]. In the NFW profile, the density of DM as a function of the radius is given by

$$\rho_{\rm NFW}(r) = \frac{\rho_s}{\frac{r}{r_s}\left(1+\frac{r}{r_s}\right)^2}\,, \tag{C.1}$$

where ρ_s denotes the core density and r_s denotes the scale radius. For distances smaller than the scale radius ($r < r_s$), NFW profile scales as $\sim 1/r$, and shows a cuspy behavior at very small radius. Whereas, for distances larger than the scale radius ($r > r_s$), NFW profile scales as $\sim 1/r^3$. These two parameters, ρ_s and r_s can be expressed in terms of the virial mass of the halo ($M_{\rm vir}$) and the concentration parameter of the halo ($c_{\rm vir} = r_{\rm vir}/r_s$) by the following two relations. *i*) The average density of the halo inside the virial radius is $200\,\rho_c$, where ρ_c is the critical density of our Universe and *ii*) the virial mass of the halo is the total mass contained in the virial radius. From the first criterion we get

$$\langle\rho\rangle = \frac{M_{\rm vir}}{\frac{4}{3}\pi c_{\rm vir}^3 r_s^3} = 200\rho_c\,. \tag{C.2}$$

From the second criterion we get

$$M_{\rm vir} = \int_{r=0}^{r_{\rm vir}} 4\pi r^2 \rho_{\rm NFW}(r) dr = 4\pi\rho_s r_s^3 \left(\log\left(1+c_{\rm vir}\right) - \frac{c_{\rm vir}}{1+c_{\rm vir}}\right)\,. \tag{C.3}$$

By solving the Eqs. C.2 and C.3, one can obtain ρ_s and r_s in terms of the $M_{\rm vir}$ and $c_{\rm vir}$. For Milky Way like galaxies we take $c_{\rm vir} = 13.31$ and $M_{\rm vir} = 0.82 \times 10^{12}\,M_\odot$ [312], and it

implies $\rho_s = 0.43\,\mathrm{GeV/cm^3}$ and $r_s = 14.88\,\mathrm{kpc}$.

Apart from this cuspy NFW profile, DM density profiles can also have a core at smaller radii, motivated by the measurement of the Galactic rotation curves. This includes Isothermal profile, Burkert profile, etc., and their functional forms are given by

$$\rho_{\rm iso}(r) = \frac{\rho_s}{1 + \left(\frac{r}{r_s}\right)^2}\,, \tag{C.4}$$

$$\rho_{\rm bur}(r) = \frac{\rho_s}{\left(1 + \frac{r}{r_s}\right)\left(1 + \left(\frac{r}{r_s}\right)^2\right)}\,, \tag{C.5}$$

where ρ_s and r_s denotes the core density and scale radius, respectively. For Milky Way like galaxy, these parameters are $\rho_s = 1.387\,\mathrm{GeV/cm^3}$ and $r_s = 4.38\,\mathrm{kpc}$ for Isothermal profile & $\rho_s = 0.712\,\mathrm{GeV/cm^3}$ and $r_s = 12.67\,\mathrm{kpc}$ for Burkert profile [402].

Bibliography

[1] F. Zwicky, *Die Rotverschiebung von extragalaktischen Nebeln*, *Helv. Phys. Acta* **6** (1933) 110.

[2] V. C. Rubin and W. K. Ford, Jr., *Rotation of the Andromeda Nebula from a Spectroscopic Survey of Emission Regions*, *Astrophys. J.* **159** (1970) 379.

[3] D. Clowe, M. Bradac, A. H. Gonzalez, M. Markevitch, S. W. Randall, C. Jones et al., *A direct empirical proof of the existence of dark matter*, *Astrophys. J. Lett.* **648** (2006) L109 [astro-ph/0608407].

[4] Planck collaboration, N. Aghanim et al., *Planck 2018 results. VI. Cosmological parameters*, *Astron. Astrophys.* **641** (2020) A6 [1807.06209].

[5] R. Massey, T. Kitching and J. Richard, *The dark matter of gravitational lensing*, *Rept. Prog. Phys.* **73** (2010) 086901 [1001.1739].

[6] J. R. Primack, *Dark matter and structure formation*, in *Midrasha Mathematicae in Jerusalem: Winter School in Dynamical Systems*, 7, 1997, astro-ph/9707285.

[7] B. Dasgupta, A. Gupta and A. Ray, *Dark matter capture in celestial objects: Improved treatment of multiple scattering and updated constraints from white dwarfs*, *JCAP* **08** (2019) 018 [1906.04204].

[8] B. Dasgupta, A. Gupta and A. Ray, *Dark matter capture in celestial objects: light mediators, self-interactions, and complementarity with direct detection*, *JCAP* **10** (2020) 023 [2006.10773].

[9] B. Dasgupta, R. Laha and A. Ray, *Low Mass Black Holes from Dark Core Collapse*, *Phys. Rev. Lett.* **126** (2021) 141105 [2009.01825].

[10] B. Dasgupta, R. Laha and A. Ray, *Neutrino and positron constraints on spinning primordial black hole dark matter*, *Phys. Rev. Lett.* **125** (2020) 101101 [1912.01014].

[11] A. Ray, R. Laha, J. B. Muñoz and R. Caputo, *Near future MeV telescopes can discover asteroid-mass primordial black hole dark matter*, *Phys. Rev. D* **104** (2021) 023516 [2102.06714].

[12] S. Mittal, A. Ray, G. Kulkarni and B. Dasgupta, *Constraining primordial black holes as dark matter using the global 21-cm signal with X-ray heating and excess radio background*, 2107.02190.

[13] G. Bertone and D. Hooper, *History of dark matter*, *Rev. Mod. Phys.* **90** (2018) 045002 [1605.04909].

[14] D. Paraficz, J. P. Kneib, J. Richard, A. Morandi, M. Limousin, E. Jullo et al., *The Bullet cluster at its best: weighing stars, gas, and dark matter*, *Astronomy and Astrophysics* **594** (2016) A121 [1209.0384].

[15] B. Paczynski, *Gravitational Microlensing by the Galactic Halo*, *Astrophysical Journal* **304** (1986) 1.

[16] K. Griest, *Galactic Microlensing as a Method of Detecting Massive Compact Halo Objects*, *Astrophys. J.* **366** (1991) 412.

[17] M. Markevitch, A. H. Gonzalez, D. Clowe, A. Vikhlinin, L. David, W. Forman et al., *Direct constraints on the dark matter self-interaction cross-section from the merging galaxy cluster 1E0657-56*, *Astrophys. J.* **606** (2004) 819 [astro-ph/0309303].

[18] M. Milgrom, *A Modification of the Newtonian dynamics as a possible alternative to the hidden mass hypothesis*, *Astrophys. J.* **270** (1983) 365.

[19] S. S. McGaugh, *A tale of two paradigms: the mutual incommensurability of ΛCDM and MOND*, *Can. J. Phys.* **93** (2015) 250 [1404.7525].

[20] S. Boran, S. Desai, E. O. Kahya and R. P. Woodard, *GW170817 Falsifies Dark Matter Emulators*, *Phys. Rev. D* **97** (2018) 041501 [1710.06168].

[21] M. Lisanti, M. Moschella, N. J. Outmezguine and O. Slone, *Testing Dark Matter and Modifications to Gravity using Local Milky Way Observables*, *Phys. Rev. D* **100** (2019) 083009 [1812.08169].

[22] L. Hui, J. P. Ostriker, S. Tremaine and E. Witten, *Ultralight scalars as cosmological dark matter*, *Phys. Rev. D* **95** (2017) 043541 [1610.08297].

[23] N. Menci, A. Merle, M. Totzauer, A. Schneider, A. Grazian, M. Castellano et al., *Fundamental physics with the Hubble Frontier Fields: constraining Dark Matter models with the abundance of extremely faint and distant galaxies*, *Astrophys. J.* **836** (2017) 61 [1701.01339].

[24] K. K. Rogers and H. V. Peiris, *Strong Bound on Canonical Ultralight Axion Dark Matter from the Lyman-Alpha Forest*, *Phys. Rev. Lett.* **126** (2021) 071302 [2007.12705].

[25] S. Tremaine and J. E. Gunn, *Dynamical role of light neutral leptons in cosmology*, *Phys. Rev. Lett.* **42** (1979) 407.

[26] A. Boyarsky, O. Ruchayskiy and D. Iakubovskyi, *A Lower bound on the mass of Dark Matter particles*, *JCAP* **03** (2009) 005 [0808.3902].

[27] J. Alvey, N. Sabti, V. Tiki, D. Blas, K. Bondarenko, A. Boyarsky et al., *New constraints on the mass of fermionic dark matter from dwarf spheroidal galaxies*, *Mon. Not. Roy. Astron. Soc.* **501** (2021) 1188 [2010.03572].

[28] C. M. Ho and R. J. Scherrer, *Limits on MeV Dark Matter from the Effective Number of Neutrinos*, *Phys. Rev. D* **87** (2013) 023505 [1208.4347].

[29] N. Sabti, J. Alvey, M. Escudero, M. Fairbairn and D. Blas, *Refined Bounds on MeV-scale Thermal Dark Sectors from BBN and the CMB*, *JCAP* **01** (2020) 004 [1910.01649].

[30] K. Griest and M. Kamionkowski, *Unitarity limits on the mass and radius of dark-matter particles*, *Phys. Rev. Lett.* **64** (1990) 615.

[31] J. Smirnov and J. F. Beacom, *TeV-Scale Thermal WIMPs: Unitarity and its Consequences*, *Phys. Rev. D* **100** (2019) 043029 [1904.11503].

[32] T. Lin, *Dark matter models and direct detection*, *PoS* **333** (2019) 009 [1904.07915].

[33] B. W. Lee and S. Weinberg, *Cosmological Lower Bound on Heavy Neutrino Masses*, *Phys. Rev. Lett.* **39** (1977) 165.

[34] J. R. Ellis, J. S. Hagelin, D. V. Nanopoulos, K. A. Olive and M. Srednicki, *Supersymmetric Relics from the Big Bang*, *Nucl. Phys. B* **238** (1984) 453.

[35] G. Steigman and M. S. Turner, *Cosmological Constraints on the Properties of Weakly Interacting Massive Particles*, *Nucl. Phys. B* **253** (1985) 375.

[36] M. Srednicki, R. Watkins and K. A. Olive, *Calculations of Relic Densities in the Early Universe*, *Nucl. Phys. B* **310** (1988) 693.

[37] K. Griest and D. Seckel, *Three exceptions in the calculation of relic abundances*, *Phys. Rev. D* **43** (1991) 3191.

[38] L. Roszkowski, E. M. Sessolo and S. Trojanowski, *WIMP dark matter candidates and searches—current status and future prospects*, *Rept. Prog. Phys.* **81** (2018) 066201 [1707.06277].

[39] G. Arcadi, M. Dutra, P. Ghosh, M. Lindner, Y. Mambrini, M. Pierre et al., *The waning of the WIMP? A review of models, searches, and constraints*, *Eur. Phys. J. C* **78** (2018) 203 [1703.07364].

[40] R. K. Leane, T. R. Slatyer, J. F. Beacom and K. C. Y. Ng, *GeV-scale thermal WIMPs: Not even slightly ruled out*, *Phys. Rev. D* **98** (2018) 023016 [1805.10305].

[41] R. D. Peccei and H. R. Quinn, *CP Conservation in the Presence of Instantons*, *Phys. Rev. Lett.* **38** (1977) 1440.

[42] S. Weinberg, *A new light boson?*, *Phys. Rev. Lett.* **40** (1978) 223.

[43] F. Wilczek, *Problem of strong p and t invariance in the presence of instantons*, *Phys. Rev. Lett.* **40** (1978) 279.

[44] J. E. Kim and G. Carosi, *Axions and the Strong CP Problem*, *Rev. Mod. Phys.* **82** (2010) 557 [0807.3125].

[45] P. Arias, D. Cadamuro, M. Goodsell, J. Jaeckel, J. Redondo and A. Ringwald, *WISPy Cold Dark Matter*, *JCAP* **06** (2012) 013 [1201.5902].

[46] D. J. E. Marsh, *Axion Cosmology*, *Phys. Rept.* **643** (2016) 1 [1510.07633].

[47] P. W. Graham, I. G. Irastorza, S. K. Lamoreaux, A. Lindner and K. A. van Bibber, *Experimental Searches for the Axion and Axion-Like Particles*, *Ann. Rev. Nucl. Part. Sci.* **65** (2015) 485 [1602.00039].

[48] F. Chadha-Day, J. Ellis and D. J. E. Marsh, *Axion dark matter: What is it and why now?*, *Sci. Adv.* **8** (2022) abj3618 [2105.01406].

[49] S. Dodelson and L. M. Widrow, *Sterile-neutrinos as dark matter*, *Phys. Rev. Lett.* **72** (1994) 17 [hep-ph/9303287].

[50] X.-D. Shi and G. M. Fuller, *A New dark matter candidate: Nonthermal sterile neutrinos*, *Phys. Rev. Lett.* **82** (1999) 2832 [astro-ph/9810076].

[51] A. D. Dolgov and S. H. Hansen, *Massive sterile neutrinos as warm dark matter*, *Astropart. Phys.* **16** (2002) 339 [hep-ph/0009083].

[52] J. Lesgourgues and S. Pastor, *Massive neutrinos and cosmology*, *Phys. Rept.* **429** (2006) 307 [astro-ph/0603494].

[53] A. Kusenko, *Sterile neutrinos: The Dark side of the light fermions*, *Phys. Rept.* **481** (2009) 1 [0906.2968].

[54] M. Drewes et al., *A White Paper on keV Sterile Neutrino Dark Matter*, *JCAP* **01** (2017) 025 [1602.04816].

[55] K. N. Abazajian, *Sterile neutrinos in cosmology*, *Phys. Rept.* **711-712** (2017) 1 [1705.01837].

[56] A. Boyarsky, M. Drewes, T. Lasserre, S. Mertens and O. Ruchayskiy, *Sterile neutrino Dark Matter*, *Prog. Part. Nucl. Phys.* **104** (2019) 1 [1807.07938].

[57] B. Dasgupta and J. Kopp, *Sterile Neutrinos*, *Phys. Rept.* **928** (2021) 1 [2106.05913].

[58] G. Jungman, M. Kamionkowski and K. Griest, *Supersymmetric dark matter*, *Phys. Rept.* **267** (1996) 195 [hep-ph/9506380].

[59] J. F. Gunion, D. Hooper and B. McElrath, *Light neutralino dark matter in the NMSSM*, *Phys. Rev. D* **73** (2006) 015011 [hep-ph/0509024].

[60] G. B. Gelmini and P. Gondolo, *Neutralino with the right cold dark matter abundance in (almost) any supersymmetric model*, *Phys. Rev. D* **74** (2006) 023510 [hep-ph/0602230].

[61] N. Arkani-Hamed, A. Delgado and G. F. Giudice, *The Well-tempered neutralino*, *Nucl. Phys. B* **741** (2006) 108 [hep-ph/0601041].

[62] C. Cheung, L. J. Hall, D. Pinner and J. T. Ruderman, *Prospects and Blind Spots for Neutralino Dark Matter*, *JHEP* **05** (2013) 100 [1211.4873].

[63] L. J. Hall, Y. Nomura and S. Shirai, *Spread Supersymmetry with Wino LSP: Gluino and Dark Matter Signals*, *JHEP* **01** (2013) 036 [1210.2395].

[64] A. Delgado and M. Quirós, *Higgsino Dark Matter in the MSSM*, *Phys. Rev. D* **103** (2021) 015024 [2008.00954].

[65] E. Witten, *Cosmic separation of phases*, *Phys. Rev. D* **30** (1984) 272.

[66] J. Madsen, *Astrophysical Limits on the Flux of Quark Nuggets*, *Phys. Rev. Lett.* **61** (1988) 2909.

[67] K. Lawson and A. R. Zhitnitsky, *Isotropic Radio Background from Quark Nugget Dark Matter*, *Phys. Lett. B* **724** (2013) 17 [1210.2400].

[68] A. Atreya, A. Sarkar and A. M. Srivastava, *Reviving quark nuggets as a candidate for dark matter*, *Phys. Rev. D* **90** (2014) 045010 [1405.6492].

[69] Y. Bai, A. J. Long and S. Lu, *Dark Quark Nuggets*, *Phys. Rev. D* **99** (2019) 055047 [1810.04360].

[70] Y. Bai and A. J. Long, *Six Flavor Quark Matter*, *JHEP* **06** (2018) 072 [1804.10249].

[71] S. R. Coleman, *Q-balls*, *Nucl. Phys. B* **262** (1985) 263.

[72] A. Kusenko and M. E. Shaposhnikov, *Supersymmetric Q balls as dark matter*, *Phys. Lett. B* **418** (1998) 46 [hep-ph/9709492].

[73] E. Krylov, A. Levin and V. Rubakov, *Cosmological phase transition, baryon asymmetry and dark matter Q-balls*, *Phys. Rev. D* **87** (2013) 083528 [1301.0354].

[74] E. Aubourg, P. Bareyre, S. Bréhin, M. Gros, M. Lachièze-Rey, B. Laurent et al., *Evidence for gravitational microlensing by dark objects in the Galactic halo*, *Nature* **365** (1993) 623.

[75] P. O. Mazur and E. Mottola, *Gravitational vacuum condensate stars*, *Proc. Nat. Acad. Sci.* **101** (2004) 9545 [gr-qc/0407075].

[76] G. Chapline and P. H. Frampton, *A new direction for dark matter research: intermediate mass compact halo objects*, *JCAP* **11** (2016) 042 [1608.04297].

[77] Y. B. Zel'dovich and I. D. Novikov, *The Hypothesis of Cores Retarded during Expansion and the Hot Cosmological Model*, *Soviet Astronomy AJ* **10** (1967) 602.

[78] S. Hawking, *Gravitationally collapsed objects of very low mass*, *Mon. Not. Roy. Astron. Soc.* **152** (1971) 75.

[79] B. J. Carr and S. W. Hawking, *Black holes in the early Universe*, *Mon. Not. Roy. Astron. Soc.* **168** (1974) 399.

[80] G. F. Chapline, *Cosmological effects of primordial black holes*, *Nature* **253** (1975) 251.

[81] B. J. Carr, *The Primordial black hole mass spectrum*, *Astrophys. J.* **201** (1975) 1.

[82] B. Carr, K. Kohri, Y. Sendouda and J. Yokoyama, *Constraints on primordial black holes*, *Rept. Prog. Phys.* **84** (2021) 116902 [2002.12778].

[83] B. J. Carr, K. Kohri, Y. Sendouda and J. Yokoyama, *New cosmological constraints on primordial black holes*, *Phys. Rev. D* **81** (2010) 104019 [0912.5297].

[84] B. Carr and F. Kuhnel, *Primordial Black Holes as Dark Matter: Recent Developments*, *Ann. Rev. Nucl. Part. Sci.* **70** (2020) 355 [2006.02838].

[85] A. M. Green and B. J. Kavanagh, *Primordial Black Holes as a dark matter candidate*, *J. Phys. G* **48** (2021) 043001 [2007.10722].

[86] A. Hook, *TASI Lectures on the Strong CP Problem and Axions*, *PoS* **TASI2018** (2019) 004 [1812.02669].

[87] S. S. Gershtein and Y. B. Zel'dovich, *Rest Mass of Muonic Neutrino and Cosmology*, *ZhETF Pisma Redaktsiiu* **4** (1966) 174.

[88] R. Cowsik and J. McClelland, *An Upper Limit on the Neutrino Rest Mass*, *Phys. Rev. Lett.* **29** (1972) 669.

[89] M. I. Vysotsky, A. D. Dolgov and Y. B. Zeldovich, *Cosmological Restriction on Neutral Lepton Masses*, *JETP Lett.* **26** (1977) 188.

[90] K. Sato and M. Kobayashi, *Cosmological Constraints on the Mass and the Number of Heavy Lepton Neutrinos*, *Prog. Theor. Phys.* **58** (1977) 1775.

[91] P. Hut, *Limits on Masses and Number of Neutral Weakly Interacting Particles*, *Phys. Lett. B* **69** (1977) 85.

[92] D. A. Dicus, E. W. Kolb and V. L. Teplitz, *Cosmological upper bound on heavy-neutrino lifetimes*, *Phys. Rev. Lett.* **39** (1977) 168.

[93] T. R. Slatyer, *Indirect Detection of Dark Matter*, in *Theoretical Advanced Study Institute in Elementary Particle Physics: Anticipating the Next Discoveries in Particle Physics*, pp. 297–353, 2018, 1710.05137, DOI.

[94] G. Steigman, B. Dasgupta and J. F. Beacom, *Precise Relic WIMP Abundance and its Impact on Searches for Dark Matter Annihilation*, *Phys. Rev. D* **86** (2012) 023506 [1204.3622].

[95] M. W. Goodman and E. Witten, *Detectability of certain dark-matter candidates*, *Phys. Rev. D* **31** (1985) 3059.

[96] XENON collaboration, E. Aprile et al., *Dark Matter Search Results from a One Ton-Year Exposure of XENON1T*, *Phys. Rev. Lett.* **121** (2018) 111302 [1805.12562].

[97] Y. Kahn and T. Lin, *Searches for light dark matter using condensed matter systems*, 2108.03239.

[98] A. K. Drukier, K. Freese and D. N. Spergel, *Detecting Cold Dark Matter Candidates*, *Phys. Rev. D* **33** (1986) 3495.

[99] R. Bernabei et al., *First model independent results from DAMA/LIBRA-phase2*, *Nucl. Phys. Atom. Energy* **19** (2018) 307 [1805.10486].

[100] XENON collaboration, E. Aprile et al., *Excess electronic recoil events in XENON1T*, *Phys. Rev. D* **102** (2020) 072004 [2006.09721].

[101] P. Adari, A. Aguilar-Arevalo, D. Amidei, G. Angloher, E. Armengaud, C. Augier et al., *EXCESS workshop: Descriptions of rising low-energy spectra*, *arXiv e-prints* (2022) arXiv:2202.05097 [2202.05097].

[102] N. Kurinsky, D. Baxter, Y. Kahn and G. Krnjaic, *Dark matter interpretation of excesses in multiple direct detection experiments*, *Phys. Rev. D* **102** (2020) 015017 [2002.06937].

[103] R. K. Leane et al., *Snowmass2021 Cosmic Frontier White Paper: Puzzling Excesses in Dark Matter Searches and How to Resolve Them*, 2203.06859.

[104] J. E. Gunn, B. W. Lee, I. Lerche, D. N. Schramm and G. Steigman, *Some astrophysical consequences of the existence of a heavy stable neutral lepton.*, *Astrophysical Journal* **223** (1978) 1015.

[105] F. W. Stecker, *The cosmic gamma -ray background from the annihilation of primordial stable neutral heavy leptons.*, *Astrophysical Journal* **223** (1978) 1032.

[106] J. Silk and M. Srednicki, *Cosmic-ray antiprotons as a probe of a photino-dominated universe*, *Phys. Rev. Lett.* **53** (1984) 624.

[107] M. Kamionkowski and M. S. Turner, *Distinctive positron feature from particle dark-matter annihilations in the galatic halo*, *Phys. Rev. D* **43** (1991) 1774.

[108] J. Ellis, R. Flores, K. Freese, S. Ritz, D. Seckel and J. Silk, *Cosmic ray constraints on the annihilations of relic particles in the galactic halo*, *Physics Letters B* **214** (1988) 403.

[109] F. W. Stecker, S. Rudaz and T. F. Walsh, *Galactic antiprotons from photinos*, *Phys. Rev. Lett.* **55** (1985) 2622.

[110] MAGIC, Fermi-LAT collaboration, M. L. Ahnen et al., *Limits to Dark Matter Annihilation Cross-Section from a Combined Analysis of MAGIC and Fermi-LAT Observations of Dwarf Satellite Galaxies*, *JCAP* **02** (2016) 039 [1601.06590].

[111] C. A. Argüelles, A. Diaz, A. Kheirandish, A. Olivares-Del-Campo, I. Safa and A. C. Vincent, *Dark matter annihilation to neutrinos*, *Rev. Mod. Phys.* **93** (2021) 035007 [1912.09486].

[112] Super-Kamiokande collaboration, K. Choi et al., *Search for neutrinos from annihilation of captured low-mass dark matter particles in the Sun by Super-Kamiokande*, *Phys. Rev. Lett.* **114** (2015) 141301 [1503.04858].

[113] ANTARES collaboration, S. Adrian-Martinez et al., *Limits on Dark Matter Annihilation in the Sun using the ANTARES Neutrino Telescope*, *Phys. Lett. B* **759** (2016) 69 [1603.02228].

[114] IceCube collaboration, R. Abbasi et al., *Search for GeV-scale dark matter annihilation in the Sun with IceCube DeepCore*, *Phys. Rev. D* **105** (2022) 062004 [2111.09970].

[115] R. K. Leane, K. C. Y. Ng and J. F. Beacom, *Powerful Solar Signatures of Long-Lived Dark Mediators*, *Phys. Rev. D* **95** (2017) 123016 [1703.04629].

[116] C. Arina, M. Backović, J. Heisig and M. Lucente, *Solar γ rays as a complementary probe of dark matter*, *Phys. Rev. D* **96** (2017) 063010 [1703.08087].

[117] HAWC collaboration, A. Albert et al., *Constraints on Spin-Dependent Dark Matter Scattering with Long-Lived Mediators from TeV Observations of the Sun with HAWC*, *Phys. Rev. D* **98** (2018) 123012 [1808.05624].

[118] Fermi-LAT collaboration, M. Ajello et al., *Fermi-LAT Observations of High-Energy γ-Ray Emission Toward the Galactic Center*, *Astrophys. J.* **819** (2016) 44 [1511.02938].

[119] Fermi-LAT collaboration, M. Ackermann et al., *The Fermi Galactic Center GeV Excess and Implications for Dark Matter*, *Astrophys. J.* **840** (2017) 43 [1704.03910].

[120] L. Goodenough and D. Hooper, *Possible Evidence For Dark Matter Annihilation In The Inner Milky Way From The Fermi Gamma Ray Space Telescope*, 0910.2998.

[121] A. Cuoco, M. Krämer and M. Korsmeier, *Novel dark matter constraints from antiprotons in light of ams-02*, *Phys. Rev. Lett.* **118** (2017) 191102.

[122] M.-Y. Cui, Q. Yuan, Y.-L. S. Tsai and Y.-Z. Fan, *Possible dark matter annihilation signal in the ams-02 antiproton data*, *Phys. Rev. Lett.* **118** (2017) 191101.

[123] AMS collaboration, M. Aguilar et al., *Towards Understanding the Origin of Cosmic-Ray Positrons*, *Phys. Rev. Lett.* **122** (2019) 041102.

[124] T. Siegert, R. Diehl, G. Khachatryan, M. G. H. Krause, F. Guglielmetti, J. Greiner et al., *Gamma-ray spectroscopy of Positron Annihilation in the Milky Way*, *Astron. Astrophys.* **586** (2016) A84 [1512.00325].

[125] E. Bulbul, M. Markevitch, A. Foster, R. K. Smith, M. Loewenstein and S. W. Randall, *Detection of An Unidentified Emission Line in the Stacked X-ray spectrum of Galaxy Clusters*, *Astrophys. J.* **789** (2014) 13 [1402.2301].

[126] A. Boyarsky, O. Ruchayskiy, D. Iakubovskyi and J. Franse, *Unidentified Line in X-Ray Spectra of the Andromeda Galaxy and Perseus Galaxy Cluster*, *Phys. Rev. Lett.* **113** (2014) 251301 [1402.4119].

[127] S. Matsumoto, K. Fujii, T. Honda, S. Kanemura, T. Nabeshima, N. Okada et al., *Observing the Coupling between Dark Matter and Higgs Boson at the ILC*, in *International Linear Collider Workshop*, 6, 2010, 1006.5268.

[128] F. Kahlhoefer, *Review of LHC Dark Matter Searches*, *Int. J. Mod. Phys. A* **32** (2017) 1730006 [1702.02430].

[129] A. Boveia and C. Doglioni, *Dark Matter Searches at Colliders*, *Ann. Rev. Nucl. Part. Sci.* **68** (2018) 429 [1810.12238].

[130] M. Y. Khlopov, *Primordial Black Holes*, *Res. Astron. Astrophys.* **10** (2010) 495 [0801.0116].

[131] C.-P. Ma and E. Bertschinger, *Cosmological perturbation theory in the synchronous versus conformal Newtonian gauge*, astro-ph/9401007.

[132] B. J. Carr, *The primordial black hole mass spectrum.*, *Astrophysical Journal* **201** (1975) 1.

[133] M. Shibata and M. Sasaki, *Black hole formation in the Friedmann universe: Formulation and computation in numerical relativity*, *Phys. Rev. D* **60** (1999) 084002 [gr-qc/9905064].

[134] I. Musco, J. C. Miller and L. Rezzolla, *Computations of primordial black hole formation*, *Class. Quant. Grav.* **22** (2005) 1405 [gr-qc/0412063].

[135] I. Musco, J. C. Miller and A. G. Polnarev, *Primordial black hole formation in the radiative era: Investigation of the critical nature of the collapse*, *Class. Quant. Grav.* **26** (2009) 235001 [0811.1452].

[136] T. Harada, C.-M. Yoo and K. Kohri, *Threshold of primordial black hole formation*, *Phys. Rev. D* **88** (2013) 084051 [1309.4201].

[137] P. Villanueva-Domingo, O. Mena and S. Palomares-Ruiz, *A brief review on primordial black holes as dark matter*, *Front. Astron. Space Sci.* **8** (2021) 87 [2103.12087].

[138] W. H. Press and P. Schechter, *Formation of galaxies and clusters of galaxies by selfsimilar gravitational condensation*, *Astrophys. J.* **187** (1974) 425.

[139] V. De Luca, G. Franciolini, A. Kehagias, M. Peloso, A. Riotto and C. Ünal, *The Ineludible non-Gaussianity of the Primordial Black Hole Abundance*, *JCAP* **07** (2019) 048 [1904.00970].

[140] V. Atal and C. Germani, *The role of non-gaussianities in Primordial Black Hole formation*, *Phys. Dark Univ.* **24** (2019) 100275 [1811.07857].

[141] M. Boudaud and M. Cirelli, *Voyager 1 $e^{\pm}$ Further Constrain Primordial Black Holes as Dark Matter*, *Phys. Rev. Lett.* **122** (2019) 041104 [1807.03075].

[142] N. Smyth, S. Profumo, S. English, T. Jeltema, K. McKinnon and P. Guhathakurta, *Updated Constraints on Asteroid-Mass Primordial Black Holes as Dark Matter*, *Phys. Rev. D* **101** (2020) 063005 [1910.01285].

[143] K. Griest, A. M. Cieplak and M. J. Lehner, *New Limits on Primordial Black Hole Dark Matter from an Analysis of Kepler Source Microlensing Data*, *Phys. Rev. Lett.* **111** (2013) 181302.

[144] MACHO collaboration, R. A. Allsman et al., *MACHO project limits on black hole dark matter in the 1-30 solar mass range*, *Astrophys. J. Lett.* **550** (2001) L169 [astro-ph/0011506].

[145] EROS-2 collaboration, P. Tisserand et al., *Limits on the Macho Content of the Galactic Halo from the EROS-2 Survey of the Magellanic Clouds*, *Astron. Astrophys.* **469** (2007) 387 [astro-ph/0607207].

[146] L. Wyrzykowski et al., *The OGLE View of Microlensing towards the Magellanic Clouds. IV. OGLE-III SMC Data and Final Conclusions on MACHOs*, *Mon. Not. Roy. Astron. Soc.* **416** (2011) 2949 [1106.2925].

[147] T. D. Brandt, *Constraints on MACHO Dark Matter from Compact Stellar Systems in Ultra-Faint Dwarf Galaxies*, *Astrophys. J. Lett.* **824** (2016) L31 [1605.03665].

[148] Y. Ali-Haïmoud and M. Kamionkowski, *Cosmic microwave background limits on accreting primordial black holes*, *Phys. Rev. D* **95** (2017) 043534 [1612.05644].

[149] M. Raidal, V. Vaskonen and H. Veermäe, *Gravitational Waves from Primordial Black Hole Mergers*, *JCAP* **09** (2017) 037 [1707.01480].

[150] LIGO Scientific, Virgo collaboration, B. P. Abbott et al., *Search for Subsolar Mass Ultracompact Binaries in Advanced LIGO's Second Observing Run*, *Phys. Rev. Lett.* **123** (2019) 161102 [1904.08976].

[151] M. Zumalacarregui and U. Seljak, *Limits on stellar-mass compact objects as dark matter from gravitational lensing of type Ia supernovae*, *Phys. Rev. Lett.* **121** (2018) 141101 [1712.02240].

[152] B. J. Carr, K. Kohri, Y. Sendouda and J. Yokoyama, *Constraints on primordial black holes from the Galactic gamma-ray background*, *Phys. Rev. D* **94** (2016) 044029 [1604.05349].

[153] A. Arbey, J. Auffinger and J. Silk, *Constraining primordial black hole masses with the isotropic gamma ray background*, *Phys. Rev. D* **101** (2020) 023010 [1906.04750].

[154] G. Ballesteros, J. Coronado-Blázquez and D. Gaggero, *X-ray and gamma-ray limits on the primordial black hole abundance from Hawking radiation*, *Phys. Lett. B* **808** (2020) 135624 [1906.10113].

[155] R. Laha, J. B. Muñoz and T. R. Slatyer, *INTEGRAL constraints on primordial black holes and particle dark matter*, *Phys. Rev. D* **101** (2020) 123514 [2004.00627].

[156] A. Coogan, L. Morrison and S. Profumo, *Direct Detection of Hawking Radiation from Asteroid-Mass Primordial Black Holes*, *Phys. Rev. Lett.* **126** (2021) 171101 [2010.04797].

[157] T. Siegert, C. Boehm, F. Calore, R. Diehl, M. G. H. Krause, P. D. Serpico et al., *An INTEGRAL/SPI view of reticulum II: particle dark matter and primordial black holes limits in the MeV range*, *Mon. Not. Roy. Astron. Soc.* **511** (2022) 914 [2109.03791].

[158] J. Iguaz, P. D. Serpico and T. Siegert, *Isotropic X-ray bound on Primordial Black Hole Dark Matter*, *Phys. Rev. D* **103** (2021) 103025 [2104.03145].

[159] S. Chen, H.-H. Zhang and G. Long, *Revisiting the constraints on primordial black hole abundance with the isotropic gamma-ray background*, *Phys. Rev. D* **105** (2022) 063008 [2112.15463].

[160] C. M. Lee and M. Ho Chan, *The Evaporating Primordial Black Hole Fraction in Cool-core Galaxy Clusters*, *Astrophys. J.* **912** (2021) 24 [2103.12354].

[161] J. Berteaud, F. Calore, J. Iguaz, P. D. Serpico and T. Siegert, *Strong constraints on primordial black hole dark matter from 16 years of INTEGRAL/SPI observations*, 2202.07483.

[162] S. Wang, D.-M. Xia, X. Zhang, S. Zhou and Z. Chang, *Constraining primordial black holes as dark matter at JUNO*, *Phys. Rev. D* **103** (2021) 043010 [2010.16053].

[163] V. De Romeri, P. Martínez-Miravé and M. Tórtola, *Signatures of primordial black hole dark matter at DUNE and THEIA*, *JCAP* **10** (2021) 051 [2106.05013].

[164] R. Calabrese, D. F. G. Fiorillo, G. Miele, S. Morisi and A. Palazzo, *Primordial black hole dark matter evaporating on the neutrino floor*, *Phys. Lett. B* **829** (2022) 137050 [2106.02492].

[165] N. Bernal, V. Muñoz Albornoz, S. Palomares-Ruiz and P. Villanueva-Domingo, *Current and future neutrino limits on the abundance of primordial black holes*, 2203.14979.

[166] W. DeRocco and P. W. Graham, *Constraining Primordial Black Hole Abundance with the Galactic 511 keV Line*, *Phys. Rev. Lett.* **123** (2019) 251102 [1906.07740].

[167] R. Laha, *Primordial Black Holes as a Dark Matter Candidate Are Severely Constrained by the Galactic Center 511 keV γ -Ray Line*, *Phys. Rev. Lett.* **123** (2019) 251101 [1906.09994].

[168] V. Poulin, J. Lesgourgues and P. D. Serpico, *Cosmological constraints on exotic injection of electromagnetic energy*, *JCAP* **03** (2017) 043 [1610.10051].

[169] S. Clark, B. Dutta, Y. Gao, L. E. Strigari and S. Watson, *Planck Constraint on Relic Primordial Black Holes*, *Phys. Rev. D* **95** (2017) 083006 [1612.07738].

[170] P. Stöcker, M. Krämer, J. Lesgourgues and V. Poulin, *Exotic energy injection with ExoCLASS: Application to the Higgs portal model and evaporating black holes*, *JCAP* **03** (2018) 018 [1801.01871].

[171] H. Poulter, Y. Ali-Haïmoud, J. Hamann, M. White and A. G. Williams, *CMB constraints on ultra-light primordial black holes with extended mass distributions*, 1907.06485.

[172] S. K. Acharya and R. Khatri, *CMB and BBN constraints on evaporating primordial black holes revisited*, *JCAP* **06** (2020) 018 [2002.00898].

[173] J. Cang, Y. Gao and Y. Ma, *Prospects of Future CMB Anisotropy Probes for Primordial Black Holes*, *JCAP* **05** (2021) 051 [2011.12244].

[174] H. Kim, *A constraint on light primordial black holes from the interstellar medium temperature*, *Mon. Not. Roy. Astron. Soc.* **504** (2021) 5475 [2007.07739].

[175] R. Laha, P. Lu and V. Takhistov, *Gas heating from spinning and non-spinning evaporating primordial black holes*, *Phys. Lett. B* **820** (2021) 136459 [2009.11837].

[176] M. H. Chan and C. M. Lee, *Constraining Primordial Black Hole Fraction at the Galactic Centre using radio observational data*, *Mon. Not. Roy. Astron. Soc.* **497** (2020) 1212 [2007.05677].

[177] B. Dutta, A. Kar and L. E. Strigari, *Constraints on MeV dark matter and primordial black holes: Inverse Compton signals at the SKA*, *JCAP* **03** (2021) 011 [2010.05977].

[178] S. Clark, B. Dutta, Y. Gao, Y.-Z. Ma and L. E. Strigari, *21 cm limits on decaying dark matter and primordial black holes*, *Phys. Rev. D* **98** (2018) 043006 [1803.09390].

[179] A. Halder and M. Pandey, *Probing the effects of primordial black holes on 21-cm EDGES signal along with interacting dark energy and dark matter–baryon scattering*, *Mon. Not. Roy. Astron. Soc.* **508** (2021) 3446 [2101.05228].

[180] A. Halder and S. Banerjee, *Bounds on abundance of primordial black hole and dark matter from EDGES 21-cm signal*, *Phys. Rev. D* **103** (2021) 063044 [2102.00959].

[181] P. K. Natwariya, A. C. Nayak and T. Srivastava, *Constraining spinning primordial black holes with global 21-cm signal*, *Mon. Not. Roy. Astron. Soc.* **510** (2021) 4236 [2107.12358].

[182] J. Cang, Y. Gao and Y.-Z. Ma, *21-cm constraints on spinning primordial black holes*, *JCAP* **03** (2022) 012 [2108.13256].

[183] A. K. Saha and R. Laha, *Sensitivities on non-spinning and spinning primordial black hole dark matter with global 21 cm troughs*, 2112.10794.

[184] P. Montero-Camacho, X. Fang, G. Vasquez, M. Silva and C. M. Hirata, *Revisiting constraints on asteroid-mass primordial black holes as dark matter candidates*, *JCAP* **08** (2019) 031 [1906.05950].

[185] Y. Génolini, P. Serpico and P. Tinyakov, *Revisiting primordial black hole capture into neutron stars*, *Phys. Rev. D* **102** (2020) 083004 [2006.16975].

[186] A. Katz, J. Kopp, S. Sibiryakov and W. Xue, *Femtolensing by Dark Matter Revisited*, *JCAP* **12** (2018) 005 [1807.11495].

[187] W. H. Press and D. N. Spergel, *Capture by the sun of a galactic population of weakly interacting, massive particles*, *Astrophysical Journal* **296** (1985) 679.

[188] A. Gould, *Resonant Enhancements in WIMP Capture by the Earth*, *Astrophys. J.* **321** (1987) 571.

[189] A. Gould, *WIMP Distribution in and Evaporation From the Sun*, *Astrophys. J.* **321** (1987) 560.

[190] G. Bertone and M. Fairbairn, *Compact Stars as Dark Matter Probes*, *Phys. Rev. D* **77** (2008) 043515 [0709.1485].

[191] C. Kouvaris, *WIMP Annihilation and Cooling of Neutron Stars*, *Phys. Rev. D* **77** (2008) 023006 [0708.2362].

[192] C. Kouvaris and P. Tinyakov, *Can Neutron stars constrain Dark Matter?*, *Phys. Rev. D* **82** (2010) 063531 [1004.0586].

[193] A. de Lavallaz and M. Fairbairn, *Neutron Stars as Dark Matter Probes*, *Phys. Rev. D* **81** (2010) 123521 [1004.0629].

[194] D. Hooper, D. Spolyar, A. Vallinotto and N. Y. Gnedin, *Inelastic Dark Matter As An Efficient Fuel For Compact Stars*, *Phys. Rev. D* **81** (2010) 103531 [1002.0005].

[195] M. McCullough and M. Fairbairn, *Capture of Inelastic Dark Matter in White Dwarves*, *Phys. Rev. D* **81** (2010) 083520 [1001.2737].

[196] J. Bramante, A. Delgado and A. Martin, *Multiscatter stellar capture of dark matter*, *Phys. Rev. D* **96** (2017) 063002 [1703.04043].

[197] M. Baryakhtar, J. Bramante, S. W. Li, T. Linden and N. Raj, *Dark Kinetic Heating of Neutron Stars and An Infrared Window On WIMPs, SIMPs, and Pure Higgsinos*, *Phys. Rev. Lett.* **119** (2017) 131801 [1704.01577].

[198] N. Raj, P. Tanedo and H.-B. Yu, *Neutron stars at the dark matter direct detection frontier*, *Phys. Rev. D* **97** (2018) 043006 [1707.09442].

[199] N. F. Bell, G. Busoni and S. Robles, *Heating up Neutron Stars with Inelastic Dark Matter*, *JCAP* **09** (2018) 018 [1807.02840].

[200] C.-S. Chen and Y.-H. Lin, *Reheating neutron stars with the annihilation of self-interacting dark matter*, *JHEP* **08** (2018) 069 [1804.03409].

[201] J. F. Acevedo, J. Bramante, R. K. Leane and N. Raj, *Warming Nuclear Pasta with Dark Matter: Kinetic and Annihilation Heating of Neutron Star Crusts*, *JCAP* **03** (2020) 038 [1911.06334].

[202] N. F. Bell, G. Busoni, M. E. Ramirez-Quezada, S. Robles and M. Virgato, *Improved treatment of dark matter capture in white dwarfs*, *JCAP* **10** (2021) 083 [2104.14367].

[203] K. Hamaguchi, N. Nagata and K. Yanagi, *Dark Matter Heating vs. Rotochemical Heating in Old Neutron Stars*, *Phys. Lett. B* **795** (2019) 484 [1905.02991].

[204] D. A. Camargo, F. S. Queiroz and R. Sturani, *Detecting Dark Matter with Neutron Star Spectroscopy*, *JCAP* **09** (2019) 051 [1901.05474].

[205] N. F. Bell, G. Busoni and S. Robles, *Capture of Leptophilic Dark Matter in Neutron Stars*, *JCAP* **06** (2019) 054 [1904.09803].

[206] R. Garani and J. Heeck, *Dark matter interactions with muons in neutron stars*, *Phys. Rev. D* **100** (2019) 035039 [1906.10145].

[207] A. Joglekar, N. Raj, P. Tanedo and H.-B. Yu, *Relativistic capture of dark matter by electrons in neutron stars*, *Phys. Lett.* **B** (2020) 135767 [1911.13293].

[208] A. Joglekar, N. Raj, P. Tanedo and H.-B. Yu, *Dark kinetic heating of neutron stars from contact interactions with relativistic targets*, *Phys. Rev. D* **102** (2020) 123002 [2004.09539].

[209] C. Ilie, J. Pilawa and S. Zhang, *Comment on "Multiscatter stellar capture of dark matter"*, *Phys. Rev. D* **102** (2020) 048301 [2005.05946].

[210] N. F. Bell, G. Busoni, S. Robles and M. Virgato, *Improved Treatment of Dark Matter Capture in Neutron Stars*, *JCAP* **09** (2020) 028 [2004.14888].

[211] J. Bramante, *Dark matter ignition of type Ia supernovae*, *Phys. Rev. Lett.* **115** (2015) 141301 [1505.07464].

[212] P. W. Graham, R. Janish, V. Narayan, S. Rajendran and P. Riggins, *White Dwarfs as Dark Matter Detectors*, *Phys. Rev. D* **98** (2018) 115027 [1805.07381].

[213] J. F. Acevedo and J. Bramante, *Supernovae Sparked By Dark Matter in White Dwarfs*, *Phys. Rev. D* **100** (2019) 043020 [1904.11993].

[214] G. D. Mack, J. F. Beacom and G. Bertone, *Towards Closing the Window on Strongly Interacting Dark Matter: Far-Reaching Constraints from Earth's Heat Flow*, *Phys. Rev. D* **76** (2007) 043523 [0705.4298].

[215] G. D. Mack and A. Manohar, *Closing the window on high-mass strongly interacting dark matter*, *Journal of Physics G Nuclear Physics* **40** (2013) 115202 [1211.1951].

[216] B. Chauhan and S. Mohanty, *Constraints on leptophilic light dark matter from internal heat flux of Earth*, *Phys. Rev. D* **94** (2016) 035024 [1603.06350].

[217] J. Bramante, A. Buchanan, A. Goodman and E. Lodhi, *Terrestrial and Martian Heat Flow Limits on Dark Matter*, *Phys. Rev. D* **101** (2020) 043001 [1909.11683].

[218] R. Garani and P. Tinyakov, *Constraints on Dark Matter from the Moon*, *Phys. Lett. B* **804** (2020) 135403 [1912.00443].

[219] S. L. Adler, *Planet-bound dark matter and the internal heat of Uranus, Neptune, and hot-Jupiter exoplanets*, *Phys. Lett. B* **671** (2009) 203 [0808.2823].

[220] S. Mitra, *Uranus' anomalously low excess heat constrains strongly interacting dark matter*, *Phys. Rev. D* **70** (2004) 103517 [astro-ph/0408341].

[221] M. Kawasaki, H. Murayama and T. Yanagida, *Can the strongly interacting dark matter be a heating source of Jupiter?*, *Prog. Theor. Phys.* **87** (1992) 685.

[222] R. K. Leane and J. Smirnov, *Exoplanets as Sub-GeV Dark Matter Detectors*, *Phys. Rev. Lett.* **126** (2021) 161101 [2010.00015].

[223] Super-Kamiokande collaboration, S. Desai et al., *Search for dark matter WIMPs using upward through-going muons in Super-Kamiokande*, *Phys. Rev. D* **70** (2004) 083523 [hep-ex/0404025].

[224] Super-Kamiokande collaboration, T. Tanaka et al., *An Indirect Search for WIMPs in the Sun using 3109.6 days of upward-going muons in Super-Kamiokande*, *Astrophys. J.* **742** (2011) 78 [1108.3384].

[225] ANTARES collaboration, S. Adrian-Martinez et al., *First results on dark matter annihilation in the Sun using the ANTARES neutrino telescope*, *JCAP* **11** (2013) 032 [1302.6516].

[226] ANTARES collaboration, S. Adrián-Martínez et al., *A search for Secluded Dark Matter in the Sun with the ANTARES neutrino telescope*, *JCAP* **05** (2016) 016 [1602.07000].

[227] IceCube collaboration, M. G. Aartsen et al., *Search for annihilating dark matter in the Sun with 3 years of IceCube data*, *Eur. Phys. J. C* **77** (2017) 146 [1612.05949].

[228] IceCube collaboration, M. G. Aartsen et al., *Improved limits on dark matter annihilation in the Sun with the 79-string IceCube detector and implications for supersymmetry*, *JCAP* **04** (2016) 022 [1601.00653].

[229] M. M. Boliev, S. V. Demidov, S. P. Mikheyev and O. V. Suvorova, *Search for muon signal from dark matter annihilations inthe Sun with the Baksan Underground Scintillator Telescope for 24.12 years*, *JCAP* **09** (2013) 019 [1301.1138].

[230] Baikal collaboration, A. D. Avrorin et al., *Search for neutrino emission from relic dark matter in the Sun with the Baikal NT200 detector*, *Astropart. Phys.* **62** (2015) 12 [1405.3551].

[231] M. Pospelov, A. Ritz and M. B. Voloshin, *Secluded WIMP Dark Matter*, *Phys. Lett. B* **662** (2008) 53 [0711.4866].

[232] B. Batell, M. Pospelov, A. Ritz and Y. Shang, *Solar Gamma Rays Powered by Secluded Dark Matter*, *Phys. Rev. D* **81** (2010) 075004 [0910.1567].

[233] P. Schuster, N. Toro and I. Yavin, *Terrestrial and Solar Limits on Long-Lived Particles in a Dark Sector*, *Phys. Rev. D* **81** (2010) 016002 [0910.1602].

[234] P. Schuster, N. Toro, N. Weiner and I. Yavin, *High Energy Electron Signals from Dark Matter Annihilation in the Sun*, *Phys. Rev. D* **82** (2010) 115012 [0910.1839].

[235] N. F. Bell and K. Petraki, *Enhanced neutrino signals from dark matter annihilation in the Sun via metastable mediators*, *JCAP* **04** (2011) 003 [1102.2958].

[236] R. Allahverdi, Y. Gao, B. Knockel and S. Shalgar, *Indirect Signals from Solar Dark Matter Annihilation to Long-lived Right-handed Neutrinos*, *Phys. Rev. D* **95** (2017) 075001 [1612.03110].

[237] C. Niblaeus, A. Beniwal and J. Edsjo, *Neutrinos and gamma rays from long-lived mediator decays in the Sun*, *JCAP* **11** (2019) 011 [1903.11363].

[238] A. Cuoco, P. De La Torre Luque, F. Gargano, M. Gustafsson, F. Loparco, M. N. Mazziotta et al., *A search for dark matter cosmic-ray electrons and positrons from the Sun with the Fermi Large Area Telescope*, *Phys. Rev. D* **101** (2020) 022002 [1912.09373].

[239] M. N. Mazziotta, F. Loparco, D. Serini, A. Cuoco, P. De La Torre Luque, F. Gargano et al., *Search for dark matter signatures in the gamma-ray emission towards the Sun with the Fermi Large Area Telescope*, *Phys. Rev. D* **102** (2020) 022003 [2006.04114].

[240] Fermi-LAT collaboration, D. Serini, F. Loparco and M. N. Mazziotta, *Constraints on dark matter scattering with long-lived mediators using gamma-rays from the Sun*, *PoS* **ICRC2019** (2020) 544.

[241] R. K. Leane, T. Linden, P. Mukhopadhyay and N. Toro, *Celestial-Body Focused Dark Matter Annihilation Throughout the Galaxy*, *Phys. Rev. D* **103** (2021) 075030 [2101.12213].

[242] R. K. Leane and T. Linden, *First Analysis of Jupiter in Gamma Rays and a New Search for Dark Matter*, 2104.02068.

[243] N. F. Bell, J. B. Dent and I. W. Sanderson, *Solar gamma ray constraints on dark matter annihilation to secluded mediators*, *Phys. Rev. D* **104** (2021) 023024 [2103.16794].

[244] M. H. Chan and C. M. Lee, *Constraining the spin-independent elastic scattering cross section of dark matter using the Moon as a detection target and the background neutrino data*, *Phys. Rev. D* **102** (2020) 023024 [2007.01589].

[245] N. F. Bell, M. J. Dolan and S. Robles, *Searching for dark matter in the Sun using Hyper-Kamiokande*, *JCAP* **11** (2021) 004 [2107.04216].

[246] I. Goldman and S. Nussinov, *Weakly Interacting Massive Particles and Neutron Stars*, *Phys. Rev. D* **40** (1989) 3221.

[247] A. Gould, B. T. Draine, R. W. Romani and S. Nussinov, *Neutron Stars: Graveyard of Charged Dark Matter*, *Phys. Lett. B* **238** (1990) 337.

[248] C. Kouvaris and P. Tinyakov, *Constraining Asymmetric Dark Matter through observations of compact stars*, *Phys. Rev. D* **83** (2011) 083512 [1012.2039].

[249] S. D. McDermott, H.-B. Yu and K. M. Zurek, *Constraints on Scalar Asymmetric Dark Matter from Black Hole Formation in Neutron Stars*, *Phys. Rev. D* **85** (2012) 023519 [1103.5472].

[250] C. Kouvaris and P. Tinyakov, *Excluding Light Asymmetric Bosonic Dark Matter*, *Phys. Rev. Lett.* **107** (2011) 091301 [1104.0382].

[251] T. Güver, A. E. Erkoca, M. Hall Reno and I. Sarcevic, *On the capture of dark matter by neutron stars*, *JCAP* **05** (2014) 013 [1201.2400].

[252] C. Kouvaris and P. Tinyakov, *(Not)-constraining heavy asymmetric bosonic dark matter*, *Phys. Rev. D* **87** (2013) 123537 [1212.4075].

[253] C. Kouvaris and P. Tinyakov, *Growth of Black Holes in the interior of Rotating Neutron Stars*, *Phys. Rev. D* **90** (2014) 043512 [1312.3764].

[254] N. F. Bell, A. Melatos and K. Petraki, *Realistic neutron star constraints on bosonic asymmetric dark matter*, *Phys. Rev. D* **87** (2013) 123507 [1301.6811].

[255] J. Bramante, K. Fukushima and J. Kumar, *Constraints on bosonic dark matter from observation of old neutron stars*, *Phys. Rev. D* **87** (2013) 055012 [1301.0036].

[256] A. O. Jamison, *Effects of gravitational confinement on bosonic asymmetric dark matter in stars*, *Phys. Rev. D* **88** (2013) 035004 [1304.3773].

[257] J. Bramante, K. Fukushima, J. Kumar and E. Stopnitzky, *Bounds on self-interacting fermion dark matter from observations of old neutron stars*, *Phys. Rev. D* **89** (2014) 015010 [1310.3509].

[258] J. Bramante and T. Linden, *Detecting Dark Matter with Imploding Pulsars in the Galactic Center*, *Phys. Rev. Lett.* **113** (2014) 191301 [1405.1031].

[259] R. Garani, Y. Genolini and T. Hambye, *New Analysis of Neutron Star Constraints on Asymmetric Dark Matter*, *JCAP* **05** (2019) 035 [1812.08773].

[260] G.-L. Lin and Y.-H. Lin, *Analysis on the black hole formations inside old neutron stars by isospin-violating dark matter with self-interaction*, *JCAP* **08** (2020) 022 [2004.05312].

[261] G. D. Starkman, A. Gould, R. Esmailzadeh and S. Dimopoulos, *Opening the window on strongly interacting dark matter*, *Phys. Rev. D* **41** (1990) 3594.

[262] J. F. Acevedo, J. Bramante, A. Goodman, J. Kopp and T. Opferkuch, *Dark Matter, Destroyer of Worlds: Neutrino, Thermal, and Existential Signatures from Black Holes in the Sun and Earth*, *JCAP* **04** (2021) 026 [2012.09176].

[263] A. R. Zentner, *High-Energy Neutrinos From Dark Matter Particle Self-Capture Within the Sun*, *Phys. Rev. D* **80** (2009) 063501 [0907.3448].

[264] C. Kouvaris, *Limits on Self-Interacting Dark Matter*, *Phys. Rev. Lett.* **108** (2012) 191301 [1111.4364].

[265] J. Fan, A. Katz and J. Shelton, *Direct and indirect detection of dissipative dark matter*, *JCAP* **06** (2014) 059 [1312.1336].

[266] J. Chen, Z.-L. Liang, Y.-L. Wu and Y.-F. Zhou, *Long-range self-interacting dark matter in the Sun*, *JCAP* **12** (2015) 021 [1505.04031].

[267] C.-S. Chen, G.-L. Lin and Y.-H. Lin, *Complementary Test of the Dark Matter Self-Interaction by Direct and Indirect Detections*, *JCAP* **01** (2016) 013 [1505.03781].

[268] C. Gaidau and J. Shelton, *A Solar System Test of Self-Interacting Dark Matter*, *JCAP* **06** (2019) 022 [1811.00557].

[269] B. Bertoni, A. E. Nelson and S. Reddy, *Dark Matter Thermalization in Neutron Stars*, *Phys. Rev. D* **88** (2013) 123505 [1309.1721].

[270] R. Garani, A. Gupta and N. Raj, *Observing the thermalization of dark matter in neutron stars*, *Phys. Rev. D* **103** (2021) 043019 [2009.10728].

[271] J. R. Neeley, M. Marengo, G. Bono, V. F. Braga, M. Dall'Ora, P. B. Stetson et al., *On the Distance of the Globular Cluster M4 (NGC 6121) Using RR Lyrae Stars. II. Mid-infrared Period-luminosity Relations.*, *Astrophysical Journal* **808** (2015) 11 [1505.07858].

[272] R. H. Helm, *Inelastic and Elastic Scattering of 187-Mev Electrons from Selected Even-Even Nuclei*, *Phys. Rev.* **104** (1956) 1466.

[273] CRESST collaboration, F. Petricca et al., *First results on low-mass dark matter from the CRESST-III experiment*, *J. Phys. Conf. Ser.* **1342** (2020) 012076 [1711.07692].

[274] SuperCDMS collaboration, R. Agnese et al., *Low-mass dark matter search with CDMSlite*, *Phys. Rev. D* **97** (2018) 022002 [1707.01632].

[275] R. Garani and S. Palomares-Ruiz, *Evaporation of dark matter from celestial bodies*, 2104.12757.

[276] PandaX-II collaboration, X. Ren et al., *Constraining Dark Matter Models with a Light Mediator at the PandaX-II Experiment*, *Phys. Rev. Lett.* **121** (2018) 021304 [1802.06912].

[277] S. Guillot, G. G. Pavlov, C. Reyes, A. Reisenegger, L. Rodriguez, B. Rangelov et al., *Hubble Space Telescope Nondetection of PSR J2144–3933: The Coldest Known Neutron Star*, *Astrophys. J.* **874** (2019) 175 [1901.07998].

[278] J. P. Gardner et al., *The James Webb Space Telescope*, *Space Sci. Rev.* **123** (2006) 485 [astro-ph/0606175].

[279] D. Crampton, L. Simard and D. Silva, *TMT Science and Instruments*, *Astrophys. Space Sci. Proc.* (2009) 279 [0801.3634].

[280] R. Maiolino et al., *A Community Science Case for E-ELT HIRES*, 1310.3163.

[281] T. W. Baumgarte and S. L. Shapiro, *Neutron Stars Harboring a Primordial Black Hole: Maximum Survival Time*, *Phys. Rev. D* **103** (2021) L081303 [2101.12220].

[282] C. B. Richards, T. W. Baumgarte and S. L. Shapiro, *Accretion onto a small black hole at the center of a neutron star*, *Phys. Rev. D* **103** (2021) 104009 [2102.09574].

[283] S. C. Schnauck, T. W. Baumgarte and S. L. Shapiro, *Accretion onto black holes inside neutron stars with piecewise-polytropic equations of state: Analytic and numerical treatments*, *Phys. Rev. D* **104** (2021) 123021 [2110.08285].

[284] P. Giffin, J. Lloyd, S. D. McDermott and S. Profumo, *Neutron Star Quantum Death by Small Black Holes*, 2105.06504.

[285] S. W. Randall, M. Markevitch, D. Clowe, A. H. Gonzalez and M. Bradac, *Constraints on the Self-Interaction Cross-Section of Dark Matter from Numerical Simulations of the Merging Galaxy Cluster 1E 0657-56*, *Astrophys. J.* **679** (2008) 1173 [0704.0261].

[286] LIGO Scientific, Virgo collaboration, B. P. Abbott et al., *GW190425: Observation of a Compact Binary Coalescence with Total Mass* $\sim 3.4 M_\odot$, *Astrophys. J. Lett.* **892** (2020) L3 [2001.01761].

[287] LIGO Scientific, Virgo collaboration, R. Abbott et al., *GW190814: Gravitational Waves from the Coalescence of a 23 Solar Mass Black Hole with a 2.6 Solar Mass Compact Object*, *Astrophys. J. Lett.* **896** (2020) L44 [2006.12611].

[288] LIGO Scientific, KAGRA, VIRGO collaboration, R. Abbott et al., *Observation of Gravitational Waves from Two Neutron Star–Black Hole Coalescences*, *Astrophys. J. Lett.* **915** (2021) L5 [2106.15163].

[289] R. N. Manchester, G. B. Hobbs, A. Teoh and M. Hobbs, *The Australia Telescope National Facility pulsar catalogue*, *Astron. J.* **129** (2005) 1993 [astro-ph/0412641].

[290] S. Shandera, D. Jeong and H. S. G. Gebhardt, *Gravitational Waves from Binary Mergers of Subsolar Mass Dark Black Holes*, *Phys. Rev. Lett.* **120** (2018) 241102 [1802.08206].

[291] C. Kouvaris, P. Tinyakov and M. H. G. Tytgat, *NonPrimordial Solar Mass Black Holes*, *Phys. Rev. Lett.* **121** (2018) 221102 [1804.06740].

[292] F. Capela, M. Pshirkov and P. Tinyakov, *Constraints on primordial black holes as dark matter candidates from capture by neutron stars*, *Phys. Rev. D* **87** (2013) 123524 [1301.4984].

[293] V. Takhistov, *Transmuted Gravity Wave Signals from Primordial Black Holes*, *Phys. Lett. B* **782** (2018) 77 [1707.05849].

[294] C. Conroy, A. Loeb and D. N. Spergel, *Evidence against Dark Matter Halos Surrounding the Globular Clusters MGC1 and NGC 2419*, *Astrophysical Journal* **741** (2011) 72 [1010.5783].

[295] S. Naoz and R. Narayan, *Globular Clusters and Dark Satellite Galaxies through the Stream Velocity*, *Astrophys. J. Lett.* **791** (2014) L8 [1407.3795].

[296] T. J. Hurst and A. R. Zentner, *On the Ejection of Dark Matter from Globular Clusters*, *Mon. Not. Roy. Astron. Soc.* **494** (2020) 4687 [1910.00665].

[297] K. M. Zurek, *Asymmetric Dark Matter: Theories, Signatures, and Constraints*, *Phys. Rept.* **537** (2014) 91 [1308.0338].

[298] K. Petraki and R. R. Volkas, *Review of asymmetric dark matter*, *Int. J. Mod. Phys. A* **28** (2013) 1330028 [1305.4939].

[299] P. Madau and M. Dickinson, *Cosmic Star Formation History*, *Ann. Rev. Astron. Astrophys.* **52** (2014) 415 [1403.0007].

[300] LIGO Scientific, Virgo collaboration, R. Abbott et al., *Population Properties of Compact Objects from the Second LIGO-Virgo Gravitational-Wave Transient Catalog*, *Astrophys. J. Lett.* **913** (2021) L7 [2010.14533].

[301] Z.-C. Chen and Q.-G. Huang, *Merger Rate Distribution of Primordial-Black-Hole Binaries*, *Astrophys. J.* **864** (2018) 61 [1801.10327].

[302] M. Raidal, C. Spethmann, V. Vaskonen and H. Veermäe, *Formation and Evolution of Primordial Black Hole Binaries in the Early Universe*, *JCAP* **02** (2019) 018 [1812.01930].

[303] F. Özel and P. Freire, *Masses, Radii, and the Equation of State of Neutron Stars*, *Ann. Rev. Astron. Astrophys.* **54** (2016) 401 [1603.02698].

[304] F. M. Jiménez-Esteban, S. Torres, A. Rebassa-Mansergas, G. Skorobogatov, E. Solano, C. Cantero et al., *A white dwarf catalogue from Gaia-DR2 and the Virtual Observatory*, *Monthly Notices of the Royal Astronomical Society* **480** (2018) 4505 [1807.02559].

[305] M. Sasaki, T. Suyama, T. Tanaka and S. Yokoyama, *Primordial Black Hole Scenario for the Gravitational-Wave Event GW150914*, *Phys. Rev. Lett.* **117** (2016) 061101 [1603.08338].

[306] Y. Ali-Haïmoud, E. D. Kovetz and M. Kamionkowski, *Merger rate of primordial black-hole binaries*, *Phys. Rev. D* **96** (2017) 123523 [1709.06576].

[307] M. Sasaki, T. Suyama, T. Tanaka and S. Yokoyama, *Primordial black holes—perspectives in gravitational wave astronomy*, *Class. Quant. Grav.* **35** (2018) 063001 [1801.05235].

[308] S. R. Taylor and J. R. Gair, *Cosmology with the lights off: standard sirens in the Einstein Telescope era*, *Phys. Rev. D* **86** (2012) 023502 [1204.6739].

[309] C. Porciani and P. Madau, *On the Association of gamma-ray bursts with massive stars: implications for number counts and lensing statistics*, *Astrophys. J.* **548** (2001) 522 [astro-ph/0008294].

[310] J. F. Navarro, C. S. Frenk and S. D. M. White, *The Structure of cold dark matter halos*, *Astrophys. J.* **462** (1996) 563 [astro-ph/9508025].

[311] J. F. Navarro, C. S. Frenk and S. D. M. White, *A Universal density profile from hierarchical clustering*, *Astrophys. J.* **490** (1997) 493 [astro-ph/9611107].

[312] M. Cautun, A. Benítez-Llambay, A. J. Deason, C. S. Frenk, A. Fattahi, F. A. Gómez et al., *The milky way total mass profile as inferred from Gaia DR2*, *Monthly Notices of the Royal Astronomical Society* **494** (2020) 4291 [1911.04557].

[313] M. Evans et al., *A Horizon Study for Cosmic Explorer: Science, Observatories, and Community*, 2109.09882.

[314] M. Maggiore et al., *Science Case for the Einstein Telescope*, *JCAP* **03** (2020) 050 [1912.02622].

[315] T. Nakamura et al., *Pre-DECIGO can get the smoking gun to decide the astrophysical or cosmological origin of GW150914-like binary black holes*, *PTEP* **2016** (2016) 093E01 [1607.00897].

[316] S. R. Taylor, J. R. Gair and I. Mandel, *Hubble without the Hubble: Cosmology using advanced gravitational-wave detectors alone*, *Phys. Rev. D* **85** (2012) 023535 [1108.5161].

[317] B. R. Safdi, Z. Sun and A. Y. Chen, *Detecting Axion Dark Matter with Radio Lines from Neutron Star Populations*, *Phys. Rev. D* **99** (2019) 123021 [1811.01020].

[318] R. Nan, D. Li, C. Jin, Q. Wang, L. Zhu, W. Zhu et al., *The Five-Hundred Aperture Spherical Radio Telescope (fast) Project*, *International Journal of Modern Physics D* **20** (2011) 989 [1105.3794].

[319] A. Weltman et al., *Fundamental physics with the Square Kilometre Array*, *Publ. Astron. Soc. Austral.* **37** (2020) e002 [1810.02680].

[320] V. Takhistov, G. M. Fuller and A. Kusenko, *Test for the Origin of Solar Mass Black Holes*, *Phys. Rev. Lett.* **126** (2021) 071101 [2008.12780].

[321] KAGRA, LIGO Scientific, Virgo, VIRGO collaboration, B. P. Abbott et al., *Prospects for observing and localizing gravitational-wave transients with Advanced LIGO, Advanced Virgo and KAGRA*, *Living Rev. Rel.* **21** (2018) 3 [1304.0670].

[322] O. A. Hannuksela, T. E. Collett, M. Çalışkan and T. G. F. Li, *Localizing merging black holes with sub-arcsecond precision using gravitational-wave lensing*, *Mon. Not. Roy. Astron. Soc.* **498** (2020) 3395 [2004.13811].

[323] H. Yang, W. E. East and L. Lehner, *Can we distinguish low mass black holes in neutron star binaries?*, *Astrophys. J.* **856** (2018) 110 [1710.05891].

[324] M. Fasano, K. W. K. Wong, A. Maselli, E. Berti, V. Ferrari and B. S. Sathyaprakash, *Distinguishing double neutron star from neutron star-black hole binary populations with gravitational wave observations*, *Phys. Rev. D* **102** (2020) 023025 [2005.01726].

[325] S. Datta, K. S. Phukon and S. Bose, *Recognizing black holes in gravitational-wave observations: Challenges in telling apart impostors in mass-gap binaries*, *Phys. Rev. D* **104** (2021) 084006 [2004.05974].

[326] D. N. Page, *Particle Emission Rates from a Black Hole: Massless Particles from an Uncharged, Nonrotating Hole*, *Phys. Rev. D* **13** (1976) 198.

[327] D. N. Page, *Particle Emission Rates from a Black Hole. 2. Massless Particles from a Rotating Hole*, *Phys. Rev. D* **14** (1976) 3260.

[328] J. H. MacGibbon and B. R. Webber, *Quark and gluon jet emission from primordial black holes: The instantaneous spectra*, *Phys. Rev. D* **41** (1990) 3052.

[329] J. H. MacGibbon, *Quark and gluon jet emission from primordial black holes. 2. The Lifetime emission*, *Phys. Rev. D* **44** (1991) 376.

[330] J. H. MacGibbon, B. J. Carr and D. N. Page, *Do Evaporating Black Holes Form Photospheres?*, *Phys. Rev. D* **78** (2008) 064043 [0709.2380].

[331] A. Arbey and J. Auffinger, *BlackHawk: A public code for calculating the Hawking evaporation spectra of any black hole distribution*, *Eur. Phys. J. C* **79** (2019) 693 [1905.04268].

[332] A. Arbey and J. Auffinger, *Physics Beyond the Standard Model with BlackHawk v2.0*, *Eur. Phys. J. C* **81** (2021) 910 [2108.02737].

[333] S. Ando and K. Sato, *Relic neutrino background from cosmological supernovae*, *New J. Phys.* **6** (2004) 170 [astro-ph/0410061].

[334] J. F. Beacom, *The Diffuse Supernova Neutrino Background*, *Ann. Rev. Nucl. Part. Sci.* **60** (2010) 439 [1004.3311].

[335] C. Lunardini, *Diffuse supernova neutrinos at underground laboratories*, *Astropart. Phys.* **79** (2016) 49 [1007.3252].

[336] Super-Kamiokande collaboration, K. Bays et al., *Supernova Relic Neutrino Search at Super-Kamiokande*, *Phys. Rev. D* **85** (2012) 052007 [1111.5031].

[337] KamLAND collaboration, A. Gando et al., *A study of extraterrestrial antineutrino sources with the KamLAND detector*, *Astrophys. J.* **745** (2012) 193 [1105.3516].

[338] Borexino collaboration, M. Agostini et al., *Search for low-energy neutrinos from astrophysical sources with Borexino*, *Astropart. Phys.* **125** (2021) 102509 [1909.02422].

[339] S. Clesse and J. García-Bellido, *Massive Primordial Black Holes from Hybrid Inflation as Dark Matter and the seeds of Galaxies*, *Phys. Rev. D* **92** (2015) 023524 [1501.07565].

[340] B. Carr, T. Tenkanen and V. Vaskonen, *Primordial black holes from inflaton and spectator field perturbations in a matter-dominated era*, *Phys. Rev. D* **96** (2017) 063507 [1706.03746].

[341] T. Matsuda, *Primordial black holes from cosmic necklaces*, *JHEP* **04** (2006) 017 [hep-ph/0509062].

[342] J. F. Beacom and M. R. Vagins, *GADZOOKS! Anti-neutrino spectroscopy with large water Cherenkov detectors*, *Phys. Rev. Lett.* **93** (2004) 171101 [hep-ph/0309300].

[343] Hyper-Kamiokande collaboration, K. Abe et al., *Hyper-Kamiokande Design Report*, 1805.04163.

[344] P. N. Okele and M. J. Rees, *Observational consequences of positron production by evaporating black holes*, *Astronomy and Astrophysics* **81** (1980) 263.

[345] J. H. MacGibbon and B. J. Carr, *Cosmic Rays from Primordial Black Holes*, *Astrophysical Journal* **371** (1991) 447.

[346] P. H. Frampton and T. W. Kephart, *Primordial black holes, Hawking radiation and the early universe*, *Mod. Phys. Lett. A* **20** (2005) 1573 [hep-ph/0503267].

[347] C. Bambi, A. D. Dolgov and A. A. Petrov, *Primordial black holes and the observed Galactic 511-keV line*, *Phys. Lett. B* **670** (2008) 174 [0801.2786].

[348] C. Keith and D. Hooper, *511 keV excess and primordial black holes*, *Phys. Rev. D* **104** (2021) 063033 [2103.08611].

[349] N. Prantzos et al., *The 511 keV emission from positron annihilation in the Galaxy*, *Rev. Mod. Phys.* **83** (2011) 1001 [1009.4620].

[350] A. Alexis, P. Jean, P. Martin and K. Ferriere, *Monte Carlo modelling of the propagation and annihilation of nucleosynthesis positrons in the Galaxy*, *Astron. Astrophys.* **564** (2014) A108 [1402.6110].

[351] J. F. Beacom and H. Yuksel, *Stringent constraint on galactic positron production*, *Phys. Rev. Lett.* **97** (2006) 071102 [astro-ph/0512411].

[352] J. C. Higdon, R. E. Lingenfelter and R. E. Rothschild, *The Galactic Positron Annihilation Radiation & The Propagation of Positrons in the Interstellar Medium*, *Astrophys. J.* **698** (2009) 350 [0711.3008].

[353] F. H. Panther, *Positron Transport and Annihilation in the Galactic Bulge*, *Galaxies* **6** (2018) 39 [1801.09365].

[354] R. Bartels, D. Gaggero and C. Weniger, *Prospects for indirect dark matter searches with MeV photons*, *JCAP* **05** (2017) 001 [1703.02546].

[355] A. W. Strong, I. V. Moskalenko and O. Reimer, *Diffuse continuum gamma-rays from the galaxy*, *Astrophys. J.* **537** (2000) 763 [astro-ph/9811296].

[356] A. W. Strong, H. Bloemen, R. Diehl, W. Hermsen and V. Schoenfelder, *Comptel skymapping: A New approach using parallel computing*, *Astrophys. Lett. Commun.* **39** (1999) 209 [astro-ph/9811211].

[357] A. W. Strong, *Interstellar Gamma Rays and Cosmic Rays:. New Insights from Fermi-Lat and Integral*, in *Cosmic Rays for Particle and Astroparticle Physics* (S. Giani, C. Leroy and P. G. Rancoita, eds.), pp. 473–481, June, 2011, 1101.1381, DOI.

[358] K. Watanabe, D. H. Hartmann, M. D. Leising and L. S. The, *The Diffuse gamma-ray background from supernovae*, *Astrophys. J.* **516** (1999) 285 [astro-ph/9809197].

[359] Y. Fukada, S. Hayakawa, M. Ikeda, I. Kasahara, F. Makino and Y. Tanaka, *Rocket Observation of Energy Spectrum of Diffuse Hard X-Rays*, *Astrophysics and Space Science* **32** (1975) L1.

[360] D. E. Gruber, J. L. Matteson, L. E. Peterson and G. V. Jung, *The spectrum of diffuse cosmic hard x-rays measured with heao-1*, *Astrophys. J.* **520** (1999) 124 [astro-ph/9903492].

[361] R. L. Kinzer, G. V. Jung, D. E. Gruber, J. L. Matteson, Peterson and L. E., *Diffuse Cosmic Gamma Radiation Measured by HEAO 1*, *Astrophysical Journal* **475** (1997) 361.

[362] G. Weidenspointner et al., *The comptel instrumental line background*, *AIP Conf. Proc.* **510** (2000) 581 [astro-ph/0012332].

[363] T. D. P. Edwards and C. Weniger, *A Fresh Approach to Forecasting in Astroparticle Physics and Dark Matter Searches*, *JCAP* **02** (2018) 021 [1704.05458].

[364] T. D. P. Edwards and C. Weniger, *swordfish: Efficient Forecasting of New Physics Searches without Monte Carlo*, 1712.05401.

[365] M. T. Doornhein, *Uses and Limitations of Fisher Forecasting in Setting Upper Limits on the Interaction Strength of Dark Matter, MSc thesis*, 2018.

[366] J. McEnery, A. van der Horst, A. Dominguez, A. Moiseev, A. Marcowith, A. Harding et al., *All-sky Medium Energy Gamma-ray Observatory: Exploring the Extreme Multimessenger Universe*, in *Bulletin of the American Astronomical Society*, vol. 51, p. 245, Sept., 2019, 1907.07558.

[367] K. C. Y. Ng, R. Laha, S. Campbell, S. Horiuchi, B. Dasgupta, K. Murase et al., *Resolving small-scale dark matter structures using multisource indirect detection*, *Phys. Rev. D* **89** (2014) 083001 [1310.1915].

[368] C. Winkler et al., *The INTEGRAL mission*, *Astron. Astrophys.* **411** (2003) L1.

[369] Fermi-LAT collaboration, W. B. Atwood et al., *The Large Area Telescope on the Fermi Gamma-ray Space Telescope Mission*, *Astrophys. J.* **697** (2009) 1071 [0902.1089].

[370] V. Schoenfelder, H. Aarts, K. Bennett, H. de Boer, J. Clear, W. Collmar et al., *Instrument Description and Performance of the Imaging Gamma-Ray Telescope COMPTEL aboard the Compton Gamma-Ray Observatory*, *Astrophysical Journal, Supplement* **86** (1993) 657.

[371] D. Coe, *Fisher Matrices and Confidence Ellipses: A Quick-Start Guide and Software*, 0906.4123.

[372] D. Ghosh, D. Sachdeva and P. Singh, *Future Constraints on Primordial Black Holes from XGIS-THESEUS*, 2110.03333.

[373] S. Furlanetto, S. P. Oh and F. Briggs, *Cosmology at Low Frequencies: The 21 cm Transition and the High-Redshift Universe*, *Phys. Rept.* **433** (2006) 181 [astro-ph/0608032].

[374] J. R. Pritchard and A. Loeb, *21-cm cosmology*, *Rept. Prog. Phys.* **75** (2012) 086901 [1109.6012].

[375] R. Barkana, *The Rise of the First Stars: Supersonic Streaming, Radiative Feedback, and 21-cm Cosmology*, *Phys. Rept.* **645** (2016) 1 [1605.04357].

[376] J. P. Wild, *The Radio-Frequency Line Spectrum of Atomic Hydrogen and its Applications in Astronomy.*, *Astrophysical Journal* **115** (1952) 206.

[377] S. A. Wouthuysen, *On the excitation mechanism of the 21-cm (radio-frequency) interstellar hydrogen emission line.*, *Astronomical Journal* **57** (1952) 31.

[378] G. B. Field, *Excitation of the Hydrogen 21-CM Line*, *Proceedings of the IRE* **46** (1958) 240.

[379] S. Mittal and G. Kulkarni, *Ly α coupling and heating at cosmic dawn*, *Mon. Not. Roy. Astron. Soc.* **503** (2021) 4264 [2009.10746].

[380] G. B. Rybicki and I. P. Dell'Antonio, *The Time development of a resonance line in the expanding universe*, *Astrophys. J.* **427** (1994) 603 [astro-ph/9312006].

[381] J. E. Gunn and B. A. Peterson, *On the Density of Neutral Hydrogen in Intergalactic Space.*, *Astrophysical Journal* **142** (1965) 1633.

[382] R. Barkana and A. Loeb, *Detecting the earliest galaxies through two new sources of 21cm fluctuations*, *Astrophys. J.* **626** (2005) 1 [astro-ph/0410129].

[383] C. M. Hirata, *Wouthuysen-Field coupling strength and application to high-redshift 21 cm radiation*, *Mon. Not. Roy. Astron. Soc.* **367** (2006) 259 [astro-ph/0507102].

[384] J. R. Pritchard and S. R. Furlanetto, *Descending from on high: lyman series cascades and spin-kinetic temperature coupling in the 21 cm line*, *Mon. Not. Roy. Astron. Soc.* **367** (2006) 1057 [astro-ph/0508381].

[385] J. D. Bowman, A. E. E. Rogers, R. A. Monsalve, T. J. Mozdzen and N. Mahesh, *An absorption profile centred at 78 megahertz in the sky-averaged spectrum*, *Nature* **555** (2018) 67 [1810.05912].

[386] J. Dowell and G. B. Taylor, *The Radio Background Below 100 MHz*, *Astrophys. J. Lett.* **858** (2018) L9 [1804.08581].

[387] D. J. Fixsen, A. Kogut, S. Levin, M. Limon, P. Lubin, P. Mirel et al., *ARCADE 2 Measurement of the Absolute Sky Brightness at 3-90 GHz*, *Astrophysical Journal* **734** (2011) 5 [0901.0555].

[388] C. Feng and G. Holder, *Enhanced global signal of neutral hydrogen due to excess radiation at cosmic dawn*, *Astrophys. J. Lett.* **858** (2018) L17 [1802.07432].

[389] A. Fialkov and R. Barkana, *Signature of Excess Radio Background in the 21-cm Global Signal and Power Spectrum*, *Mon. Not. Roy. Astron. Soc.* **486** (2019) 1763 [1902.02438].

[390] H. Liu, G. W. Ridgway and T. R. Slatyer, *Code package for calculating modified cosmic ionization and thermal histories with dark matter and other exotic energy injections*, *Phys. Rev. D* **101** (2020) 023530 [1904.09296].

[391] H. Liu, T. R. Slatyer and J. Zavala, *Contributions to cosmic reionization from dark matter annihilation and decay*, *Phys. Rev. D* **94** (2016) 063507 [1604.02457].

[392] R. Hills, G. Kulkarni, P. D. Meerburg and E. Puchwein, *Concerns about modelling of the EDGES data*, *Nature* **564** (2018) E32 [1805.01421].

[393] A. Chatterjee, T. R. Choudhury and S. Mitra, *CosmoReionMC: a package for estimating cosmological and astrophysical parameters using CMB, Lyman-α absorption, and global 21 cm data*, *Mon. Not. Roy. Astron. Soc.* **507** (2021) 2405 [2101.11088].

[394] J. Mirocha and S. R. Furlanetto, *What does the first highly-redshifted 21-cm detection tell us about early galaxies?*, *Mon. Not. Roy. Astron. Soc.* **483** (2019) 1980 [1803.03272].

[395] J. Goodman and J. Weare, *Ensemble samplers with affine invariance*, *Communications in Applied Mathematics and Computational Science* **5** (2010) 65.

[396] D. Foreman-Mackey, D. W. Hogg, D. Lang and J. Goodman, *emcee: The MCMC Hammer*, *Publ. Astron. Soc. Pac.* **125** (2013) 306 [1202.3665].

[397] E. Bugaev and P. Klimai, *Constraints on amplitudes of curvature perturbations from primordial black holes*, *Phys. Rev. D* **79** (2009) 103511 [0812.4247].

[398] A. S. Josan, A. M. Green and K. A. Malik, *Generalised constraints on the curvature perturbation from primordial black holes*, *Phys. Rev. D* **79** (2009) 103520 [0903.3184].

[399] G. Sato-Polito, E. D. Kovetz and M. Kamionkowski, *Constraints on the primordial curvature power spectrum from primordial black holes*, *Phys. Rev. D* **100** (2019) 063521 [1904.10971].

[400] A. Kalaja, N. Bellomo, N. Bartolo, D. Bertacca, S. Matarrese, I. Musco et al., *From Primordial Black Holes Abundance to Primordial Curvature Power Spectrum (and back)*, *JCAP* **10** (2019) 031 [1908.03596].

[401] L. Husdal, *On Effective Degrees of Freedom in the Early Universe*, *Galaxies* **4** (2016) 78 [1609.04979].

[402] M. Boudaud, M. Cirelli, G. Giesen and P. Salati, *A fussy revisitation of antiprotons as a tool for Dark Matter searches*, *JCAP* **05** (2015) 013 [1412.5696].